RESEARCH TOPICS IN WIND ENERGY 1

Dimitrios I. Chortis

Structural Analysis of Composite Wind Turbine Blades

Nonlinear Mechanics and Finite Element Models with Material Damping

European Academy of Wind Energy

Springer

Research Topics in Wind Energy

Volume 1

Series Editor

Joachim Peinke

For further volumes:
http://www.springer.com/series/11859

Dimitrios I. Chortis

Structural Analysis of Composite Wind Turbine Blades

Nonlinear Mechanics and Finite Element Models with Material Damping

Springer

Dimitrios I. Chortis
Department of Mechanical Engineering
and Aeronautics
Structural Analysis and Active
Materials Group
Applied Mechanics Laboratory
University of Patras
Patras
Greece

ISSN 2196-7806 ISSN 2196-7814 (electronic)
ISBN 978-3-319-00863-9 ISBN 978-3-319-00864-6 (eBook)
DOI 10.1007/978-3-319-00864-6
Springer Cham Heidelberg New York Dordrecht London

Library of Congress Control Number: 2013941372

Printed on acid-free paper

Springer is part of Springer Science+Business Media (www.springer.com)

This Book is dedicated to

my parents, Giannis and Sofia,

my sister Dionysia,

my wife Ioanna

Abstract

The aim of the current work is the development of finite element models capable of predicting the damping and the damped structural dynamic response of laminated composite blades and beams. The book is divided into two main parts, of which the first one studies the material coupling effect on the static and modal characteristics of composite structures. New damping coupling terms are formulated and incorporated into a linear beam finite element to better capture the composite material and structural coupling effects.

The second part describes the theoretical framework for predicting the nonlinear damping and damped vibration of laminated composite structures due to large in-plane tensile and compressive forces. A nonlinear beam finite element for composite strips is developed capable of capturing the effects of geometric nonlinearity on the damping of composite laminates. The damping mechanics consider a strain based Kelvin viscoelastic model and Green-Lagrange nonlinear strain expressions, which introduce geometric nonlinearity into the formulation. Incorporation of first-order shear deformation theory into the equations of motion provides the linear and new nonlinear cross-section stiffness and damping terms. Within each element, the stain field is approximated by linear interpolation shape functions. An incremental-iterative methodology is formulated into the finite element solver, based on the Newton-Raphson technique in order to obtain the system solution at each iteration, till the final convergence is achieved. For the sake of completeness, a series of experimental measurements were carried out for the composite strip, subject to tensile and buckling loads. Correlations with theoretical predictions gave credence to the ability of the nonlinear finite element to predict damping of composite structures undergoing large displacements and rotations in the nonlinear regime. The finite element was further extended to include the nonlinear analysis of large-scale hollow composite structures. New first- and second-order stiffness and damping terms were developed and incorporated into an updated nonlinear beam finite element, capable of capturing the effect of rotational stresses on the static and modal characteristics of composite beams and blades.

Keywords: Nonlinear damping, composites beams, wind-turbine blades, nonlinear finite element, membrane stiffening, buckling, material coupling.

Contents

Chapter 1
Introduction

The main objective of this work is the development of finite element models capable of predicting the structural damping and the damped structural response of laminated composite blades and beams. The theoretical framework presented in the current work consists of two main parts. Firstly, the material coupling effect on the static and modal characteristics of composite structures is investigated. New damping terms encompassing strong material coupling effects are formulated and incorporated into a new 3-D beam finite element capable of predicting the modal characteristics of composite structures. The second part deals with the inclusion of nonlinear effects due to large rotations and initial stresses, the prediction of nonlinear damped structural dynamics and the characterization of the damping of laminated composite strips subject to large in-plane tensile and compressive loads. The nonlinear section mechanics were incorporated into a new nonlinear tubular beam finite element and a research finite element analysis code which enable the computational prediction of nonlinear characteristics of composite blades. The finite element is first applied and experimentally validated for the case of composite strips subject to initial tensile and compressive loads. Based on the successful validation of the nonlinear strip element, an extended nonlinear tubular beam finite element for the damping prediction in more complicated composite structures, such as wind-turbine blade models, is also formulated and presented.

1.1 The Significance of the General Problem

The maximization of wind-turbine energy output density and cost performance is achieved through large rotors with longer and more flexible composite blade configurations, which exceed 60m in length (Figure 1.1). Advanced Carbon/ Epoxy and Glass/Epoxy composite systems are extensively used in new blade designs. These composite materials systems and laminates improve the stiffness/mass and strength/mass ratios and also provide damping which is beneficial for the passive control of vibratory, aeroelastic and acoustic loads, in a variety of structural applications. The structural dynamics and the characterization

D.I. Chortis, *Structural Analysis of Composite Wind Turbine Blades*,
Research Topics in Wind Energy 1,
DOI: 10.1007/978-3-319-00864-6_1,

and prediction of structural composite damping parameters in such rotors exceeds the range of known linear models, hence the inclusion of nonlinear effects into analytical and computational formulations becomes essential for describing the complex structural dynamic behavior of large-scale composite structures, such as wind-turbine and helicopter blades. While the impact of geometric nonlinear effects on the dynamic stiffness and modal frequencies of pre-stressed composite shell structures is well understood, their respective impact on composite damping and on the extension-shear material coupling of blade structures remains mostly unknown.

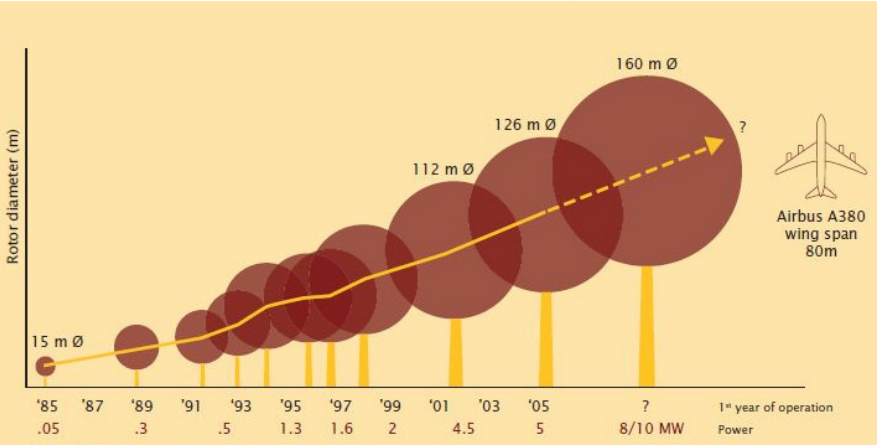

Fig. 1.1 Evolution of wind-turbine blades size

Consequently, the development of damped mechanics models and finite elements for understanding and predicting the complex nonlinear damped structural dynamic behavior of composite laminates subject to large deformations are important steps for improving vibrational, viscoelastic and aeroelastic response of large composite blade structures.

The last fifteen years significant European projects have been carried out in the area of structural analysis of large wind-turbine blades. Among them, DAMBLADE (2006) and UPWIND (2011) integrated EU projects contributed to the introduction of advanced blade concepts with integrated structural design parameters. DAMPBLADE research program enabled the development of damped wind-turbine blade models to study the structural damping in terms of tailoring the laminate damping properties. Its activities included development and characterization of damped composite materials and the evaluation of new technology trends by means of designing, fabricating and full-scale testing of an innovative realistic 19m wind-turbine blade. As far as UpWind, it is the largest-ever EU-funded research and development project on wind energy. Its main contributions were focused on upscaling a reference 5MW wind turbine rotor blade up to 10MW and eventually up to 20MW, reaching a rotor diameter of

150m and 250m, respectively. Within UpWind activities new design tools, concerning the aeroelastic, aerodynamic behavior and the structural integrity of multi-MW turbines, were developed to account for the challenging nonlinear structural response of these composite blade structures.

1.2 Scope and Objectives

The theoretical framework presented in the current work aims to the development of new nonlinear mechanics models and beam finite elements based on the first-order shear deformation theory capable of predicting the structural damped dynamic response of composite beams and blades. The main objectives of this book are summarized below:

- Inclusion and evaluation of material coupling effects on the prediction of static and damped modal characteristics of composite blades structures of various cross-sections and geometries. The developed linear finite element encompasses multi-scale section mechanics models for predicting the stiffness and damping of each composite ply, of the composite skin laminates and eventually of the whole tubular beam section. The damping terms due to material and section coupling are introduced. The capability of the analytical and computational models to predict the structural dynamic behavior of composite blades and beams with non-negligible coupling effects is also quantified.
- Formulation of a nonlinear beam finite element for composite strips subject to large in-plane tensile and buckling loads and characterization of the nonlinear damping and damped vibration response of the structure. The strip finite element provides an excellent case for understanding and validating the nonlinear stiffness and damping predictions in pre-stressed beams and strips transitioning from the pre- to the post-buckling region. The prediction of critical buckling loads and stable buckling paths, as well as the associated nonlinear dynamic response for composite strips could be correlated with measured experimental results.
- Validation of the nonlinear finite element code through comparisons between theoretical predictions and experimental measurements for the case of composite strips. Validation cases will demonstrate the value of the developed beam finite element and will give credence to the new formulated nonlinear stiffness and damping terms.
- Upgrade to a nonlinear hollow beam finite element which will be capable of predicting the static response and the modal damping of large-scale blades subject both to rotational stresses and gravitational loads. Development of nonlinear damped computational structural dynamic models for composite blades is needed to model effects due to large deformations, such as the stress stiffening of long composite structures with complex cross-section geometry and lamination.

1.3 Chapters Outline

The book consists of seven chapters. In the present one, after a brief introduction, the general problem and its significance are reported. The main objectives, which will be analytically investigated throughout this work, are also presented. The structure of the following chapters depends mainly on the type of the developed finite elements and the theoretical frameworks presented in each case.

Second chapter includes an extensively literature survey regarding the international journal articles and conference papers related to the subject and the objectives of the current work. The most important analytical models concerning the prediction of structural damping of composite structures are overviewed. Firstly, the existing models for the undamped structural analysis of thin-walled composite beams and blades are outlined, which are further categorized into linear models with emphasis on the material coupling effect, nonlinear beam theory models with emphasis in analytical solution methods and finite element approaches and works concerning the effect of buckling loading on composite structures. The second part of this chapter summarizes approaches dealing with the introduction of damping in the governing equations of linear and nonlinear formulations for composite structures. This part begins with the macro- and micro-mechanical approaches of damping and then a brief summary on the discrete layer damping models is presented for the sake of completeness. Thereafter, some important works on the prediction of nonlinear damping in composite structures are outlined, which include both analytical solutions and experimental measurements.

Third chapter presents the modeling and evaluation of the effect of material coupling on the structural damping of various composite structures. A beam finite element is developed based on linear kinematic assumptions. The formulation includes composite material coupling effects, first in the element section stiffness and damping matrices and finally into the structural stiffness and damping matrices of the blade. The chapter structure includes the constitutive equations and the strain-displacement relation of the composite ply. Then the blade cross-section mechanics and the formulation of the respective linear stiffness, damping and mass terms of the cross-section are presented. Building upon the damping mechanics, an extended beam finite element is developed capable of providing the stiffness and damping matrices of the structure, which contain new material coupling terms, essential for describing the structural dynamics response of composite beams and blades. The capability of the developed beam finite element to predict the static and the damped modal characteristics of composite structures is quantified by a series of validation cases. Numerical results illustrate the material coupling effect on the static response, natural frequencies and modal loss factor values of composite Carbon/Epoxy box-section beams with various ply angle laminations. Additional comparisons between predicted and measured natural frequencies and modal damping values are shown to quantify the effect of new coupling terms on a Glass/Epoxy small model blade with anti-symmetric angle-ply laminations. In addition, a realistic 19m wind-turbine model is modeled and correlations with experimental measurements are also presented. Finally, the

damped beam finite element is applied to predict the cross-section stiffness and mass properties as well as the modal characteristics of a 61.5m rotor blade.

Fourth chapter reports the theoretical framework regarding the development of a nonlinear finite element for composite strips. The formulation of a plate-beam finite element begins from the composite ply level and ends up to the final beam element stiffness and damping matrices. The governing equations of composite laminates are described, subject to large Green-Lagrange strains, assuming a Kelvin viscoelastic solid. Effective and linearized (tangential) damping and stiffness laminate matrices are formulated assuming first-order shear theory. The constitutive equations, kinematic assumptions and the damping coefficients at composite ply level are also presented. Furthermore, the differential form of the stress equilibrium equation is stated and therefore, based on the principle of virtual work, the weak formulation of the equilibrium equations, being valid for nonlinear as well as linear stress-strain relations, is reported. The damping mechanics and nonlinear structural dynamics formulation continues at section level of the composite strip. The laminate kinematics consider the first-order shear deformation theory assumptions. Incorporation of the constitutive equation into the variational form of equations of motion and integrating over the laminate thickness, yields the detailed expressions of the linear and nonlinear stiffness, damping and mass terms of the finite element. Within each element, the stain field is approximated by linear interpolation shape functions, which ensure the accuracy and the convergence of the solution. Based on these shape functions, the element structural matrices of the system are provided, which depend on the nodal degrees of freedom of the nonlinear solution. Consequently an incremental-iterative methodology is formulated into the finite element solver, based on the Newton-Raphson technique. Collecting the common coefficients and taking into account the contribution of all finite elements the total stiffness, damping and mass matrices of the structure are synthesized. After applying the boundary conditions, the nonlinear static and modal characteristics of the composite structure are obtained. The solution of the linearized system equations takes place in each iteration, till the final convergence is achieved. In each iteration the finite element code calculates both the effective and the tangential (linearized) nonlinear structural matrices as well as the imbalance vector between the external and internal forces. For the sake of completeness, the theoretical background of the small amplitude free-vibration analysis as well as the displacement control method are also described. The Gauss integration method is applied throughout the nonlinear solution in order to calculate the numerical integrations.

Fifth chapter investigates the nonlinear response of the composite strip subject to large in-plane tension and buckling loads and studies the effect of geometric nonlinearities on the modal frequencies and modal loss factor values of composite strips with various angle-ply laminations. The necessary information about the experimental procedure followed for the Glass/Epoxy composite material characterization and the extraction of its elastic properties and damping coefficients is extensively described. In addition, measurements of modal frequency and modal loss factor values of the beam subject to increasing tension or buckling load along its longitudinal axis are presented. The capabilities of the damped beam element to predict the structural stiffness and modal damping values

are highlighted through a series of validation cases. First, numerical results quantify the contribution of the new nonlinear damping and stiffness cross-section terms on the modal frequencies and damping of composite beams of various angle-ply laminations under in-plane tensile loads. Experiments are conducted on cross-ply Glass/Epoxy composite beams and their modal characteristics are measured for various values of increasing in-plane loads. Thereafter, the response of the composite strip as it transitions from the pre- to the post-buckling regime is demonstrated. Numerical studies evaluate the contribution of second-order nonlinear terms on the modal damping of composite plate-strips under in-plane compressive loads in the pre- and the post-buckling region. Overall, validations between predicted and experimental modal loss factors and frequencies of the beams are presented, both for the tensile and compressive loading, which give credence to the developed nonlinear beam finite element.

In the sixth chapter, an updated composite beam finite element formulation for modeling the damped structural analysis of large-scale blades is presented, which includes nonlinear effects due to large displacements and rotations. The new element objective is the prediction of both the static response and the damped dynamic behavior of long composite blades in the nonlinear range. The tubular beam finite element is based on the formulation of the strip element, that was extensively described in the fourth chapter of the manuscript. The introduction of the full Green-Lagrange axial strain expression into the variational form of equation of motion provides the nonlinear stiffness and damping matrices of the blade section. For the sake of completeness, all the formulated first- and second-order effective and tangential terms are presented in analytical expressions. Numerical results regarding the static and modal characteristics of box-section beams with various laminations are also presented. Emphasis is given on the nonlinear loss factor values and their trends variation when the structure undergoes stiffening effects. Theoretical predictions for a 54m girder box-section beam, which consists the structural part of the UP 61.5m wind-turbine blade, are also carried out. Supposing that the girder beam subjects to gravitational loads and rotational stresses, the nonlinear code is capable of describing the stiffening effect on the natural frequencies and the modal damping of the whole composite structure.

In the seventh chapter the main concluding remarks of the this work are presented. Correlation cases between numerical results and experimental measurements in terms of modal damping predictions are also discussed. Finally, directions for future research beyond the content of the current work are recommended.

1.4 DAMPBEAM Finite Element Code

Thework presented in this book was based on a linear finite element code, called "DAMPBEAM", which enables the prediction of the linear damped response of composite beam and blade structures. The linear version of "DAMPBEAM" code was firstly developed and evaluated by Saravanos and coworkers (2006).

This book presents an updated version of "DAMPBEAM" code was developed, capable of describing the effect of new linear stiffness and damping terms and predicting the nonlinear static and modal characteristics of large composite structures. It includes integrated multi-level damping mechanics, which enable the prediction of the structure nonlinear damped response. The composite structural dynamics analysis cycle is schematically presented in Figure 1.2 and described in the following two paragraphs. In summary, the nonlinear element contains new nonlinear terms, whereas, the nonlinear solution is attained through an iterative procedure.

The analysis begins at the composite ply level, where the damping coefficients and mechanical properties of the composite ply are introduced into the nonlinear beam finite element code input. The next key stages include the calculation of stiffness and damping terms firstly at skin laminate and then at section level of the structure. That enables the detailed analysis of complex composite beams and blades, which consist of segments with various laminations and different cross-section shapes. New nonlinear stiffness and damping terms are included at this point. Then, taking into account the number of nodal degrees of freedom at each node and the approximation of the strain field by the shape functions, the beam element stiffness, damping and mass matrices are formulated.

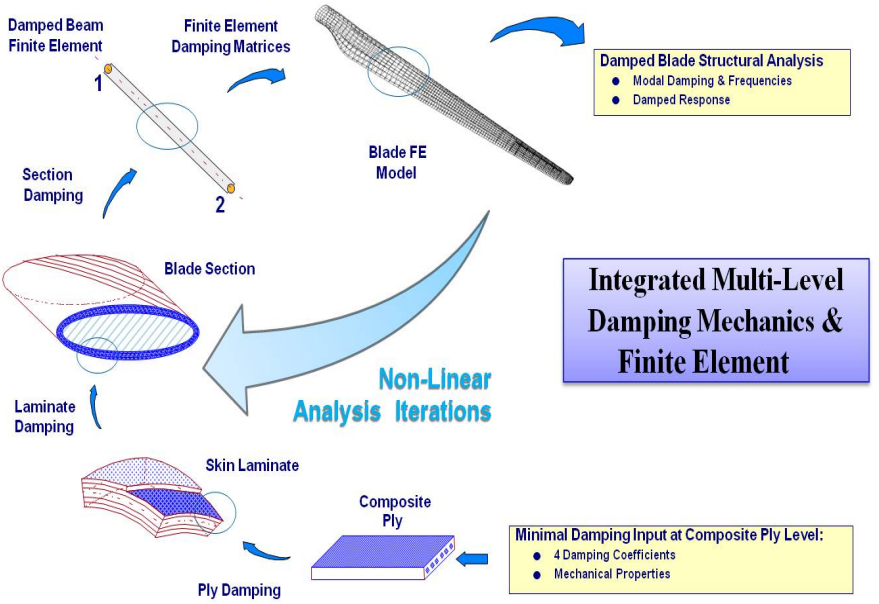

Fig. 1.2 Composite structural dynamics analysis cycle of the DAMPBEAM finite element code

Assembly of all beam element matrices, yields the structural stiffness and damping matrices of the blade. The terms consisting these matrices are

categorized based on their order of nonlinearity. The final step to the problem solution is the incorporation of the proper iterative technique into the solver of the finite element code, which will ensure the convergence at each iteration till the nonlinear equilibrium of the composite structure is achieved.

Chapter 2

Historical Review on the Linear and Nonlinear Damped Structural Behavior of Composite Structures

The present chapter describes the work reported in the area of structural analysis and structural dynamics of composite blade structures. Emphasis is given in the literature survey on analytical beam finite element models which assume linear kinematic assumptions in the constitutive equations. The effect of material coupling terms both in stiffness and damping structural matrices is also presented in the following paragraphs. However, the maximization of wind-turbine blades performance through longer rotor blades in combination with the development of new more flexible helicopter blade designs made the development of new nonlinear models essential regarding their structural analysis.

2.1 Development of Models for the Undamped Structural Analysis of Thin-Walled Composite Beams and Blades

This category includes analytical models for the structural analysis of composite box-section beams as well as the effect of material coupling on their static and dynamic behavior. The literature framework is based on linear kinematic assumptions for the structure section kinematics and includes significant work on the introduction of material coupling effects in structures response.

2.1.1 Nonlinear Beam Theory Models

The purpose of this section is to present some of the most important beam theory formulations and finite elements for predicting the static and undamped dynamic response of composite beams and blades. An extended review on the development of engineering beam theories for helicopter rotor blades was reported by Kunz (1994), which compared and evaluated significant works in this scientific area. Houbolt and Brooks (1958) presented a new formulation for the linear aeroelastic rotor blade analysis based on a linear set of equations of motion. In their work, they developed differential equations for the lateral and torsional deformation of

D.I. Chortis, *Structural Analysis of Composite Wind Turbine Blades*,
Research Topics in Wind Energy 1,
DOI: 10.1007/978-3-319-00864-6_2,

twisted rotating beams applied to helicopter rotor and propeller blades. Improvements on the Houbolt and Brooks formulation were made by Hodges and Dowell (1974), who extended their work in order to include nonlinear phenomena. Their theory was intended for application to long, straight, slender, homogeneous, isotropic beams including dominant nonlinear terms in the equations of motion obtained by two complementary methods; Hamilton's principle and the Newtonian method. Contributions to the development of nonlinear equations of motions of rotor blades have also been made by Rosen and Friedmann (1978), assuming cases with small strain and finite rotations.

Hodges (1988) presented a literature review on modeling of composite rotor blades by separating the existing works into two categories; the ones using an analytical approach to calculate the cross-section stiffness properties and the studies adopting the finite element approach, the latter offering a modeling flexibility on the estimation of elastic properties of structures with general cross-section geometry.

2.1.1.1 Analytical Solution Methods

As far as the analytical approach is concerned, Berdichevsky (1979 and 1981) reported the variational-asymptotic method (VAM) where the geometrically nonlinear problem of the three-dimensional theory of elasticity of beam-like structures was found to be splitted into a nonlinear one-dimensional analysis and a linear two-dimensional analysis, leading to the determination of the cross-sectional stiffness constants. Danielson and Hodges (1987) developed a simple matrix expression for the strain components of a beam in which the displacements and rotations are large. The advantage of their method is that incorporates nonlinear effects without a significant increase of complexity. Hong and Chopra (1985) calculated analytically the cross-sectional properties of a rotor blade, modeled as a composite laminated single-cell box-beam. The strain-displacement relation formulation was based on Hodges and Dowell work, while they used the Hamilton's principle to obtain the equations of motion. Hong and Chopra (1986) extended their work on the aeroelastic analysis of rotor blades by modeling them as an I-section composite beam consisting of laminates with laminas having orthotropic material properties. Hodges et al. (1992) reported a reduced 4x4 stiffness model, based on nonlinear three-dimensional elasticity, which is associated with extension, torsion and two bending measures. An extension to this work was reported by Cesnik et al. (1996), where the curvature and twist of the undeformed state of the beam were incorporated into the kinematical equations. The framework of the variational asymptotic methodology for beams with arbitrary cross-sections geometry was better described by Cesnik (1994), who outlined the applications of this extended work in modeling highly twisted or curved beams, such as rotor blades and prop-fans. Cesnik and Hodges (1997) developed a numerical solution program, the so called VABS, providing the calculation of the cross-sectional stiffness constants matrix for arbitrary cross section, including thin- and thick-walled box beams. The VABS engineering software was further developed by Yu et al. (2002) to include initially curved and

twisted composite beams with arbitrary choice of reference line and validated with an ABAQUS commercial shell element model. Volovoi and Hodges (2000 and 2002) presented a linear asymptotically theory for thin-walled prismatic composite beams which takes into account the shell-bending strain measures. Their formulation included four variables associated with extension, twist and bending in two orthogonal directions. Based on that framework, typical examples for single- and multi-celled thin-walled composite beams were reported and correlated with Berdichevsky et al. (1992). Significant work on the assessment of various beam theories was also reported by Volovoi et al. (2001) and Hodges (2006).

2.1.1.2 Finite Element Approaches

The finite element method was widely used for the analysis of composite beam structures such as wind turbine and helicopter rotor blades. Bathe et al. (1975) presented a detailed review on finite element incremental formulations up to that point, which included large displacements, large strains and material nonlinearities. Wood and Zienkiewicz (1977) reported a two-dimensional finite element solution for geometrically nonlinear problems by introducing a modified isoparametric element for structures containing straight or curved members. The results referred to correlation cases between the finite element predictions and analytical solutions. Ishizaki and Bathe (1980) presented finite element-based solutions for the dynamic analysis of shell structures, including geometric and material nonlinearities. Their work also dealt with the effect of initial imperfections on the static and dynamic buckling behavior of the shell structures. Giavotto et al. (1983) reported a finite element-based linear cross-sectional analysis for the calculation of stiffness and stresses of beam-section structures made of anisotropic and non-homogeneous materials. In addition, they incorporated their model into a computer program and presented correlation cases between predicted results and experimental measurements. Bauchau (1985) developed a beam theory for thin-walled cross-sections assuming that each cross-section is infinitely rigid in its own plane and calculated the eigenvalue problem. Bauchau and Hong (1987) continue this work to include the analysis of initially twisted and curved composite beams. Again the formulation referred to thin-wall beams (TWB) made of composite material which undergo large displacements and rotations but small strains. The nonlinear solution of the problem was based on an iterative technique that uses the linearized equations of the system. The same authors (1988) made a step further to their previous formulation by considering nonlinear terms into the strain-displacement equations. More specifically they introduced a squared shearing term in the Green-Lagrange strain expressions, which consequently introduced a kinematic coupling between extension and twist of the composite structure. The results coming out of this work underlined the contribution of nonlinear terms to the stiffening of the beam subject to axial loading. Kosmatka and Friedmann (1989) reported an analytical model for determining the free-vibration characteristics of advanced composite turbopropellers (prop-fans). A finite element model was obtained from Hamilton's

principle allowing generally anisotropic material behavior, arbitrary cross-sectional properties, large pre-twist angles, out-of-plane cross-section warping, and geometrically nonlinear behavior. The natural frequencies and mode shapes of the structure were calculated assuming linear perturbations about the nonlinear static equilibrium position of the blade. Kalfon and Rand (1993) presented nonlinear theoretical modeling for thin-walled composite helicopter blades assuming nonlinear geometry of the structure which was loaded by axial loads due to its rotation. The solution was achieved by an iterative procedure and theoretical predictions were correlated with numerical results provided by Chandra et al. (1988), as well as experimental measurements. Friedmann and Kosmatka (1993) developed a two-node beam element with 4 degrees of freedom per node based on Hamilton's principle using interdependent cubic and quadratic shape functions for the transverse and rotational displacements of the beam. In 1995, Kosmatka expanded this finite element to predict the buckling load and vibrational behavior of axially-loaded isotropic and composite beams for a variety of beam-lengths and boundary conditions. Bhaskar and Librescu (1995) formulated a nonlinear theory for open or closed composite thin-walled beams taking into account finite displacements and large twist angles. They also included non-classical effects, such as the transverse shear deformation and restrained warping of the cross-section, to study the static dynamic stability and nonlinear torsion of composite beams. In the same decade Hodges and co-workers (Cesnik and Hodges (1997) and Yu et al. (2002)) tried to incorporate VAM into finite element-based cross-sectional analyses in order to provide more consistent results.

Varelis and Saravanos (2004) developed a theoretical framework and a finite element for predicting the nonlinear response of active piezoelectric shells and plates due to large displacements and rotations. An eight-node plate finite element was developed with nonlinear Green-Lagrange strain expressions introduced into the governing equations and kinematic assumptions taken from the mixed-field laminate theory. The shell element is capable of predicting the quasi-static response of composite beams and plates through the incremental-iterative Newton-Raphson solution technique. The same authors presented an extended work (2006a) where they implemented the aforementioned shell element for the prediction of the coupled nonlinear response of smart laminated piezoelectric cylindrical shells undergoing large deformations and snap-through buckling. In order to overcome the snap-through instability of the shell structures subject to pressure loading, the displacement control and arc-length methods were formulated into the Newton-Raphson nonlinear solver.

Saravanos et al. (2006) presented a beam finite element for the damped structural dynamic analysis of tubular composite beams and blades. Linear kinematic assumptions were introduced into the beam formulation, taken from the first-order shear deformation theory (Reissner (1945) and Mindlin (1951)), and the element was capable of predicting the stiffness properties of the structure at each cross-section and at each segment of the cross-section. The unique feature of this beam element was its capability to predict the structural damping of the composite structure. The credibility of the stiffness terms of the developed beam element was

validated with predictions of Volovoi et al. (2000 and 2002) on Carbon/Epoxy box-section cantilever beams with geometric data and material properties taken from Smith and Chopra (1991), and later with measured modal damping and frequency data of model and full-scale wind turbine blades. Vo and Lee (2009) applied a variational formulation, based on the classical laminate theory, to obtain the cross-sectional stiffness matrix of geometrically nonlinear composite structures. Based on the analytical model, the authors developed a displacement-based one-dimensional finite element model capable of predicting the static response of thin-walled box beams and addressing the effects of fiber orientation, and laminate stacking sequence. Recently, Carrera and coworkers reported refined theories for beams with arbitrary cross-section geometries, which include high-order warping terms and applied them on the static (2011a) and free-vibration analysis (2011b) of various beam configurations.

2.1.2 Incorporation of Material Coupling in the Static and Dynamic Analysis of Composite Beams

The material coupling effect was an important issue of great interest for engineers involved in the area of wind-turbine and helicopter rotor blades. Complicated cross-sectional geometries, combined axial, bending and torsional loading cases and extended use of anisotropic composite laminates necessitated the extensive study of these effects in order to obtain maximum structural and aeroelastic efficiency. Nowadays, the impact of material coupling is of high importance in composite beam-like structures, such as long wind-turbine blades, as they affect the aerodynamic loads and the ultimate fatigue loading of the blade.

Mansfield and Sobey (1979) associated composite materials with the aeroelastic tailoring of helicopter blades and developed a model which simplified the blade structure to a thin-walled shell neglecting all warping effects. The numerical analysis applied on tubes representative of GFRP blades and used to obtain a first insight of the role of elastic coupling on rotor blades. Stemple and Lee (1988), developed a finite element formulation to study the combined bending, torsional and extensional behavior of composite helicopter rotor blades and later (1989) they upgraded the beam element to include large deflections or finite rotations. Although the geometries presented were rather simple, indicative results captured the material coupling effects on a composite cylinder under vertical loading. Barbero et al. (1993) presented a simple formulation for computing the bending and shear stiffness of Timoshenko's beam theory for thin-walled laminated beams with open and closed cross-sections subjected to bending and axial loads. This formulation was expanded by Massa and Barbero (1998) to include torque and shear forces. Both papers take into account the flexural-torsional coupling and shear flexibility due to the bending of the structure.

Chandra et al. presented experimental work (1990) as well as comparisons with an analytical model for a Graphite/Epoxy composite box-section beam, reported by Smith and Chopra (1991) and Chandra and Chopra (1992), exhibiting bending-torsion, extension-torsion and bending-shear coupling, typical of helicopter rotor blades. Hodges et al. (1991) evaluated the effect of ply lay-up on natural

frequencies and mode shapes for thin-walled beams of circular cross-section and how the material and geometric configuration are associated with extension-shear-bending coupled modes of the composite structure. Chandra and Chopra (1992) used a Newtonian approach to correlate the vibration characteristics of thin-walled Glass/Epoxy, Kevlar/Epoxy and Carbon/Epoxy symmetric beams encompassing bending-torsion and extension-shear coupling, as well as anti-symmetric beams encompassing extension-torsion and bending-shear couplings. Ganguli and Chopra (1996) conducted a multiobjective aeroelastic optimization for a helicopter blade with two-cell composite blades by altering the composite ply angles. Using an analytical formulation they studied the benefits of composite bending-torsion coupling to the direction of reducing the vibration loads and enhancing the rotor stability at higher rotational speeds. Jung et al. (2002) reported an analytical method, based on first-order shear deformation theory (FSDT) for the prediction of elastic couplings of composite rotor blades. They took into account the influence of shell wall thickness and consequently assumed bending and shear deformations of the structure. Furthermore, they presented correlation cases with Volovoi and Hodges (2000), Berdichevsky et al (1992) and MSC/NASTRAN commercial finite element package, regarding the static behavior of composite beams with both symmetric and anti-symmetric lay-up configurations and the effect of slenderness ratio on box-section and an open-section I-beam.

A series of works have also been presented by Kosmatka, which dealt with pre-twisted beams with arbitrary cross-section geometry made of isotropic or composite materials. Kosmatka (1992) presented an analytical model, based on the Ritz method, including extension-bending-torsion coupling effects of an initially twisted isotropic elastic beam having irregular cross-sections. The formulation is based on four strain components; the extension strain, two bending curvatures and the twist per unit beam length, described in a curvilinear coordinate system. Bhumbla and Kosmatka (1996) presented a nonlinear finite element approach, where a six-node triangular element was developed for the analysis of spinning laminated composite shell structures, based on first-order shear deformation theory. Results outlined the effects of pre-twist, laminate lay-up and rotational speed on the static and dynamic behavior of spinning pre-twisted plates and gave credence to the developed finite element in comparison with other commercial triangular finite elements.

Librescu and co-workers developed a significant framework in the area of material coupling effects. Song and Librescu (1993) focused their work on the free-vibration of cantilevered composite aircraft wings and evaluated the effect of material coupling on the bending eigenfrequencies of those composite structures. The same authors (1997) addressed the problem of the structural elastic coupling of spinning thin-walled composite beams, rotating with a constant angular speed and its effect on the structural natural frequencies. They reached to the conclusion that structural tailoring can be successfully employed to enhance the structural behavior at larger spin rates. Librescu et al. (1997) proposed another perspective of the structural tailoring by applying their numerical model to control the vibration of composite structures by using piezoelectric adaptive materials as strain actuators on lightweight structures, such as helicopter blades. Song et al. (2000) based on the same theory, studied the effect of beam pre-twist, axial

compressive load and the symmetry of the cross-section on the natural frequencies and instability of the structural system and reported that the material tailoring could have a drastic effect on the enhancement of frequency-load interaction. For the case of nonrotating thin-walled beams Qin and Librescu (2001) and (2002) presented static and dynamic validation cases for single-cell box beams. The comparisons revealed excellent agreement not only for static validations with Volovoi et al. (2001) and Smith and Chopra (1991) models but also for dynamic correlation cases of Chandra and Chopra (1992). Yu et al. (2002) based on the engineering software VABS, presented the means to capture all the elastic coupling caused by initial curvature, twist and anisotropic material effects and reached to the conclusion that extension- and bending-shear couplings have influence on the static behavior of these composite beams. Oh et al. (2003) reported an extensive work on the Librescu structural model for a pre-twisted rotating composite thin-walled beam mounted on a rigid hub, exhibiting coupled flapping-lagging-transverse shear vibrations. Emphasis was given on the effect of material ply-angle orientation as well as that on the effect of angular velocity on coupled bending vibrations and eigenfrequencies of the beam.

Saravanos et al. (2006) presented a beam finite element where emphasis placed on the prediction of structural damping from skin laminations exhibiting negligible extension-shear coupling. The effect of the coupling stiffness terms on static and vibrational characteristics of composite beams of various cross-section shapes was also investigated. Based on this work, Chortis et al. (2012) expanded the formulation to include the respective damping coupling terms and evaluated the effect of material coupling effect on a series of validation cases of various composite structures. The formulation included composite material coupling effects, first in the blade section stiffness and damping matrices and finally into the structural stiffness and damping matrices of the blade. Numerical results demonstrated the material coupling effect on the static response, natural frequencies and modal loss factor values of composite Carbon/Epoxy box-section beams with various ply angle laminations. Modal damping predictions quantified the effect of new coupling damping terms on a Glass/Epoxy small model blade with anti-symmetric angle-ply laminations. Furthermore, a realistic 19m wind-turbine blade was modeled and correlations with experimental measurements were also presented. The developed damped beam element was applied for the simulation of a 61.5m rotor blade, whose cross-section stiffness properties and modal characteristics were also predicted.

2.1.3 Effect of Rotational and Buckling Loads on Composite Structures

There is a drastic effect of rotational stresses and compressive loads on composite structures, which affects their structural instability and damping behavior. The majority of articles published in this scientific area associated the tensile or buckling loads with the natural frequencies of the structure and less with the prediction of the modal damping values.

Rotational stresses effect was first investigated on the performance of conventional turbo-propellers and hingeless helicopter blades (Ormiston and

Hodges 1972). Hodges and co-workers (1990 and 2006) presented a series of works concerning the free-vibration analysis of rotating beams. Kosmatka and Labid (1993) reported an extensive experimental database on the behavior of spinning, pre-twisted Graphite/Epoxy composite plates of various geometries and lay-up configurations. They investigated the effect of centrifugal forces on the static and modal characteristics of symmetric and anti-symmetric rotated plates, reaching to the conclusion that increasing rotational speed caused the stiffening of the structure. Thereafter, they associated the natural frequencies behavior with the geometry coupling of the pre-twisted plate. Bazoune (2005) reported an extensive survey on the modal frequency values of centrifugally stiffened beams. The review dealt with the determination of natural frequencies and the associated mode shapes of rotating beams subject to rotational stresses. Virgin (2007) investigated the pre-stressing of thin elastic structures and its effect on the natural frequencies due to axial tensile and membrane loads.

Examples of buckling loading include cases associated with gravitational forces on rotating wind-turbine blades, local buckling of the compressed section due to bending, or pressure loads on light-weight composite shell structures. A brief literature survey on this subject includes the review of Leissa (1987), who presents a summary of the buckling and post-buckling studies of composite laminated plates. Kosmatka (1995) developed a two-node Timoshenko beam element capable of predicting the buckling load and natural frequencies of axially-loaded isotropic and composite beams, while Di Sciuva and Icardi (1995) reported a formulation regarding the static stability equations for initial buckling of laminated Timoshenko beams under transverse and compressive loads. Among others, Engelstad et al. (1992) focused their work on the post-buckling response of panels under compression, while Starnes and Rouse (1985) presented experimental work on Graphite/Epoxy panels loaded in compression. A detailed summary of experimental buckling methods in thin-walled structures concerning columns, beams and plates is reported by Singer et al. (1997). Varelis and Saravanos (2004) and (2006a) presented coupled mechanics and finite element formulations for analyzing the buckling and post-buckling response of active piezocomposite shells and plates. In addition, they formulated a shell finite element method (2006b), which was correlated by experimental results on the prediction of the nonlinear effects on piezocomposite beams subject to large quasi-static deflections and initial stresses. Furthermore, they implemented the displacement control method (Batz and Dhatt (1979)), into the finite element solution in order to overcome stiffness matrix singularities near the critical buckling point. Recently, Lindgaard and Lund (2011) reported a unified approach to nonlinear buckling optimization for composite cylindrical shells using fiber angle parameterization. Theoretical predictions were correlated with commercial FE package results reaching to the conclusion that the nonlinear buckling could be optimized with respect to a general type stability, i.e. critical point stability, especially in cases where geometrically nonlinear effects cannot be ignored. Analytical solutions were also presented by Lesieutre (2009) and Kosmatka (2010). They studied the effect of buckling loads on the stiffness and the damping of composite strips both analytically and experimentally and their main contribution is described in a following paragraph of the present chapter.

2.1.4 Brief Description of Multi-body Dynamic System Approaches

Multi-body dynamic analysis was originally developed as a tool for performing simulations of mechanisms using rigid bodies connected by joints and evolved to the point where it can handle nonlinear flexible systems with arbitrary geometries. Shabana (1985) presented a finite element formulation for viscoelastic analysis of multi-body systems based on a linear Kelvin-Voigt viscoelastic model. A slider crank mechanism made of steel was considered and its modal modes of vibration were employed to describe its deformation. The same author (1986) expanded the finite element scheme to include the dynamic response of multi-body systems with components manufactured by composite orthotropic materials. Significant review papers have also been reported in the area of multi-body systems, including (i) the surveys of Boutaghou and Erdman (1993a and 1993b), who reported the existing formulations up to that point regarding flexible beams undergoing large motions; (ii) the review of Shabana (1997) on basic approaches used in computer aided kinematic and dynamic analysis of flexible mechanical systems. Bauchau et al. (2001) described the multi-body dynamics approach to the modeling of rotorcraft systems. Complex rotor configurations of arbitrary topology were modeled through the assembly of basic components, which included rigid and deformable bodies as well as joint elements. Furthermore, efficient time integration algorithms for dealing with the nonlinear equations and resulting from the proposed formulation were also developed. Kunz (2001) used the double pendulum system to demonstrate a method based on Hamilton's weak principle for assembling and solving the final equations of a multi-body system. In that work, validations with analytical solutions were carried out in order to demonstrate the computational efficiency and the accuracy of the presented methodology.

Riziotis and Voutsinas (1997) presented preliminary results and evaluations of their aerodynamic and structural prediction tool (GAST) on two representative 500 KW wind-turbine machines. The code considered the different parts of the whole machine, i.e. blades, drive train and tower as flexible beams which were introduced as independent bodies with appropriate kinematic and dynamic junction conditions. Correlation cases between GAST predictions and experimental measurements were on a satisfactory level and set the basis for evaluating more complex types of wind-turbine machines. Riziotis (2003) applied the multi-body technique to the elastodynamic analysis of horizontal axis wind-turbine machines. Moving a step further, combination of the former solution with the complete machine aerodynamic analysis, resulted in the prediction of the full coupled aeroelastic response of the structure. To that direction, the coupled model was applied to characterize the aeroelastic behavior of several realistic multi-MW machines. The formulation included a second-order nonlinear beam theory which could describe more adequately large deformations. Large displacements were regarded as rigid body motions and were taken into account by formulating the dynamics of the system within the context of nonlinear multi-body theory (Riziotis and Voutsinas 2006). Assessment of the coupled aeroelastic model is also carried out on a 2.8 MW machine by correlating experimental measurements with three sets of simulation results including linear and nonlinear beam theories.

2.2 Damping Models for Composite Structures

In the following subsections the damping mechanics literature incorporated into macro- and micro-mechanical approaches is discussed. In addition, the works in the area of discrete layer damping as well as some methods regarding the damping optimization in composite structures will also be presented for the sake of completeness. Analytical expressions of various damping parameters, as well as some useful piece of information about basic damping models are reported in Appendix B.

2.2.1 Macro- and Micro-mechanical Models of Damping

The characterization of damping of a composite material is an essential parameter, which affects its static and dynamic structural behavior. The review of the available literature on composite damping includes both analytical studies and experiments on fiber reinforced structures. There are various computational models in the area of damping mechanics of composite materials and laminates. Analytical predictions of damping are based mainly on the correspondence principle and the strain energy method. Hashin (1970) developed the correspondence principle with viscoelastic models to derive the effective complex moduli of fiber reinforced materials. Schultz and Tsai (1968 and 1969) provided experimental measurements of the storage and the loss moduli of unidirectional Glass/Epoxy composite beams. Adams et al. (1969) conducted experiments on unidirectional carbon and glass fiber reinforced plastics in order to calculate the longitudinal damping. Based on this technique, Adams and Bacon (1973a) developed a macro-mechanical model for damping and in parallel they reported a new apparatus in which the flexural damping and dynamic modulus could be determined. The main advantage of the new apparatus was the elimination of the extraneous damping by testing the specimens under free-free support conditions. The same year Adams and Bacon (1973b) presented a theoretical model for the prediction of damping in beams and plates by defining the specific damping capacity (SDC) as the ratio of dissipated to stored strain energy. Gibson and Plunkett (1976) presented comparisons of measurements of the complex moduli with predicted values of Glass/Epoxy composite beams, reaching to the conclusion that damping was sensitive to the frequency whereas the elastic properties were not. Bagley and Torvik (1983) examined a fractional derivative model for viscoelastic materials and calculated the loss factor as the ratio of the dissipated to the maximum stored energy of the material. In addition they outlined the construction and solution of the finite element equations of motion for viscoelastically damped structures. Ni and Adams (1984) developed a comprehensive mathematical technique for predicting the damping of laminated composite beams based on Adams and Bacon's work. They calculated experimentally the SDC both in glass and carbon beams of various types of cross-ply laminations and the results were in excellent agreement with their theoretical

predictions. Suarez et al. (1986) and Gibson et al. (1982) studied experimentally the effect of fiber aspect ratio as well as of fiber orientation on the loss factor values of unidirectional short fibers composites. Moreover, Wren and Kinra (1988) and (1992) used experimental apparatus in order to determine the structural damping of metal-matrix composites. Crane and Gillespie (1991) measured experimentally the damping of a composite cantilever beam test specimen excited with an impulse excitation. They reached to the conclusion that damping is affected by the fiber-matrix type and fiber orientation, whereas it is insensitive to specimen thickness. Adams and Maheri (1994) correlated the measured SDC values of glass and carbon pre-preg symmetric angle-ply and off-axis composite beams with predicted results based on Adams and Bacon damping criterion (1973b). They also studied both experimentally and numerically the effect of beams aspect ratio, fiber orientation and stress amplitude on the SDC. Eldred et al. (1995) reported a comparison on the Kelvin-Voigt damping model with a three and four parameter fractional order constitutive relationships, reaching to the conclusion that the derivative models provided a substantially better model over much larger bandwidth. Pritz (1996) proposed a four parameter fractional derivative model for describing the variation of damping properties of polymers in a wide frequency range, provided that there is one symmetric loss peak. This model was capable of correcting the inaccuracies introduced by the spring-dashpot models, which defined the stress-strain relationship in the time domain by linear differential equation.

The finite element analysis has been used by Cawley and Adams (1978) and Lin et al. (1983) to predict the natural frequencies and SDC of composite plates. An analytical macro-mechanical model was presented by Crane and Gillespie (1992), which combined the elastic-viscoelastic correspondence principle with the classical laminate theory (CLT). The new contribution of this work included the prediction of composite loss factor incorporating its frequency dependence into the analysis. In addition, the effect of fiber orientation on loss factor values was experimentally validated and correlated with relative results from Adams and Bacon (1973b). Maheri and Adams (1995) presented a damped element based on the damping criterion of Adams and Bacon, whose predictions were in good agreement with the respective experimental results conducted in a previous work of the authors (1993).

Various analytical models were also developed using the micro-mechanical approach to damping analysis of composite structures. Chang and Bert (1973) reported micro-mechanical models for the calculation of stiffness and damping in fiber-reinforced composites. Bicos and Springer (1989) studied the free damped vibration of composite plate and shells using a computer code to calculate the natural frequencies, mode shapes and damping factors of plates and panels supported under various conditions. Saravanos and Chamis (1990a) presented an integrated micromechanics theory for the on-axis and off-axis damping capacity of unidirectional composites. In contrast to many previous works, which were restricted to ply damping associated with the longitudinal normal stress or the in-plane shear stress or both, in their proposed unified approach all six damping

coefficients related to six stresses were considered. This methodology also assumed anisotropic dissipative fiber properties, included the friction due to broken fibers and incorporated hygrothermal effects on the elastic and the damping properties of the material. The same year the authors extended their work to include various composite angle plies and laminates (1990b). More specifically, for the case of quasi-isotropic laminations, correlations between predicted and experimental results in addition with comparisons of Ni and Adams (1984) gave credence to their developed damping micromechanics theory. Saravanos and Chamis (1991) presented an integrated finite element based method for the simulation of damping of composite structures. In contrast to the limitations of other methods, such as Cawley and Adams (1978) and Lin et al. (1983), the developed finite element was applicable to both plate and shell-type structures and general laminate configurations. Furthermore, the effect of structural geometry on the structural damping of composite beams, plates and shells was illustrated. Lesieutre (1994) used the complex modulus approach to represent the dissipative properties of transversely isotropic materials, such as unidirectional fiber-reinforced composites. Singh and Gupta (1994) applied first-order deformation theory (FSDT) on layered composite cylindrical shells to predict the loss factor values corresponding to various shell modes. They used the complex modulus approach for harmonic vibrations which was based on the correspondence principle of linear viscoelasticity to obtain the variation of loss factors with shell parameters. Rikards et al. (1995) developed a triangular finite element and predicted the damping by the energy dissipation method for composite plates using a correspondence principle.

Extended work has also been carried out, both numerically and experimentally, for the damping prediction of more realistic structures, such as composite beams, blades and shells. Philippidis et al. (1997) and (2001) predicted the transient forced vibration response of a 10m blade and by conducting experimental damping measurements, the tuning of Rayleigh damping coefficients of a detailed finite element model was achieved. Verification of theoretical predictions was accomplished satisfactorily by comparing with experimental data. Plagianakos and Saravanos (2003) presented a finite element method for predicting the damping of doubly curved laminates and laminated shell composite structures. Damping mechanics calculated the structural modal loss factors using the energy dissipation method. The section kinematics assumed FSDT and therefore an eight-node shell damping finite element was formulated. Correlation cases between predicted and experimental results quantified the ability of the finite element to predict modal damping values and natural frequencies of thin and intermediately thick shell structures. Saravanos et al. (2004) presented a brief description of a theoretical framework for predicting the damping of composite wind-turbine blades with hollow laminated sections. An extended work was reported by Saravanos et al. (2006) where the analytical formulation of a shear beam finite element for the damped structural analysis of composite blades with hollow laminated cross-sections was incorporated into the so called DAMPBEAM finite element code. The novel damped three-dimensional shear beam finite element was capable of

providing the stiffness, mass and damping matrices and of predicting the natural frequencies and modal damping of hollow blades with various laminate configurations. In addition, the modal frequency/damping values of Glass/Polyester composite strips, and beams of uniform elliptical and circular sections were correlated with the damped shell developed by Plagianakos and Saravanos (2003) and the relative values for composite box-section beams were compared with a commercial shell finite element. Berthelot (2006) used the Ritz method to analyze the damping properties of rectangular unidirectional composite plates in combination with experimental characterization of damping in cantilever composite beam specimens subjected to an impulse input.

Chortis et al. (2007) presented a preliminary work based on Saravanos et al. (2006) beam element, which included material coupling effects on damping level of the structure cross-section. Notable differences in predictions were observed in modal damping loss factor and natural frequencies values of Carbon/Epoxy box-section beams for a range of ply angles between $\theta=0^0$ to 90^0. Chortis et al. (2012) expanded their previous work on the effect of material coupling terms by predicting the modal frequency/damping values of small composite model blades. Furthermore, the capabilities of the damped beam element (Saravanos et al. 2006) in predicting the modal loss factor of a realistic 19m wind turbine blade, part of the DampBlade project (2006), were also presented.

2.2.2 Discrete Layer Damping Model Theories

The previously reported structural models fail in the case of very thick composite sandwich sections, or composite laminates with constrained polymer damping layers. For this reason, analytical solutions and finite elements were developed for the prediction of passive damping of laminated plate and shell structures using discrete layer model theories. Among other Gibson and Plunkett (1976), Ni and Adams (1984) and Alam and Asnani (1986 and 1987) presented important works in this field.

Based on their previous work, firstly Saravanos and Chamis (1992a) presented preliminary results and later Saravanos (1994) reported an integrated methodology for the calculation of passive damping based on a discrete layer damping theory (DLDT) for thick laminates/structures including interlaminate shear strains and damping calculation. The formulation of developed DLDT method used linear displacement approximations at each discrete layer of the composite structure. Comparison of classical laminate damping theory (CLDT) with DLDT showed that for very thin laminates both theories gave identical results, whereas the latter one provided better predictions for cross-ply laminations at low aspect ratios and higher-order modes at high temperatures. The potential of the method in capturing the effects of interlaminar stresses due to the laminate configuration of thicker composite plates was further illustrated by Saravanos (1993), who built a four-node bilinear element with damping analysis capabilities. Saravanos and Pereira (1992) used the aforementioned theory to demonstrate the impact of embedded interlaminar damping layers in composite laminates and their effect on natural

frequencies and mode shapes of specialty composite structures (1995). Taylor and Nayfeh (1997) reported an analytical solution taking into consideration discrete layer kinematic assumptions with linear displacement approximations capable of predicting the modal damping capacity of simply supported, thick multilayered composite plate strips. Zapfe and Lesieutre (1999) developed a discrete layer finite element for the dynamic analysis of laminated beams with integral viscoelastic layers for the prediction of modal frequencies and loss factors of cantilever sandwich beams. Lee and Kosmatka (2002) predicted the modal characteristics of cantilevered laminated plates with embedded damping layers using a discrete layer triangular element including higher-order terms in the displacement approximation through the thickness. Moreover, they provided correlations between predicted, experimental and computational results by a commercial finite element package. Plagianakos and Saravanos (2003) formulated a novel plate finite element for the prediction of the total damping capacity of laminated piezocomposite plate structures. According to this method, modal damping and frequencies were predicted from the calculation of the complex eigenvalues-poles of the discretized dynamic equations. The credibility of this method was validated by a series of experimental cases of Graphite/Epoxy beams under various support conditions. The same authors based on the linear layerwise formulations by Saravanos (1993 and 1994) developed a new high-order discrete layer formulation (2004), where quadratic and cubic fields were added in the kinematics of each discrete layer, while maintaining displacement compatibility. The capabilities of the layerwise high-order mechanics included among others the prediction of modal frequencies, damping, through thickness displacement and strain and stress fields in both composite and sandwich beams using the modal strain energy dissipation method. Expanding this work, Plagianakos and Saravanos (2009) developed an integrated formulation which begins with the damped composite ply and is capable of predicting the modal damping in composite plate structures.

2.2.3 Optimization of Composite Damping

Damping in fiber-reinforced materials is highly tailorable and controlled by constituent parameters such as the fiber/matrix properties, the fiber volume ratio and the ply orientation angles. Adams and Bacon (1973) illustrated the effect of fiber orientation and laminate geometry on the flexural and torsional damping of composite materials. Saravanos and Chamis (1990c) presented a method for tailoring plate and shell composite structures for optimal forced damped dynamic response. Their study was based on the finite element method and the criteria for the tailoring of damping were the fiber volume ratios as well as the reduction of the maximum resonance amplitudes by a factor of two (2) while keeping frequencies in the feasible frequency domain.

Hwang and Gibson (1992) reported an extended review regarding the strain energy-based finite element approaches for the estimation of damping in composite structures. Their work was also focused on the optimization of damping of composite materials and structures. To that direction, Saravanos and Chamis (1992) developed a multiobjective optimal design methodology including

micromechanics, laminate and structural shape parameters. The objectives of their methodology included the minimization of the damped resonance amplitudes (or the maximization of modal damping), weight and material cost. Hufenbach et al. (2002) reported an analytical method for the vibration and damping behavior of composite cylindrical shells. Their work included elementary optimization studies for optimizing damping by altering the lay-up and the radius of the CFRP cylindrical structure.

The DAMPBEAM code was applied within the activities of DAMPBLADE project (2006 and Saravanos 2004) to investigate the effect of ply angle and lamination tailoring on the modal frequencies and modal damping of a 19m Glass/Polyester wind-turbine blade. The damping was optimized using a damped polyester resin and by altering the ply orientation of non-unidirectional plies. Maheri (2010) used the theoretical predictions of modal response of a square layered FRP panel to investigate the variation of modal damping with respect to variables such as the laminate lay-up, mode shapes and boundary conditions.

2.3 Theoretical Framework for the Prediction of Nonlinear Damping in Composite Structures

The estimation of damping parameters is essential for composite structures and especially for those subject to large displacements and rotations, such as wind-turbine rotors. Composite blades undergo extreme loadings and therefore the inclusion of nonlinear effects into the damping mechanics is more than necessary.

Torvik (2002) published a work where several standard measurements for determining the damping of linear one-degree of freedom systems were considered and the consequence of stiffness and damping nonlinearities on these measurements were determined. In addition, Torvik (2011) presented the methodology for estimating system damping from the bandwidth of the amplitude response to a specific excitation and studied the consequences of the asymmetry of the response function resulting from an amplitude-dependent stiffness.

Kosmatka (2008) studied both analytically and experimentally the damping response of a beam subject to an initial axial force. This work included: a) analytical results for the axial tension and compression of an Euler-Bernoulli beam composed by a homogenous material with viscous damping; (b) experimental measurements for various composite beams under the same loading conditions. Especially for the case of the applied axial compressive load, the results till the buckling point, indicated decreasing undamped frequency and increasing modal damping values. Kosmatka (2010) expanded his previous work by examining the vibration response of a geometrically-imperfect post-buckled Carbon/Epoxy beam. The effect of a compressive load on the trends of natural frequency and modal damping were investigated, while the beam transitions from the pre- to the post-buckled region. The analytical solution is based on a simply supported beam which is approximated as one degree of freedom (1-DOF) system

and the experimental results were conducted using the displacement control loading method without taking any measurement near the buckling point area.

Recently, Lesieutre (2009) presented analytical solutions based on classical laminate theory which included the effect of membrane loads on the modal damping of composite structures. The solutions considered several damping models and the association of each model with the modal damping prediction was described. In detail, Lesieutre studied the effect of increasing tensile loads both on the natural frequency and the modal damping. Theoretical predictions, which quantified the effect of compressive loads on the modal characteristics, were also presented. Furthermore, a viscous damping model was proposed (2010), which predicted constant modal damping independent of frequency. The developed analytical model yields modal damping for simply-supported flexural beams that is very nearly independent of frequency (mode number). The theoretical predictions were also validated through a simple beam finite element with 2 DOF at each node (lateral displacement and slope), using kinematic assumptions associated with Bernoulli-Euler beam theory.

Chortis et al. (2011) presented the theoretical framework for the nonlinear damped analysis of composite strips. Damping mechanics and nonlinear structural dynamics formulations enable the inclusion of nonlinear effects due to in-plane loads and large deformations on both structural stiffness and damping of laminated composite strips. The governing equations of composite laminates are described, subject to large Green-Lagrange strains, assuming a Kelvin viscoelastic solid. The credibility of the developed nonlinear beam finite element is validated through correlations with experimental measurements on cross-ply Glass/Epoxy beam-strips subject to in-plane tensile loading. Chortis et al. (2013) based on the aforementioned nonlinear formulation, updated the beam element in order to predict nonlinear damping of composite strips undergoing in-plane buckling. The excellent correlation between theoretical predictions and experimental measurements gave credence to the nonlinear beam capabilities to capture the effect of geometric nonlinearities on beam-strip modal damping.

Chapter 3

Linear Material Coupling Effect on Structural Damping of Composite Beams and Blades

The current chapter presents the theoretical background for the damped dynamic analysis of composite beams and blades encompassing material coupling effects. The formulation includes composite material coupling effects, first in the cross-section stiffness and damping matrices and finally into the structural stiffness and damping matrices of the blade. In the following sections, new coupling damping cross-section terms associated with non-negligible ply stiffness and damping terms are formulated. In detail, this chapter consists of seven subsections. Firstly, a brief description of the developed damped beam finite element is presented. The second subsection reports the constitutive equations as well as the strain-displacement relations of the composite ply. Accordingly, the third subsection deals with the blade cross-section mechanics and the formulation of the respective linear stiffness, damping and mass terms of the cross-section. In the fourth subsection, building upon the damping mechanics, an extended beam finite element is developed capable of providing the stiffness and damping matrices of the structure, which contain new material coupling terms, essential for describing the structural dynamics response of composite beams and blades. The capability of the developed beam finite element to predict the static and the damped modal characteristics of composite structures is quantified by a series of validation cases in the fifth subsection of the present chapter. Numerical results illustrate the material coupling effect on natural frequencies and modal loss factor values of composite Carbon/Epoxy box-section beams with various ply angle laminations. Additional comparisons between predicted and measured natural frequencies and modal damping values are shown to quantify the effect of new coupling terms on a Glass/Epoxy small model blade with anti-symmetric angle-ply laminations. A realistic 19m wind-turbine model is also modeled and correlations with experimental measurements are presented. In the sixth subsection, the damped beam finite element is applied for the prediction of the cross-section stiffness and mass properties and the modal characteristics of a 61.5m rotor blade. The major concluding remarks are reported in the last subsection of the present chapter.

D.I. Chortis, *Structural Analysis of Composite Wind Turbine Blades*,
Research Topics in Wind Energy 1,
DOI: 10.1007/978-3-319-00864-6_3, © Springer International Publishing Switzerland 2013

3.1 Tubular Laminated Beam

This subsection provides a brief description of the damped beam mechanics of composite structures having a tubular laminated cross-section of arbitrary shape, as the one shown in Figure 3.1.

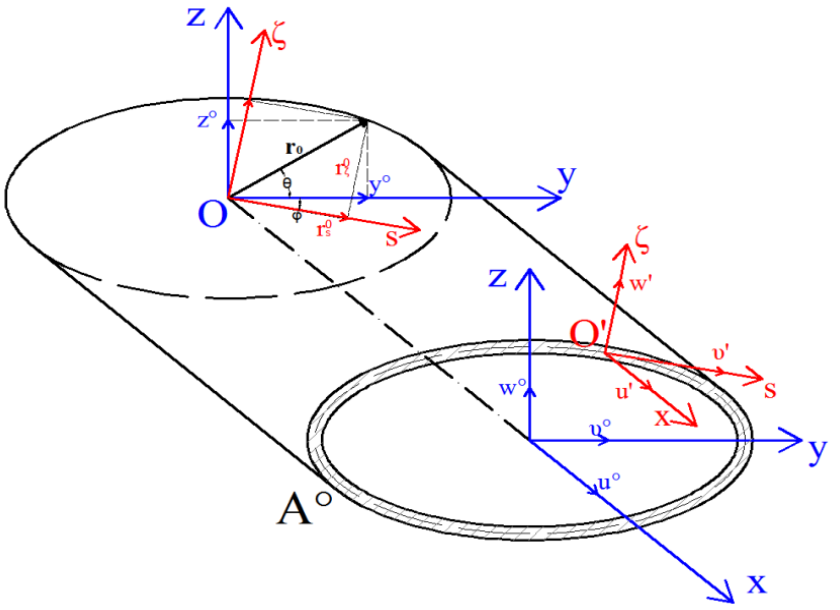

Fig. 3.1 Typical hollow beam cross-section geometry and coordinate systems

The section skin may entail various segments of arbitrary lamination, which are defined around its mid-plane. The beam is considered to be neither curved nor pre-twisted. The equivalent cross-section properties are defined in the Cartesian coordinate system O_{xyz}, whereas the skin lamination, composite ply properties and the equivalent properties of the skin laminate are defined in terms of the local curvilinear system $O'_{xs\zeta}$. The assumed positive directions of the coordinate systems as well as the various levels of analysis have been also schematically depicted in Figure 3.1 and are in detail presented within the next sections of the present chapter.

3.2 Composite Ply Level

The formulation of the beam begins at the composite ply level, which is considered to behave as an orthotropic material. The material properties are defined in the material coordinate system of the composite ply, $O_{1'2'3'}$, as shown in

Figure 3.2a, where 1'-axis is parallel to fibers direction, 2'-axis is perpendicular to 1'-axis and both of them are on the same level and perpendicular to 3'-axis. When the material coordinate system coincides with the global coordinate system, O_{123}, the ply is called on-axis, whereas in the case that the material system is rotated by an angle θ with refer to the global coordinate system, the ply is called off-axis (Figure 3.2b).

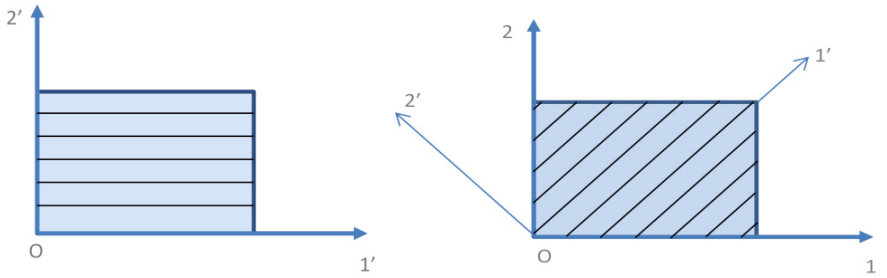

(a) (b)

Fig. 3.2 a) Material coordinate system of an on-axis composite ply; b) Global and material coordinate system of an off-axis composite ply

3.2.1 Constitutive Equations

Structural damping calculation starts at the composite ply level. Each composite ply of the laminate is assumed to have viscoelastic behavior, such that the assumption of a cyclic loading yields the complex stress component $\boldsymbol{\sigma}_c$, which is given by the following relation,

$$\boldsymbol{\sigma}_c = \left(\left[\mathbf{Q}_c \right] + j \left[\mathbf{Q}_c \right] \left[\boldsymbol{\eta}_c \right] \right) \boldsymbol{\varepsilon}_c \tag{3.1}$$

where $\boldsymbol{\sigma}_c$, $\boldsymbol{\varepsilon}_c$ are the engineering stress and strain in extended vectorial notation, respectively, $\left[\mathbf{Q}_c \right]$ is the off-axis ply stiffness matrix, $\left[\boldsymbol{\eta}_c \right]$ is the off-axis damping matrix and j is the imaginary unit. The subscript c indicates that the previous quantities are defined with respect to the structural axes of the local curvilinear coordinate system $O'_{xs\zeta}$.

The characterization of a composite ply damping coefficients is crucial in problems involving the calculation of the structural damping. For the case of an on-axis composite ply the damping matrix $\left[\boldsymbol{\eta}_l \right]$ at the material coordinate system $O_{1'2'3'}$ has the following diagonal form,

$$\left[\boldsymbol{\eta}_l \right] = \mathrm{diag}(\eta_{l1}, \eta_{l2}, \eta_{l3}, \eta_{l4}, \eta_{l5}, \eta_{l6}) \tag{3.2}$$

where, l denotes the material system and 1', 2' and 3' are the longitudinal, transverse and through-thickness axes. Moreover, η_{l1} is the longitudinal (direction 11), η_{l2} the transverse in-plane (direction 22), η_{l3} the transverse through the thickness (direction 33), η_{l6} the in-plane shear (direction 12), η_{l4} the interlaminar shear (direction 23), and $\eta_{l5}=\eta_{l6}$ is the interlaminar shear (direction 13) loss factor. These damping values will be used as input in the developed finite element code for the calculation of the plate-beam damping. According to the kinematic assumptions the transverse shear strain is equal to zero and therefore the term η_{l3} is neglected. Consequently, Eq. (3.2) becomes:

$$[\boldsymbol{\eta}_{\mathbf{l}}]=\mathrm{diag}(\eta_{l1},\eta_{l2},\eta_{l4},\eta_{l5},\eta_{l6}) \tag{3.3}$$

For the case where the material coordinate system has been rotated with refer to the global coordinate system by a θ angle, the composite ply damping is described by the off-axis damping matrix $[\boldsymbol{\eta}_{\mathbf{c}}]$, which is related to the on-axis damping coefficients by the following relation,

$$[\boldsymbol{\eta}_{\mathbf{c}}]=[\mathbf{R}]^{\mathbf{T}}[\boldsymbol{\eta}_{\mathbf{l}}][\mathbf{R}]^{-\mathbf{T}} \tag{3.4}$$

where, $[\mathbf{R}]$ is a proper rotation matrix, described in Appendix C; and symbol T indicates transpose matrix. Thus, the off-axis damping matrix of the composite ply takes the form,

$$[\boldsymbol{\eta}_{\mathbf{c}}]=\begin{bmatrix} \eta_{c11} & \eta_{c12} & 0 & 0 & 0 \\ \eta_{c21} & \eta_{c22} & 0 & 0 & 0 \\ 0 & 0 & \eta_{c44} & \eta_{c45} & 0 \\ 0 & 0 & \eta_{c54} & \eta_{c55} & 0 \\ 0 & 0 & 0 & 0 & \eta_{c66} \end{bmatrix} \tag{3.5}$$

and it is obvious that is a non-diagonal matrix including damping coupling terms in the global coordinate system. The damping variables, which are introduced as input in the finite element code are η_{l1}, η_{l2}, η_{l5} and η_{l6}.

3.2.2 Strain-Displacement Relations

The compatibility strain equations associate the engineering strains with the displacements for a composite ply. Based on that, the expressions of the normal and shear strains in the curvilinear system $O'_{xs\zeta}$ are,

$$\begin{aligned}
\varepsilon_x(x,s,\zeta,t) &= \varepsilon_{xx}(x,s,\zeta,t) = u_{,x} \\
\varepsilon_s(x,s,\zeta,t) &= \varepsilon_{ss}(x,s,\zeta,t) = 0 \\
\varepsilon_\zeta(x,s,\zeta,t) &= \varepsilon_{\zeta\zeta}(x,s,\zeta,t) = 0 \\
\varepsilon_{xs}(x,s,\zeta,t) &= \upsilon_{,x} + u_{,s} \\
\varepsilon_{x\zeta}(x,s,\zeta,t) &= w_{,x} + u_{,\zeta} \\
\varepsilon_{s\zeta}(x,s,\zeta,t) &= w_{,s} + u_{,\zeta} \cong 0
\end{aligned} \tag{3.6}$$

where ε_x, ε_s, ε_ζ refer to the normal strains, $\varepsilon_{x\zeta}$, $\varepsilon_{s\zeta}$ refer to the out-of-plane shear strains and ε_{xs} refers to the in-plane shear strain. All the aforementioned expressions correspond to linear strains of the composite ply.

3.2.3 Equations of Motion

3.2.3.1 Differential Form of Stress Equilibrium Equation

The response of an elastic composite ply is described by the differential form of the stress equilibrium equation, which is valid for any point of the composite ply and has the form,

$$\rho \ddot{u}_i = \sigma_{ij,j} + b_i \qquad i,j = 1,...3 \tag{3.7}$$

where, ρ is the material density; u_i is the mechanical displacement vector; σ_{ij} is the tensor of the applied mechanical stresses at the specific point of the ply and b_i indicates the external body forces per unit volume of the structure. In Eq. (3.7), double superscript dot indicates time differentiation, whereas the comma as a subscript indicates space differentiation.

3.2.3.2 Weak Formulation

Equation (3.7) is a simple form of a differential equation which could yield the exact solution of problems with simple geometry and common support and force conditions. Nevertheless, even for the case of one-dimensional problems the solution is difficult enough to be found, especially when the structure consists of complicated geometry. In such cases, variational formulations are used and applied to the whole volume of the structure. The application of the principle of virtual work in combination with the differential form of stress equilibrium equation, which refers to one point of the ply, yields the "variational form" or the so called "weak form", suitable for the three-dimensional stress analysis of composite structures.

$$\delta \mathbf{u}^{\mathrm{T}} \boldsymbol{\Psi} = \int_V \delta \boldsymbol{\varepsilon}^{\mathrm{T}} \boldsymbol{\sigma} \mathrm{d}V + \int_V \delta \mathbf{u}^{\mathrm{T}} \rho \ddot{\mathbf{u}} \mathrm{d}V - \int_V \delta \mathbf{u}^{\mathrm{T}} \mathbf{b} \mathrm{d}V - \int_\Gamma \delta \bar{\mathbf{u}}^{\mathrm{T}} \bar{\boldsymbol{\tau}} \mathrm{d}\Gamma = 0 \tag{3.8}$$

In the above equilibrium equation symbol δ indicates a virtual variation of displacement around the equilibrium point, where term δu is equal to zero. Likewise, $\bar{\tau}$ is the vector of the external forces applied on the boundary area Γ and V represents the total volume of the composite structure. When the system is not at the equilibrium point, $\boldsymbol{\Psi}$ is the imbalance vector between the internal and external forces acting on the structure, which vanishes at the equilibrium point.

The first integral in the RHS of Eq. (3.8) represents the variation of the strain and dissipated energy of the deformed shape of the structure, the second one the variation of kinetic energy and the last two integrals the variation of the work of body and external forces, which act on the boundary Γ of the ply.

3.3 Composite Cross-Section Mechanics

This subsection objective is to provide the necessary theoretical background for the formulation of the section stiffness, damping and mass terms of the beam finite element. More specifically, the stiffness and damping terms will be formulated and analytically described.

3.3.1 Section Kinematics

Blade kinematics is based upon a first-order shear deformation theory. It assumes extension along x-axis, bending around y and z directions, shear deformations on xy and xz planes and torsion around x-axis. The displacements at each point of the cross-section are expressed in the Cartesian coordinate system $\mathrm{O}_{\mathrm{xyz}}$ and have the following form,

$$\begin{aligned} u(x,y,z,t) &= u^0(x,t) + z\beta_y(x,t) + y\beta_z(x,t) + \theta_{,x}(x)\Psi(y,z) \\ \upsilon(x,y,z,t) &= \upsilon^0(x,t) - z\theta(x) \\ w(x,y,z,t) &= w^0(x,t) + y\theta(x) \end{aligned} \tag{3.9}$$

where: u^0, υ^0 and w^0 are the displacements of the section at the origin of the coordinate system $\mathrm{O}_{\mathrm{xyz}}$; β_y and β_z are bending rotation angles about axes y and z, respectively; θ is the twisting angle and $\Psi(y,z)$ is the secondary warping of the section; superscript 0 indicates mid-section and the comma in the subscripts indicates differentiation. In the curvilinear system $\mathrm{O'}_{\mathrm{xs}\zeta}$ (Figure 3.1), kinematic assumptions of Eqs. (3.9) are transformed to the following form,

$$u'(x,s,\zeta,t)=u^0(x,t)+\beta_y(x,t)\left(z^0+y^0_{,s}\zeta\right)+\beta_z(x,t)\left(y^0-z^0_{,s}\zeta\right)+\theta_{,x}(x)\left(-r^0_\zeta\zeta+\Psi^0(s)\right)$$

$$v'(x,s,\zeta,t)=v^0(x,t)-\theta(x)\left(r^0_\zeta+\zeta\right) \tag{3.10}$$

$$w'(x,s,\zeta,t)=w^0(x,t)+\theta(x)r^0_s$$

where $\left(y^0,z^0\right)$ and $\left(r^0_s,r^0_\zeta\right)$ are the projections of the vector $\mathbf{r^0}$ describing the distance between a point O' on the skin mid-surface from point O on the section x -axis, on the respective axes of coordinate systems O_{xyz} and $O'_{xs\zeta}$; $\Psi(s,z)=\left(-r^0_\zeta\zeta+\Psi^0(s)\right)$ is the secondary warping function of the section. Figure 3.3 illustrates the generalized displacements of the composite beam cross-section and their respective positive directions.

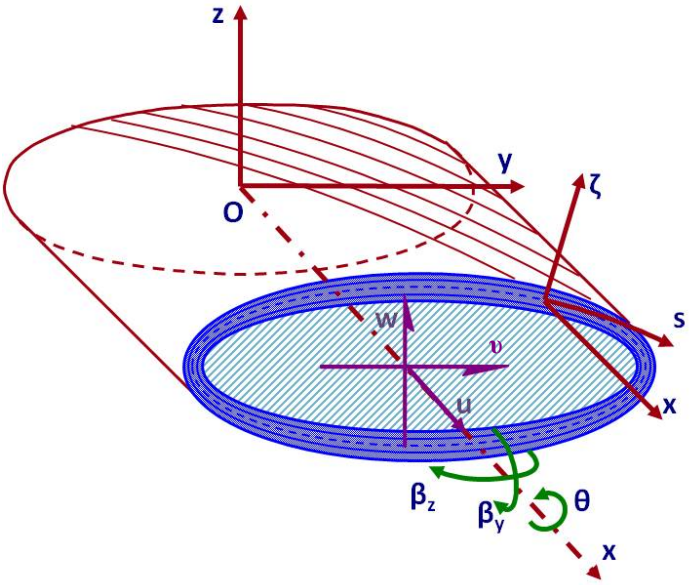

Fig. 3.3 Composite tubular beam cross-section generalized displacements

Incorporation of compatibility strain Eqs. (3.6) with kinematic assumptions of Eqs. (3.9) and (3.10) yields the normal and the shear strains acting on the structure cross-section,

$$\varepsilon_x(x,s,\zeta,t)=\varepsilon_x^0(x,t)+k_{xy}(x,t)\left(z^0+y_{,s}^0\zeta\right)+k_{xz}(x,t)\left(y^0-z_{,s}^0\zeta\right)+k_{\theta\theta}(x)\left(-r_\zeta^0\zeta+\Psi^0(s)\right)$$

$$\varepsilon_{xs}(x,s,\zeta,t)=\varepsilon_{xz}^0(x)z_{,s}^0+\varepsilon_{xy}^0(x)y_{,s}^0+\varepsilon_{xs}^{0t}(x,s)-2k_\theta(x)\zeta \tag{3.11}$$

$$\varepsilon_{x\zeta}(x,s,\zeta,t)=\varepsilon_{xz}^0(x)y_{,s}^0-\varepsilon_{xy}^0(x)z_{,s}^0$$

The previous generalized strains, which equivalently describe the section deformation include the axial strain, ε_x^0, the transverse shear strains ε_{xy}^0, ε_{xz}^0, the bending curvatures k_{xy}, k_{xz} and the twisting curvatures k_θ, $k_{\theta\theta}$. The second twisting curvature $k_{\theta\theta}$ expresses second-order variation and is assumed to be negligible with respect to other generalized strains.

Engineering strains,

$$\varepsilon_x^0=u_{,x}^0$$

$$\varepsilon_{xy}^o=v_{,x}^o+\beta_z \tag{3.12}$$

$$\varepsilon_{xz}^o=w_{,x}^o+\beta_y$$

Curvatures,

$$k_{xy}=\beta_{y,x}$$

$$k_{xz}=\beta_{z,x} \tag{3.13}$$

$$k_\theta=\theta_{,x}$$

3.3.2 Variational Form of Beam Equations of Motion

The equations of motion of the beam (Eq.(3.8)) could be, alternatively described by the following variational form,

$$\int_0^L \mathrm{d}x\int_A \delta H\mathrm{d}s\mathrm{d}\zeta+\int_0^L \mathrm{d}x\int_A \delta W_d\mathrm{d}s\mathrm{d}\zeta+\int_0^L \mathrm{d}x\int_A \delta T\mathrm{d}s\mathrm{d}\zeta+\oint_\Gamma \delta\bar{\mathbf{u}}^{\mathrm{T}}\bar{\boldsymbol{\tau}}\mathrm{d}\Gamma=0 \tag{3.14}$$

where: H, W_d and T are the strain, dissipated and kinetic energy, respectively; $\bar{\tau}$ are surface tractions on the free surface Γ; A is the cross-sectional area covered by material and L is the length of the beam. Symbol δ indicates virtual variation.

In Eq. (3.15) the variation of the strain energy, over the cross-sectional area becomes,

$$\delta H^{\sec} = \int_A \delta\boldsymbol{\varepsilon}_{\mathbf{c}}^{\mathbf{T}}\boldsymbol{\sigma}_{\mathbf{c}}\mathrm{d}s\mathrm{d}\zeta = \oint \mathrm{d}s \int_h \delta\boldsymbol{\varepsilon}_{\mathbf{c}}^{\mathbf{T}}\left[\mathbf{Q}_{\mathbf{c}}\right]\boldsymbol{\varepsilon}_{\mathbf{c}}\mathrm{d}\zeta = \oint \left\{\delta\boldsymbol{\varepsilon}^{\mathbf{0}^{\mathbf{T}}}, \delta\mathbf{k}^{\mathbf{T}}\right\}\begin{bmatrix}\mathbf{A}_{\mathbf{s}} & \mathbf{B}_{\mathbf{s}} \\ \mathbf{B}_{\mathbf{s}}^{\mathbf{T}} & \mathbf{D}_{\mathbf{s}}\end{bmatrix}\begin{Bmatrix}\boldsymbol{\varepsilon}^{\mathbf{0}} \\ \mathbf{k}\end{Bmatrix}\mathrm{d}s \tag{3.15}$$

where, the subscript s denotes the skin laminate of the structure. Respectively, the variation of dissipated energy due to composite damping over the section vibration cycle is,

$$\delta W_d^{\sec} = \int_A \delta\boldsymbol{\varepsilon}_{\mathbf{c}}^{\mathbf{T}}\left[\mathbf{Q}_{\mathbf{c}}\right]\left[\boldsymbol{\eta}_{\mathbf{c}}\right]\boldsymbol{\varepsilon}_{\mathbf{c}}\mathrm{d}s\mathrm{d}\zeta = \oint ds \int_h \delta\boldsymbol{\varepsilon}_{\mathbf{c}}^{\mathbf{T}}\left[\mathbf{Q}_{\mathbf{c}}\right]\left[\boldsymbol{\eta}_{\mathbf{c}}\right]\boldsymbol{\varepsilon}_{\mathbf{c}}\mathrm{d}\zeta \tag{3.16}$$

The complete form of the off-axis strains and stresses of a rotated composite ply are,

$$\begin{aligned}\boldsymbol{\varepsilon}_{\boldsymbol{c}} &= \{\varepsilon_{c1}, \varepsilon_{c2}, \varepsilon_{c4}, \varepsilon_{c5}, \varepsilon_{c6}\} = \{\varepsilon_{cx}, \varepsilon_{cs}, \varepsilon_{cs\zeta}, \varepsilon_{cx\zeta}, \varepsilon_{cxs}\} \\ \boldsymbol{\sigma}_{\boldsymbol{c}} &= \{\sigma_{c1}, \sigma_{c2}, \sigma_{c4}, \sigma_{c5}, \sigma_{c6}\} = \{\sigma_{cx}, \sigma_{cs}, \sigma_{cs\zeta}, \sigma_{cx\zeta}, \sigma_{cxs}\}\end{aligned} \tag{3.17}$$

where, c indicates off-axis ply.

Matrices $\left[\mathbf{Q}_{\mathbf{c}}\right]$ and $\left[\boldsymbol{\eta}_{\mathbf{c}}\right]$ are the equivalent off-axis stiffness and damping (loss factor) matrices of the composite ply with respect to the curvilinear system $O'_{xs\zeta}$, defined in the Appendix C. The damping matrix $\left[\boldsymbol{\eta}_{\mathbf{c}}\right]$ is related to three in-plane damping coefficients of the composite ply, which are the longitudinal, transverse and in-plane shear loss factors, respectively (Saravanos 1993). It is pointed out that both ply stiffness and damping matrices include axial in-plane shear coupling terms, Q_{16} and η_{16}, respectively.

The kinetic energy variation $\delta T^{\sec}$, is represented by the integral over the cross-sectional area,

$$\delta T^{\sec} = \int_A -\delta\mathbf{u}^{\mathbf{T}}\mathrm{diag}(\boldsymbol{\rho})\ddot{\mathbf{u}}\mathrm{d}s\mathrm{d}\zeta = \oint \mathrm{d}s \int_h -\delta\mathbf{u}^{\mathbf{T}}\mathrm{diag}(\boldsymbol{\rho})\ddot{\mathbf{u}}\mathrm{d}\zeta \tag{3.18}$$

In the above equations, **diag(ρ)** is the diagonal matrix with diagonal elements equal to the mass density ρ of the ply and h is the thickness of the skin laminate. The detailed form of the equivalent mass cross-section matrices is reported by Saravanos et al. (2006) and is also provided in Appendix C.

3.3.3 Section Stiffness Terms

Using the strain expressions provided by Eqs. (3.11) in combination with Eq. (3.15), integrating over the skin thickness and around the skin midline, the stored strain energy of the section is finally expressed in terms of the generalized strains and the equivalent section stiffness terms, as follows,

$$\delta H^{\sec} = \oint \left(\delta \boldsymbol{\varepsilon}^{\mathbf{0}^{\mathrm{T}}} \left[\mathbf{A}^{\mathbf{0}} \right] \boldsymbol{\varepsilon}^{\mathbf{0}} + 2 \delta \boldsymbol{\varepsilon}^{\mathbf{0}^{\mathrm{T}}} \left[\mathbf{B}^{\mathbf{0}} \right] \mathbf{k} + \delta \mathbf{k}^{\mathrm{T}} \left[\mathbf{D}^{\mathbf{0}} \right] \mathbf{k} \right) \mathrm{d}s = \left\{ \delta \boldsymbol{\varepsilon}^{\mathbf{0}^{\mathrm{T}}}, \quad \delta \mathbf{k}^{\mathrm{T}} \right\} \begin{bmatrix} \left[\mathbf{A}^{\mathbf{0}} \right] & \left[\mathbf{B}^{\mathbf{0}} \right] \\ \left[\mathbf{B}^{\mathbf{0}} \right]^{\mathrm{T}} & \left[\mathbf{D}^{\mathbf{0}} \right] \end{bmatrix} \begin{Bmatrix} \boldsymbol{\varepsilon}^{\mathbf{0}} \\ \mathbf{k} \end{Bmatrix} \tag{3.19}$$

where, $\boldsymbol{\varepsilon}^{\mathbf{0}} = \left\{ \varepsilon_x^0, \varepsilon_{x\zeta}^0, \varepsilon_{xs}^0 \right\}$ and $\mathbf{k} = \left\{ k_{xy}, k_{xz}, k_\theta \right\}$ represent the equivalent strain and curvature of the section, respectively. The previous equation yields the equivalent extensional-shear, coupling and flexural-torsional stiffness matrices $\left[\mathbf{A}^{\mathbf{0}} \right]$, $\left[\mathbf{B}^{\mathbf{0}} \right]$ and $\left[\mathbf{D}^{\mathbf{0}} \right]$, of the cross-section, having the form,

$$\left[\mathbf{A}^{\mathbf{0}} \right] = \begin{bmatrix} A_{11}^0 & \bar{A}_{15}^0 & \bar{A}_{16}^0 \\ \bar{A}_{51}^0 & A_{55}^0 & A_{56}^0 \\ \bar{A}_{61}^0 & A_{65}^0 & A_{66}^0 \end{bmatrix}, \quad \left[\mathbf{B}^{\mathbf{0}} \right] = \begin{bmatrix} B_{11}^0 & B_{12}^0 & \bar{B}_{16}^0 \\ \bar{B}_{51}^0 & \bar{B}_{52}^0 & B_{56}^0 \\ \bar{B}_{61}^0 & \bar{B}_{62}^0 & B_{66}^0 \end{bmatrix}, \quad \left[\mathbf{D}^{\mathbf{0}} \right] = \begin{bmatrix} D_{11}^0 & D_{12}^0 & \bar{D}_{16}^0 \\ D_{21}^0 & D_{22}^0 & \bar{D}_{26}^0 \\ \bar{D}_{61}^0 & \bar{D}_{62}^0 & D_{66}^0 \end{bmatrix} \tag{3.20}$$

The overbar indicates the section stiffness terms, named thereafter as stiffness coupling terms, which depend directly to the extension-shear coupling stiffness components of the skin laminate A_{16}, B_{16}, D_{16},, These coupling terms induce coupling between extension-shear (A_{15}^0 and A_{16}^0), coupling between extension and torsion (B_{16}^0) and coupling between bending and torsion (D_{16}^0 and D_{26}^0). The coupling terms vanish if the respective skin laminate coupling stiffness is negligible or zero $\left(Q_{16} = 0 \right)$. Detailed description of the stiffness terms is provided by Saravanos et al. (2006) and their expressions are reported in Appendix C.

3.3.4 Section Damping Terms

The significance of the third chapter of the present worklies in part on the formulation of the section coupling damping terms of the beam finite element. To that direction, similarly to the section stiffness terms, the substitution of Eqs. (3.11) into the dissipated energy Eq. (3.16) in combination with the integration over the cross-sectional area, yields the dissipated energy of the section, $W_d^{\sec}$,

$$\delta W_d^{\sec} = \oint \left(\delta \boldsymbol{\varepsilon}^{\mathbf{0}^{\mathrm{T}}} \left[\mathbf{A}_{\mathbf{d}}^{\mathbf{0}} \right] \boldsymbol{\varepsilon}^{\mathbf{0}} + \delta \boldsymbol{\varepsilon}^{\mathbf{0}^{\mathrm{T}}} \left[\mathbf{B}_{\mathbf{d}}^{\mathbf{0}} \right] \mathbf{k} + \delta \mathbf{k}^{\mathrm{T}} \left[\mathbf{B}_{\mathbf{d}}^{\mathbf{0}^{\mathrm{T}}} \right] \boldsymbol{\varepsilon}^{\mathbf{0}} + \delta \mathbf{k}^{\mathrm{T}} \left[\mathbf{D}_{\mathbf{d}}^{\mathbf{0}} \right] \mathbf{k} \right) \mathrm{d}s \tag{3.21}$$

which can be alternatively written in the following form,

$$\delta W_d^{\sec} = \left\{ \delta \boldsymbol{\varepsilon}^{\mathbf{0}^{\mathrm{T}}}, \quad \delta \mathbf{k}^{\mathrm{T}} \right\} \begin{bmatrix} \left[\mathbf{A}_{\mathbf{d}}^{\mathbf{0}} \right] & \left[\mathbf{B}_{\mathbf{d}}^{\mathbf{0}} \right] \\ \left[\mathbf{B}_{\mathbf{d}}^{\mathbf{0}} \right]^{\mathrm{T}} & \left[\mathbf{D}_{\mathbf{d}}^{\mathbf{0}} \right] \end{bmatrix} \begin{Bmatrix} \boldsymbol{\varepsilon}^{\mathbf{0}} \\ \mathbf{k} \end{Bmatrix} \tag{3.22}$$

The dissipated energy of the section is expressed in terms of the arbitrary combination of cyclic strain and bending curvatures and twisting angles. $\left[\mathbf{A_d^0}\right]$, $\left[\mathbf{B_d^0}\right]$ and $\left[\mathbf{D_d^0}\right]$ are the damping matrices having the following form,

$$\left[\mathbf{A_d^0}\right]=\begin{bmatrix} A_{d11}^0 & \bar{A}_{d15}^0 & \bar{A}_{d16}^0 \\ \bar{A}_{d51}^0 & A_{d55}^0 & A_{d56}^0 \\ \bar{A}_{d61}^0 & A_{d65}^0 & A_{d66}^0 \end{bmatrix}, \qquad \left[\mathbf{B_d^0}\right]=\begin{bmatrix} B_{d11}^0 & B_{d12}^0 & \bar{B}_{d16}^0 \\ \bar{B}_{d51}^0 & \bar{B}_{d52}^0 & B_{d56}^0 \\ \bar{B}_{d61}^0 & \bar{B}_{d62}^0 & B_{d66}^0 \end{bmatrix},$$

$$\left[\mathbf{D_d^0}\right]=\begin{bmatrix} D_{d11}^0 & D_{d12}^0 & \bar{D}_{d16}^0 \\ D_{d21}^0 & D_{d22}^0 & \bar{D}_{d26}^0 \\ \bar{D}_{d61}^0 & \bar{D}_{d62}^0 & D_{d66}^0 \end{bmatrix} \tag{3.23}$$

In Eq. (3.23), the $\left[\mathbf{A_d^0}\right]$, $\left[\mathbf{B_d^0}\right]$ and $\left[\mathbf{D_d^0}\right]$ damping matrices express the equivalent damping and energy dissipation per unit length of the beam due to extension-shear, extension-bending coupling and bending-torsion deformation, respectively. Saravanos et al. (2006) have already formulated the damping terms which are independent of the material coupling effect and indicated without the overbar. The detailed form of these terms is provided in Appendix C for sake of completeness. *The terms with overbar, indicating damping coupling, are new contribution of the present work and are associated with extension-shear ply coupling, induced by nonzero ply stiffness* Q_{c16} *and damping* η_{c16} *coefficients*.

They include:

Extension-shear damping coupling terms,

$$\bar{A}_{d15}^0=\oint\left(A_{d16}z_{,s}^0\right)\mathrm{d}s$$

$$\bar{A}_{d16}^0=\oint\left(A_{d16}y_{,s}^0\right)\mathrm{d}s \tag{3.24}$$

Flexural-torsional damping coupling terms,

$$\bar{D}_{d16}^0=\oint\left(-A_{d16}A_h z^0-B_{d16}\left(A_h y_{,s}^0+2z^0\right)-2D_{d16}y_{,s}^0\right)\mathrm{d}s$$

$$\bar{D}_{d26}^0=\oint\left(-A_{d16}A_h y^0+B_{d16}\left(A_h z_{,s}^0-2y^0\right)+2D_{d16}z_{,s}^0\right)\mathrm{d}s \tag{3.25}$$

and the damping coupling terms,

$$\bar{B}_{d16}^{0} = \oint \left(-A_{d16}A_h - 2B_{d16}\right) \mathrm{d}s$$

$$\bar{B}_{d51}^{0} = \oint \left(A_{d16}z^0 + B_{d16}y_{,s}^{0}\right) z_{,s}^{0} \mathrm{d}s$$

$$\bar{B}_{d52}^{0} = \oint \left(A_{d16}y^0 - B_{d16}z_{,s}^{0}\right) z_{,s}^{0} \mathrm{d}s \tag{3.26}$$

$$\bar{B}_{d61}^{0} = \oint \left(A_{d16}z^0 + B_{d16}y_{,s}^{0}\right) y_{,s}^{0} \mathrm{d}s$$

$$\bar{B}_{d62}^{0} = \oint \left(A_{d16}y^0 - B_{d16}z_{,s}^{0}\right) y_{,s}^{0} \mathrm{d}s$$

In the above equations, $\left[\mathbf{A_d}\right]$, $\left[\mathbf{B_d}\right]$, $\left[\mathbf{D_d}\right]$ are effective extensional, coupling and flexural loss stiffness matrices of the skin laminate. In addition, y^0, z^0 are the coordinates of the skin laminate midline, s is the curvilinear length; $y_{,s}^{0} = \mathrm{d}y^0/\mathrm{d}s$, $z_{,s}^{0} = \mathrm{d}z^0/\mathrm{d}s$ are derivatives of the midline coordinates. Finally, $A_h = A_0/\lambda h$, where A_0 and λ are geometric section parameters defined by,

$$A_0 = \oint r_{\zeta}^{0} \mathrm{d}s, \quad \lambda = \oint \frac{1}{h} \mathrm{d}s \tag{3.27}$$

3.3.5 Section Mass Terms

The substitution of the displacement relations (Eq. (3.10)) into the kinetic energy variation (Eq. (3.18)), and subsequently the integration firstly over the thickness (h) and then along the skin midline (s), yields the kinetic energy of the section in terms of generalized displacement.

$$\delta T^{\mathrm{sec}} = \oint \left(\delta \mathbf{u^{0T}} \mathbf{m^A} \ddot{\mathbf{u}}^{\mathbf{0}} + 2\delta \mathbf{u^{0T}} \mathbf{m^B} \ddot{\boldsymbol{\beta}} + \delta \boldsymbol{\beta}^{\mathbf{T}} \mathbf{m^D} \ddot{\boldsymbol{\beta}}\right) \mathrm{d}s \tag{3.28}$$

where $\mathbf{u^0} = \left\{u^0, \quad v^0, \quad w^0\right\}$ and $\boldsymbol{\beta} = \left\{\beta_y, \quad \beta_z, \quad \theta\right\}$ represent the average displacements and rotations of the section, respectively. Likewise, $\mathbf{m^A}$, $\mathbf{m^B}$, $\mathbf{m^D}$ are the equivalent linear mass, coupling and rotational inertia matrices of the cross-section, per unit length, having the detailed form,

$$\mathbf{m^A}=\begin{bmatrix} m_{11}^A & 0 & 0 \\ 0 & m_{11}^A & 0 \\ 0 & 0 & m_{11}^A \end{bmatrix},\quad \mathbf{m^B}=\begin{bmatrix} m_{11}^B & m_{12}^B & m_{13}^B \\ 0 & 0 & m_{23}^B \\ 0 & 0 & m_{33}^B \end{bmatrix},\quad \mathbf{m^D}=\begin{bmatrix} m_{11}^D & m_{12}^D & m_{13}^D \\ m_{21}^D & m_{22}^D & m_{23}^D \\ m_{31}^D & m_{32}^D & m_{33}^D \end{bmatrix} \tag{3.29}$$

The detailed expressions of each terms included in the $\mathbf{m^A}$, $\mathbf{m^B}$, $\mathbf{m^D}$ matrices have already been presented Saravanos et al. (2006) and included in the Appendix C for the sake of completeness of the current work.

3.4 Structural Level

The next key step is the incorporation of the cross-section stiffness, damping and mass terms into the developed damped beam mechanics and the formulation of the respective finite element structural matrices.

3.4.1 Damped Beam Finite Element Formulation

A shear beam finite element is formulated for the damped dynamic analysis of tubular composite beam structures (Figure 3.4) such as wind-turbine blades. The element has 6 DOFs at each node (indicated with superscript i),

$$\mathbf{U_e^i}=\left\{u^{oi},\quad v^{oi},\quad w^{oi},\quad \beta_y^i,\quad \beta_z^i,\quad \theta^i\right\} \tag{3.30}$$

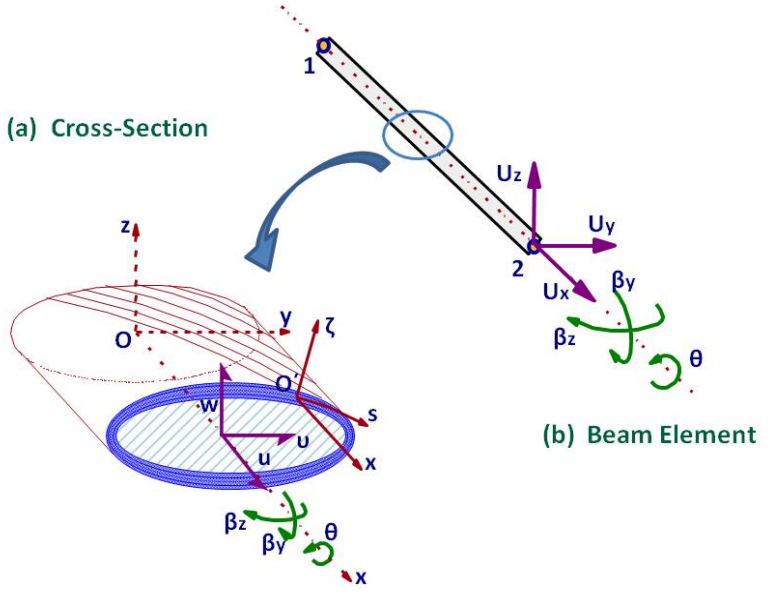

Fig. 3.4 Tubular laminated composite beam element: (a) Cross-section module; (b) Finite element.

which are respectively: the three displacements u, v, w at the origin O_{xyz} of the section, the two bending rotation angles β_y and β_z and the twisting angle θ. The previous 6 DOFs admit deformations of the beam in all dimensions, therefore it is termed thereafter as three-dimensional shear beam element.

3.4.1.1 Shape Functions of the Tubular Beam Finite Element

The generalized displacements along the axis of the beam are approximated by c^0 continuous interpolation functions $N^i(x)$. These functions are consistently used within along this work and their detailed form is presented in the fourth chapter. The approximation of the generalized displacements along the axis of the beam is described analytically by the following relations,

$$u^o(x) \cong \sum_{i=1}^{n} N^i(x) u^{oi} \quad v^o(x) \cong \sum_{i=1}^{n} N^i(x) v^{oi} \quad w^o(x) \cong \sum_{i=1}^{n} N^i(x) w^{oi}$$

$$\beta_y(x) \cong \sum_{i=1}^{n} N^i(x) \beta_y^i \quad \beta_z(x) \cong \sum_{i=1}^{n} N^i(x) \beta_y^i \quad \theta(x) \cong \sum_{i=1}^{n} N^i(x) \theta^i \tag{3.31}$$

where $N^i(x)$ is the interpolation function and the superscript i indicates nodal variables. The developed beam finite element has $n=2$ nodes and due to that fact the interpolation functions are linear. Based on the fact that there are six DOFs at each node, there will be: 2 nodes x 6 DOF per node = 12 DOF at each beam finite element.

The relation between the generalized strains and curvatures and the nodal DOF values at the finite element, is shown in the next set of equations,

$$\varepsilon_x^0 = u_{,x}^0 \cong N_{,x}^i(x) u^i$$

$$\varepsilon_{xy}^o = v_{,x}^o + \beta_z \cong N_{,x}^i(x) v^i + N^i(x) \beta_z{}^i$$

$$\varepsilon_{xz}^o = w_{,x}^o + \beta_y \cong N_{,x}^i(x) w^i + N^i(x) \beta_y{}^i$$

$$k_{xy} = \beta_{y,x} \cong N_{,x}^i(x) \beta_y{}^i \tag{3.32}$$

$$k_{xz} \cong N_{,x}^i(x) \beta_z{}^i$$

$$k_\theta = \theta_{,x} \cong N_{,x}^i(x) \theta^i$$

Writing the above expressions in a matrix form and separating in-plane from shear terms, it results to the following two equations,

In-plane terms,

$$\begin{Bmatrix} \varepsilon_x^0 \\ k_{xy} \\ k_{xz} \\ k_\theta \end{Bmatrix} \cong \sum_{i=1}^{n} \begin{bmatrix} N_{,x}^i(x) & 0 & 0 & 0 \\ 0 & N_{,x}^i(x) & 0 & 0 \\ 0 & 0 & N_{,x}^i(x) & 0 \\ 0 & 0 & 0 & N_{,x}^i(x) \end{bmatrix} \begin{Bmatrix} u^{0i} \\ \beta_y^{\,i} \\ \beta_z^{\,i} \\ \theta^i \end{Bmatrix} \tag{3.33}$$

The first RHS matrix is the in-plane strain shape matrix and for sake of brevity is indicated as $\left[R_o^i \right]$.

Shear terms,

$$\begin{Bmatrix} \varepsilon_{xz}^o \\ \varepsilon_{xy}^o \end{Bmatrix} \cong \sum_{i=1}^{n} \begin{bmatrix} 0 & N_{,x}^i(x) & N^i(x) & 0 \\ N_{,x}^i(x) & 0 & 0 & N^i(x) \end{bmatrix} \begin{Bmatrix} v^{0i} \\ w^{0i} \\ \beta_y^{\,i} \\ \beta_z^{\,i} \end{Bmatrix} \tag{3.34}$$

The first RHS matrix is the shear strain shape matrix and for sake of brevity is indicated as $\left[R_{sh}^i \right]$.

The combination of these two strain shape matrices, yields the total strain matrix $\left[R_{tot}^i \right]$ of the beam element, which is the RHS matrix in Eq. (3.35).

$$\begin{Bmatrix} \varepsilon_x^0 \\ \varepsilon_{xz}^o \\ \varepsilon_{xy}^o \\ k_{xy} \\ k_{xz} \\ k_\theta \end{Bmatrix} \cong \sum_{i=1}^{n} \begin{bmatrix} N_{,x}^i(x) & 0 & 0 & 0 & 0 & 0 \\ 0 & 0 & N_{,x}^i(x) & N^i(x) & 0 & 0 \\ 0 & N_{,x}^i(x) & 0 & 0 & N^i(x) & 0 \\ 0 & 0 & 0 & N_{,x}^i(x) & 0 & 0 \\ 0 & 0 & 0 & 0 & N_{,x}^i(x) & 0 \\ 0 & 0 & 0 & 0 & 0 & N_{,x}^i(x) \end{bmatrix} \begin{Bmatrix} u^{0i} \\ v^{0i} \\ w^{0i} \\ \beta_y^{\,i} \\ \beta_z^{\,i} \\ \theta^i \end{Bmatrix} \tag{3.35}$$

3.4.1.2 Total Structural Matrices of the Beam Finite Element

The next step includes the combination of the displacement field approximation (Eq. (3.31)) with the expressions of the strain, dissipated and kinetic energy of the beam cross-section and with the vector of the generalized strains (Eqs. (3.12) and (3.13)), which finally provides the total stiffness, damping and mass matrices of the beam finite element.

I. Element stiffness matrix,

$$\left[K_e\right]^{ij}=\sum_{i=1}^{2}\sum_{j=1}^{2}\int_{L_e}\left(\left[R_{tot}^{i}\right]^{T}\begin{bmatrix}\left[\mathbf{A^0}\right] & \left[\mathbf{B^0}\right]\\ \left[\mathbf{B^0}\right]^{\mathbf{T}} & \left[\mathbf{D^0}\right]\end{bmatrix}\left[R_{tot}^{j}\right]\right)\mathrm{d}x \tag{3.36}$$

II. Element damping matrix,

$$\left[C_e\right]^{ij}=\sum_{i=1}^{2}\sum_{j=1}^{2}\int_{L_e}\left(\left[R_{tot}^{i}\right]^{T}\begin{bmatrix}\left[\mathbf{A_d^0}\right] & \left[\mathbf{B_d^0}\right]\\ \left[\mathbf{B_d^0}\right]^{\mathbf{T}} & \left[\mathbf{D_d^0}\right]\end{bmatrix}\left[R_{tot}^{j}\right]\right)\mathrm{d}x \tag{3.37}$$

III. Element mass matrix,

$$\left[M_e\right]^{ij}=\sum_{i=1}^{2}\sum_{j=1}^{2}\int_{L_e}\left(\left[N^{i}\right]^{T}\begin{bmatrix}\left[\mathbf{m^A}\right] & \left[\mathbf{m^B}\right]\\ \left[\mathbf{m^B}\right]^{\mathbf{T}} & \left[\mathbf{m^D}\right]\end{bmatrix}\left[N^{j}\right]\right)\mathrm{d}x \tag{3.38}$$

where $i,j=1,2$ are the element nodes and $\left[R_{tot}^{i}\right]$ and $\left[N^{i}\right]$ are the total strain and displacement shape function matrices of the beam element, respectively.

3.4.1.3 Calculation of Structural Matrices at the Local Coordinate System of the Element

The calculation of the integrals presented in Eqs. ((3.36)-(3.38)) takes place in the local coordinate system (ξ) of the developed element. Analytical information about the transformation from the global to the local coordinate system is provided in the fourth chapter (Eqs. 4.52-4.53) of the book. Based on the transformation $\mathrm{d}x=(L_e/2)\mathrm{d}\xi$ (Eq. (4.53)) and the different integration limits: $0\rightarrow L_e$ to $-1\rightarrow 1$ from the global to the local coordinate system, respectively, the aforementioned structural matrices become,

I. Element stiffness matrix at the local coordinate system,

$$\left[K_e\right]^{ij}=\sum_{i=1}^{2}\sum_{j=1}^{2}\int_{-1}^{1}\left(\left[R_{tot}^{i}\right]^{T}\begin{bmatrix}\left[\mathbf{A^0}\right] & \left[\mathbf{B^0}\right]\\ \left[\mathbf{B^0}\right]^{\mathbf{T}} & \left[\mathbf{D^0}\right]\end{bmatrix}\left[R_{tot}^{j}\right]\right)\frac{L_e}{2}\mathrm{d}\xi \tag{3.39}$$

II. Element damping matrix at the local coordinate system,

$$\left[C_e\right]^{ij}=\sum_{i=1}^{2}\sum_{j=1}^{2}\int_{-1}^{1}\left(\left[R_{tot}^{i}\right]^{T}\begin{bmatrix}\left[\mathbf{A_d^0}\right] & \left[\mathbf{B_d^0}\right]\\ \left[\mathbf{B_d^0}\right]^{\mathbf{T}} & \left[\mathbf{D_d^0}\right]\end{bmatrix}\left[R_{tot}^{j}\right]\right)\frac{L_e}{2}\mathrm{d}\xi \tag{3.40}$$

III. Element mass matrix at the local coordinate system,

$$\left[M_e\right]^{ij} = \sum_{i=1}^{2}\sum_{j=1}^{2}\int_{-1}^{1}\left(\left[N^i\right]^T\begin{bmatrix}\left[\mathbf{m^A}\right] & \left[\mathbf{m^B}\right]\\ \left[\mathbf{m^B}\right]^{\mathbf{T}} & \left[\mathbf{m^D}\right]\end{bmatrix}\left[N^j\right]\right)\frac{L_e}{2}\mathrm{d}\xi \tag{3.41}$$

The line integrals are calculated using the Gauss integration method, which is also described in the fourth chapter of the present work. At this point it should be underlined that the in-plane terms are calculated at two integration points, whereas the shear terms using one integration point, in order to avoid the shear locking of the beam. Furthermore, the final stiffness, damping and mass matrices of each beam finite element have square form with dimensions 12x12,

$$\left[K_e\right]_{12x12} \mapsto \begin{bmatrix}\left[K_e\right]_{6x6}^{11} & \left[K_e\right]_{6x6}^{12}\\ \left[K_e\right]_{6x6}^{21} & \left[K_e\right]_{6x6}^{22}\end{bmatrix} \tag{3.42}$$

3.4.2 Discrete System of Equations of Motion

An important step towards the final modeling of the composite structure is the formulation of the total structural matrices based on the assembly of the finite elements. Through proper collection of the previous element matrices terms, which correspond to the common nodes of the structure, the total stiffness $\left[\mathbf{K}\right]$, mass $\left[\mathbf{M}\right]$ and damping $\left[\mathbf{C}\right]$ matrices of the beam finite element are synthesized.

Assuming harmonic motion and taking into account the governing equations of motion ((3.15)-(3.18)), the final discrete set of equations describes the free-vibration response of the beam by the following relation,

$$-\omega^2[\mathbf{M}]\mathbf{U} + j[\mathbf{C}]\mathbf{U} + [\mathbf{K}]\mathbf{U} = \mathbf{0} \tag{3.43}$$

3.4.3 Calculation of the Modal Loss Factor of the Composite Beam

Direct solution of Eq. (3.43) yields the complex eigenvalues of the system. An alternative approximate dissipated energy method, used herein, relies on the numerical solution of the undamped system $\left(\left[\mathbf{C}\right]=\mathbf{0}\right)$, which provides the undamped modal frequencies and the relative mode shapes of the beam structure. The modal loss factor of the m-eigenshape is given by the following relation,

$$\eta_m = \frac{\int_{L_x} W_d \, \mathrm{d}x}{\int_{L_x} H \, \mathrm{d}x} \tag{3.44}$$

where W_d, and H are the dissipated and the stored energy, respectively, of the beam for the mth undamped eigenshape. The modal loss factors of the beam are calculated as the ratio of the dissipated energy to the maximum stored modal energy of the respective undamped mode shape $\mathbf{U}_m$,

$$\eta_m = \frac{1}{2\pi} \frac{\mathbf{U}_\mathbf{m}^\mathbf{T} [\mathbf{C}] \mathbf{U}_\mathbf{m}}{\mathbf{U}_\mathbf{m}^\mathbf{T} [\mathbf{K}] \mathbf{U}_\mathbf{m}} \tag{3.45}$$

Using the previous described formulation, a beam finite element with $n = 2$ nodes and linear shape functions was developed and encoded into the research FE analysis code DAMPBEAM (2006), which predicts the damped dynamic characteristics (natural frequencies and modal damping) of the beam model, using the energy method described above.

3.5 Validation of Coupling Terms

Numerical results evaluate the present method and quantify the effect of coupling terms on a series of validation cases on composite structures, which, first include the static response and the modal characteristics of Carbon/Epoxy box-section beams. Then, the natural frequencies and the modal loss factor values of a small Glass/Epoxy model blade are predicted and validated towards available experimental measurements. Furthermore, the developed finite element is applied to the prediction of the modal characteristics of a 19m realistic wind-turbine blade. Finally, the capabilities of the developed beam finite element to predict the cross-section structural properties and the modal characteristics of a 61.5m wind-turbine blade will also be presented.

3.5.1 Box-Section Carbon/Epoxy Beams

The effect of material coupling was first predicted on a L=0.762m long Carbon/Epoxy uniform box-section beam for two lamination cases proposed by Volovoi and Hodges (2000 and 2002) and shown in Figure 3.5a. Case I has $[\theta/-\theta]_3$, $[-\theta/\theta]_3$, $[\theta]_6$ and $[-\theta]_6$ skin laminations at the left, right, top and bottom side, respectively (Figure 3.5b), and exhibits high material coupling. Case II consists of two shear webs (left and right side) having $[\pm 45]_3$ skin laminations and two flanges (top and bottom side) having $[\theta]_6$ and $[-\theta]_6$ laminations, respectively (Figure 3.5c). The mechanical properties of the Carbon/Epoxy composite material were taken from Volovoi and Hodges (2000 and 2002) and are shown in Table 3.1.

Table 3.1 Mechanical properties of Carbon/Epoxy composite material

ρ (Kg/m^3)	E_{11} (GPa)	E_{22} (GPa)	G_{12} (GPa)	v_{12}	η_{l1} (%)	η_{l2} (%)	η_{l5} (%)	η_{l6} (%)
1578	141.9	9.78	6.13	0.24	0.750	2.297	2.866[a]	2.866

[a]Not measured

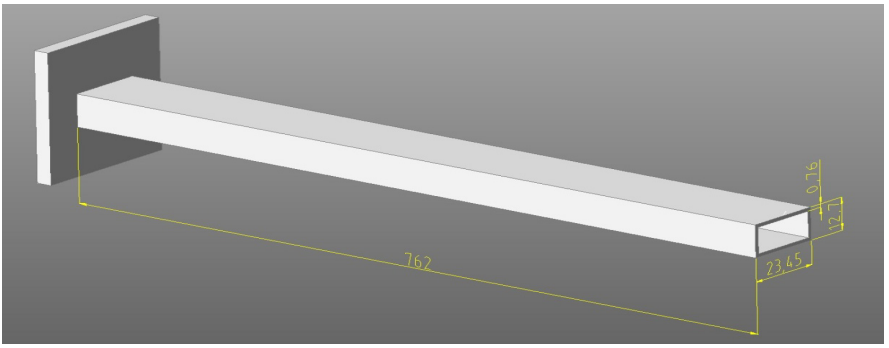

(a)

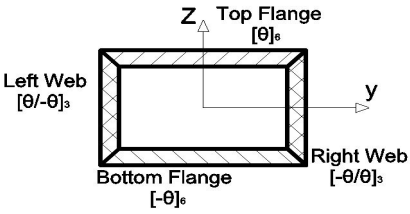

(b)

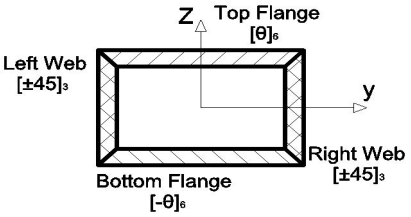

(c)

Fig. 3.5 Box-section Carbon/Epoxy composite beam: (a) Geometric data; (b) Case I; (c) Case II lay-up configurations

3.5.1.1 Static Response of Carbon/Epoxy Beam

Emphasis is placed to the inclusion of composite material coupling effects, first into the blade section stiffness and damping matrices and finally into the stiffness and damping matrices of the beam finite element. Figure 3.6, Figure 3.7 and Figure 3.8 show the predicted tip displacement, tip slope and tip twist for the case I of the above beam for a transverse tip load of 4.45N, for the respective cases of including and neglecting the material coupling terms described in Eqs. (3.20) and (3.23). In all diagrams the ply angle θ, of section skin laminations ranges from 0^0 to 90^0 degrees.

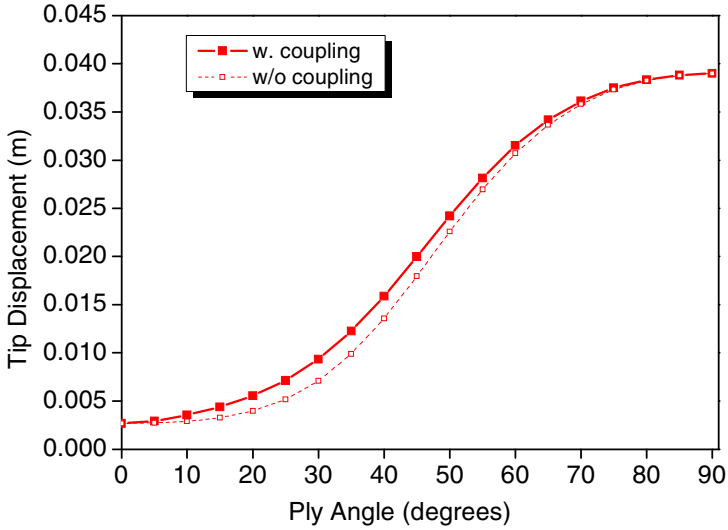

Fig. 3.6 Tip displacement of box-section Carbon/Epoxy beam

There is a substantial improvement in the predicted values of tip displacement and bending angle when material coupling is included in the finite element, in the range of ply orientations yielding non-negligible shear-extension coupling.

Moreover, as illustrated in Figure 3.8, the inclusion of material coupling terms in the model captures the twisting of the beam, while the finite element neglecting material coupling fails to do so.

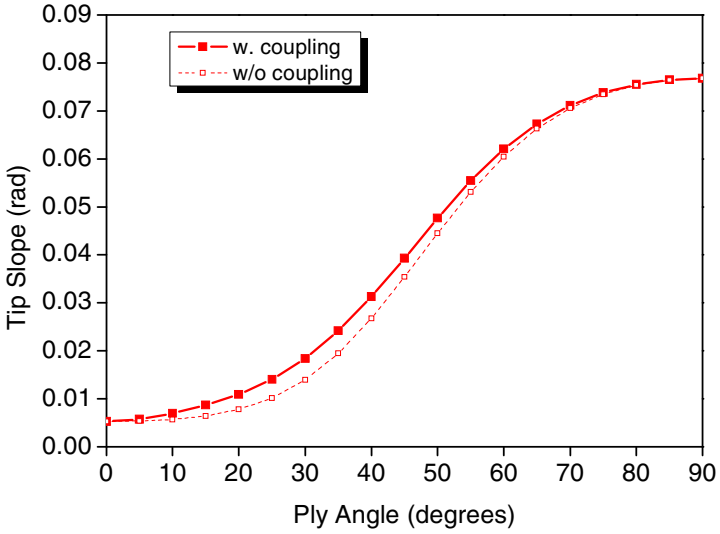

Fig. 3.7 Tip slope of box-section Carbon/Epoxy beam

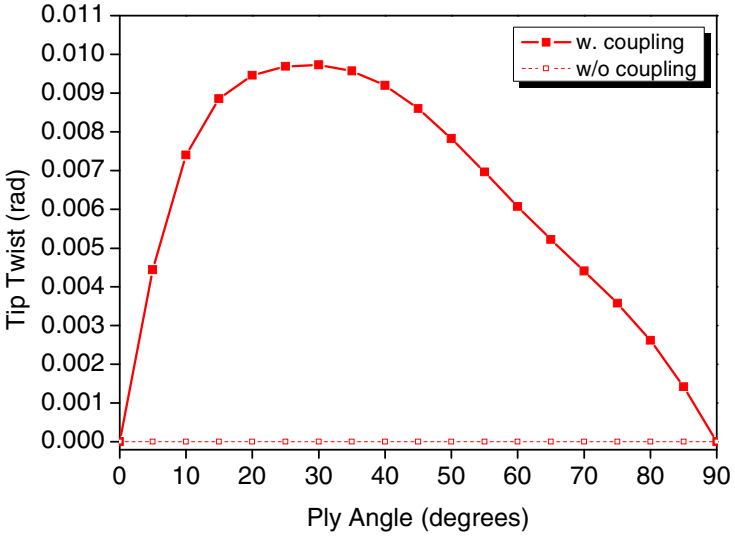

Fig. 3.8 Tip twist of box-section Carbon/Epoxy beam

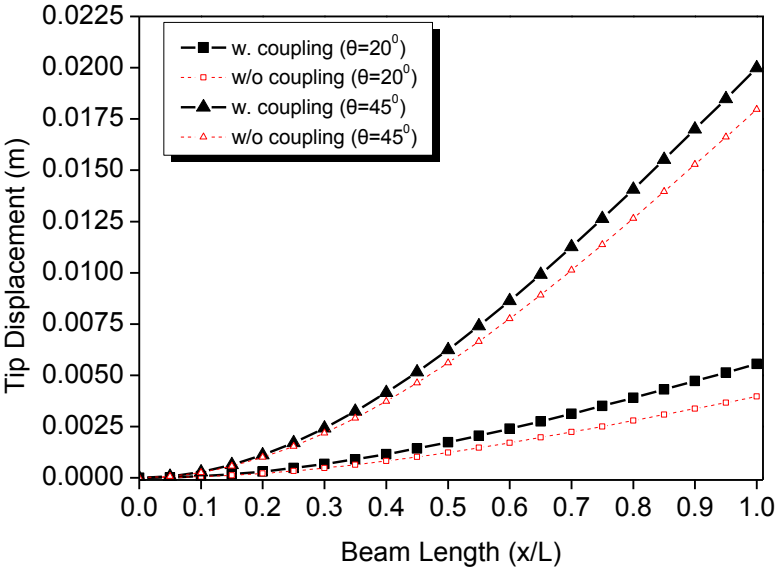

Fig. 3.9 Transverse displacement of Carbon/Epoxy box-section beam for $\theta=20^0$ and $\theta=45^0$

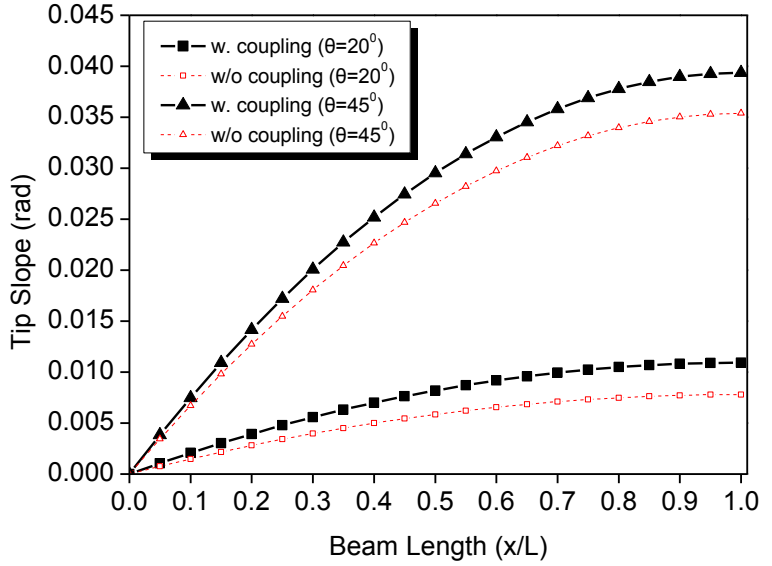

Fig. 3.10 Bending angle of Carbon/Epoxy box-section beam for $\theta=20^0$ and $\theta=45^0$

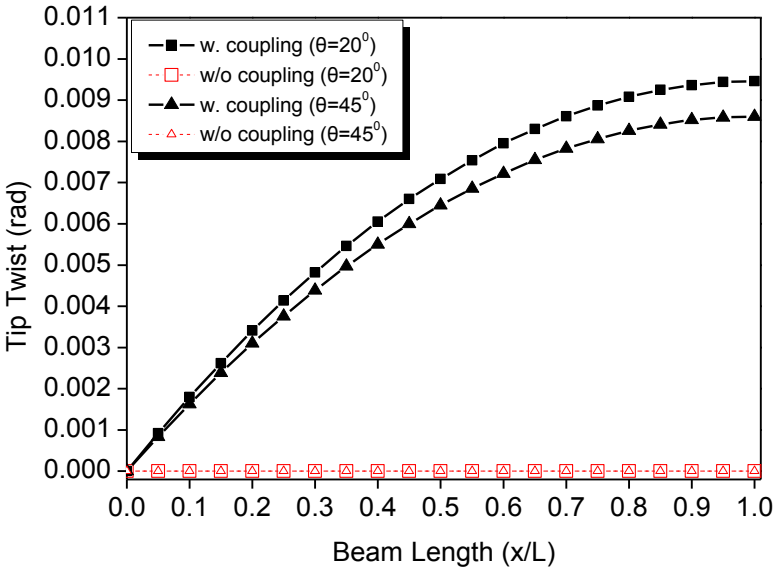

Fig. 3.11 Twisting angle of Carbon/Epoxy box-section beam for $\theta=20^0$ and $\theta=45^0$

To further study the effect of material coupling on the statically deflected slope of the beam two specific ply angle values of $\theta=20^0$ and $\theta=45^0$ were selected for the case I lamination, which are shown in Figure 3.9, Figure 3.10 and Figure 3.11. The results indicate that the effect of coupling terms is stronger at $\theta=20^0$ and also the deviation between the coupled and the uncoupled model increases near the tip of the composite beam, where the displacement, the bending angle and the twist obtain their maximum values.

3.5.1.2 Modal Characteristics of Carbon/Epoxy Beam

Notable differences in predictions were observed to the static characteristics of the blade with the coupling inclusion. Similar differences were presented in modal damping and natural frequency predictions of the box beam for a range of ply angles of case I and case II laminations.

Figure 3.12 illustrates the predicted first flapping modal frequency for the cases I and II when the material coupling terms in Eqs. (3.20) and (3.23) are included or neglected. In both cases, the models that include coupling terms, predict lower frequency values and consequently indicate increased compliance of the blade, than the respective model cases which neglected the material coupling terms. Moreover, the effect of coupling terms is more pronounced in case I, manifested as higher deviation between the coupled and the uncoupled model in the range between $\theta=5^0$ to 40^0.

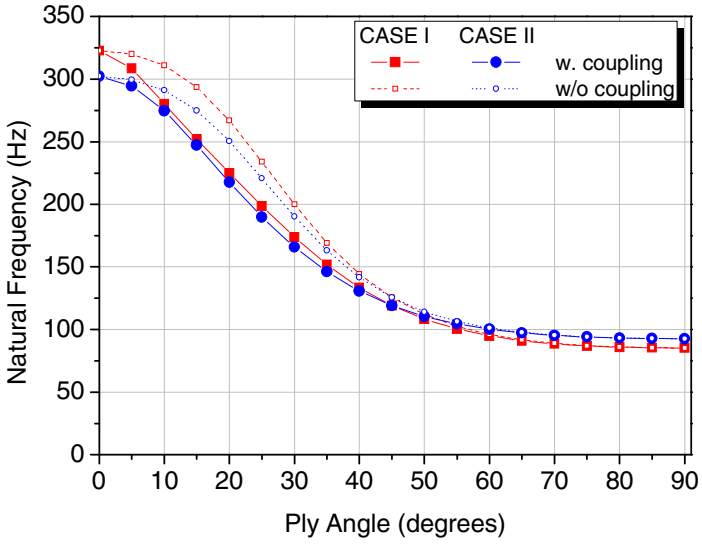

Fig. 3.12 First flapping frequency of Carbon/Epoxy box-section beam

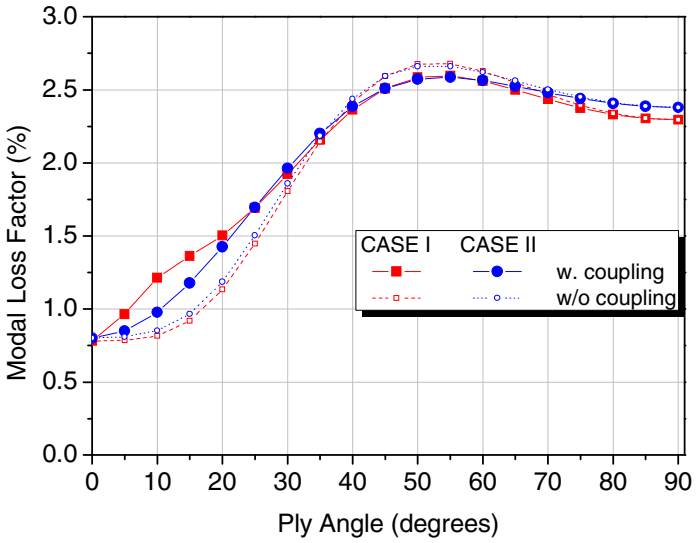

Fig. 3.13 First modal loss factor of Carbon/Epoxy box-section beam

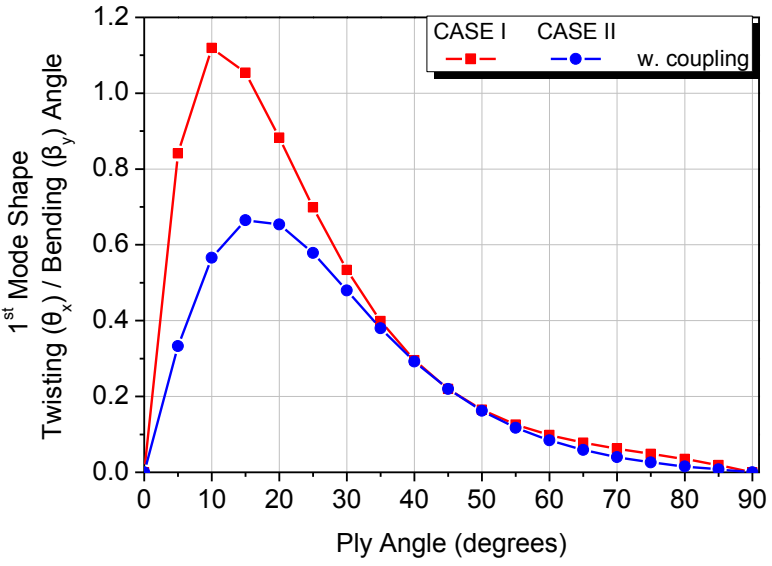

Fig. 3.14 First mode shape of Carbon/Epoxy box-section beam including material coupling terms

Figure 3.13 shows modal damping predictions for the first mode (first flapping). The inclusion of stiffness and damping coupling terms provides higher predictions for the modal damping in the range of ply angles between $\theta=5^0$ and 35^0. In particular, in the ply range from $\theta=5^0$ to 20^0 the coupled model for case I yields higher modal damping predictions than the case II model, which is probably attributed to the lamination of the shear webs.

Similarly, Figure 3.14 illustrates the severe effect of stiffness torsion/bending coupling on the first bending mode of the blade for various ply angles. In both cases the present model predicts substantial torsion/bending coupling in the range from $\theta=5^0$ to 35^0, yet, case I provides significantly higher coupling values, due to the presence of shear webs angle ply laminations.

The capabilities of the present beam finite element to predict the static stiffness of various box-section lay-up configurations is shown in Figure 3.15 and Figure 3.16, in comparison to asymptotic beam theory results by Volovoi and Hodges (2000 and 2002) and predictions by a commercial shell finite element (ANSYS). Figure 3.15 shows the tip bending rotation of a clamped-free composite box-section beam under a transverse load of 4.45N applied at the free tip.

Likewise, Figure 3.16a-b present the tip torsional stiffness of the same beam for two different material lay-up configurations. The models involving the present beam and shell finite element, were discretized using a uniform 40 element mesh along the beam length. It is obvious that the present beam finite element follows reasonably well the predictions of the shell element. Also, it follows well the asymptotic beam theory predictions, with the exception of the case with skin laminations $[\theta_3/-\theta_3]$ at the left and top side and $[-\theta_3/\theta_3]$ at the right and bottom side.

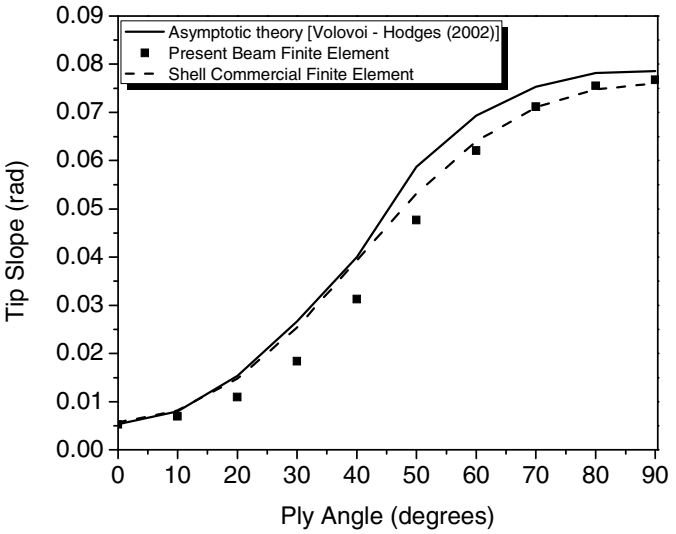

Fig. 3.15 Tip bending rotation of a clamped-free box-section Carbon/Epoxy beam with $[\theta/-\theta]_3$, $[-\theta/\theta]_3$, $[\theta]_6$ and $[-\theta]_6$ skin laminations at the left, right, top and bottom side, respectively

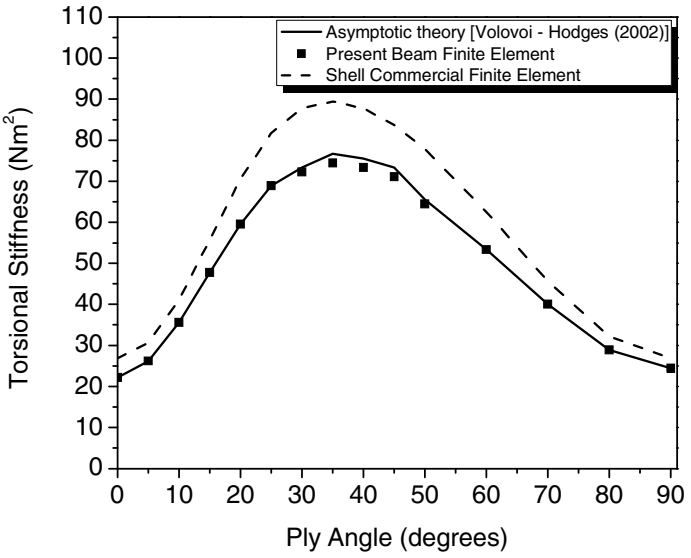

(a)

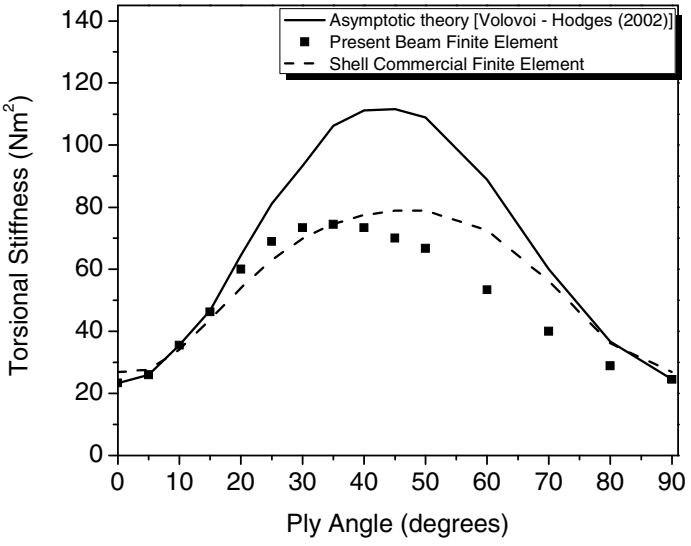

(b)

Fig. 3.16 Tip torsional stiffness of a clamped-free box-section Carbon/Epoxy beam with:(a) $[\theta_3/\text{-}\theta_3]$ at the left and right side, and $[\text{-}\theta_3/\theta_3]$ at the top and bottom side;(b) $[\theta_3/\text{-}\theta_3]$ skin laminations at the left and top side, $[\text{-}\theta_3/\theta_3]$ laminations at the right and bottom side

3.5.2 Small Model Blade

A small model blade was fabricated and its modal characteristics were experimentally measured as part of the DAMPBLADE project (2006). The mechanical properties and the damping coefficients of the Glass/Epoxy composite material were also experimentally extracted and are shown in Table 3.2.

Table 3.2 Elastic properties and damping coefficients of Glass/Epoxy small model blade

ρ (Kg/m^3)	E_{11} (GPa)	E_{22} (GPa)	G_{12} (GPa)	v_{12}	η_{l1} (%)	η_{l2} (%)	η_{l5} (%)	η_{l6} (%)
1670	23.1	8.10	2.50	0.33	0.371	0.898	1.242[a]	1.242

[a]Not measured

3.5.2.1 Blade Testing and Numerical Simulation

The small blade has uniform cross-sections with Glass/Epoxy skins of uniform thickness and entails two $[0_6/(\pm45)_2]$ girder segments. The skin lamination configurations and cross-section geometry are shown in Figure 3.17 and Table 3.3, respectively.

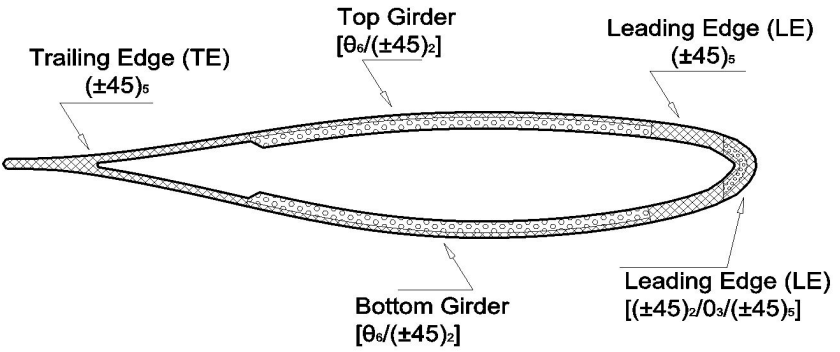

Fig. 3.17 Small model blade cross-section laminations and geometry

Table 3.3 Geometry section parameters and weight for the small model blade

Length (mm)	*Chord Length* (mm)	*Airfoil Section Thickness* (mm)	*Average Ply Thickness* (mm)	*Weight* (kg)
1540	283.5	50.0	0.80	6.0

The whole experimental procedure regarding the small model blade conducted within the activities of DAMPBLADE project (2006) and were carried out in AML by Dr. N. Chrysochoidis. The blade was tested suspended by chords in a nearly free-free configuration, thus minimizing the effects of supports on the overall modal damping of the tested blade (Figure 3.18). The structure was dynamically excited by an applied continuous swept-sine waveform point force using an electromagnetic shaker with an instrumented tip. The acceleration of the vibrating blade was measured using a tri-axial accelerometer at a grid of locations over the span of the blade. The signals from the force and accelerometer sensors were conditioned and then acquired by a data acquisition and frequency analyzer system implementing a high-speed DAQ card and customized Labview® software. The measured accelerance (acceleration/force) frequency response functions were correlated with a parametric model of complex exponentials using a least-squares fit to extract the modal characteristics of the tested blade.

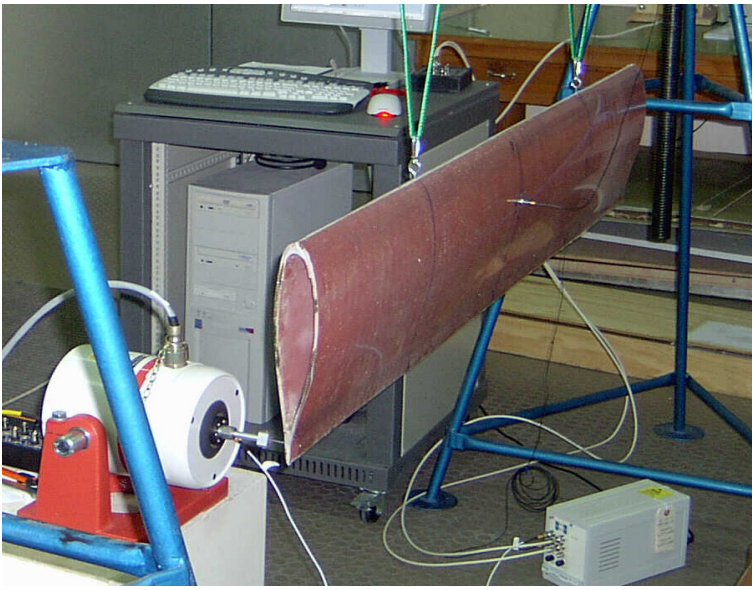

Fig. 3.18 Typical modal testing configuration for the small model blade

The modal characteristics of the aforementioned small model blade were predicted using the developed beam finite element. The comparison between the predicted and the measured modal damping and natural frequencies is shown in Table 3.4.

The present damped finite element seems to provide reasonably good predictions of both natural frequencies and modal damping for the small model blade. The deviations can be attributed to the short length of the blade, which deviates from ideal beam behavior, possible imperfections imposed by the hand lay-up fabrication method and to additional mass and damping of the adhesive

Table 3.4 Predicted and measured natural frequencies and modal damping values of the Glass/Epoxy small model blade

Mode	*Natural Frequency* (Hz)		*Modal Loss Factor* (%)	
	Beam Element	Experiment	Beam Element	Experiment
1st Flapping	81.4	79.9	0.57	0.44
2nd Flapping (torsion coupled)	222.6	211.5	0.58	0.70
1st Sweeping	278.8	306.1	0.93	0.98
2nd Sweeping	697.5	714.1	0.92	1.28
1st Torsional	193.4	193.7	0.79	0.94
2nd Torsional (flapping	389.7	391.9	0.78	0.92

putty which used to join the components of the tested blade. There is higher underestimation in the predicted results of the second sweeping mode, due to the short length and high transverse shearing of the cross-section in the chord direction. The present beam element assumes uniform shearing of the cross-section, but the results of the second sweeping mode may justify future improvements in the kinematic formulation. In summary, the new damped finite element has reasonably captured both values and trends seen in the measured modal frequencies and damping.

3.5.2.2 Effect of Coupling Terms

The effect of material coupling was investigated by predicting the modal characteristics of the small model blade with off-axis girders. Two cases of girder section laminations (Figure 3.17) were considered: in case I, the top girder segment has a $[\theta_6/(\pm 45)_2]$ lamination whereas the bottom girder segment has $[-\theta_6/(\pm 45)_2]$ from the inner to the outer girder skins; in case II, both girder segments have the same $[\theta_6/(\pm 45)_2]$ lamination. The blade cross-section skin laminations at the leading (LE) and trailing (TE) edge are shown in Figure 3.17.

A discretization of 40 uniform beam elements along blade's length was required to obtain convergence of the results, as shown in Figure 3.19 for the first two mode shapes of the small blade model.

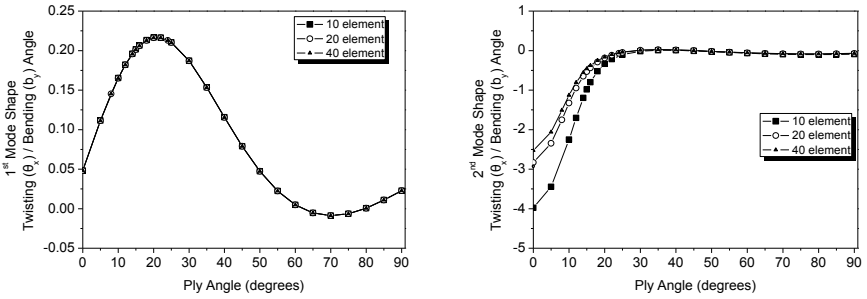

Fig. 3.19 Convergence of the small blade model: (a) First; (b) Second mode shape

Figure 3.20 and Figure 3.21 show the predicted first modal flapping frequency and damping loss factor values for a range of girder ply angle from $\theta=0^0$ to 90^0.

In case I, the inclusion of coupling yields lower modal frequency, hence predicting a more compliant blade. Similarly, the inclusion of coupling terms provides higher values of respective modal structural damping in the ply angle range from $\theta=5^0$ to 45^0. As it was expected, the difference is eliminated at $\theta=0^0$ and 90^0 where the material coupling effect is physically eliminated.

In case II the models with and without coupling terms predict identical results. The symmetry between the lay-up merely eliminates extension-shear A_{16}^0 and A_{d16}^0, the bending-shear B_{16}^0 and B_{d16}^0 and the bending-torsion coupling terms D_{16}^0 and D_{d16}^0 of the blade section.

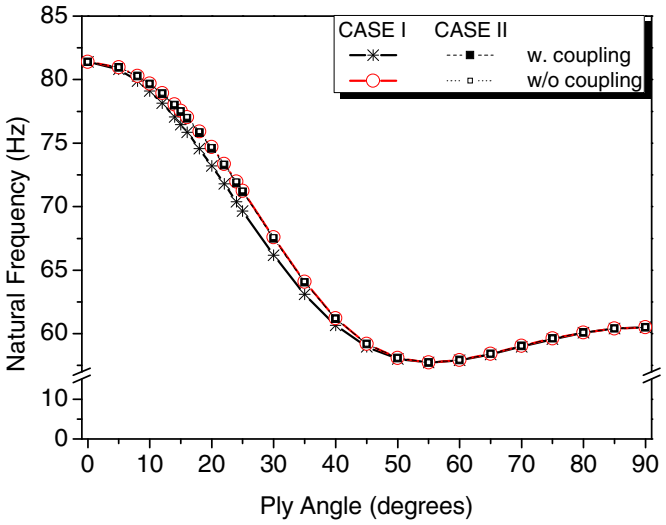

Fig. 3.20 First modal frequency of Glass/Epoxy small model blade

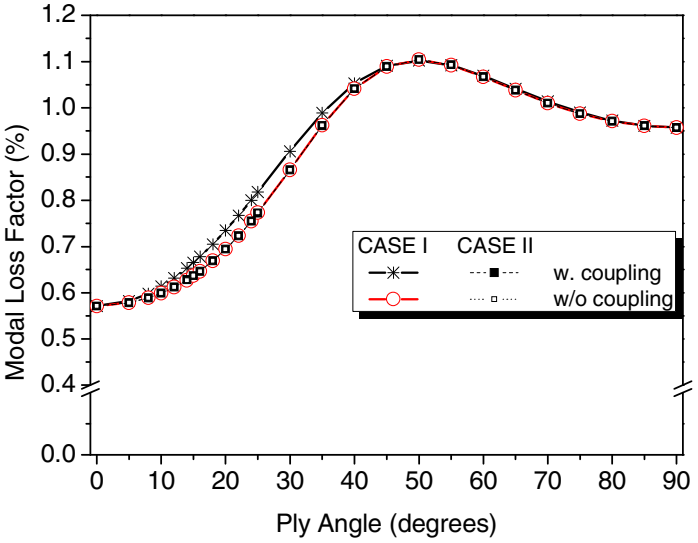

Fig. 3.21 First modal loss factor of Glass/Epoxy small model blade

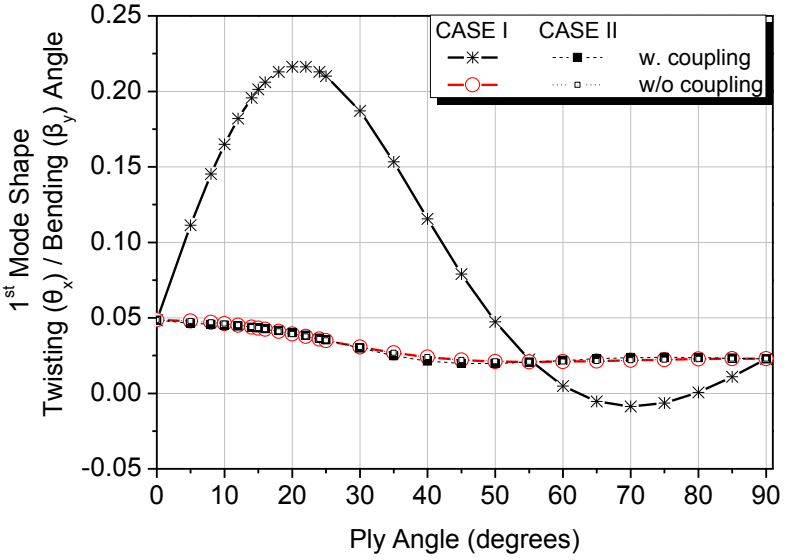

Fig. 3.22 First mode shape of Glass/Epoxy small model blade

The predicted twisting angle over the bending angle of the blade's tip node is presented in Figure 3.22, for the first flapping mode shape. The inclusion of coupling terms in case I, results in strong twisting in the flapping mode, whereas the elimination of stiffness coupling terms (see Eqs. (3.20), (3.23)), respectively, predicted very low twisting, similar to the predictions for case II. The higher

prediction of modal damping in case I (Figure 3.21) can be attributed to the nonzero coupling damping properties of the section (A^0_{d16} , B^0_{d16} , D^0_{d16}) and the twisting in the flapping mode.

3.5.3 19m Wind-Turbine Blade

The finite element code was finally applied for predicting the modal characteristics of a realistic 19m wind-turbine blade design. The blade has a complex external and internal geometry, and large part of the blade is made of Glass/Polyester composite sandwich laminates, which are supported by two shear webs along its length. The mechanical properties and the damping coefficients of the Glass/Polyester composite material are shown in Table 3.5.

Table 3.5 Mechanical properties and damping coefficients of Glass/Polyester composite material

ρ (Kg/m^3)	E_{11} (GPa)	E_{22} (GPa)	G_{12} (GPa)	v_{12}	η_{l1} (%)	η_{l2} (%)	η_{l5} (%)	η_{l6} (%)
2260	22.05	5.58	2.28	0.33	0.668	3.519	4.204[a]	4.204

[a]Not measured

A typical cross-section consists of the trailing edge (TE), leading edge (LE), shear webs (S/W) and top and bottom girder segments, each entailing different laminations. The girders entail several [0^0] UD fiber plies along the length axis of the blade. Details and geometry of a typical blade cross-section are shown in Figure 3.23.

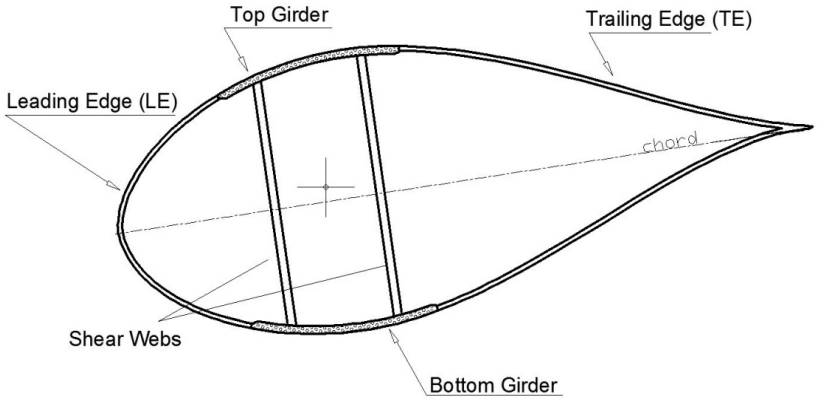

Fig. 3.23 Typical cross-section lamination segments and geometry parameters for the 19m realistic wind-turbine blade model

Table 3.6 presents the predicted natural frequencies and modal loss factors for the first two flapwise modes and the first sweeping mode of the blade.

Table 3.6 Predicted and measured natural frequencies and modal damping values of the 19m realistic wind-turbine blade model

Mode	*Natural Frequency* (Hz)		*Modal Loss Factor* (%)	
	Beam Element	Experiment	Beam Element	Experiment
1st Flapping	2.132	1.868	1.112	1.072
2nd Flapping	5.149	5.076	1.351	1.178
1st Sweeping	2.787	2.971	1.617	1.174

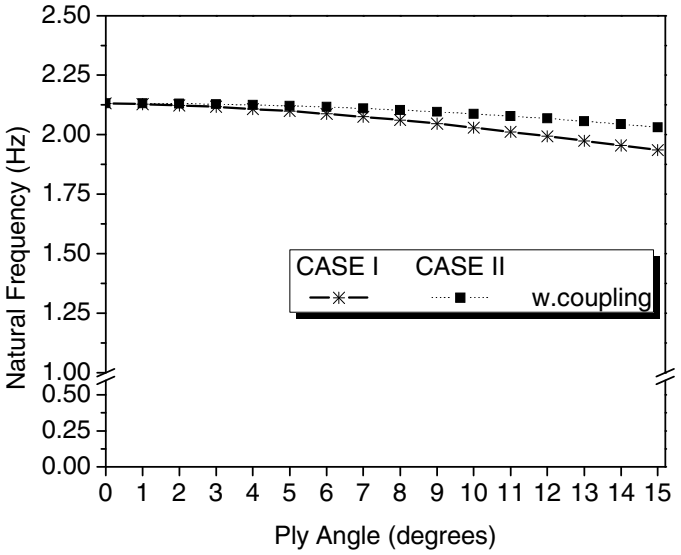

Fig. 3.24 Effect of an off-axis girder on the first flapwise modal frequency of Glass/Polyester 19m realistic wind-turbine blade

In order to investigate the material coupling effect on structural behavior of the 19m blade, two new lamination cases were incorporated into the FE code (Figure 3.23). Case I, entails laminations where only the UD $[0^0]$ plies were substituted by several $[\theta]_n$ ply angle laminations in top girder and $[-\theta]_n$ in bottom girder

segments, whereas case II entails the same $[\theta]_n$ ply angle laminations in both top and bottom girders, with refer to x-axis of blade's length. The ply angle laminations were varied in the range from $\theta=0^0$ to 15^0, where the effect of new coupling terms is expected to dominate.

Figure 3.24 and Figure 3.25 show the first modal flapping frequency and modal damping loss factor values for a range of girder ply angles between $\theta=0^0$ and 15^0, respectively. It is obvious that inclusion of new material coupling terms yields a more compliant blade, which is expressed by the lower frequency and higher damping values. In case II, the material coupling effect is almost vanished due to the lay-up symmetry in the blade cross-section, which eliminates the extension-shear coupling terms A^0_{16} and A^0_{d16}, the bending-shear coupling terms B^0_{16} and B^0_{d16} and the bending-torsion coupling terms D^0_{16} and D^0_{d16} of the cross-section.

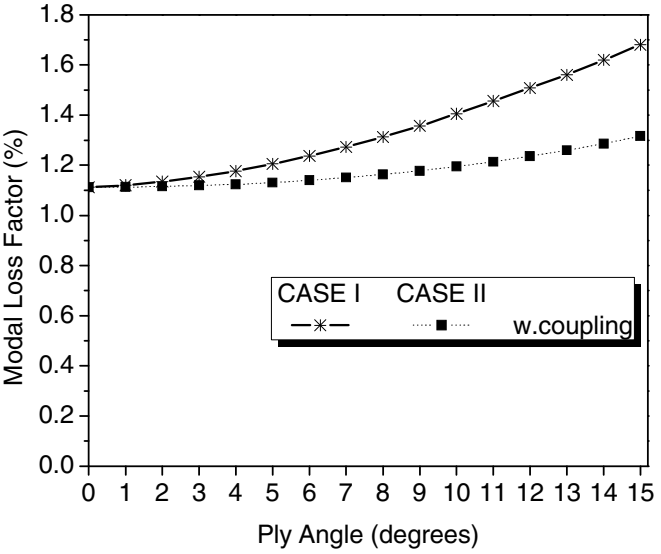

Fig. 3.25 Effect of an off-axis girder on the first flapwise modal loss factor of Glass/Polyester 19m realistic wind-turbine blade

3.6 Application of the Developed Finite Element on a 61.5m Wind-Turbine Blade Model

In the present subsection, the capabilities of the developed damped beam finite element to predict the structural properties of a 61.5m Reference Wind Turbine (RWT) blade model are presented. Within the activities of UPWIND integrated project (2011) a new blade model of 5MW was built, which in the next paragraphs

will be called as the "UP" blade model. The building procedure of the wind-turbine model consists of two main parts, the creation of cross-sections' geometry and the introduction of material lamination in each cross-section's segment. Both of these data were provided by DOWEC project and WMC (Kooijman et al. (2003) and Goezinne (2001)), respectively, and were detailed enough to allow the creation of the proper lay-up per blade sections. Therefore, the developed beam finite element and structural dynamics models were used to obtain the structural properties of the UP wind-turbine blade.

3.6.1 Advanced Cross-Section Structural Properties

The first part of the current subsection aims to the calculation of the structural properties of the 61.5m wind-turbine model. The blade was divided into 20 sections along its length in x-axis and each cross-section had a different geometry and material lamination. The distance of each cross-section from blade root is shown in Figure 3.26.

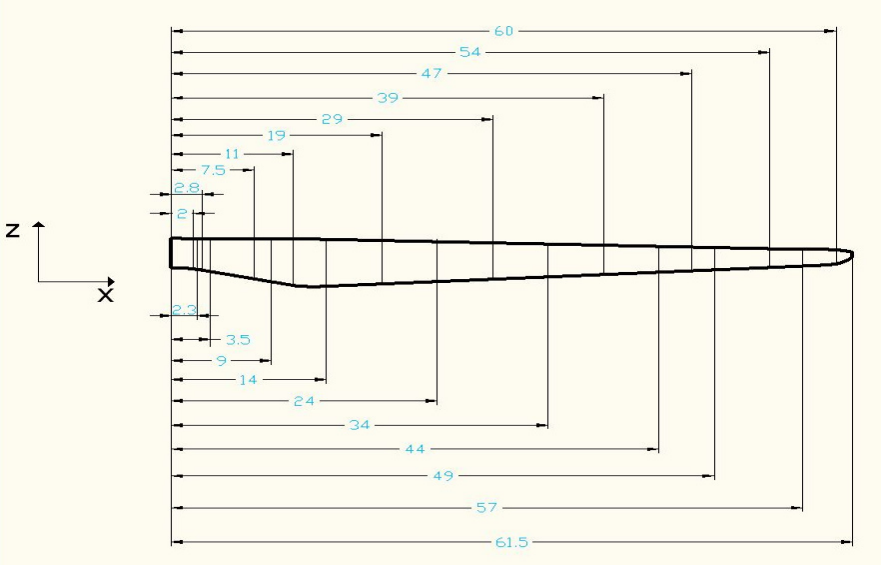

Fig. 3.26 Cross-sections used in UP blade and their distance from blade root

Totally, five different material properties where introduced into UP blade model to obtain the most realistic simulation per segment of blade's cross-section. These material properties refer to Glass/Epoxy fabrics and structural foams layers and they are presented in Table 3.7.

Table 3.7 Mechanical properties of 61.5m UP wind-turbine blade composite materials

Material Number	Material Name	ρ (Kg/m^3)	E_{11} (GPa)	E_{22} (GPa)	E_{33} (GPa)	G_{12} (GPa)	G_{23} (GPa)	G_{13} (GPa)	ν_{12}	ν_{23}	ν_{13}
UD	Gl/Epoxy	1869	38.9	9.0	9.0	3.6	3.6	3.6	0.25	0.45	0.25
TRIAX-1	Gl/Epoxy	1826	24.8	11.5	11.5	4.9	4.9	3.0	0.42	0.25	0.42
ANGPLY	Gl/Epoxy	1789	11.7	11.7	11.7	9.8	9.8	9.8	0.50	0.25	0.25
FOAM-1	Struct. Foam	200	256e-3	256e-3	256e-3	22e-3	22e-3	22e-3	0.30	0.30	0.30
FOAM-2	Struct. Foam	45	25.e-3	25e-3	25e-3	12e-3	12e-3	12e-3	0.30	0.30	0.30

Regarding the materials properties of Table 3.7, the following assumptions should be taken into consideration:

- Material UD consists of unidirectional layers parallel to x-axis of the wind-turbine blade.
- Material TRIAX is a lamination consisting of three layers: [0/±45].
- Material ANGPLY is a lamination consisting of two angle ply layers: [±45].
- Materials FOAM-1 and FOAM-2 are PVC structural foams used in leading edge (LE) and shear webs (S/W) of the blade, respectively.

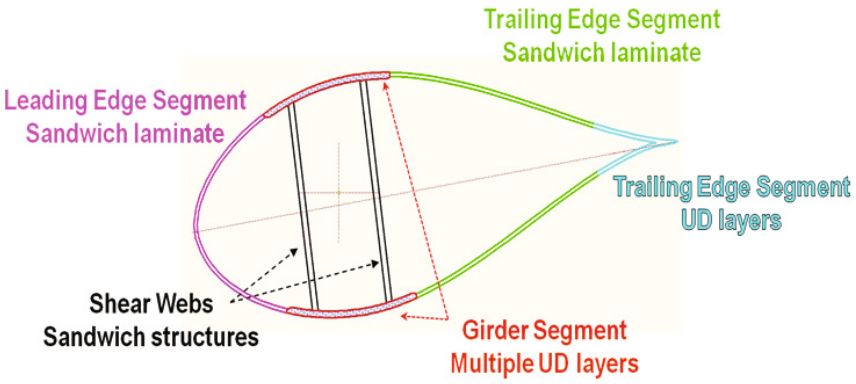

Fig. 3.27 Segments of a typical cross-section of the UP wind-turbine blade

In Figure 3.27 a typical cross-section of UP wind-turbine model is presented. The section lies on the $y-z$ level of blade coordinate system and consists of several sandwich segments which are detailed modeled into the developed beam finite element code. The leading edge (LE), SANDWICH and UD trailing edges (TE), the girders and the shear webs consist of different lay-up configurations, due to the different role that they play on the structural and aeroelastic response of the whole wind-turbine structure.

Each segment of each cross-section has the following laminations:

- **Leading Edge Segment**: Sandwich structure with TRIAX skins and FOAM-1 core.
- **Girder Segment**: Skins of TRIAX and multiple UD layers.
- **Sandwich Trailing Edge Segment**: Sandwich structure with TRIAX skins and FOAM-1 core.
- **UD Trailing Edge Segment**: Skins of TRIAX and multiple UD layers.
- **Shear Webs**: Sandwich structures with ANGPLY skins and FOAM-2 core.

Further analytical information about the 61.5m 5MW blade lay-up configuration is provided in Appendix E. In order to verify the credibility of UP blade model, the predicted results were validated with the RWT and DOWEC-WMC existing data per blade cross-section.

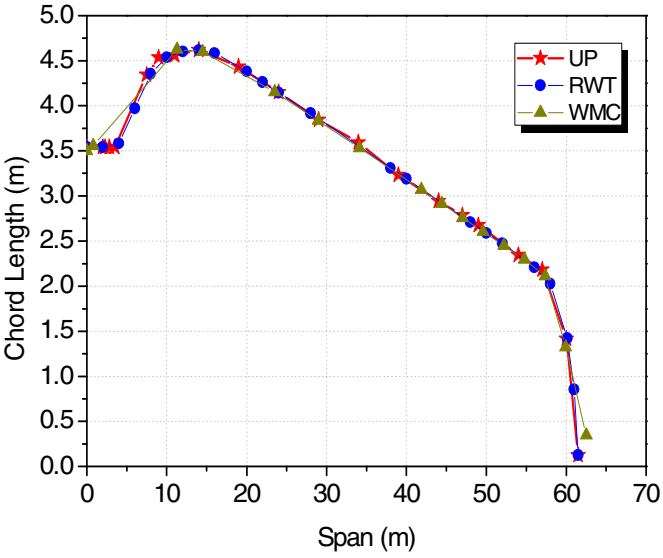

Fig. 3.28 Comparison of chord length along blade span

The developed finite element code has the capability of calculating the stiffness, mass and damping section matrices. In addition, after synthesizing the global structural system, the code provides the modal frequencies and modal damping of the whole blade structure. In Figure 3.28 the cross-sections chord length variation along blade x-axis is presented. It is obvious that the correlation between UP and RWT model is almost excellent along blade radius, which ensures the geometrical requirements for the structural analysis of the blade.

The correspondence between the equivalent section stiffness terms and the traditional beam theory section properties is the following,

$$A_{11}^0 = E_x A, \quad A_{55}^0 = G_{xz} A, \quad A_{66}^0 = G_{xy} A$$

$$D_{11}^0 = E_{b_x} I_y, \quad D_{12}^0 = E_{b_{xy}} I_{yz}, \quad D_{22}^0 = E_{b_y} I_z, \quad D_{66}^0 = G_\tau J \tag{3.46}$$

where A is the area covered by material of each cross-section; E_x, E_{b_i} are the equivalent axial and flexural modulus of elasticity, respectively; G_τ is the equivalent torsional modulus of elasticity; I_y, I_{yz}, I_z are the inertia moments and J is the polar inertia moment.

In order to calculate the mass and stiffness properties of the 61.5m blade model, the UP model assumed 20 sections-finite elements along its length. The code has the capability of predicting the following axial force and cross-section stiffness values, which are in detail presented in Appendix E,

A_{11}^0	:	Force applied on the cross-section w.r.t. axial direction (x-axis)
D_{11}^0	:	Cross-section stiffness w.r.t. flapping direction (around y-axis)
D_{22}^0	:	Cross-section stiffness w.r.t. edgewise direction (around z-axis)
D_{33}^0	:	Cross-section torsional stiffness w.r.t. axial direction (twist around x-axis)

The variation of mass and stiffness properties along blade length is better described in the next figures, where the UP beam model is compared with RWT and DOWEC-WMC relative ones. The beam mass density (Figure 3.29) highly depends on the dimensions ($y-z$ coordinates) of each cross-section and on the number of UD layers in girder segments. Observing Figure 3.29, makes it clear that the convergence between the UP and RWT paper case blade model is almost excellent for all cross-sections. The prediction of the cross-sectional stiffness properties was important to better understand the structural behavior of the 61.5m

wind-turbine blade. In Figure 3.30 the flapping stiffness along blade length is presented. The correlation of results is on an adequate level and follows the RWT and WMC values.

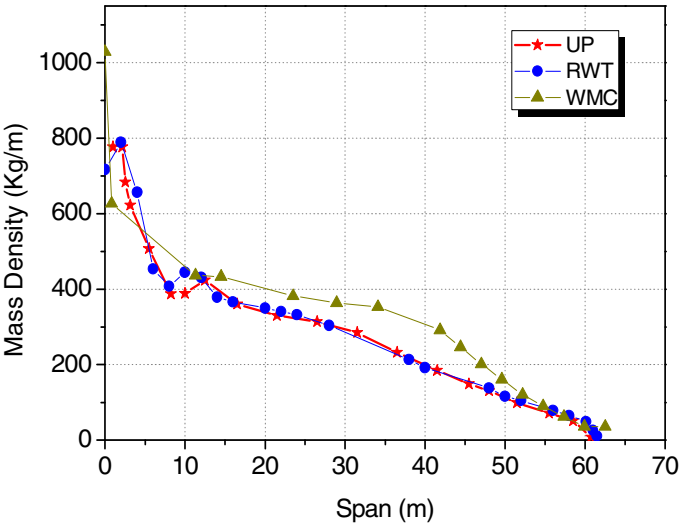

Fig. 3.29 Comparison of beam mass density along blade span

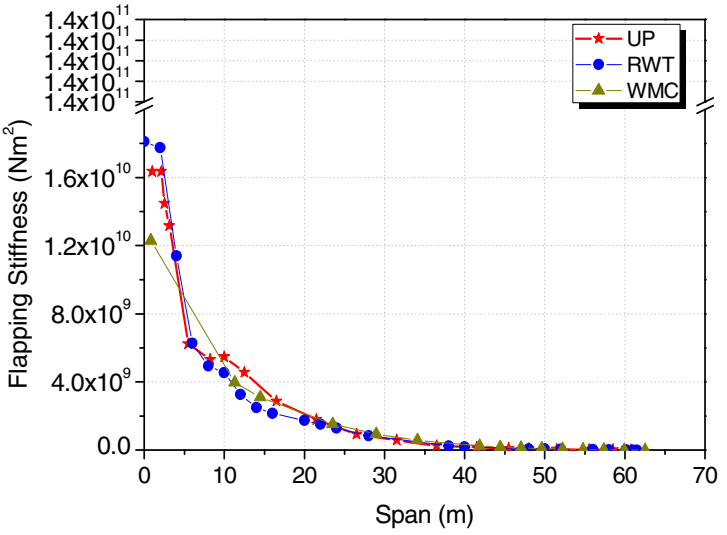

Fig. 3.30 Comparison of flapping stiffness along blade span

A minor deviation observed from 9m to 14m is attributed to the high number of UD layers in girder segments of cross-sections, which increase directly the stiffness with refer to the flapping direction of the structure.

In Figure 3.31 and Figure 3.32 the stiffness in the edgewise and torsional directions are presented, respectively. It is obvious that the UP beam model approaches the RWT values along the blade's span whereas the DOWEC-WMC model underestimates the edgewise stiffness of the blade.

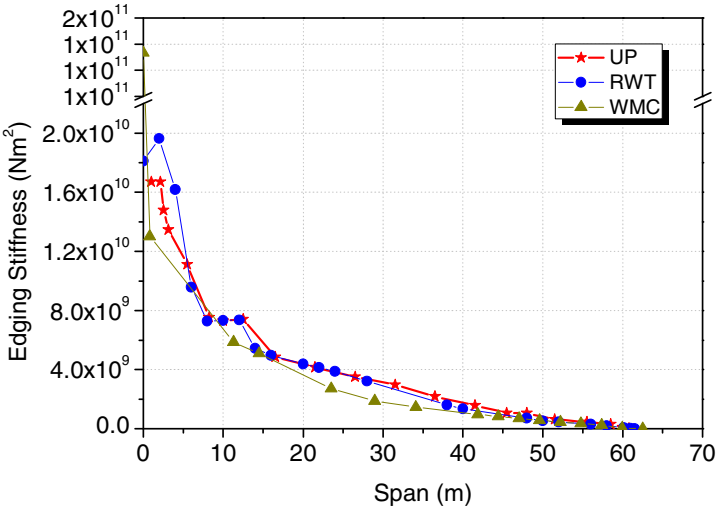

Fig. 3.31 Comparison of edgewise stiffness along blade span

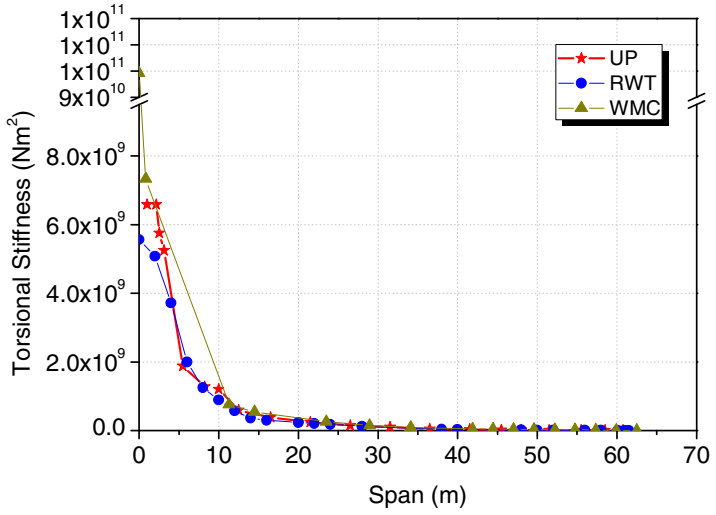

Fig. 3.32 Comparison of torsional stiffness along blade span

As far as the torsional stiffness is concerned, UP model presents an underestimation at root of the blade where the cross-sections have a circular shape. This minor deviation vanishes during the transition from the circular to the airfoil cross-sections which constitute the main body of the wind-turbine blade.

3.6.2 Modal Analysis of the Wind-Turbine Blade

The second part of the 61.5m rotor blade analysis includes the calculation of its modal characteristics. Table 3.8 presents the modal frequencies and modal loss factor values of the 61.5m wind-turbine model.

Table 3.8 Natural frequencies and modal loss factor values of UP 61.5m wind-turbine

Mode	*Natural Frequency* (Hz)	*Loss Factor* (%)
1st Rotor Flapwise	0.680	0.826
2nd Rotor Flapwise	1.815	0.881
3rd Rotor Flapwise	3.867	0.931
4th Rotor Flapwise	7.191	1.030
5th Rotor Flapwise	11.237	1.119
1st Rotor Edgewise	0.889	1.259
2nd Rotor Edgewise	3.238	1.334
1st Rotor Torsional	6.676	1.945
2nd Rotor Torsional	11.617	1.910

3.7 Conclusions

In the third chapter a theoretical framework was presented to predict the linear damped structural dynamics of composite beams and blades exhibiting material coupling. New damping terms encompassing strong material coupling effects were

incorporated into a new damped 3-D beam finite element, capable of predicting the modal characteristics of composite structures.

The effect of new material coupling terms was evaluated on box-section beams, on a small model blade and on a realistic 19m wind-turbine model. In addition, the cross-section structural properties and the modal characteristics of a 61.5m rotor blade were predicted by the developed beam finite element. Based on the obtained numerical results the following major conclusions can be summarized:

1) In all previous structures, the introduction of the new stiffness and damping coupling section terms appears to capture the effect of material coupling by predicting a more compliant structure having lower modal frequencies and higher modal damping values.
2) Evaluation cases carried out on box-section composite beams quantified the material coupling effect on static characteristics and modal frequency and damping values.
3) There is a reasonably good correlation between experimental data and numerical results obtained by the present finite element for the case of the small model blade.
4) Notable differences in the predictions of modal characteristics where exhibited for anti-symmetric ply-angle girder laminations $[0_6/(\pm 45)_2]$, when the [0] plies were rotated by an angle [θ] in the top girder and [-θ] in the bottom girder laminations, in the range from $\theta=5^0$ to 45^0.
5) The inclusion of new coupling cross-section terms for the case of a realistic 19m wind-turbine blade, yielded substantial differences in modal damping and frequency predictions between sections with high coupling (top and bottom girders with rotated plies of angle $[\theta]_n$ and $[-\theta]_n$, respectively) and sections with negligible ply stiffness and damping coupling terms (both girders with rotated plies of angle $[\theta]_n$). The inclusion of material coupling terms seems to significantly improve the structural damping prediction of the blade.
6) There is an excellent correlation of stiffness and mass properties between UP 61.5m blade model and the RWT paper case blade for blade cross-sections along its length. The developed beam finite element code is also capable of predicting the modal frequencies and modal damping of UP wind-turbine blade.

The novelty points of the third chapter are:

* The development of new cross-section damping terms, which take into account the coupling effects induced by the composite material of the structure.

* The prediction of modal loss factor and natural frequencies values of composite structures of various cross-section shapes and the experimental correlation where available.
* The investigation of material coupling effect on a realistic 19m wind-turbine blade model consisting of off-axis girder segments, which improved the structural damping prediction of the blade.

Chapter 4

Nonlinear Damping Mechanics and Finite Element Model for the Static and Damped Free-Vibration Analysis of Composite Strips

The current chapter presents the theoretical framework for the study of the nonlinear response of composite strips. The analysis of composites strips is considered to be an intermediate step before moving to tubular sections and beam elements, which provides valuable insight and understanding of the nonlinear composite damping behavior of these simple structural configurations, moreover offers an opportunity for experimental verification. Nevertheless, there is a void in current literature and technology which is also covered by this chapter. The damping mechanics and nonlinear structural dynamics formulations enable the inclusion of nonlinear effects due to in-plane loads and large deformations on both structural stiffness and damping of laminated composite strips.

In the following sections the formulation of a plate-beam finite element will be presented beginning from the composite ply level up to the final beam element stiffness and damping matrices. The governing equations of composite laminates are described, subject to large Green-Lagrange strains, assuming a Kelvin viscoelastic solid. Effective and linearized damping and stiffness laminate matrices are formulated assuming first-order shear theory. In detail, the present chapter consists of ten subsections. In the first, the constitutive equations and the kinematic assumptions on composite ply level are presented. Furthermore, the stress equilibrium equation is stated in differential form and based on the principle of virtual work, the weak formulation of the equilibrium equations, being valid for nonlinear as well as linear stress-strain relations, is presented. In the second subsection the laminate kinematics based on the first-order shear deformation theory are shown.

In the third subsection the detailed expressions of the cross-section stiffness, damping and mass terms are also reported. Next, the damped nonlinear strip element formulation is presented, where the new nonlinear stiffness and damping matrices forms both in the global and local coordinate system are shown. Fifth subsection provides a brief description of the solution methodology, based on the Newton-Raphson incremental-iterative technique. In the sixth subsection the complete set of equations of the final system is reported, containing also the formulation for the linearized structural matrices of the composite structure.

D.I. Chortis, *Structural Analysis of Composite Wind Turbine Blades*,
Research Topics in Wind Energy 1,
DOI: 10.1007/978-3-319-00864-6_4,

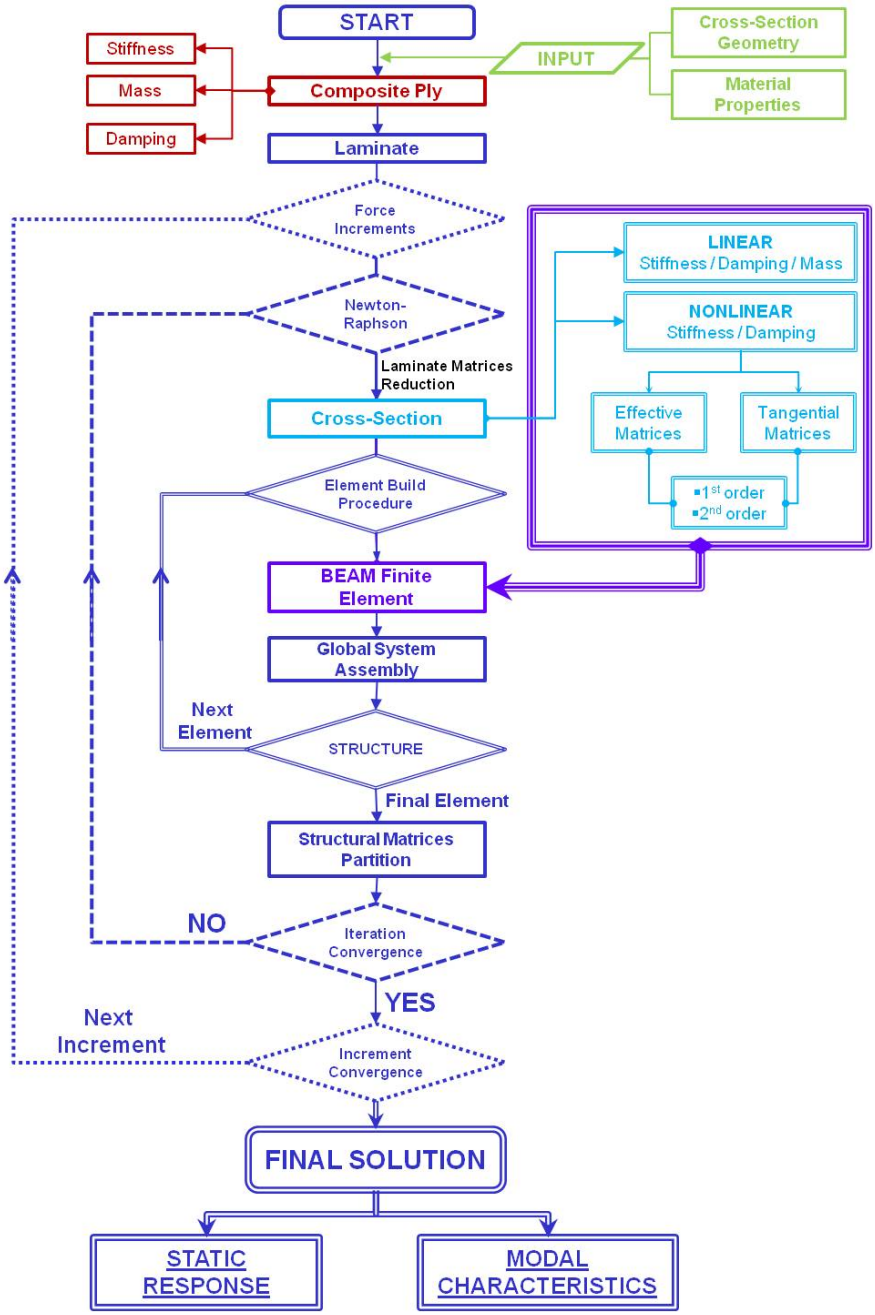

Fig. 4.1 Schematic algorithm flow of the nonlinear finite element code

The theoretical background developed within the present chapter is valid for composite strips subject to tension or buckling loads. In the former case, the small amplitude free-vibration procedure is in detail described in the seventh subsection. Accordingly, eighth subsection presents the displacement control methodology, which was implemented as solver into the nonlinear finite element code in order to describe the response of the composite strip as it transitions from the pre- to post-buckling regime. In the ninth subsection the numerical integration methodology followed along the current work is presented, whereas in the last subsection the major concluding remarks of the present chapter are summarized. The aforementioned finite element procedure is schematically illustrated in Figure 4.1.

4.1 Composite Ply Level

One of the most important benefits of composite material structures is the tailoring of their stiffness and damping properties by adjusting the fiber orientation, the material, the thickness or some other important parameters of each composite ply. The mechanical properties and the damping coefficients of the composite ply, actually determine the elastic and damping properties of the laminate, respectively. Therefore, the constitutive equations, the stress-strain relation as well as the equilibrium stress equations should firstly refer to the composite ply of the structure.

4.1.1 Constitutive Equations

A strain based Kelvin viscoelastic constitutive model was considered to better describe the relation between the ply stresses and strains, having the following form,

$$\boldsymbol{\sigma}_{\mathbf{c}} = \left[\mathbf{Q}^{*}_{\mathbf{cs}}\right]\boldsymbol{\varepsilon}_{\mathbf{c}} + \left[\mathbf{Q}^{*}_{\mathbf{cd}}\right]\dot{\boldsymbol{\varepsilon}}_{\mathbf{c}} \tag{4.1}$$

where:

$$\boldsymbol{\varepsilon}_{\mathbf{c}} = \{\varepsilon_{c1}, \varepsilon_{c5}\} = \{\varepsilon_{cx}, \varepsilon_{cxz}\}$$

$$\boldsymbol{\sigma}_{\mathbf{c}} = \{\sigma_{c1}, \sigma_{c5}\} = \{\sigma_{cx}, \sigma_{cxz}\} \tag{4.2}$$

ε_{c1}, ε_{c5} and σ_{c1}, σ_{c5} are the off-axis normal and shear strains and stresses of a rotated composite ply, respectively; c indicates off-axis ply. Likewise, $\mathbf{Q}^{*}_{\mathbf{cs}}$ and $\mathbf{Q}^{*}_{\mathbf{cd}}$ are the reduced off-axis stiffness and damping matrices of the composite ply, indicated by the subscripts s and d, respectively. The reduction from the 6x6 full form to the final matrices is achieved by the inversion of the compliance matrices, described in detail in Appendix C. In the rest of this chapter the reduced stiffness and damping matrices are used and the asterisk symbol is omitted for the sake of brevity. By substituting Eqs. (4.2) into Eq. (4.1), the latter takes the following form,

$$\begin{Bmatrix} \sigma_{c1} \\ \sigma_{c5} \end{Bmatrix} = \begin{bmatrix} Q_{cs11} & 0 \\ 0 & Q_{cs55} \end{bmatrix} \begin{Bmatrix} \varepsilon_{c1} \\ \varepsilon_{c5} \end{Bmatrix} + \begin{bmatrix} Q_{cd11} & 0 \\ 0 & Q_{cd55} \end{bmatrix} \begin{Bmatrix} \dot{\varepsilon}_{c1} \\ \dot{\varepsilon}_{c5} \end{Bmatrix} \tag{4.3}$$

This is a simple viscoelastic model in the time domain, which predicted modal damping reasonably well.

4.1.2 Composite Ply Damping

The detailed form of the on-axis and off-axis composite ply stiffness and damping matrices has already been presented in the third chapter and Appendix C of the book.

The equivalent reduced off-axis damping matrix $[\mathbf{Q_{cd}}]$ and stiffness matrix $[\mathbf{Q_{cs}}]$ of a composite ply contain only in-plane and out-of-plane shear damping coefficients, and are related by the following equation,

$$\omega[\mathbf{Q_{cd}}] = [\mathbf{Q_{cs}}][\boldsymbol{\eta}_{\mathbf{c}}] \tag{4.4}$$

where ω is the time frequency.

4.1.3 Equations of Motion

This paragraph has already been reported in previous chapter and it is included herein to ensure continuity of the theoretical framework presented in the following paragraphs of the fourth chapter.

4.1.3.1 Differential Form of Stress Equilibrium Equation

The differential form of the stress equilibrium equation, which is valid for any point of the composite ply is the following,

$$\rho \ddot{u}_i = \sigma_{ij,j} + b_i \qquad i, j = 1,2 \tag{4.5}$$

where, ρ is the material density; u_i is the mechanical displacement vector; σ_{ij} is the tensor of the applied mechanical stresses at the specific point of the ply and b_i indicates the external body forces per unit volume of the structure. In Eq. (4.5) the double superscript dot indicates time differentiation, whereas the comma as a subscript indicates space differentiation.

4.1.3.2 Weak Formulation

Equation (4.5) is a simple form of a differential equation which could yield the exact solution of problems with simple geometry and common support and force conditions. Nevertheless, even for the case of one-dimensional problems the

solution is difficult enough to be found, especially when the structure has complicated geometry. In such cases, variational formulations are used, which are applied to the whole volume of the structure. The application of the principle of virtual work in combination with the differential form of stress equilibrium equation, which refers to one point of the ply, yields the "variational form" or the so called "weak form", suitable for the three-dimensional stress analysis of composite structures.

$$\delta\mathbf{u}^{\mathrm{T}}\boldsymbol{\Psi} = \int_V \delta\boldsymbol{\varepsilon}^{\mathrm{T}}\boldsymbol{\sigma}\mathrm{d}V + \int_V \delta\mathbf{u}^{\mathrm{T}}\rho\ddot{\mathbf{u}}\mathrm{d}V - \int_V \delta\mathbf{u}^{\mathrm{T}}\mathbf{b}\mathrm{d}V - \int_\Gamma \delta\bar{\mathbf{u}}^{\mathrm{T}}\bar{\boldsymbol{\tau}}\mathrm{d}\Gamma = 0 \tag{4.6}$$

In the above equilibrium equation the symbol δ indicates a virtual variation of displacement around the equilibrium point, where the term δu is equal to zero. Likewise, $\bar{\tau}$ is the vector of the external forces applied on the boundary area Γ and V represents the total volume of the composite structure. When the system is not at the equilibrium point, $\boldsymbol{\Psi}$ is the imbalance vector between the internal and external forces acting on the structure, which vanishes at the equilibrium point.

4.2 Laminate Level

Each laminate of the structure could consist of one or more composite plies, with different material and geometric properties as well as various lay-up configurations. Consequently, the composite laminate exhibits an anisotropic behavior which is expressed through its stiffness and damping properties. Combination of the section kinematics with the stress-strain compatibility equations will provide the analytical expressions for the linear and nonlinear stiffness, damping and mass matrices, presented in the rest of this chapter.

4.2.1 Section Kinematics

The first-order shear section deformation theory (Reisner 1945 and Mindlin 1951) was considered, which admits extension along x-axis, bending in z direction and shear in x and z directions (Figure 4.2).

According to FSDT the transverse edge of a beam does not remain perpendicular to the midsurface after deformation, as illustrated in Figure 4.2. Moreover, the normal displacement u follows a linear distribution along the thickness of the laminate, whereas the transverse displacement w is independent of the thickness coordinate z.

The kinematic assumptions are the first step in order to build the nonlinear beam finite element formulation and have the following form,

$$\begin{aligned} u(x,z,t) &= u^0(x,t) + z\beta_x(x,t) \\ w(x,z,t) &= w^0(x,t) \end{aligned} \tag{4.7}$$

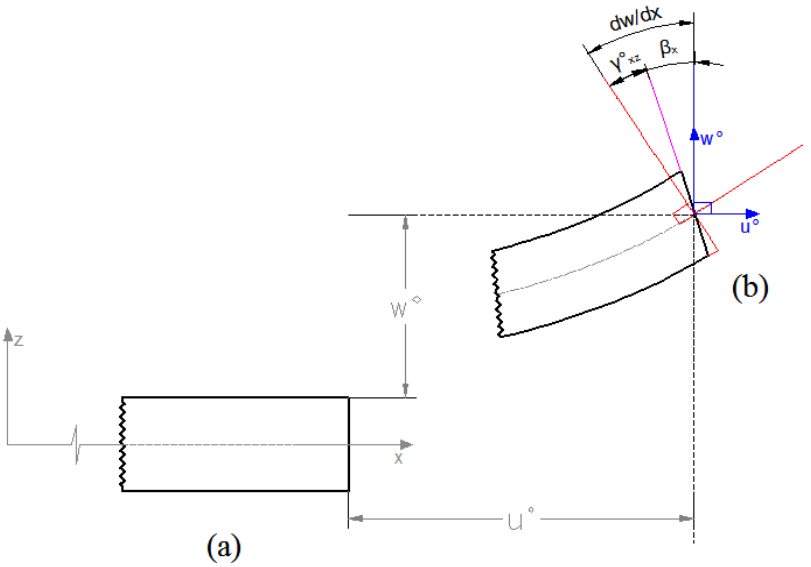

Fig. 4.2 Beam under the assumptions of FSDT: (a) Undeformed geometry; (b) Deformed edge shape

where: u, w are the displacement components of the section and β_x is the bending rotation angle around y-axis; superscript 0 indicates mid-section and the comma in the subscripts indicates differentiation.

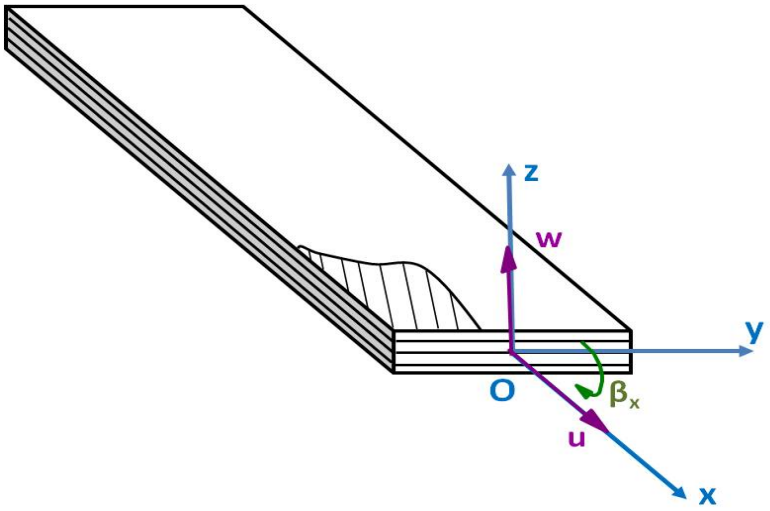

Fig. 4.3 Composite laminate coordinate system and beam element nodal degrees of freedom

4.2.2 Strains-Displacements Compatibility Equations

In order to capture the effect of initial in-plane loads, a nonlinear Green-Lagrange normal strain component was considered. The shear strain acting on the cross-section is assumed to remain linear. Thus, the strains acting on the section have the following form,

$$\varepsilon_x = u_{,x} + \frac{1}{2} w_{,x}^2$$
$$\varepsilon_{xz} = u_{,z} + w_{,x} \tag{4.8}$$

where, $\boldsymbol{\varepsilon}$ are the engineering strains. Combining Eqs. (4.7) and (4.8), the detailed normal and shear strains of the section are expressed as follows,

$$\varepsilon_x(x,z) = \varepsilon_x^0(x) + \frac{1}{2} w_{,x}^{0^2}(x) + z k_x(x)$$
$$\varepsilon_{xz}(x,z) = w_{,x}^0 + \beta_x \tag{4.9}$$

The previous generalized strains, which equivalently describe the deformation of the section, include the linear axial strain ε_x^0, the transverse shear strain, ε_{xz}^0 the bending curvature k_x and the nonlinear axial strain due to large deformations $\varepsilon_x^L(x)$. The generalized strains could be categorized in the following form,

Linear strains,

$$\varepsilon_x^0 = u_{,x}^0$$
$$\varepsilon_{xz}^0 = w_{,x}^0 + \beta_x \tag{4.10}$$

Curvature,

$$k_x = \beta_{x,x} \tag{4.11}$$

Nonlinear Strain,

$$\varepsilon_x^L(x) = \frac{1}{2} w_{,x}^{0^2} \tag{4.12}$$

4.3 Composite Laminate Section Matrices

The equations of motion of the beam (Eq.(4.6)) could be, alternatively described by the following variational form,

$$\int_0^L \mathrm{d}x \int_A \delta H \mathrm{d}A + \int_0^L \mathrm{d}x \int_A \delta \mathrm{T} \mathrm{d}A + \oint_\Gamma \delta \bar{\mathbf{u}}^{\mathrm{T}} \bar{\boldsymbol{\tau}} \mathrm{d}\Gamma = 0 \tag{4.13}$$

where: H and T are the strain and kinetic energy; $\bar{\tau}$ are surface tractions on the free surface Γ; A is the cross-sectional area covered by material and L is the length of the beam.

The strain energy variation of the section δH^{sec} is represented by the integral over the cross-sectional area as follows:

$$\delta H^{\mathrm{sec}} = b \int_h \delta \boldsymbol{\varepsilon}_{\mathbf{c}}^{\mathrm{T}} \boldsymbol{\sigma}_{\mathbf{c}} \mathrm{d}z \tag{4.14}$$

Substituting Eq. (4.1) into Eq. (4.14), the final expression for the strain energy variation over the cross-sectional area is:

$$\delta H^{\mathrm{sec}} = b \int_h \left(\delta \boldsymbol{\varepsilon}_{\mathbf{c}}^{\mathrm{T}} \left(\left[\mathbf{Q}_{\mathbf{cs}} \right] \boldsymbol{\varepsilon}_{\mathbf{c}} + \left[\mathbf{Q}_{\mathbf{cd}} \right] \dot{\boldsymbol{\varepsilon}}_{\mathbf{c}} \right) \right) \mathrm{d}z = \delta H_s + \delta H_{ds} \tag{4.15}$$

where, δH_s and δH_{ds} are the expressions for the strain and dissipated energy variation of the cross-section, respectively; b is the width of the section.

4.3.1 Section Stiffness Terms

Replacing the normal and shear strain expressions provided by Eq. (4.9), into Eq. (4.14), integrating firstly over the laminate thickness and assuming negligible transverse normal and shear laminate stresses N_y, N_{xy}, N_{yz} and transverse and shear moments M_y, M_{xy} along the coordinate axes, O_{xyz}, the stored strain energy in the section takes the form,

$$\begin{aligned}
\delta H_s &= \int_h \delta \varepsilon_x \sigma_x \mathrm{d}z + \int_h \delta \varepsilon_{xz} \sigma_{xz} \mathrm{d}z = \int_h \left(\delta \varepsilon_x^0 + \delta \varepsilon_x^L, + \delta k_x z \right) \sigma_x \mathrm{d}z + \int_h \delta \varepsilon_{xz} \sigma_{xz} \mathrm{d}z \\
&= \delta \varepsilon_x^0 N_x + \delta \varepsilon_x^L N_x + \delta k_x M_x + \delta \varepsilon_{xz} N_{xz} \\
&= \delta u_{,x}^0 \left(N_x^0 + A_{11} \varepsilon_x^L \right) + \delta w_{,x}^0 \left(N_x^0 + A_{11} \varepsilon_x^L \right) w_{,x}^0 + \delta k_x \left(B_{11} u_{,x}^0 + B_{11} \varepsilon_x^L + D_{11} k_x \right) + \delta \varepsilon_{xz} A_{55} \varepsilon_{xz} \\
&= \left\{ \delta u_{,x}^0 N_x^0 + \delta k_x M_x^0 + \delta \varepsilon_{xz} A_{55} \varepsilon_{xz} \right\} + \left\{ \delta u_{,x}^0 A_{11} \varepsilon_x^L + \delta w_{,x}^0 N_x^0 w_{,x}^0 + \delta k_x B_{11} \varepsilon_x^L \right\} + \left\{ \delta w_{,x}^0 A_{11} \varepsilon_x^L w_{,x}^0 \right\}
\end{aligned} \tag{4.16}$$

where the pre-stressing effect is expressed by the following force and moment terms,

$$N_x^0 = A_{11}u_{,x}^0 + B_{11}k_x$$
$$M_x^0 = B_{11}u_{,x}^0 + D_{11}k_x \tag{4.17}$$

The variation of strain energy terms are collected based on linear and nonlinear strain components, and the section strain energy (Eq. (4.16)) becomes,

$$\delta H_s = \delta H_{s_0} + \delta H_{s_1} + \delta H_{s_2} \tag{4.18}$$

where, H_{s_0}, H_{s_1}, H_{s_2} are the cross-section strain energy terms, containing linear and nonlinear components. Each one of these terms provides respectively the linear and nonlinear stiffness terms of the section.

$$\delta H_{s_0} = \left\{\delta\varepsilon_x^0, \delta\varepsilon_{xz}^0, \delta k_x\right\}\left[\mathbf{K_{s_0}}\right]\begin{Bmatrix} u_{,x}^0 \\ \varepsilon_{xz}^0 \\ k_x \end{Bmatrix}$$
$$\delta H_{s_1} = \left\{\delta u_{,x}^0, \delta w_{,x}^0, \delta k_x\right\}\left[\mathbf{K_{s_1}}\right]\begin{Bmatrix} u_{,x}^0 \\ w_{,x}^0 \\ k_x \end{Bmatrix} \tag{4.19}$$
$$\delta H_{s_2} = \left\{\delta u_{,x}^0, \delta w_{,x}^0, \delta k_x\right\}\left[\mathbf{K_{s_2}}\right]\begin{Bmatrix} u_{,x}^0 \\ w_{,x}^0 \\ k_x \end{Bmatrix}$$

The linear stiffness matrix $\left[\mathbf{K_{s_0}}\right]$ contains the well-known linear extensional-shear coupling and flexural-torsional stiffness terms $\left[\mathbf{A^0}\right]$, $\left[\mathbf{B^0}\right]$ and $\left[\mathbf{D^0}\right]$ of the cross-section (Saravanos et al. 2006),

$$\left[\mathbf{K_{s_0}}\right] = \begin{bmatrix} A_{11} & 0 & B_{11} \\ 0 & A_{55} & 0 \\ B_{11} & 0 & D_{11} \end{bmatrix} \tag{4.20}$$

The nonlinear stiffness matrices $\left[\mathbf{K_{s_1}}\right]$ and $\left[\mathbf{K_{s_2}}\right]$ refer to first- and second-order nonlinear strain terms, respectively, having the following form,

$$\left[\mathbf{K}_{\mathbf{s_1}}\right]=\begin{bmatrix}0 & \frac{1}{2}w_{,x}^{0}A_{11} & 0\\ 0 & N_x^0 & 0\\ 0 & \frac{1}{2}w_{,x}^{0}B_{11} & 0\end{bmatrix} \tag{4.21}$$

$$\left[\mathbf{K}_{\mathbf{s_2}}\right]=\begin{bmatrix}0 & 0 & 0\\ 0 & \frac{1}{2}w_{,x}^{0^2}A_{11} & 0\\ 0 & 0 & 0\end{bmatrix} \tag{4.22}$$

The stiffness matrix contains a linear diagonal term proportional to the preload stress, and nonlinear terms proportional to the rotation angle.

In the above Eqs. ((4.20)-(4.22)) $\mathbf{A_{ij}}$, $\mathbf{B_{ij}}$ and $\mathbf{D_{ij}}$ are the extensional, coupling and flexural stiffness matrices of the laminate section, respectively, whereas A_{55} is the extensional stiffness term referring to the out of plane shear strain ε_{xz}. They are related with the section stiffness Q_{ij} by the following relations,

$$\left\langle \mathbf{A_{ij}}, \mathbf{B_{ij}}, \mathbf{D_{ij}} \right\rangle = \sum_{k=1}^{n} \int_{z_k}^{z_{k+1}} \mathbf{Q}_{\mathbf{cs_{ik}}}^{\mathbf{k}} \left\langle 1, z, z^2 \right\rangle \mathrm{d}z \qquad i, j = 1$$

$$\mathbf{A_{ij}} = \sum_{k=1}^{n} \int_{z_k}^{z_{k+1}} \mathbf{Q}_{\mathbf{cs_{ik}}}^{\mathbf{k}} \mathrm{d}z \qquad i, j = 5 \tag{4.23}$$

4.3.2 Section Damping Terms

The same procedure is followed in order to find the final form of the section damping terms of the composite structure. Combining Eqs. (4.1), (4.9) and (4.15) and collecting the terms based on their order of nonlinear terms, the dissipated strain of the section takes the form,

$$\delta H_{ds} = \int_h \delta \boldsymbol{\varepsilon}_{\mathbf{c}}^{\mathbf{T}} \left[\mathbf{Q}_{\mathbf{cd}}\right] \dot{\boldsymbol{\varepsilon}}_{\mathbf{c}} \mathrm{d}z =$$

$$\begin{aligned}
&= \delta u_{,x}^0 \left(A_{d11} \dot{u}_{,x}^0 + A_{d11} w_{,x}^0 \dot{w}_{,x}^0 + B_{d11} \dot{k}_x \right) + \delta w_{,x}^0 \left(w_{,x}^0 A_{d11} \dot{u}_{,x}^0 + w_{,x}^{0^2} A_{d11} \dot{w}_{,x}^0 + w_{,x}^0 B_{d11} \dot{k}_x \right) \\
&+ \delta k_x \left(B_{d11} \dot{u}_{,x}^0 + B_{d11} w_{,x}^0 \dot{w}_{,x}^0 + D_{d11} \dot{k}_x \right) + \delta \varepsilon_{xz} A_{d55} \dot{\varepsilon}_{xz} \\
&= \left\{ \delta u_{,x}^0 (A_{d11} \dot{u}_{,x}^0 + B_{d11} \dot{k}_x) + \delta k_x (B_{d11} \dot{u}_{,x}^0 + D_{d11} \dot{k}_x) + \delta \varepsilon_{xz} A_{d55} \dot{\varepsilon}_{xz} \right\} \\
&+ \left\{ \delta u_{,x}^0 w_{,x}^0 A_{d11} \dot{w}_{,x}^0 + \delta w_{,x}^0 w_{,x}^0 A_{d11} \dot{u}_{,x}^0 + \delta w_{,x}^0 w_{,x}^0 B_{d11} \dot{k}_x + \delta k_x w_{,x}^0 B_{d11} \dot{w}_{,x}^0 \right\} \\
&+ \left\{ \delta w_{,x}^0 w_{,x}^{0^2} A_{d11} \dot{w}_{,x}^0 \right\}
\end{aligned} \tag{4.24}$$

In the above, $\left[\mathbf{A_d}\right]$, $\left[\mathbf{B_d}\right]$ and $\left[\mathbf{D_d}\right]$ are equivalent extensional-shear, coupling and flexural damping matrices of the laminate, respectively, defined in Appendix C. In the last three lines of the above equation, the dissipated energy contains linear and nonlinear terms and similarly to the stored strain energy, they are categorized as follows,

$$\delta H_{ds} = \delta H_{ds_0} + \delta H_{ds_1} + \delta H_{ds_2} \tag{4.25}$$

where, H_{ds_0}, H_{ds_1}, H_{ds_2} are the cross-section dissipated energy terms, containing linear and nonlinear components, having the form,

$$\begin{aligned}
\delta H_{ds_0} &= \left\{ \delta \varepsilon_x^0, \delta \varepsilon_{xz}^0, \delta k_x \right\} \left[\mathbf{C_{ds_0}} \right] \begin{Bmatrix} \dot{u}_{,x}^0 \\ \dot{\varepsilon}_{xz}^0 \\ \dot{k}_x \end{Bmatrix} \\
\delta H_{ds_1} &= \left\{ \delta u_{,x}^0, \delta w_{,x}^0, \delta k_x \right\} \left[\mathbf{C_{ds_1}} \right] \begin{Bmatrix} \dot{u}_{,x}^0 \\ \dot{w}_{,x}^0 \\ \dot{k}_x \end{Bmatrix} \\
\delta H_{ds_2} &= \left\{ \delta u_{,x}^0, \delta w_{,x}^0, \delta k_x \right\} \left[\mathbf{C_{ds_2}} \right] \begin{Bmatrix} \dot{u}_{,x}^0 \\ \dot{w}_{,x}^0 \\ \dot{k}_x \end{Bmatrix}
\end{aligned} \tag{4.26}$$

In the above expressions, among the equivalent section damping matrices of the section, $\left[\mathbf{C}_{\mathbf{ds}_0}\right]$ is the linear laminate damping matrix (Saravanos et al. (2006)),

$$\left[\mathbf{C}_{\mathbf{ds}_0}\right]=\begin{bmatrix} A_{d11} & 0 & B_{d11} \\ 0 & A_{d55} & 0 \\ B_{d11} & 0 & D_{d11} \end{bmatrix} \tag{4.27}$$

The first-order nonlinear damping matrix $\left[\mathbf{C}_{\mathbf{ds}_1}\right]$ contains terms which exhibit first-order nonlinear dependence to the generalized section displacements.

$$\left[\mathbf{C}_{\mathbf{ds}_1}\right]=\begin{bmatrix} 0 & w^0_{,x}A_{d11} & 0 \\ w^0_{,x}A_{d11} & 0 & w^0_{,x}B_{d11} \\ 0 & w^0_{,x}B_{d11} & 0 \end{bmatrix} \tag{4.28}$$

It was first introduced by Chortis et al. (2011) and its effect was studied on pre-stressed composite beams in tension.

The second-order nonlinear damping matrix, $\left[\mathbf{C}_{\mathbf{ds}_2}\right]$, has the form,

$$\left[\mathbf{C}_{\mathbf{ds}_2}\right]=\begin{bmatrix} 0 & 0 & 0 \\ 0 & w^{0^2}_{,x}A_{d11} & 0 \\ 0 & 0 & 0 \end{bmatrix} \tag{4.29}$$

The second-order nonlinear damping terms, are critical in describing the nonlinear damping during the buckling and post-buckling response of composite strips.

By observing the above linear and nonlinear damping matrices, it is noted that all nonlinear damping terms will act as modifiers of the flexural damping of the beam, and are proportional to the rotation $w^0_{,x}$. If the beam remains in the linear regime, i.e. negligible initial in-plane stresses and rotations, the flexural damping of the beam is contributed only by term D_{d11} which in previous works was termed as flexural laminate damping. When the beam enters into the nonlinear regime and is subject to large rotations, strong additional damping terms are introduced which couple flexure and extension; these terms are proportional to the extensional damping coefficient A_{d11} of the laminate.

Especially, the case of buckling and post-buckling, also considered in this chapter, provides an excellent case to study the effect of $\mathbf{C}_{\mathbf{ds}_1}$ and $\mathbf{C}_{\mathbf{ds}_2}$ terms on the structural damping of the strip, since the effect of rotations is not negligible. As the magnitude of the rotation increases, the effect of laminate configuration on structural damping will be governed mainly by extensional damping terms A_d

and less by flexural damping D_d. Finally it will be shown in the fifth chapter that laminates with unsymmetric laminations ($B_{d11} \neq 0$) may introduce additional nonlinear damping terms due to extension-flexure coupling, which increase the damping of the composite structure.

4.3.3 Section Mass Terms

The kinetic energy variation, δT^{sec}, is represented by the integral over the cross-sectional area,

$$\delta T^{\text{sec}} = \int_A -\delta \mathbf{u}^{\mathbf{T}} \text{diag}(\boldsymbol{\rho}) \ddot{\mathbf{u}} \, \mathrm{d}\xi \, \mathrm{d}\eta = b \int_h -\delta \mathbf{u}^{\mathbf{T}} \text{diag}(\boldsymbol{\rho}) \ddot{\mathbf{u}} \, \mathrm{d}z \tag{4.30}$$

In the above equations, **diag(ρ)** indicates a diagonal matrix with diagonal elements equal to the mass density ρ of the ply and h is the thickness of the skin laminate and could be re-written in the following form,

$$\delta T^{\text{sec}} = b \int_h -\delta \mathbf{u}^{\mathbf{T}} \text{diag}(\boldsymbol{\rho}) \ddot{\mathbf{u}} \, \mathrm{d}z = b \int_h -\left(\delta \mathrm{u} \rho \ddot{\mathrm{u}} + \delta \mathrm{w} \rho \ddot{\mathrm{w}} \right) \mathrm{d}z \tag{4.31}$$

Substituting the displacements equations (Eq. (4.7)) into the kinetic energy equation (Eq. (4.31)), and performing the integration over the thickness of the laminate, the kinetic energy of the section is expressed in terms of the generalized displacements and the resultant mass matrices,

$$\delta T^{\text{sec}} = b \int_h \left(\delta \mathbf{u}^{\mathbf{0T}} \mathbf{m}^{\mathbf{A}} \ddot{\mathbf{u}}^{\mathbf{0}} + \delta \mathbf{u}^{\mathbf{0T}} \mathbf{m}^{\mathbf{B}} \ddot{\boldsymbol{\beta}} + \delta \boldsymbol{\beta}^{\mathbf{T}} \mathbf{m}^{\mathbf{B}} \ddot{\mathbf{u}}^{\mathbf{0}} + \delta \boldsymbol{\beta}^{\mathbf{T}} \mathbf{m}^{\mathbf{D}} \ddot{\boldsymbol{\beta}} \right) \mathrm{d}z \tag{4.32}$$

where $\mathbf{u}^{\mathbf{0}} = \{u^0, w^0\}$ and $\boldsymbol{\beta} = \{\beta_x\}$ represent the average displacements and rotations of the section, respectively. Likewise, $\mathbf{m}^{\mathbf{A}}$, $\mathbf{m}^{\mathbf{B}}$ and $\mathbf{m}^{\mathbf{D}}$ are the equivalent mass, coupling and rotational inertia matrices of the laminate section, per unit length, defined in Appendix C.

4.4 Structural Level

After estimating the stiffness, damping and mass terms of the laminate section, the next key step concerns the development of a computational method capable of analyzing the nonlinear response of composite strips under large displacements and rotations. To that direction the finite element method was chosen for the nonlinear analysis of the composite structure in combination with an incremental-iterative technique based on the Newton-Raphson technique for the solution of the final system of equations.

4.4.1 Damped Nonlinear Beam Finite Element

The finite element method is based on the discretization of the structure into the minimum number of finite elements which ensure the convergence of the results. In the present work the composite beam structures are analyzed using a 2-node beam finite element. Supposing that the total length of the structure consists of K number of beam finite elements, then Eq.(4.6), takes the following form,

$$\begin{aligned}
\delta\mathbf{u}^{\mathbf{T}}\boldsymbol{\Psi} = \sum_{e=1}^{K}\int_{L_e} & (\delta\boldsymbol{\varepsilon}_{\mathbf{x}}^{\mathbf{0}^{\mathbf{T}}}[A]\boldsymbol{\varepsilon}_{\mathbf{x}}^{\mathbf{0}} + \delta\boldsymbol{\varepsilon}_{\mathbf{x}}^{\mathbf{0}^{\mathbf{T}}}[B]\mathbf{k}_{\mathbf{x}} + \delta\mathbf{k}_{\mathbf{x}}^{\mathbf{T}}[B]\boldsymbol{\varepsilon}_{\mathbf{x}}^{\mathbf{0}} + \delta\mathbf{k}_{\mathbf{x}}^{\mathbf{T}}[D]\mathbf{k}_{\mathbf{x}} + \delta\boldsymbol{\varepsilon}_{\mathbf{xz}}^{\mathbf{0}^{\mathbf{T}}}[A_{55}]\boldsymbol{\varepsilon}_{\mathbf{xz}}^{\mathbf{0}} \\
& + \delta\boldsymbol{\varepsilon}_{\mathbf{x}}^{\mathbf{L}^{\mathbf{T}}}[A]\boldsymbol{\varepsilon}_{\mathbf{x}}^{\mathbf{0}} + \delta\boldsymbol{\varepsilon}_{\mathbf{x}}^{\mathbf{L}^{\mathbf{T}}}[A]\boldsymbol{\varepsilon}_{\mathbf{x}}^{\mathbf{L}} + \delta\boldsymbol{\varepsilon}_{\mathbf{x}}^{\mathbf{L}^{\mathbf{T}}}[B]\mathbf{k}_{\mathbf{x}} + \delta\boldsymbol{\varepsilon}_{\mathbf{x}}^{\mathbf{0}^{\mathbf{T}}}[A]\boldsymbol{\varepsilon}_{\mathbf{x}}^{\mathbf{L}} + \delta\mathbf{k}_{\mathbf{x}}^{\mathbf{T}}[B]\boldsymbol{\varepsilon}_{\mathbf{x}}^{\mathbf{L}})\mathrm{d}x \\
& + \sum_{e=1}^{K}\int_{L_e} (\delta\boldsymbol{\varepsilon}_{\mathbf{x}}^{\mathbf{0}^{\mathbf{T}}}[A_d]\dot{\boldsymbol{\varepsilon}}_{\mathbf{x}}^{\mathbf{0}} + \delta\boldsymbol{\varepsilon}_{\mathbf{x}}^{\mathbf{0}^{\mathbf{T}}}[B_d]\dot{\mathbf{k}}_{\mathbf{x}} + \delta\mathbf{k}_{\mathbf{x}}^{\mathbf{T}}[B_d]\dot{\boldsymbol{\varepsilon}}_{\mathbf{x}}^{\mathbf{0}} + \delta\mathbf{k}_{\mathbf{x}}^{\mathbf{T}}[D_d]\dot{\mathbf{k}}_{\mathbf{x}} + \delta\boldsymbol{\varepsilon}_{\mathbf{xz}}^{\mathbf{0}^{\mathbf{T}}}[A_{d55}]\dot{\boldsymbol{\varepsilon}}_{\mathbf{xz}}^{\mathbf{0}} \\
& + \delta\boldsymbol{\varepsilon}_{\mathbf{x}}^{\mathbf{L}^{\mathbf{T}}}[A_d]\dot{\boldsymbol{\varepsilon}}_{\mathbf{x}}^{\mathbf{0}} + \delta\boldsymbol{\varepsilon}_{\mathbf{x}}^{\mathbf{L}^{\mathbf{T}}}[A_d]\dot{\boldsymbol{\varepsilon}}_{\mathbf{x}}^{\mathbf{L}} + \delta\boldsymbol{\varepsilon}_{\mathbf{x}}^{\mathbf{L}^{\mathbf{T}}}[B_d]\dot{\mathbf{k}}_{\mathbf{x}} + \delta\boldsymbol{\varepsilon}_{\mathbf{x}}^{\mathbf{0}^{\mathbf{T}}}[A_d]\dot{\boldsymbol{\varepsilon}}_{\mathbf{x}}^{\mathbf{L}} + \delta\mathbf{k}_{\mathbf{x}}^{\mathbf{T}}[B_d]\dot{\boldsymbol{\varepsilon}}_{\mathbf{x}}^{\mathbf{L}})\mathrm{d}x \\
& + \int_{L_e} (\delta\mathbf{u}^{\mathbf{0}^{\mathbf{T}}}[\rho^A]\ddot{\mathbf{u}} + \delta\mathbf{u}^{\mathbf{0}^{\mathbf{T}}}[\rho^B]\ddot{\boldsymbol{\beta}} + \delta\boldsymbol{\beta}^{\mathbf{T}}[\rho^B]\ddot{\mathbf{u}} + \delta\boldsymbol{\beta}^{\mathbf{T}}[\rho^D]\ddot{\boldsymbol{\beta}})\mathrm{d}x \\
& - \int_{\Gamma} \delta\bar{\mathbf{u}}^{\mathbf{T}}\bar{\boldsymbol{\tau}}\mathrm{d}\Gamma
\end{aligned} \tag{4.33}$$

The first two lines of Eq. (4.33) refer to the strain energy; the next two lines refer to the dissipated energy; the fifth line refers to the kinetic energy and the last line express the external work produced by the applied forces.

4.4.1.1 Shape Functions of the Two-Node Beam Strip Finite Element

A three-dimensional shear beam finite element for predicting the nonlinear damped dynamic analysis of composite beams was developed encompassing the aforementioned generalized nonlinear damping mechanics. The finite elements consist of suitable shape functions which ensure continuity criteria, necessary for the accuracy and convergence of the final problem solution. The nodes numbering of the beam finite element is shown in Figure 4.4b, where each point within the element is approximated by nodal coordinate x_i according to the following relation,

$$x = \sum_{i=1}^{n} N^i(x)\, x_i \tag{4.34}$$

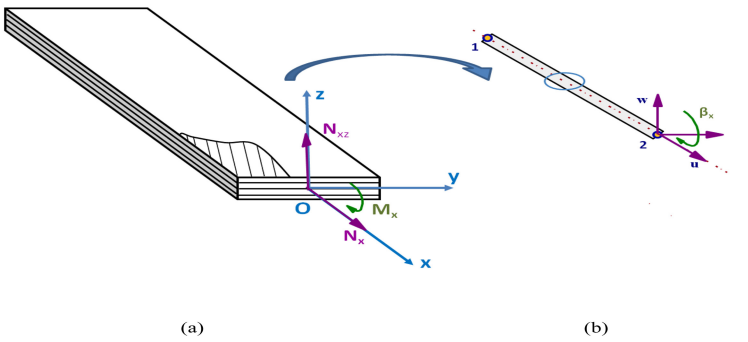

Fig. 4.4 Laminated composite strip-beam element: (a) Cross-section module; (b) Finite element

where, n is the number of element nodes (at the current work is $n=2$) and $N^i(x)$ are the c^0 continuous shape functions, having the form,

$$N^1(x)=\frac{x}{L_e}$$
$$N^2(x)=1-\frac{x}{L_e} \tag{4.35}$$

where L_e is the beam element length. The approximation of the generalized displacements along the element is given by the following relation,

$$\left\langle u^o(x),\quad w^o(x),\quad \beta_x(x)\right\rangle \cong \sum_{i=1}^{n} N^i(x)\left\langle u^{oi},\quad w^{oi},\quad \beta_x^i\right\rangle \tag{4.36}$$

where, u^{oi}, w^{oi}, β_x^i are the unknown nodal degrees of freedom, which have to be calculated. Similarly, $N^i(x)$ are known continuous polynomial functions at the element length, which are called interpolation shape functions. Due to the fact that there are three degrees of freedom at each node, there will be: 2 nodes x 3 DOF per node = 6 DOF at each beam finite element.

Usually, the shape functions refer to the local coordinate system of the element, where the numerical solution takes place. For the case of the beam finite element, the local or natural coordinate system is define by ξ, as follows,

$$\xi=\frac{2}{x_2-x_1}(x-x_1)-1 \tag{4.37}$$

From Eq. (4.37) it is easy to understand that $\xi = -1$ at node 1 and $\xi = 1$ at node 2 (Figure 4.5). The length of the element is covered when ξ changes from $-1 \to 1$.

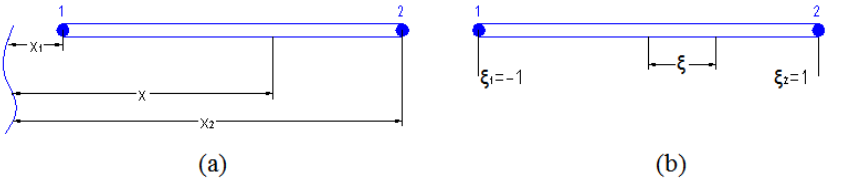

Fig. 4.5 Typical two-node beam strip finite element: (a) Global CS; (b) Local CS

The local coordinate system is used to define the shape functions, which are used for interpolating the unknown displacement field within an element. To that direction a linear distribution consisting of the following linear shape functions, is implemented (Chandrupalta and Belegundu 1991),

$$N^1(\xi) = \frac{1-\xi}{2}$$

$$N^2(\xi) = \frac{1+\xi}{2} \tag{4.38}$$

The shape functions, shown in Figure 4.6, have some interesting properties that derive from the completeness requirements imposed by rigid body motion.

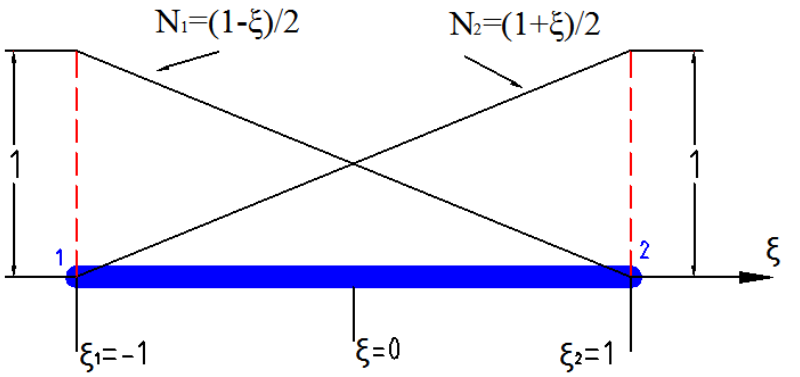

Fig. 4.6 Linear shape functions of beam finite element in the local CS

It is simple to argue that one property the shape functions must have is that:

- $N^i(x)=1$ at node i and $N^i(x)=0$ at the rest of the beam nodes

This basic property ensures the independence among the shape functions as well as the displacement continuity at the common nodes of the beam finite elements. It is therefore assumed that these shape functions allow elements to be connected together without generating gaps between them. The shape functions are continuous polynomial functions whose order and shape depend on the:

- Element type and the
- Number and distribution of DOFs within the element domain.

The relation between a) the elastic strains (linear and nonlinear) with the displacements and b) the curvatures with the rotation angles of the beam were described analytically in Eqs. (4.10)-(4.12). The next key step is to establish the relation between the generalized strains and the nodal DOF values of the finite element. This is analytically described by the next set of equations,

$$\begin{aligned}
\varepsilon_x^0 &= \frac{\mathrm{d}\mathbf{u^o}}{\mathrm{d}x} = \frac{\mathrm{d}\left(N^i\mathbf{u^{oi}}\right)}{\mathrm{d}x} = R_a^{oi}\mathbf{u^{oi}} \\
\varepsilon_{xz}^0 &= \frac{\mathrm{d}\mathbf{u^o}}{\mathrm{d}x} = \frac{\mathrm{d}\left(N^i\mathbf{u^{oi}}\right)}{\mathrm{d}x} = R_{sa}^{oi}\mathbf{u^{oi}} \\
\varepsilon_x^L &= \frac{\mathrm{d}\mathbf{u^o}}{\mathrm{d}x} = \frac{\mathrm{d}\left(N^i\mathbf{u^{oi}}\right)}{\mathrm{d}x} = R_L^{oi}\mathbf{u^{oi}} \\
k_x &= \frac{\mathrm{d}\mathbf{u^o}}{\mathrm{d}x} = \frac{\mathrm{d}\left(N^i\mathbf{u^{oi}}\right)}{\mathrm{d}x} = R_b^{oi}\mathbf{u^{oi}}
\end{aligned} \tag{4.39}$$

where ε_x^0, ε_{xz}^0, ε_x^L, k_x are the linear, shear, nonlinear strains and curvature which are developed within the finite element. Likewise, $\mathbf{u^{oi}}=\left\{u^{oi} \quad w^{oi} \quad \beta_x^i\right\}^{\mathrm{T}}$ is the vector containing the three degrees of freedom at each node of the beam finite element and R_a^{oi}, R_{sa}^{oi}, R_L^{oi}, R_b^{oi} are the matrices consisting of the shape functions $N^i(x)$ and the strain shape functions $N_{,x}^i(x)$ of the finite element. Detailed form of the aforementioned displacement and strain shape functions is reported in Appendix D of the current work.

4.4.1.2 Discrete System Equations

The next step in order to build the final structural matrices of the strip finite element is the introduction of the generalized strains and curvature analytical expression (Eq. (4.39)) into the integrated form of equations of motion (4.33), which take the following form,

$$
\begin{aligned}
\delta\mathbf{u}^{\mathbf{oi}^{\mathbf{T}}}\boldsymbol{\Psi}^{i} = &\sum_{e=1}^{K}\sum_{i=1}^{2}\sum_{j=1}^{2}\int_{L_e}(\delta\left(R_a^{oi}\mathbf{u}^{\mathbf{oi}}\right)^{T}[A]\left(R_a^{oj}\mathbf{u}^{\mathbf{oj}}\right)+\delta\left(R_a^{oi}\mathbf{u}^{\mathbf{oi}}\right)^{T}[B]\left(R_b^{oj}\mathbf{u}^{\mathbf{oj}}\right)\\
&+\delta\left(R_b^{oi}\mathbf{u}^{\mathbf{oi}}\right)^{T}[B]\left(R_a^{oj}\mathbf{u}^{\mathbf{oj}}\right)+\delta\left(R_b^{oi}\mathbf{u}^{\mathbf{oi}}\right)^{T}[D]\left(R_b^{oj}\mathbf{u}^{\mathbf{oj}}\right)+\delta\left(R_{sa}^{oi}\mathbf{u}^{\mathbf{oi}}\right)^{T}[A_{55}]\left(R_{sa}^{oj}\mathbf{u}^{\mathbf{oj}}\right)\\
&+\delta\left(R_L^{i}\mathbf{u}^{\mathbf{oi}}\right)^{T}[A]\left(R_a^{oj}\mathbf{u}^{\mathbf{oj}}\right)+\delta\left(R_L^{i}\mathbf{u}^{\mathbf{oi}}\right)^{T}[A]\left(R_L^{j}\mathbf{u}^{\mathbf{oj}}\right)+\delta\left(R_L^{i}\mathbf{u}^{\mathbf{oi}}\right)^{T}[B]\left(R_b^{oj}\mathbf{u}^{\mathbf{oj}}\right)\\
&+\delta\left(R_a^{oi}\mathbf{u}^{\mathbf{oi}}\right)^{T}[A]\left(R_L^{j}\mathbf{u}^{\mathbf{oj}}\right)+\delta\left(R_b^{oi}\mathbf{u}^{\mathbf{oi}}\right)^{T}[B]\left(R_L^{j}\mathbf{u}^{\mathbf{oj}}\right))\mathrm{d}x\\
&+\sum_{e=1}^{K}\sum_{i=1}^{2}\sum_{j=1}^{2}\int_{L_e}(\delta\left(R_a^{oi}\mathbf{u}^{\mathbf{oi}}\right)^{T}[A]\left(R_a^{oj}\dot{\mathbf{u}}^{\mathbf{oj}}\right)+\delta\left(R_a^{oi}\mathbf{u}^{\mathbf{oi}}\right)^{T}[B]\left(R_b^{oj}\dot{\mathbf{u}}^{\mathbf{oj}}\right)\\
&+\delta\left(R_b^{oi}\mathbf{u}^{\mathbf{oi}}\right)^{T}[B]\left(R_a^{oj}\dot{\mathbf{u}}^{\mathbf{oj}}\right)+\delta\left(R_b^{oi}\mathbf{u}^{\mathbf{oi}}\right)^{T}[D]\left(R_b^{oj}\dot{\mathbf{u}}^{\mathbf{oj}}\right)+\delta\left(R_{sa}^{oi}\mathbf{u}^{\mathbf{oi}}\right)^{T}[A_{55}]\left(R_{sa}^{oj}\dot{\mathbf{u}}^{\mathbf{oj}}\right)\\
&+\delta\left(R_L^{i}\mathbf{u}^{\mathbf{oi}}\right)^{T}[A]\left(R_a^{oj}\dot{\mathbf{u}}^{\mathbf{oj}}\right)+\delta\left(R_L^{i}\mathbf{u}^{\mathbf{oi}}\right)^{T}[A]\left(R_L^{j}\dot{\mathbf{u}}^{\mathbf{oj}}\right)+\delta\left(R_L^{i}\mathbf{u}^{\mathbf{oi}}\right)^{T}[B]\left(R_b^{oj}\dot{\mathbf{u}}^{\mathbf{oj}}\right)\\
&+\delta\left(R_a^{oi}\mathbf{u}^{\mathbf{oi}}\right)^{T}[A]\left(R_L^{j}\dot{\mathbf{u}}^{\mathbf{oj}}\right)+\delta\left(R_b^{oi}\mathbf{u}^{\mathbf{oi}}\right)^{T}[B]\left(R_L^{j}\dot{\mathbf{u}}^{\mathbf{oj}}\right))\mathrm{d}x\\
&+\sum_{e=1}^{K}\sum_{i=1}^{2}\sum_{j=1}^{2}\int_{Le}\delta\left(N^{i}\mathbf{u}^{\mathbf{oi}}\right)^{T}[\rho^{A}]\left(N^{j}\ddot{\mathbf{u}}^{\mathbf{oj}}\right)+2\delta\left(N^{i}\mathbf{u}^{\mathbf{oi}}\right)^{T}[\rho^{B}]\left(N^{j}\ddot{\mathbf{u}}^{\mathbf{oj}}\right)\\
&+\delta\left(N^{i}\mathbf{u}^{\mathbf{oi}}\right)^{T}[\rho^{D}]\ddot{\boldsymbol{\beta}}\left(N^{j}\ddot{\mathbf{u}}^{\mathbf{oj}}\right))\mathrm{d}x-\sum_{e=1}^{K}\sum_{i=1}^{2}\int_{\Gamma}\delta\mathbf{u}^{\mathbf{oi}^{\mathbf{T}}}\left(N^{i}\mathbf{F}^{\mathbf{i}}\right)\mathrm{d}\Gamma
\end{aligned}
\tag{4.40}
$$

Combining the previous displacement and strain approximation Eqs. (4.7)-(4.9), substituting into the equations of motion (4.15) and (4.31) and collecting the common coefficients the total stiffness $\left[\mathbf{K}\right]$, damping $\left[\mathbf{C}\right]$ and mass $\left[\mathbf{M}\right]$ matrices respectively, of the beam the equilibrium $\mathbf{u(t)}$ is provided by the following equation,

$$
\boldsymbol{\Psi}\left(\mathbf{u},\mathbf{t}\right)=\left[\mathbf{M}\right]\ddot{\mathbf{u}}\left(\mathbf{t}\right)+\left[\mathbf{C}\right]\dot{\mathbf{u}}\left(\mathbf{t}\right)+\left[\mathbf{K}\right]\mathbf{u}\left(\mathbf{t}\right)-\mathbf{F}\left(\mathbf{t}\right) \tag{4.41}
$$

The effective stiffness and damping structural matrices contain linear and nonlinear components of the following form,

$$\begin{aligned}\left[\mathbf{K}(\mathbf{u})\right]&=\left[\mathbf{K}_{\mathbf{N_0}}\right]+\left[\mathbf{K}_{\mathbf{N_1}}(\mathbf{u})\right]+\left[\mathbf{K}_{\mathbf{N_2}}(\mathbf{u^2})\right]\\ \left[\mathbf{C}(\mathbf{u})\right]&=\left[\mathbf{C}_{\mathbf{N_0}}\right]+\left[\mathbf{C}_{\mathbf{N_1}}(\mathbf{u})\right]+\left[\mathbf{C}_{\mathbf{N_2}}(\mathbf{u^2})\right]\end{aligned} \tag{4.42}$$

where, subscripts 0, $N1$ and $N2$ indicate linear, first- and second-order nonlinear components, exhibiting first- and second-order dependency to the generalized displacement vector, respectively. The detailed expression of these matrices in the global coordinate system is presented in the following set of equations,

I. Stiffness matrices,

$$\begin{aligned}\left[K_{N_0}\right]^{ij}=\sum_{i=1}^{2}\sum_{j=1}^{2}\int_{L_e}(&\left[R_a^{oi}\right]^T[A]\left[R_a^{oj}\right]+\left[R_a^{oi}\right]^T[B]\left[R_b^{oj}\right]+\\ &\left[R_b^{oi}\right]^T[B]\left[R_a^{oj}\right]+\left[R_b^{oi}\right]^T[D]\left[R_b^{oj}\right]+\left[R_{sa}^{oi}\right]^T[A_{55}]\left[R_{sa}^{oj}\right])\mathrm{d}x\end{aligned} \tag{4.43}$$

$$\begin{aligned}\left[K_{N_1}\right]^{ij}=\sum_{i=1}^{2}\sum_{j=1}^{2}\int_{L_e}(&\left[G^i\right]^T[H]^T[A]\left[R_a^{oj}\right]+\left[G^i\right]^T[H]^T[B]\left[R_b^{oj}\right]+\\ &\frac{1}{2}\left[R_a^{oi}\right]^T[A][H]\left[G^j\right]+\frac{1}{2}\left[R_b^{oi}\right]^T[B][H]\left[G^j\right])\mathrm{d}x\end{aligned} \tag{4.44}$$

$$\left[K_{N_2}\right]^{ij}=\sum_{i=1}^{2}\sum_{j=1}^{2}\int_{L_e}(\frac{1}{2}\left[G^i\right]^T[H]^T[A][H]\left[G^j\right])\mathrm{d}x \tag{4.45}$$

II. Damping matrices,

$$\begin{aligned}\left[C_{N_0}\right]^{ij}=\sum_{i=1}^{2}\sum_{j=1}^{2}\int_{L_e}(&\left[R_a^{oi}\right]^T[A_d]\left[R_a^{oj}\right]+\left[R_a^{oi}\right]^T[B_d]\left[R_b^{oj}\right]+\\ &\left[R_b^{oi}\right]^T[B_d]\left[R_a^{oj}\right]+\left[R_b^{oi}\right]^T[D_d]\left[R_b^{oj}\right]+\left[R_{sa}^{oi}\right]^T[A_{d55}]\left[R_{sa}^{oj}\right])\mathrm{d}x\end{aligned} \tag{4.46}$$

$$\begin{aligned}\left[C_{N_1}\right]^{ij}=\sum_{i=1}^{2}\sum_{j=1}^{2}\int_{L_e}(&\left[G^i\right]^T[H]^T[A_d]\left[R_a^{oj}\right]+\left[G^i\right]^T[H]^T[B_d]\left[R_b^{oj}\right]+\\ &\left[R_a^{oi}\right]^T[A_d][H]\left[G^j\right]+\left[R_b^{oi}\right]^T[B_d][H]\left[G^j\right])\mathrm{d}x\end{aligned} \tag{4.47}$$

$$\left[C_{N_2}\right]^{ij} = \sum_{i=1}^{2} \sum_{j=1}^{2} \int_{L_e} (\left[G^i\right]^T [H]^T [A_d][H]\left[G^j\right])\mathrm{d}x \tag{4.48}$$

III. Mass matrix,

$$[M]^{ij} = \sum_{i=1}^{2} \sum_{j=1}^{2} \int_{L_e} (\left[N^i\right]^T [\rho_{\mathrm{L}}]\left[N^j\right])\mathrm{d}x \tag{4.49}$$

The aforementioned element matrices have square form with dimensions 6x6, as it is shown in Eq. (4.50),

$$[Matrix]^{ij} \mapsto \left[\begin{array}{c|ccc} & DOF_u^1 & \cdots & DOF_u^{nodes} \\ \hline DOF_u^1 & & & \\ \vdots & & [K] & \\ DOF_u^{nodes} & & & \end{array}\right] \tag{4.50}$$

where $i, j = 1,2$ are the element nodes and $\left[R_a^{oi}\right]$, $\left[R_{sa}^{oi}\right]$, $\left[R_L^{oi}\right]$, $\left[R_b^{oi}\right]$ are the strain shape function matrices corresponding to the normal, shear, bending and nonlinear strains of the cross-section, respectively. Likewise, $\left[N^i\right]$ is the displacement shape function matrix and $[\rho_{\mathrm{L}}]$ is the generalized mass matrix, having the final form,

$$[\rho_{\mathrm{L}}] = \begin{bmatrix} \rho^A & 0 & \rho^B \\ 0 & \rho^A & 0 \\ \rho^B & 0 & \rho^D \end{bmatrix} \tag{4.51}$$

4.4.1.3 Transformation to the Local Coordinate System of the Element

The calculation of the integrals takes place in the local coordinate system of the element, shown in Figure 4.5b. Due to the fact that the aforementioned strain shape functions refer to the global coordinate system (x), it is necessary these expression to be transformed to the local coordinate system (ξ), where the shape function expression have already been defined (Eq. (4.38)). The derivative of the shape functions with refer to the local coordinate system is,

$$N^i_{,\xi}(\xi) = \frac{\partial N^i(\xi)}{\partial x}\frac{\partial x}{\partial \xi} \tag{4.52}$$

For the beam element case, taking into account Eq. (4.37), it is obvious that the transformation will take the form,

$$\mathrm{d}x = \frac{L_e}{2}\mathrm{d}\xi \tag{4.53}$$

Additionally, the integration limits have to change from $0 \to L_e$ to $-1 \to 1$ from the global to the local coordinate system, respectively.

4.4.1.4 Beam Element Matrices in the Local Coordinate System

In the local coordinate system, incorporation of Eq. (4.53) into the stiffness, damping and mass matrices of the global coordinate system (Eqs. (4.43)-(4.49)) yields the respective matrices in the local coordinate system, which are the following,

I. Stiffness matrices,

$$\begin{aligned}\left[K_{N_0}\right]^{ij} = \sum_{i=1}^{2}\sum_{j=1}^{2}\int_{-1}^{1} (&\left[R_a^{oi}\right]^T[A]\left[R_a^{oj}\right] + \left[R_a^{oi}\right]^T[B]\left[R_b^{oj}\right] + \\ &\left[R_b^{oi}\right]^T[B]\left[R_a^{oj}\right] + \left[R_b^{oi}\right]^T[D]\left[R_b^{oj}\right] + \left[R_{sa}^{oi}\right]^T[A_{55}]\left[R_{sa}^{oj}\right])\frac{L_e}{2}\mathrm{d}\xi\end{aligned} \tag{4.54}$$

$$\begin{aligned}\left[K_{N_1}\right]^{ij} = \sum_{i=1}^{2}\sum_{j=1}^{2}\int_{-1}^{1} (&\left[G^i\right]^T[H]^T[A]\left[R_a^{oj}\right] + \left[G^i\right]^T[H]^T[B]\left[R_b^{oj}\right] + \\ &\frac{1}{2}\left[R_a^{oi}\right]^T[A][H]\left[G^j\right] + \frac{1}{2}\left[R_b^{oi}\right]^T[B][H]\left[G^j\right])\frac{L_e}{2}\mathrm{d}\xi\end{aligned} \tag{4.55}$$

$$\left[K_{N_2}\right]^{ij} = \sum_{i=1}^{2}\sum_{j=1}^{2}\int_{-1}^{1}\left(\frac{1}{2}\left[G^i\right]^T[H]^T[A][H]\left[G^j\right]\right)\frac{L_e}{2}\mathrm{d}\xi \tag{4.56}$$

II. Damping matrices,

$$\begin{aligned}\left[C_{N_0}\right]^{ij} = \sum_{i=1}^{2}\sum_{j=1}^{2}\int_{-1}^{1} (&\left[R_a^{oi}\right]^T[A_d]\left[R_a^{oj}\right] + \left[R_a^{oi}\right]^T[B_d]\left[R_b^{oj}\right] + \\ &\left[R_b^{oi}\right]^T[B_d]\left[R_a^{oj}\right] + \left[R_b^{oi}\right]^T[D_d]\left[R_b^{oj}\right] + \left[R_{sa}^{oi}\right]^T[A_{d55}]\left[R_{sa}^{oj}\right])\frac{L_e}{2}\mathrm{d}\xi\end{aligned} \tag{4.57}$$

$$\left[C_{N_1}\right]^{ij}=\sum_{i=1}^{2}\sum_{j=1}^{2}\int_{-1}^{1}(\left[G^i\right]^T[H]^T[A_d]\left[R_a^{oj}\right]+\left[G^i\right]^T[H]^T[B_d]\left[R_b^{oj}\right]+ \left[R_a^{oi}\right]^T[A_d][H]\left[G^j\right]+\left[R_b^{oi}\right]^T[B_d][H]\left[G^j\right])\frac{L_e}{2}\mathrm{d}\xi \tag{4.58}$$

$$\left[C_{N_2}\right]^{ij}=\sum_{i=1}^{2}\sum_{j=1}^{2}\int_{-1}^{1}\left(\left[G^i\right]^T[H]^T[A_d][H]\left[G^j\right]\right)\frac{L_e}{2}\mathrm{d}\xi \tag{4.59}$$

II. Mass matrix,

$$[M]^{ij}=\sum_{i=1}^{2}\sum_{j=1}^{2}\int_{-1}^{1}\left(\left[N^i\right]^T[\rho_{\mathrm{L}}]\left[N^j\right]\right)\frac{L_e}{2}\mathrm{d}\xi \tag{4.60}$$

4.5 The Newton-Raphson Technique

The nonlinear code is capable of predicting the dynamic response of the composite beam-strip subject to large displacements and rotations. By omitting the damping and the mass matrices, Eq. (4.41) can be written in the following form,

$$\mathbf{\Psi}(\mathbf{u})=\left[\mathbf{K}(\mathbf{u})\right]\mathbf{u}-\mathbf{F} \tag{4.61}$$

where $\mathbf{\Psi}(\mathbf{u})$ is called the residual, which is a nonlinear function of the unknown solution $\mathbf{u}$. It is obvious that Eq. (4.61) cannot be solved directly because the nodal degrees of freedom are included in the stiffness matrix calculation. Therefore the implementation of a numerical method into the finite element code is necessary to obtain the solution of the nonlinear system. To that direction the Newton-Raphson incremental-iterative technique was formulated into the finite element code solver to obtain a quick and accurate solution of the nonlinear problem. The term "incremental" implies that the total applied external loads were applied incrementally, according to the relation,

$$^{n+1}F=^{n}F+\Delta F \tag{4.62}$$

An incremental solution procedure is based on the assumption of a known solution at an n increment in order to define the unknown solution at the next increment $n+1$ by the application of an external load ΔF. In the same time, the fact that $[\mathbf{K}]$ matrices exhibit nonlinear dependence to the nodal degrees of freedom, necessitates a suitable number of iterations within each increment in order the residual to become equal to zero.

Consider that the external load ΔF has been applied for an increment n and the vector of the elastic degrees of freedom has been estimated at an iteration i. The Newton-Raphson technique is based on Taylor's series expansion of the nonlinear algebraic Eq. (4.61) about the known solution. Since there is a solution $\left(u^i\right)$ at iteration i, then the Taylor theorem could be used to obtain the solution at an iteration $i+1$, taking into account only the first term of Taylor series. Therefore, Eq. (4.63) calculates the variation of elastic Δu degrees of freedom,

$$ {}^{n}\Psi^{i+1}\left(u^{i+1}\right) = {}^{n}\Psi^{i}\left(u^{i}\right) + \frac{\partial^{n}\Psi^{i}\left(u^{i}\right)}{\partial^{n}u^{i}}\Delta u^{i+1} = 0 \tag{4.63} $$

Taking into account that ΔF is constant and independent from the system nodal DOFs and substituting Eq. (4.61) into Eq. (4.63), the solution of the latter one yields,

$$ \frac{\partial^{n}\Psi^{i}\left(u^{i}\right)}{\partial^{n}u^{i}}\Delta u^{i+1} = -{}^{n}\Psi^{i}\left(u^{i}\right) \Leftrightarrow \frac{\partial\left(\left[{}^{n}K\left(u^{i}\right)\right]u^{i}\right)}{\partial^{n}u^{i}}\Delta u^{i+1} = -\left[{}^{n}K\left(u^{i}\right)\right]u^{i} + F \tag{4.64} $$

The term $\left[{}^{n}\bar{K}_{T}^{i}\right] = \dfrac{\partial\left(\left[{}^{n}K\left(u^{i}\right)\right]u^{i}\right)}{\partial^{n}u^{i}}$ is the tangential stiffness of the structure at the point of static equilibrium, whereas $\left[{}^{n}K\left(u^{i}\right)\right]$ is the effective stiffness matrix of the system. The tangential matrix for structural problems is symmetric even though the effective one is not symmetric. Detailed form of the tangential first- and second-order stiffness matrices is reported in Appendix D.

After calculating the variation of elastic Δu degrees of freedom, the new deformable state of the structure, $\left\langle u^{i+1}\right\rangle$ can be expressed by Eq. (4.65),

$$ {}^{n}u^{i+1} = {}^{n}u^{i} + \Delta u^{i+1} \tag{4.65} $$

At this point, it should be underlined that at the beginning of each iteration the tangential stiffness matrix and the residual vector must be updated using the latest available vector solution $\mathbf{u}$.

The main advantages of the Newton-Raphson incremental-iterative technique are:

- For each force increment ΔF the iterations continue till the convergence criterion $\boldsymbol{\Psi} \to \mathbf{0}$ is satisfied.
- At each iteration the present method calculates the tangential matrices $\left[\bar{\mathbf{K}}_{\mathbf{T}}\right]$ as well as the residual vector $\boldsymbol{\Psi}$, which provides the imbalance between the internal and external loads of the structure.

- The nonlinear tangential matrices $\left[\bar{\mathbf{K}}_{\mathbf{T}}\right]$ are those who define the solution approximation within each increment.

Figure 4.7 illustrates the Newton-Raphson technique for the approximation of a nonlinear solution for a single DOF problem. In each increment the necessary iterations are repeated until the imbalance vector between the internal and external forces is equal to zero $\left(\boldsymbol{\Psi} \to \mathbf{0}\right)$. The solution of the linearized Eq. (4.64) provides the variation of the nodal DOF Δu^{i+1}, and its substitution in Eq. (4.65) yields the updated DOF value, u^{i+1}. This procedure is repeated in the nonlinear finite element code till convergence is succeeded.

The main disadvantage of this method is that the calculation of the effective and tangential matrices terms as well as the imbalance vector at each iteration increases significantly the computational cost of the problem solution.

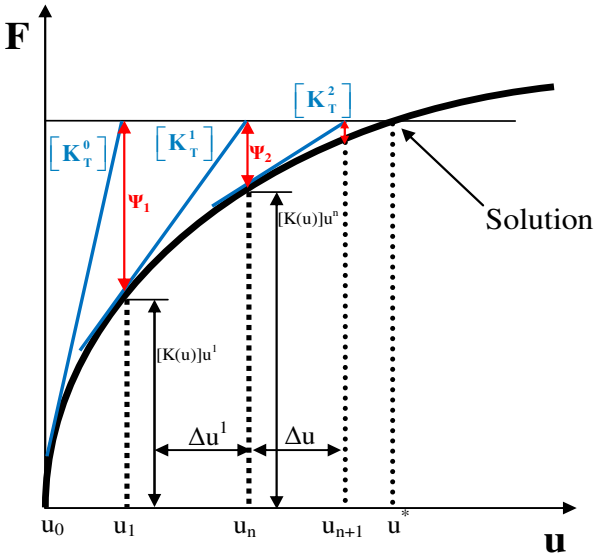

Fig. 4.7 Newton-Raphson iterative technique for a single DOF system

4.6 Final System of Equation

At the present point the detailed form of the tangential matrices of the nonlinear system will be described. The assembly of the total matrices and the application of the boundary conditions will also be presented.

4.6.1 Tangential Matrices at the Local Coordinate System of the Finite Element

The application of the aforementioned incremental-iterative technique provides the linearized expression of the nonlinear equations within each iteration, which has the following form,

$$\left[\bar{\mathbf{K}}_{\mathbf{T}}(\mathbf{u})\right]\Delta\mathbf{u} = -\left[\mathbf{K}(\mathbf{u})\right]\mathbf{u} + \mathbf{F} = -\boldsymbol{\Psi}(\mathbf{u}) \tag{4.66}$$

The total nonlinear tangential stiffness and damping matrices are,

$$\begin{aligned}\left[\bar{\mathbf{K}}(\mathbf{u})\right] &= \left[\bar{\mathbf{K}}_{\mathbf{N_0}}\right] + \left[\bar{\mathbf{K}}_{\mathbf{N_1}}(\mathbf{u})\right] + \left[\bar{\mathbf{K}}_{\mathbf{N_2}}(\mathbf{u}^2)\right] \\ \left[\bar{\mathbf{C}}(\mathbf{u})\right] &= \left[\mathbf{C}(\mathbf{u})\right] = \left[\bar{\mathbf{C}}_{\mathbf{N_0}}\right] + \left[\bar{\mathbf{C}}_{\mathbf{N_1}}(\mathbf{u})\right] + \left[\bar{\mathbf{C}}_{\mathbf{N_2}}(\mathbf{u}^2)\right]\end{aligned} \tag{4.67}$$

These matrices have the same form with the effective stiffness and damping ones and again the subscripts 0, $\mathrm{N1}$ and $\mathrm{N2}$ indicate linear, first- and second-order nonlinear dependence to the generalized section displacements, respectively. So, in the local coordinate system of the beam finite element, they are described in detail, as follows,

I. Tangential stiffness matrices,

$$\begin{aligned}\left[\bar{K}_{N_0}\right]^{ij} = \sum_{i=1}^{2}\sum_{j=1}^{2}\int_{-1}^{1} &\left(\left[R_a^{oi}\right]^T[A]\left[R_a^{oj}\right] + \left[R_a^{oi}\right]^T[B]\left[R_b^{oj}\right] + \right. \\ &\left.\left[R_b^{oi}\right]^T[B]\left[R_a^{oj}\right] + \left[R_b^{oi}\right]^T[D]\left[R_b^{oj}\right] + \left[R_{sa}^{oi}\right]^T[A_{55}]\left[R_{sa}^{oj}\right]\right)\frac{L_e}{2}\mathrm{d}\xi\end{aligned} \tag{4.68}$$

$$\begin{aligned}\left[\bar{K}_{N_1}\right]^{ij} = \sum_{i=1}^{2}\sum_{j=1}^{2}\int_{-1}^{1} &\left(\left[G^i\right]^T[H]^T[A]\left[R_a^{oj}\right] + \left[G^i\right]^T[H]^T[B]\left[R_b^{oj}\right] + \right. \\ &\left.\left[R_a^{oi}\right]^T[A][H]\left[G^j\right] + \left[R_b^{oi}\right]^T[B][H]\left[G^j\right]\right)\frac{L_e}{2}\mathrm{d}\xi\end{aligned} \tag{4.69}$$

$$\left[\bar{K}_{N_2}\right]^{ij} = \sum_{i=1}^{2}\sum_{j=1}^{2}\int_{-1}^{1}\left(\frac{3}{2}\left[G^i\right]^T[H]^T[A][H]\left[G^j\right]\right)\frac{L_e}{2}\mathrm{d}\xi \tag{4.70}$$

II. Tangential damping matrices,

$$\begin{aligned}\left[\bar{C}_{N_0}\right]^{ij} = \sum_{i=1}^{2}\sum_{j=1}^{2}\int_{-1}^{1} &\left(\left[R_a^{oi}\right]^T[A_d]\left[R_a^{oj}\right] + \left[R_a^{oi}\right]^T[B_d]\left[R_b^{oj}\right] + \right. \\ &\left.\left[R_b^{oi}\right]^T[B_d]\left[R_a^{oj}\right] + \left[R_b^{oi}\right]^T[D_d]\left[R_b^{oj}\right] + \left[R_{sa}^{oi}\right]^T[A_{d55}]\left[R_{sa}^{oj}\right]\right)\frac{L_e}{2}\mathrm{d}\xi\end{aligned} \tag{4.71}$$

$$\left[\bar{C}_{N_1}\right]^{ij} = \sum_{i=1}^{2}\sum_{j=1}^{2}\int_{-1}^{1} (\left[G^i\right]^T[H]^T[A_d]\left[R_a^{oj}\right] + \left[G^i\right]^T[H]^T[B_d]\left[R_b^{oj}\right] + \left[R_a^{oi}\right]^T[A_d][H]\left[G^j\right] + \left[R_b^{oi}\right]^T[B_d][H]\left[G^j\right])\frac{L_e}{2}\mathrm{d}\xi \tag{4.72}$$

$$\left[\bar{C}_{N_2}\right]^{ij} = \sum_{i=1}^{2}\sum_{j=1}^{2}\int_{-1}^{1} \left(\left[G^i\right]^T[H]^T[A_d][H]\left[G^j\right]\right)\frac{L_e}{2}\mathrm{d}\xi \tag{4.73}$$

The notable difference between the effective and the tangential stiffness and damping expressions is that although they contain the same terms, they are multiplied with different constants. This contributes to the reduction of the computational cost of final system solution.

4.6.2 Assembly of System Equations

The assembly of the final equations of the system is a critical step in the finite element method. Taking into account that the beam-strip finite element has two nodes, then if K is the number of elements in which the structure is descritized then $Q = K + 1$ will be the total nodes of the system. Thus, if $\mathbf{U}$ represents the nodal degrees of freedom of the total system then it can take the following form,

$$\left[\bar{\mathbf{K}}_{\mathbf{T}}(\mathbf{U})\right]_{\mathbf{3Qx3Q}}\{\Delta\mathbf{U}\}_{\mathbf{3Qx1}} = \{-\boldsymbol{\Psi}(\mathbf{U})\}_{\mathbf{3Qx1}} \tag{4.74}$$

where,

$$\{\boldsymbol{\Psi}(\mathbf{U})\}_{\mathbf{3Qx1}} = \left[\mathbf{K}(\mathbf{U})\right]_{\mathbf{3Qx3Q}}\{\mathbf{U}\}_{\mathbf{3Qx1}} - \{\mathbf{F}\}_{\mathbf{3Qx1}} \tag{4.75}$$

and the number 3 indicates the DOFs at each node of the element.

4.6.3 Boundary Conditions

After having synthesizing the total system of equations for the whole structure, the next step involves the application of the boundary conditions. The total vector of the nodal degrees of freedom $\mathbf{U}$ consists of two components: a) the vector of applied DOFs on the structure $\mathbf{U^c}$, which is known and introduced by the user into the code and b) the unknown DOFs vector, $\mathbf{U^f}$. So, vector $\mathbf{U}$ is,

$$\{\mathbf{U}\} = \begin{Bmatrix}\mathbf{U^f}\\ \mathbf{U^c}\end{Bmatrix} \tag{4.76}$$

4.6.4 Expression of the Final Set of Equations

The substitution of Eq. (4.76) into Eqs. (4.74)-(4.75), provides the final form of the system equations,

$$\left[\bar{\mathbf{K}}_{\mathbf{T}}^{\mathbf{f}} \quad \bar{\mathbf{K}}_{\mathbf{T}}^{\mathbf{c}}\right]\begin{Bmatrix}\Delta\mathbf{U}^{\mathbf{f}}\\ \Delta\mathbf{U}^{\mathbf{c}}\end{Bmatrix} = \left\{-\boldsymbol{\Psi}(\mathbf{U})\right\} = \{\mathbf{F}\} - \left[\mathbf{K}_{\mathbf{T}}^{\mathbf{f}} \quad \mathbf{K}_{\mathbf{T}}^{\mathbf{c}}\right]\begin{Bmatrix}\mathbf{U}^{\mathbf{f}}\\ \mathbf{U}^{\mathbf{c}}\end{Bmatrix} \tag{4.77}$$

Equation (4.77) gives out one step $\left\{\Delta\mathbf{U}^{\mathbf{f}}\right\}$ of the solution $\mathbf{U}^{*}$ (Figure 4.7). In order to reach the final solution, the elimination method is applied. In addition the vector of known DOFs $\mathbf{U}^{\mathbf{c}}$ is equal to zero. Thus, the final system is,

$$\left[\bar{\mathbf{K}}_{\mathbf{T}}^{\mathbf{f}}\right]\left\{\Delta\mathbf{U}^{\mathbf{f}}\right\} = \left\{-\boldsymbol{\Psi}(\mathbf{U})\right\} \tag{4.78}$$

4.7 Small-Amplitude Free-Vibration of Composite Strip

This section describes the theoretical background for the nonlinear small-amplitude free-vibration response of composite strips subject to large displacements and rotations. The effect of large deformations will be demonstrated by predicting the modal characteristics of the composite structures.

Beginning from structural level, where the total stiffness, damping and mass matrices of the strip finite element have already been formulated, Eq. (4.41) describes the nonlinear dynamic response of the composite structure at a specific time increment t,

$$\boldsymbol{\Psi}(\mathbf{u},\mathbf{t}) = \left[\mathbf{M}\right]\ddot{\mathbf{u}}(\mathbf{t}) + \left[\mathbf{C}\right]\dot{\mathbf{u}}(\mathbf{t}) + \left[\mathbf{K}\right]\mathbf{u}(\mathbf{t}) - \mathbf{F}(\mathbf{t}) \tag{4.79}$$

where $\mathbf{F}(\mathbf{t})$ indicates the time dependent external mechanical forces. For vibrating beams subject to large deformations, we specialize their motion to the case of a perturbation vibration around a nonlinear static equilibrium point $\mathbf{u}_{\mathbf{s}}$, such that,

$$\mathbf{u}(\mathbf{t}) = \mathbf{u}_{\mathbf{s}} + \bar{\mathbf{u}}(\mathbf{t}) \tag{4.80}$$

where overbar indicates perturbation quantities and $\mathbf{u}_{\mathbf{s}} \gg \bar{\mathbf{u}}(\mathbf{t})$.

By combining Eq. (4.79) with Eq. (4.80) and taking into account only the first term of Taylor's theorem, the equilibrium relation expanded about point $\mathbf{u}_{\mathbf{s}}$, takes the following form,

$$\mathbf{\Psi}(\mathbf{u},\mathbf{t})=[\mathbf{M}]\ddot{\bar{\mathbf{u}}}+\frac{\partial([\mathbf{C}]\dot{\mathbf{u}})}{\partial\dot{\mathbf{u}}}\dot{\bar{\mathbf{u}}}+([\mathbf{K}]\mathbf{u}_s-\mathbf{F}_s)+\frac{\partial([\mathbf{K}]\mathbf{u})}{\partial\mathbf{u}}\bar{\mathbf{u}}-\bar{\mathbf{F}}(\mathbf{t})=\mathbf{0} \tag{4.81}$$

It is observed that since $\mathbf{u}_s$ is the point of static equilibrium, the imbalance force vector between the internal forces and externally applied mechanical loads, vanishes,

$$\mathbf{\Psi}_s=([\mathbf{K}]\mathbf{u}_s-\mathbf{F}_s)=\mathbf{0} \tag{4.82}$$

By definition the terms $[\bar{\mathbf{K}}]=(\partial([\mathbf{K}]\mathbf{u})/\partial\mathbf{u})$, $[\bar{\mathbf{C}}]=(\partial([\mathbf{C}]\dot{\mathbf{u}})/\partial\dot{\mathbf{u}})$ are the tangential or linearized stiffness and damping of the structure at the point of static equilibrium. Hence, Eq. (4.81) takes the final form which describes the small vibration of the beam,

$$\mathbf{\Psi}(\bar{\mathbf{u}},\mathbf{u}_s,\mathbf{t})=[\mathbf{M}]\ddot{\bar{\mathbf{u}}}(\mathbf{t})+[\bar{\mathbf{C}}(\mathbf{u}_s)]\dot{\bar{\mathbf{u}}}(\mathbf{t})+[\bar{\mathbf{K}}(\mathbf{u}_s)]\bar{\mathbf{u}}(\mathbf{t})-\bar{\mathbf{F}}(\mathbf{t})=\mathbf{0} \tag{4.83}$$

The total stiffness, damping and the linearized stiffness structural matrices contain linear and both first- and second-order nonlinear components which are calculated from Eqs. ((4.18) - (4.22)), ((4.24)-(4.29)); and therefore, Eq. (4.83) take the following form,

$$\begin{aligned}
[\mathbf{K}(\mathbf{u}_s)]&=[\mathbf{K}_0]+[\mathbf{K}_{N1}(\mathbf{u}_s)]+[\mathbf{K}_{N2}(\mathbf{u}_s)]\\
[\bar{\mathbf{K}}(\mathbf{u}_s)]&=[\mathbf{K}_0]+[\bar{\mathbf{K}}_{N1}(\mathbf{u}_s)]+[\bar{\mathbf{K}}_{N2}(\mathbf{u}_s)]\\
[\mathbf{C}(\mathbf{u}_s)]&=[\bar{\mathbf{C}}(\mathbf{u}_s)]=[\mathbf{C}_0]+[\mathbf{C}_{N1}(\mathbf{u}_s)]+[\mathbf{C}_{N2}(\mathbf{u}_s)]
\end{aligned} \tag{4.84}$$

where, subscripts 0, $N1$ and $N2$ indicate linear, first- and second-order nonlinear dependence to the generalized section displacements, respectively.

The Newton-Raphson iterative technique was chosen for calculating the static equilibrium point $\mathbf{u}_s$ due to its simplicity and also because it uses the linearized stiffness matrix $[\bar{\mathbf{K}}(\mathbf{u})]$ described in Eq. (4.84).

4.8 Displacement Control Method

The main advantage of the Newton-Raphson iterative technique is that utilizes the tangential matrices of the system in order to achieve the convergence of each substep and subsequently of the final solution. The case of buckling analysis

(Figure 4.8) may involve limit points marking the transition between two stable equilibrium paths in the pre- and post-buckling regime, where the beam structure loses its stability rapidly. Figure 4.8 presents such a case, where a clamped-free beam structure is loaded with a compressive in-plane force F at its free end and is deformed in the transverse direction (w).

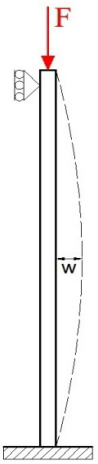

Fig. 4.8 Typical example of a clamped-free beam undergoing buckling

Figure 4.9 shows the transverse deflection w of the beam subject to buckling. The limit points A-A' define the transition area, where the linearized stiffness matrix may not be positive definite.

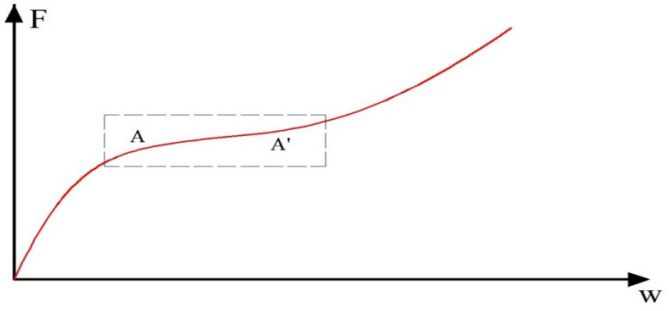

Fig. 4.9 Buckling response of a clamped-free beam and transition area from one stable equilibrium point to another (A-A')

One way to overcome this situation, is by imposing nodal displacements enabling the stable numerical calculation of structure modal characteristics even in the transition area between one stable equilibrium point to another. A Newton-Raphson iterative technique with displacement control was formulated and

implemented as part of the solution procedure for calculating the static equilibrium point $\mathbf{u}_s$. This method has the advantage to overcome the critical points where the tangential matrix becomes singular by applying an incremental imposed displacement vector on the beam model.

Supposing that the analysis begins with the first iteration i in the respective first applied displacement increment ($n=1$), the linearized Newton-Raphson equation has the following form,

$$\left[\bar{\mathbf{K}}(\mathbf{u})\right]\{\Delta\mathbf{u}\}=\{\Psi(\mathbf{u})\} \tag{4.85}$$

The displacement control method considers that the total displacement vector of the system consists of the unknown (free) and the applied (imposed) elastic degrees of freedom (DOF), indicated by the letters f and a, respectively. Thus Eq. (4.85) becomes,

$$\begin{bmatrix}\left[\bar{\mathbf{K}}_{\mathbf{ff}}(\mathbf{u})\right] & \left[\bar{\mathbf{K}}_{\mathbf{fa}}(\mathbf{u})\right]\\ \left[\bar{\mathbf{K}}_{\mathbf{af}}(\mathbf{u})\right] & \left[\bar{\mathbf{K}}_{\mathbf{aa}}(\mathbf{u})\right]\end{bmatrix}\begin{Bmatrix}\Delta\mathbf{u}^{\mathbf{f}}\\ \Delta\mathbf{u}^{\mathbf{a}}\end{Bmatrix}=\{\Psi(\mathbf{u})\} \tag{4.86}$$

Equation (4.86) provides the solution of the system as well as the corresponding applied displacement component which is considered to be an unknown variable in this method.

$$\left[\bar{\mathbf{K}}^{\mathbf{0}}_{\mathbf{ff}}(\mathbf{u})\right]\left\{\Delta\mathbf{u}^{\mathbf{f}^{\mathbf{i}}}\right\}=-\left[\bar{\mathbf{K}}^{\mathbf{0}}_{\mathbf{fa}}(\mathbf{u})\right]\left\{\Delta\mathbf{u}^{\mathbf{a}^{\mathbf{i}}}\right\}+\left\{\Psi^{\mathbf{0}}(\mathbf{u})\right\} \tag{4.87}$$

where 0 indicates the initial state of the structure and i is the first iteration. Solution of the above equation provides the unknown DOF of the system which are updated in each iteration, as follows,

$$\left\{\mathbf{u}^{\mathbf{f}^{\mathbf{i}}}\right\}=\left\{\mathbf{u}^{\mathbf{f}^{\mathbf{0}}}\right\}+\left\{\Delta\mathbf{u}^{\mathbf{f}^{\mathbf{i}}}\right\} \tag{4.88}$$

The applied mechanical DOF $\left\{\Delta\mathbf{u}^{\mathbf{a}^{\mathbf{i}}}\right\}$ should remain constant for all subsequent iterations until convergence is achieved within the first increment ($n=1$). The following conditions should therefore be satisfied,

$$\begin{aligned}\left\{\Delta\mathbf{u}^{\alpha^{\mathbf{i+1}}}\right\}&=\mathbf{0}\\ \left\{\mathbf{u}^{\alpha^{\mathbf{i}}}\right\}&=\left\{\Delta\mathbf{u}^{\alpha^{\mathbf{i}}}\right\}\end{aligned} \tag{4.89}$$

By substituting Eqs. ((4.88)-(4.89)) into Eq. (4.87), the second iteration $i+1$ is calculated by Eq. (4.90) as follows,

$$\left[\bar{\mathbf{K}}_{\mathbf{ff}}^{\mathbf{i}}(\mathbf{u})\right]\left\{\Delta\mathbf{u}^{\mathbf{f}^{\mathbf{i+1}}}\right\} = -\left[\mathbf{K}_{\mathbf{fa}}^{\mathbf{i}}(\mathbf{u})\right]\left\{\mathbf{u}^{\mathbf{a}^{\mathbf{i}}}\right\} - \left[\mathbf{K}_{\mathbf{ff}}^{\mathbf{i}}(\mathbf{u})\right]\left\{\mathbf{u}^{\mathbf{f}^{\mathbf{i}}}\right\} \tag{4.90}$$

The iteration procedure is continued until the method convergences, $\boldsymbol{\Psi \rightarrow 0}$, to the equilibrium solution point of each increment, where the reaction force of the respective applied displacement is also calculated by the following relation,

$$\{\mathbf{R}\} = \left[\bar{\mathbf{K}}_{\mathbf{af}}(\mathbf{u})\right]\left\{\mathbf{u}^{\mathbf{f}}\right\} + \left[\bar{\mathbf{K}}_{\mathbf{aa}}(\mathbf{u})\right]\left\{\mathbf{u}^{\mathbf{a}}\right\} \tag{4.91}$$

Figure 4.10 illustrates the displacement control method for the nonlinear solution of a single DOF problem.

The specified displacement is incremented and a loading parameter is evaluated for each step of the iteration procedure. The solution singularity faced by the force control method is resolved by knowing the prescribed displacement of the controlling DOF, enabling the solver to evaluate equilibrium and calculate the response for the whole model. However, the method fails due to singularity when the slope of the Force-Displacement curve becomes vertical (infinite) such in problems evolving snap-back buckling problems where the Arc Length Control Method seems to be the most powerful methodology.

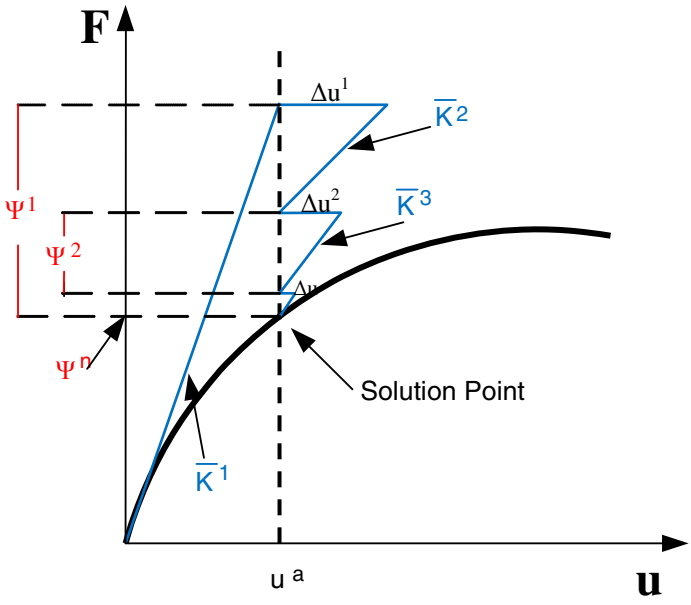

Fig. 4.10 Displacement control methodology for a single DOF system

4.9 Numerical Integration

In order to calculate the effective and tangential matrices of the structure the numerical integration method was used in the finite element code. The implementation of numerical integration is necessary due to the complex functions which have to be integrated. In the present subsection the integration along the beam finite element axis will be described.

The Gaussian quadrature approach of numerically evaluating an one-dimensional integral I is given below.

$$I = \int_{-1}^{1} f(\xi)\,\mathrm{d}\xi = \sum_{i=1}^{n} H_i f(\xi_i) \tag{4.92}$$

where n is the number of sampling points.

The method is based on the hypothesis that the one-dimensional integration is approximated by the values of function f at predefined points of the integration range ($-1 \le \xi \le 1$), the so called "Gauss points" or "sampling points", with the suitable weight factors H_i. The function f refers to the element generalized matrices multiplied with the shape function matrices.

Generally, the Gauss integration method uses a small number of sampling points, which are always within the integration range, and in such positions that the integration error is minimized especially for high-order functions. The advantage of this method is that for the case of n sampling points, the order of error is $2n$. From above, it can be concluded that the n-point Gaussian quadrature will provide an exact answer if the function f is a polynomial of order $2n-1$ or less.

The order of the shape functions is known and therefore the order of the functions in the stiffness, damping and mass integrations is also known for each element of the structure. Consequently, for the beam finite element is easy to predefine the necessary number of sampling points, capable of calculating the aforementioned integrations with the highest accuracy. The majority of the stiffness and damping terms were estimated using two sampling points.

4.10 Conclusions

Fourth chapter presented the theoretical framework for the dynamic analysis of a composite strip subject to large in-plane loads. A new nonlinear beam finite element was developed based on nonlinear kinematic assumptions, describing the geometric nonlinearities due to large deformations and rotations.

The major conclusions are summarized to the following ones:

- Incorporation of the strain-based Kelvin viscoelastic constitutive equations into the section strain energy expression yields the linear and nonlinear damping matrices of the finite element.

- The structural damping highly depends on the nonlinear response of the beam. If the beam remains in the linear regime, i.e. negligible initial in-plane stresses, the flexural damping of the beam is contributed by the flexural damping term D_{d11}. When the beam enters the nonlinear regime and is subject to large in-plane forces and rotations, strong additional damping terms are introduced which couple flexure and extension. These terms are proportional to the extensional damping term A_{d11} and section rotation.
- There is a strong effect of lamination lay-up on the structural damping of the composite structure. As the magnitude of the initial load increases, the effect of laminate configuration on structural damping will be governed mainly by extensional damping terms A_d and less by flexural damping D_d.

The novelty points of the fourth chapter are:

* The development of a theoretical framework for the prediction of nonlinear damping of composite beams under large in-plane loads. A new damped nonlinear beam finite element was formulated and the aforementioned nonlinear stiffness and damping mechanics were incorporated into a research finite code enabling computational prediction of nonlinear damping and stiffness characteristics of composite strips.
* The detailed formulation of first- and second-order stiffness and damping terms both for the effective and the tangential structural matrices of the system. The first-order terms are associated with the pre-stressing of the beam whereas the addition of second-order terms plays an essential role in the buckling and post-buckling response of the composite strip.

Chapter 5

Nonlinear Dynamic Response of Composite Plate-Beams

Composite material systems are known to provide damping which is beneficial for the passive control of vibratory, aeroelastic and acoustic loads, in a variety of structural applications. Many of such structures may be exposed to large deformations and high tensile and compressive loads.

In the present chapter the nonlinear response of the composite strip subject to in-plane tension and compressive loads will be investigated. Based on the theoretical framework developed in fourth chapter, the following sections present the nonlinear beam finite element capabilities of predicting the nonlinear initial stress and geometric effects on both structural stiffness and damping, assuming a Kelvin viscoelastic material. Fifth chapter consists of four main subsections; In the first one a brief description regarding the calculation of modal damping is recalled, whereas the second subsection includes the necessary information of the experimental procedure followed for the Glass/Epoxy composite material characterization and the extraction of its elastic properties and damping coefficients. In addition, the measurement of modal frequencies and modal loss factor values of the beam subject to increasing tension or buckling load applied along its longitudinal axis is presented. The experimental procedures and testing apparatus are briefly described. In the third subsection the capabilities of the damped beam element to predict the structural stiffness and modal damping values are shown. Numerical results quantify the contribution of the new nonlinear damping and stiffness cross-section terms on the modal frequencies and damping of composite beams of various angle-ply laminations under in-plane loads. Theoretical modal characteristic predictions are correlated with experimental measurements on Glass/Epoxy $[0_2/90_2]_s$ and $[0_2/90_2]_s$ cross-ply composite beams for various values of increasing tensile in-plane loads. Then the developed formulation is correlated with available numerical predictions and experimental measurements of a shell nonlinear element for the case of an aluminum beam specimen. Further validations between predicted and experimental modal loss factors and frequencies of composite beams subject to in-plane buckling are presented, which give credence to the developed nonlinear beam finite element and underline the contribution of first- and second-order nonlinear terms.

D.I. Chortis, *Structural Analysis of Composite Wind Turbine Blades*,
Research Topics in Wind Energy 1,
DOI: 10.1007/978-3-319-00864-6_5, © Springer International Publishing Switzerland 2013

5.1 Calculation of System Eigenfrequencies and Modal Damping

After synthesizing the aforementioned structural matrices and applying the boundary conditions, the next critical step includes the system solution at each point of static equilibrium till final convergence is achieved. Assuming harmonic motion, Eq. (4.83) may be solved either directly to yield the complex eigenvalues of the system or by using an energy approach for the calculation of structural damping. In the present work the second method is used, where the numerical solution of the undamped system provides the undamped modal frequencies and the relative mode shapes of the beam structure,

$$\left(-\omega^2\left[\mathbf{M}\right]+j\left[\bar{\mathbf{C}}\left(\mathbf{u}_s\right)\right]+\left[\bar{\mathbf{K}}\left(\mathbf{u}_s\right)\right]\right)\mathbf{U}=\mathbf{0} \tag{5.1}$$

where ω, $\mathbf{U}$ are the eigenfrequencies and the eigenvector of the system, respectively.

The dissipated energy method is accurate in problems involving low damping, i.e. like the damping of the composite materials. It also assumes that both the natural frequencies and the eigenshapes of the damped structure are very close to the respective ones of the structure without damping. Thereafter, the modal loss factor for the assumed Kelvin damping (Eq. (4.1)) is calculated as the following ratio of the respective dissipated to the maximum stored modal energy in the structure,

$$\eta_m=\frac{\omega_m}{2\pi}\frac{\bar{\mathbf{U}}_{\mathbf{m}}^{\mathbf{T}}\left[\mathbf{C}\left(\mathbf{u}\right)\right]\bar{\mathbf{U}}_{\mathbf{m}}}{\bar{\mathbf{U}}_{\mathbf{m}}^{\mathbf{T}}\left[\bar{\mathbf{K}}\left(\mathbf{u}\right)\right]\bar{\mathbf{U}}_{\mathbf{m}}} \tag{5.2}$$

where ω_m and $\bar{\mathbf{U}}_{\mathbf{m}}$ are the undamped modal frequency and modal displacement vector, respectively.

The nonlinear beam finite element and previous formulation were encoded into an updated version of a research structural dynamics code, DAMPBEAM, which is now capable of predicting both the nonlinear modal damping and frequency values of composite laminated beams subject to large in-plane loads and rotations.

5.2 Experimental Determination of Elastic and Damping Material Properties

One of the main objectives of this work deals with the prediction of nonlinear damping of composite structures undergoing large deformations.

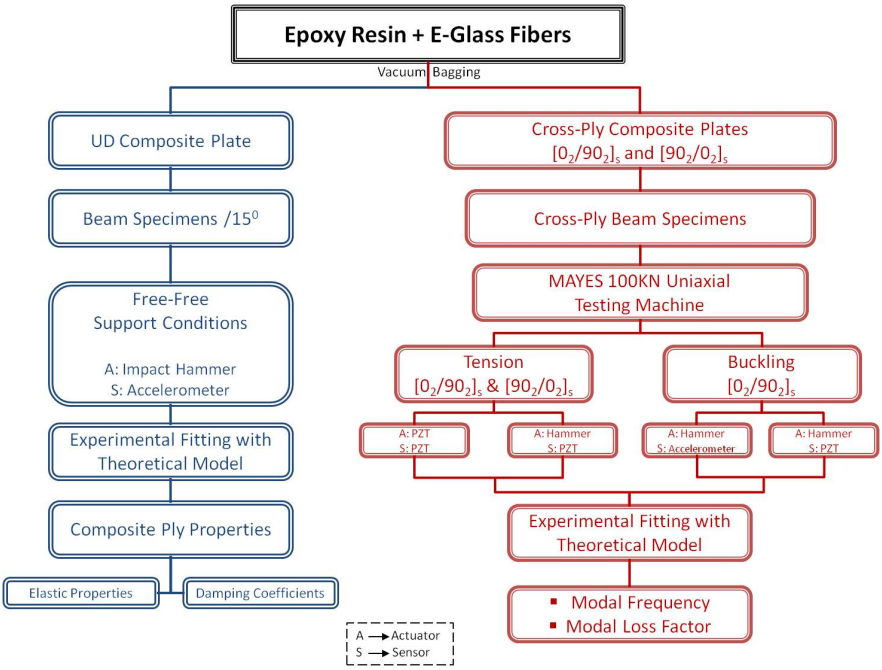

Fig. 5.1 Experimental procedure for determining: (a) Glass/Epoxy composite ply properties; (b) Modal characteristics of Glass/Epoxy cross-ply specimens under uniaxial tension and buckling

To that direction, a series of dynamic experiments were conducted in order not only to define the damping coefficients of the composite material but also to measure the nonlinear modal loss factor of the composite beam-strips and correlate them with the code theoretical predictions. The latter was necessary to ensure the credibility of the finite element code numerical prediction capabilities. The schematic flowchart of the experiments procedure followed during the current work is illustrated in Figure 5.1.

5.2.1 Extraction of Material Elastic and Damping Coefficients

The first step to quantify the effect of geometric nonlinearities on the modal characteristics of composite beams included the calculation of beam specimens material properties. The composite material characterization procedure was divided into the following three major sub-steps:

I. Fabrication of composite specimens. A single Glass/Epoxy unidirectional (UD) composite plate was fabricated at the Applied Mechanics Laboratory (AML) using the hand lay-up method. The plate consisted of six layers of E-Glass fabrics, (Porcher Industries-Composites), whose detailed properties are shown in Table 5.1.

Table 5.1 E-Glass fabrics properties

Weave	*Construction Warp/Weft* (yarn/cm)	*Weight ratio*	*Weight* (g/m^2)
Plain	5.5/6.3	90/10	0.431

The baseline epoxy matrix resin intended for fabrication of wind-turbine blades due to the high damping properties and consisted of two parts: Araldite® LY 3505 resin; and XB 3405 hardener (HUNTSMAN), whose main properties are provided in Table 5.2 and Table 5.3, respectively.

Table 5.2 Key data of Araldite® LY 3505

Aspect	*Viscosity at 25^0C (ISO 12058-1)* (mPa s)	*Density at 25^0C (ISO 1675)* (g/cm^3)	*Flash point (ISO 2719)* (^0C)
Clear liquid	6500 – 8000	1.15 – 1.20	>200

Table 5.3 Key data of hardener XB 3405

Aspect	*Viscosity at 25^0C (ISO 12058-1)* (mPa s)	*Density at 25^0C (ISO 1675)* (g/cm^3)	*Flash point (ISO 2719)* (^0C)
Clear, red liquid	70 – 90	0.95 – 1.0	109

Table 5.4 presents the epoxy resin/hardener processing data, which were followed during the composite plates construction procedure.

Table 5.4 Epoxy resin/hardener system processing data

Mix ratio (Parts by weight)	*Gelation at 23^0C* (h)	*Curing cycle at 60^0C* (h)
Resin:100 Hardner:35	Start: 2-3 End: 4-5	8-10

II. Experimental procedure developed for the damping measurement. The testing apparatus used for the determination of the elastic properties and damping coefficients of the Glass/Epoxy composite material is shown in Figure 5.2.

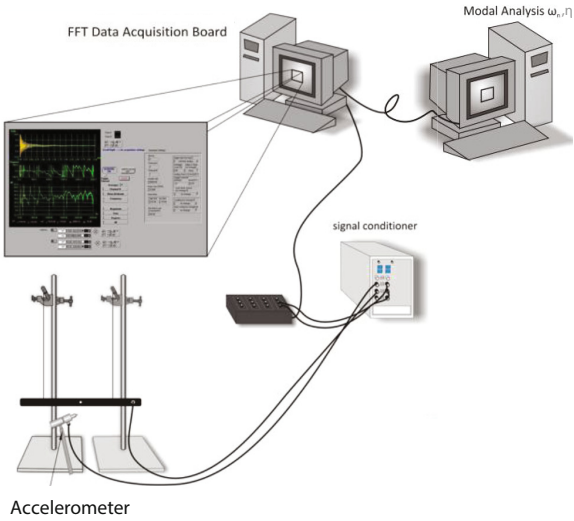

Fig. 5.2 Testing apparatus for the extraction of elastic properties and damping coefficients of the Glass/Epoxy composite system

It consists of three modules: a) Measurement of excitation and response signals; b) Data processing for the frequency response functions (FRF); c) Modal analysis for the estimation of natural frequencies and modal loss factor values of the composite structure. A miniature impact hammer was mainly used for specimen excitation, which had the capability of force measurement though a load cell. The impact force was applied at the midspan of the specimen. The response of the beam was also measured at the midspan of the specimen using a miniature (1.0gr) piezoelectric accelerometer. The sensor was attached on the specimen's surface with an epoxy adhesive.

The amplified output voltages from the load cell and the accelerometer were digitized through a high speed DAQ board and finally processed using FFT software to obtain the power spectra and FRFs of the beam. The measured FRFs were further correlated with a parametric model consisting of a series of complex exponential terms, each term approximating an individual mode with unknown modal parameters. In this manner, the modal frequencies and modal damping coefficients of the tested system were measured, such that the least square error between the model and measured frequency response functions was minimized.

III. Extraction of elastic and damping material ply coefficients. Beam specimens were cut from the unidirectional Glass/Epoxy composite plate at different angles to the fiber direction, yielding specimens with fiber orientation angles from 0^o to 90^o in increments of 15^o (Figure 5.3). The geometric data of the tested specimens are shown in Table 5.5.

Table 5.5 Geometric data for the Glass/Epoxy beam specimens under free-free support conditions

Length, L (mm)	*Width, b* (mm)	*Thickness, h* (mm)	*Weight* (g)
360	20	2.4	30

The beam specimens were subsequently tested in nearly free-free support configurations, in order to minimize damping due to friction in the supports. For this reason, the specimens were hang using strings attached at the modal lines of the first bending mode (Figure 5.2). In addition, they were supposed as thin beams ($L/h=18$) in order to minimize the effect of beam thickness and consequently the effect of the out-of-plane shear stresses. Thereafter, the equivalent experimental modal damping and modal frequency values of the first bending mode of each specimen were measured.

Fig. 5.3 Beam specimens cut from the UD Glass/Epoxy plate at 15^0 increments

Considering that the first mode refers to pure bending deformations of the thin beam specimens (only axial stresses act within the specimen inducing a non-zero bending moment), and that all specimens had a uniform through-the-thickness material, it can be reasonably assumed that the measured modal frequency values are related directly to the axial modulus of the composite material. Similarly, the modal damping of each specimen were assumed to be related directly to the axial damping of the composite.

Ply Elastic Properties

The first objective of the aforementioned experimental setup is the determination of the ply elastic properties E_{11}, E_{22}, ν_{12}, G_{12}. The compliance matrix of a composite ply in the material coordinate system (on-axis) is given by the following relation,

$$[S_l] = \begin{bmatrix} \frac{1}{E_{11}} & -\frac{\nu_{12}}{E_{11}} & 0 \\ -\frac{\nu_{12}}{E_{11}} & \frac{1}{E_{22}} & 0 \\ 0 & 0 & \frac{1}{G_{12}} \end{bmatrix} \tag{5.3}$$

The off-axis compliance matrix, $[S_c]$ is provided from the respective on-axis matrix (Eq. (5.3)), and the appropriate rotation matrix $[R]$,

$$[S_c] = [R]^T [S_l][R] \tag{5.4}$$

Consequently, by inverting the term "*11*" of Eq. (5.3), the equivalent elastic modulus in the axial direction of the beam specimen is,

$$E_{eq} = 1 / S_{c11} \tag{5.5}$$

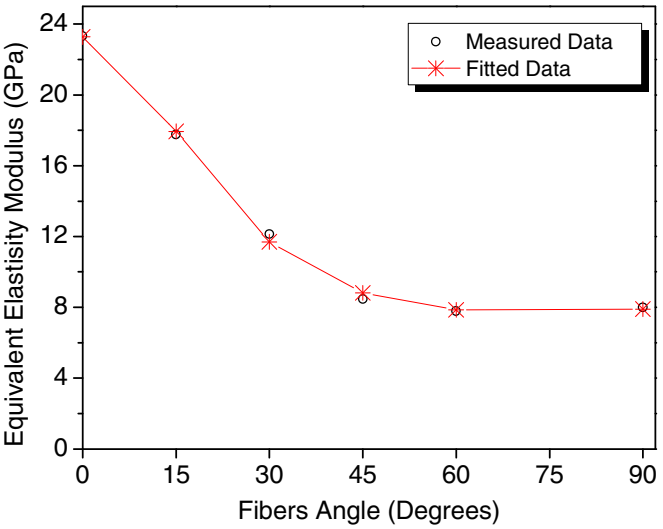

Fig. 5.4 Fitting of experimental equivalent elasticity modulus of first bending mode with the analytical model for the calculation of elastic properties of Glass/Epoxy composite material

Within the activities of Structural Analysis and Active Materials group (SAAM), a module had already been developed in MATLAB for the inverse prediction of the three elastic coefficients (longitudinal, transverse and in-plane shear) of a composite material system from the measured flexural axial modulus of all off-axis specimens. A model approximating the experimental axial flexural modulus of a laminate with the composite equivalent elastic modulus was developed, based on the least-squares minimization procedure. Figure 5.4 shows the experimental values and their approximation by the theoretical model.

Ply damping coefficients

The same procedure was followed to determine the damping coefficients of the composite ply. The elastic coefficients, which were extracted in the previous step, were subsequently introduced into the on-axis compliance matrix (Eq. (5.3)). Substitution of Eq. (5.3) into Eq. (5.4) and inversion of the latter, yields the off-axis stiffness matrix of the composite ply, $[Q_c]$,

$$[Q_c] = \begin{bmatrix} Q_{11} & Q_{12} & 0 \\ Q_{12} & Q_{22} & 0 \\ 0 & 0 & Q_{66} \end{bmatrix} \tag{5.6}$$

Likewise, the off-axis damping ply matrix is provided by the following relation,

$$[\eta_c] = [R]^T [\eta_l][R]^{-T} \tag{5.7}$$

where $[\eta_l]$ is the on-axis damping ply matrix when the material coordinate system coincides with the global respective one,

$$[\eta_l] = \begin{bmatrix} \eta_{l1} & 0 & 0 \\ 0 & \eta_{l2} & 0 \\ 0 & 0 & \eta_{l6} \end{bmatrix} \tag{5.8}$$

According to the Love-Kirchhoff plate theory, the off-axis stiffness (Eq. (5.6)) and damping (Eq. (5.7)) matrices are essential of the calculation of extensional, coupling and flexural stiffness and damping terms of the laminate, which have the following form,

$$
\begin{aligned}
A_{ij} &= \sum_{k=1}^{n} Q_{cij}^{(k)} \left(z_k - z_{k-1} \right) = \sum_{k=1}^{n} Q_{cij}^{(k)} h_k \\
B_{ij} &= \frac{1}{2} \sum_{k=1}^{n} Q_{cij}^{(k)} \left(z_k^2 - z_{k-1}^2 \right) = \sum_{k=1}^{n} Q_{cij}^{(k)} h_k \overline{z}_k = 0 \\
D_{ij} &= \frac{1}{3} \sum_{k=1}^{n} Q_{cij}^{(k)} \left(z_k^3 - z_{k-1}^3 \right) = \sum_{k=1}^{n} Q_{cij}^{(k)} \left(h_k \overline{z}_k^2 + \frac{h_k^3}{12} \right)
\end{aligned}
\tag{5.9}
$$

$$
\begin{aligned}
A_{dij} &= \sum_{k=1}^{n} h_k Q_{cij}^{(k)} \eta_{cij}^{(k)} \\
B_{dij} &= \sum_{k=1}^{n} h_k \overline{z}_k Q_{cij}^{(k)} \eta_{cij}^{(k)} = 0 \\
D_{dij} &= \sum_{k=1}^{n} Q_{cij}^{(k)} \eta_{cij}^{(k)} \left(h_k \overline{z}_k^2 + \frac{h_k^3}{12} \right)
\end{aligned}
$$

where $i, j = 1, 2, 6$; h_k is the thickness of the k[th] ply; and $\overline{z}_k$ is the distance between the mid-plane of the k[th] ply and the mid-plane of the laminate. These geometric parameters are better illustrated in Figure 5.5.

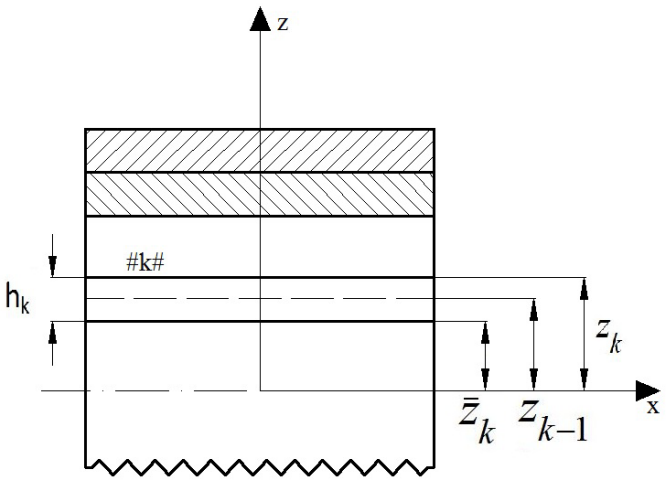

Fig. 5.5 Geometric position of the k[th] ply of the composite laminate

Due to the symmetric structure of the laminate, the coupling stiffness and damping terms (B_{ij}, B_{dij}) are equal to zero. Thus, the constitutive equations of the laminate take the form,

$$\begin{Bmatrix} \mathbf{N} \\ \mathbf{M} \end{Bmatrix} = \begin{bmatrix} [\mathbf{A}]_{3x3} & \mathbf{0} \\ \mathbf{0} & [\mathbf{D}]_{3x3} \end{bmatrix} \begin{Bmatrix} \boldsymbol{\varepsilon}^{\mathbf{0}} \\ \mathbf{k} \end{Bmatrix} \tag{5.10}$$

where the vectors $\boldsymbol{\varepsilon}^{\mathbf{0}} = \{\varepsilon_1^0, \ \varepsilon_2^0, \ \varepsilon_6^0\}$, $\mathbf{k} = \{k_1, \ k_2, \ k_6\}$ represent the mid-plane strains and curvatures, respectively. Likewise, $\mathbf{N} = \{N_1, \ N_2, \ N_6\}$, $\mathbf{M} = \{M_1, \ M_2, \ M_6\}$ are the external forces and torques applied at the mid-plane of the laminate. Supposing that the beam specimens are under free-flexure conditions ($N_1 \neq 0, \ M_1 \neq 0, \ N_2 = N_6 = M_2 = M_6 = 0$), Eq. (5.10) becomes,

$$\begin{Bmatrix} \varepsilon_1^0 \\ k_1 \end{Bmatrix} = \begin{bmatrix} A_{11}^{-1} & 0 \\ 0 & D_{11}^{-1} \end{bmatrix} \begin{Bmatrix} N_1 \\ M_1 \end{Bmatrix} \tag{5.11}$$

The bending ply loss factor is therefore expressed as the ratio of the respective dissipated to the maximum stored modal energy in the beam specimen and has the form,

$$\eta_b = \frac{1}{2\pi} \left(\frac{k_1^T [D_{d11}] k_1}{k_1^T [D_{11}] k_1} \right) \tag{5.12}$$

The same module (SAAM) was applied for the inverse prediction of the three modal loss factors ($\eta_{l1}, \ \eta_{l2}, \ \eta_{l6}$) of the composite material system from the measured flexural damping of the off-axis beam specimens. A model approximating the experimental axial loss factor of a laminate with the composite equivalent flexural loss factor was developed, using the least-squares minimization procedure to yield the three damping coefficients of the individual composite plies. Figure 5.6 shows the experimental values and their approximation by the theoretical model.

Figure 5.7 presents a typical FRF signal for the case of a Glass/Epoxy beam specimen with 0^0 plies. Figure 5.8 illustrates typical first mode magnitude and phase angles of measured frequency response function data, along with the fitted parametric model for the extraction of modal frequencies and damping.

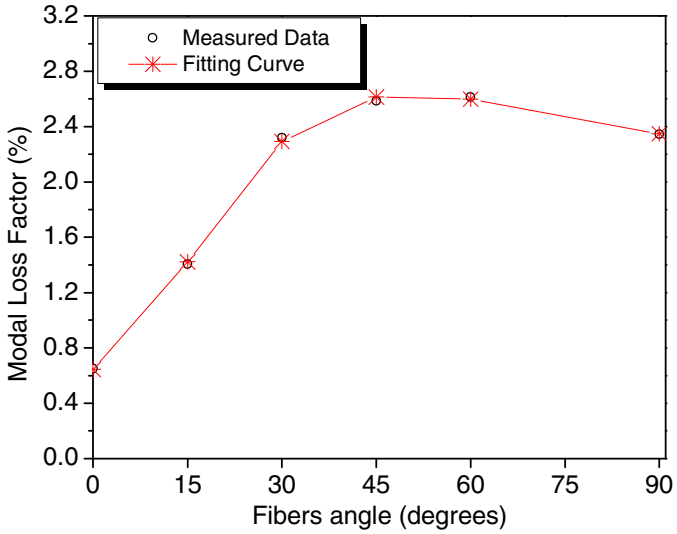

Fig. 5.6 Fitting of experimental equivalent loss factor of first bending mode with the analytical model for the calculation of damping coefficients of Glass/Epoxy composite material

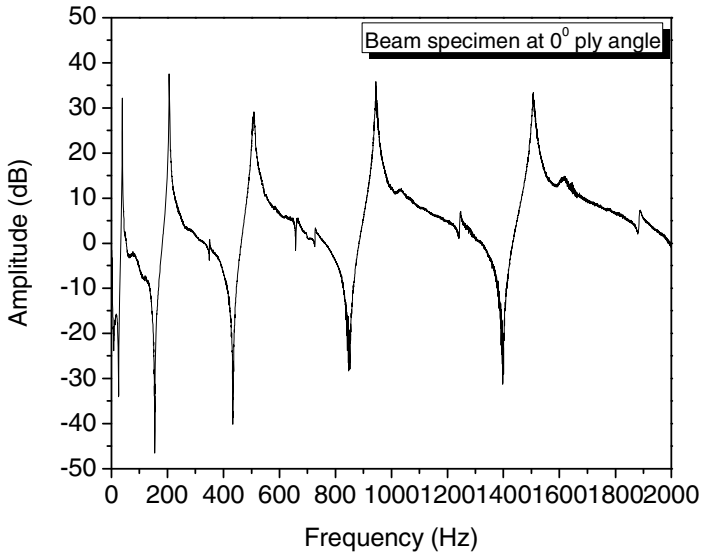

Fig. 5.7 Typical Frequency Response Function (FRF) diagram for the case of a Glass/Epoxy beam specimen with 0^0 ply angle

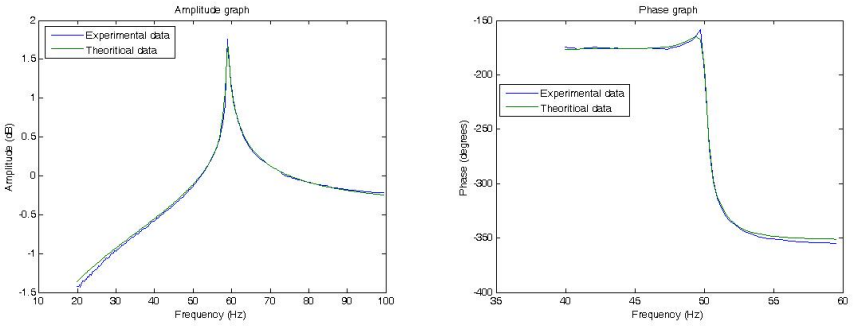

(a) (b)

Fig. 5.8 Fitting of measured Frequency Response Function data with the analytical model: (a) Amplitude diagram; (b) Phase angle diagram

5.2.2 Relation of Damping with Natural Frequency

The Kelvin material damping model is a viscous damping model in the time domain that yields modal damping values, which are frequency dependent. The relation of the measured loss factor with the frequency is,

$$\omega D_{d11} = \eta_L D_{11} \tag{5.13}$$

The proof of Eq. (5.13) is in detail reported in Appendix B.

Based on the experimental data shown in Figure 5.9 the elastic coefficients and the loss factors of the Glass/Epoxy material shown in Table 5.6, were extracted following the procedure described by Chrysochoidis (2001). As expected from Figure 5.9, the measured loss factors of the composite material were practically insensitive to the natural frequency, hence in the rest of this work, the RHS of the above Eq. (5.13) was taken to be invariable to frequency. *As a result, the frequency term in nominator of Eq. (5.2) will cancel out, and the modal loss factor will be effectively invariable to modal frequency.*

The elastic properties and damping coefficient values of the composite ply are shown in Table 5.6. These values are introduced as input in the nonlinear finite element code in order to obtain numerical predictions which will be further correlated with additional experimental measurements of Glass/Epoxy beam specimens subject to increasing in-plane loads.

Table 5.6 Mechanical properties of Glass/Epoxy material

Ply thickness t_l (mm)	ρ (Kg/m^3)	E_{11} (GPa)	E_{22} (GPa)	G_{12} (GPa)	ν_{12}	η_{l1} (%)	η_{l2} (%)	η_{l5} (%)	η_{l6} (%)
0.3375	1744	25.1	10.9	4.7	0.31	0.528	0.978	1.442[a]	1.442

[a]Not measured

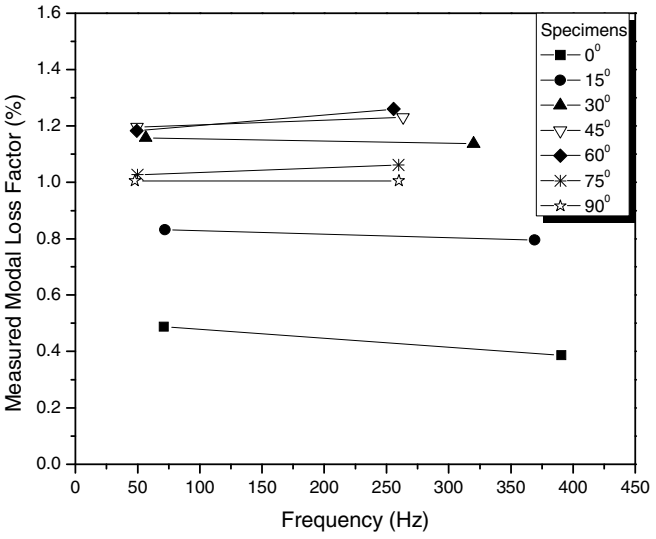

Fig. 5.9 Sensitivity of measured modal loss factor values to the natural frequency for the first and second bending mode of a Glass/Epoxy beam specimens per 15^0 ply angle increments

5.2.3 Damped Modal Testing of Composite Beam Modal Characteristics

5.2.3.1 Tension Experimental Procedure

The first part of the experimental procedure dealt with the damped dynamic characteristics of cross-ply Glass/Epoxy composite beams, subject to tension, which were experimentally measured and subsequently correlated with numerical predictions of the nonlinear finite element code. Two composite plates with $[0_2/90_2]_s$ and $[90_2/0_2]_s$ laminations were fabricated at AML using hand lay-up with vacuum bag consolidation. The glass fibers and epoxy resin properties are the same with those indicated in Table 5.1-Table 5.3. Using a sliding mitre saw, beam specimens were subsequently cut in dimensions shown in Table 5.7.

Table 5.7 Geometric data of $[0_2/90_2]_s$ and $[90_2/0_2]_s$ Glass/Epoxy beam specimens

Length, L (mm)	*Width, b* (mm)	*Thickness, h* (mm)	*Weight* (g)
400	30.6	2.7	74

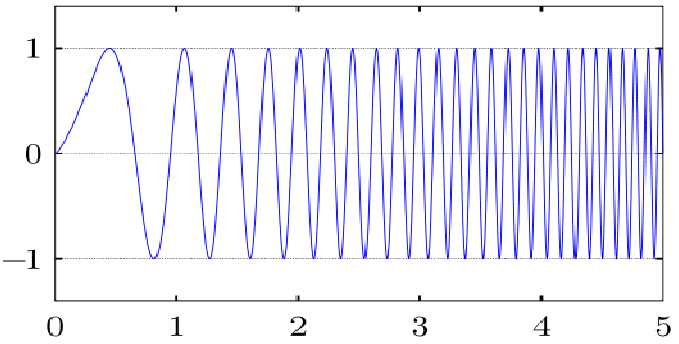

Fig. 5.10 Swept-sine time signal applied on the piezoceramic actuator

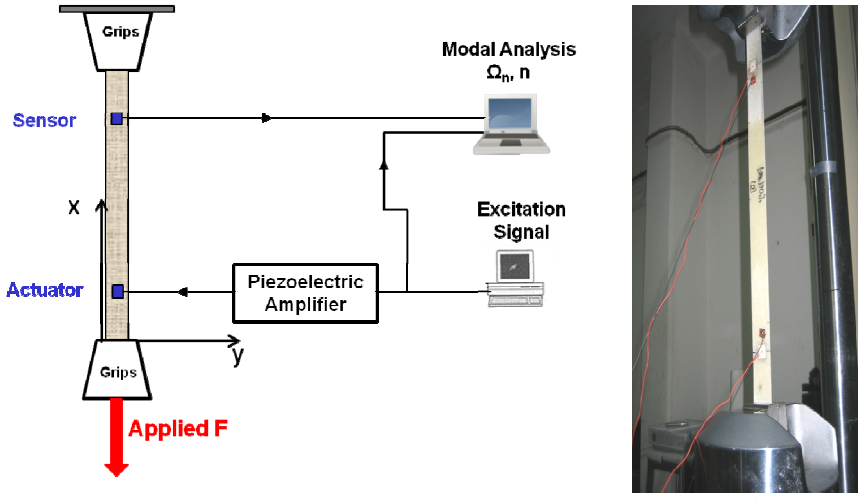

(a) (b)

Fig. 5.11 Tension experimental procedure: (a) Setup configuration; (b) Glass/Epoxy beam specimen testing using two piezoceramic plates as actuator and sensor

The beams were attached on a hydraulic uniaxial testing machine MAYES 100KN of AML with both ends being clamped by hydraulic wedge grips; one remaining immovable while an in-plane displacement was applied to the other end at a rate of 0.02mm/min and during the load application, vibration analysis tests were performed for various in-plane tensile load increments. A beam with similar dimensions, made of a very low damping material (Aluminum) was also tested to estimate the external damping introduced by the grips. Figure 5.11a presents the experimental setup configuration.

The dynamic tests were performed using two different excitation methods. In the first method, two PZT-5 piezoceramic plates (12.5mm x 12.5mm), one acting as actuator and the other as sensor respectively, were adhered on the same surface near the clamped edges (Figure 5.11a). The beams were self-excited through the actuator using a swept-sine time signal with a frequency range between 1 and 2500Hz (Figure 5.10).

In the second method of excitation, an impact hammer was used to better excite the first bending mode of the beam and the response was measured via the piezoceramic sensor. The output voltage at the piezoelectric sensor was simultaneously acquired by a high-speed data acquisition board and spectral analyzer to obtain the frequency response functions of the beam, as the in-plane tensile load was progressing. A parametric model consisting of a series of complex exponential terms, each term approximating an individual mode, was used to extract the modal frequencies and modal loss factors of the tested beam from the measured frequency response functions.

5.2.3.2 Buckling Experimental Procedure

The damped dynamic characteristics of cross-ply Glass/Epoxy composite beams (Figure 5.12), subject to buckling were experimentally measured and subsequently correlated with numerical predictions of the present method. Experiments were conducted using the same Glass/Epoxy $[0_2/90_2]_s$ cross-ply lamination beam specimens with material properties and dimensions given in Table 5.6 and Table 5.7, respectively.

The beams were attached on the same hydraulic uniaxial testing machine MAYES 100KN with both ends being clamped by hydraulic wedge grips; one end remaining immovable while an in-plane displacement was applied to the other end. Unlike to the tension experiments, this time in the buckling tests a rate of 0.01mm/min was applied to provide a more constant and stable transition from the pre-to the post-buckling region of the composite beam. In addition, the lower displacement rate ensured more accurate experimental measurements of the modal characteristics and the transverse deflection at beam midspan.

At specified load increments, the displacement was held constant and vibration analysis tests were performed using an impact hammer. The response was measured with two different sensors: a PZT-5 piezoceramic sensor plate, adhered on the beam surface near the clamped edge (Figure 5.12) and a miniature accelerometer adhered at the midspan of the beam (Figure 5.13).

The output voltage at the piezoelectric sensor was simultaneously acquired by a high-speed data acquisition board and spectral analyzer to obtain the frequency response functions of the beam, as the in-plane buckling load was progressing. The same parametric model consisting of a series of complex exponential terms, each term approximating an individual mode, was used to extract the modal frequencies and modal loss factors of the tested beam from the measured frequency response functions. A linear variable differential transformer (LVDT)

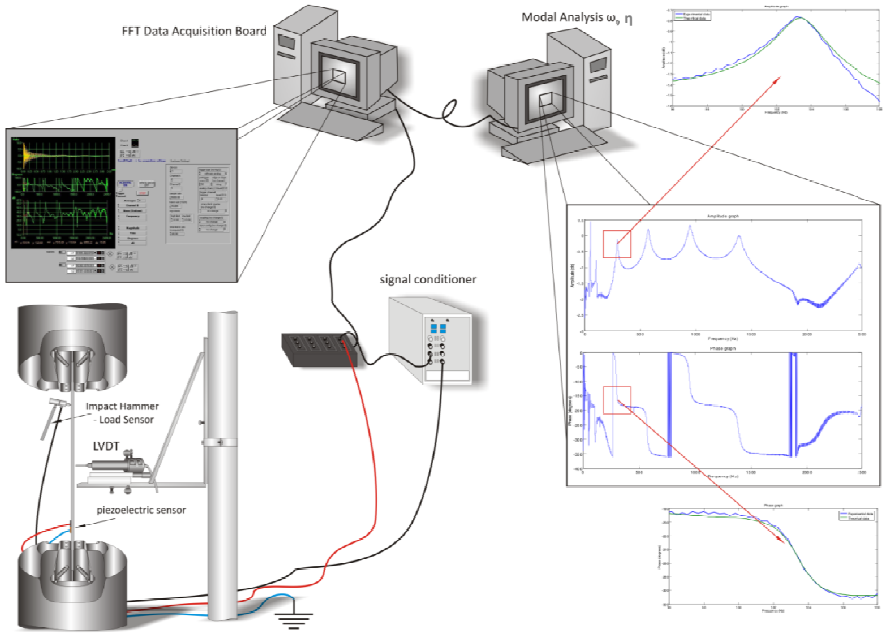

Fig. 5.12 Buckling experimental setup using a piezoceramic sensor plate and typical amplitude and phase fitting graphs

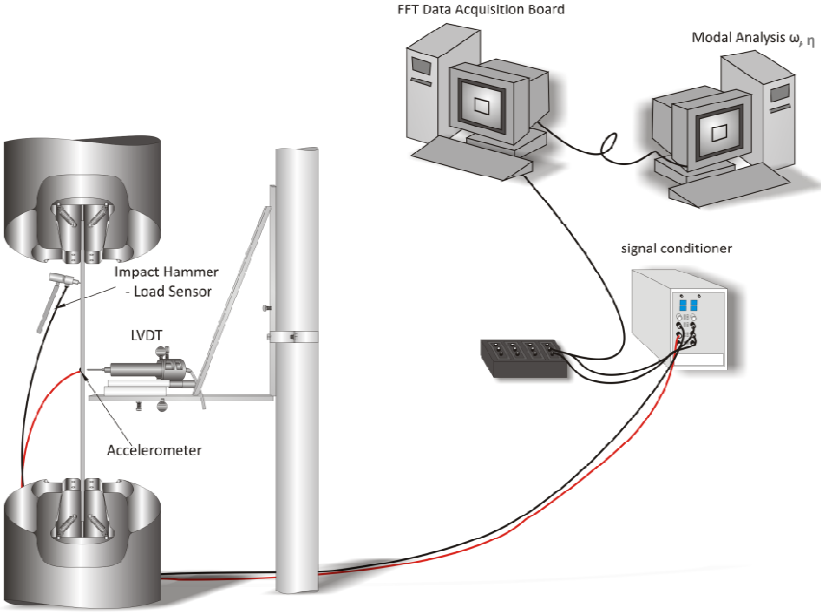

Fig. 5.13 Buckling experimental setup using an impact hammer and an accelerometer as sensor

was also set at the midspan of the beam to measure the transverse displacement during the application of the axial compressive displacement. In Figure 5.12 and Figure 5.13 the experimental setup is shown for the two measured sets, using: I) a piezoceramic sensor and II) an accelerometer. In both sets an impact hammer was used to better excite the first bending mode of the composite strip.

5.3 Numerical Results

Application of the nonlinear finite element code provided a series of validations cases for the composite strip which were subsequently correlated with available experimental measurements. Theoretical predictions investigated the effect of initial stresses and geometrical nonlinearities, due to in-plane tensile and compressive loads, on the modal characteristics of the composite strip. Furthermore, theoretical predictions of an aluminum plate-beam specimen are presented and validated towards a nonlinear shell FE numerical results and its respective experimental measuremets.

5.3.1 Effect of In-Plane Tensile Load

The developed nonlinear finite element was evaluated by predicting the modal frequency and modal damping values of Glass/Epoxy plate beams. Firstly, the modal characteristics of two cross-ply beam specimens are presented and correlated with the respective experimental measurements. The second set of results includes numerical predictions of the nonlinear code for quasi-isotropic laminate configurations.

5.3.1.1 Cross-Ply Composite Strips

The modal characteristics of the tested clamped-clamped beams under tensile in-plane loading were predicted and compared with the measured experimental results.

A. Validation of nonlinear stiffness terms

Excellent correlation was obtained between numerical and experimental results for the natural frequencies of $[0_2/90_2]_s$ and $[90_2/0_2]_s$ beam specimens. Figure 5.14 and Figure 5.15 present the first three and first four bending natural frequencies of the $[0_2/90_2]_s$ and $[90_2/0_2]_s$ beam specimens, respectively. All natural frequencies increase with the applied tensile load due to membrane stiffening which is modeled by the stiffness component $\left[\bar{\mathbf{K}}_{\mathbf{N1}}\right]$.

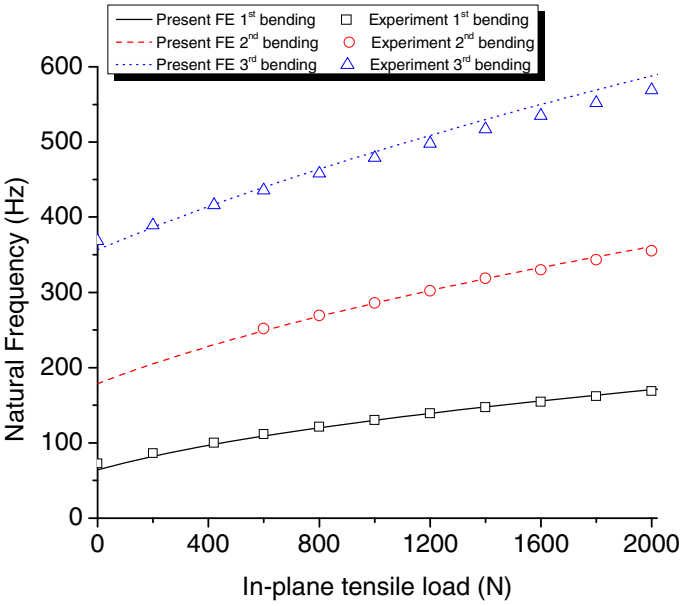

Fig. 5.14 Bending natural frequencies of the $[0_2/90_2]_s$ clamped-free Glass/Epoxy plate-beam under a increasing tensile load

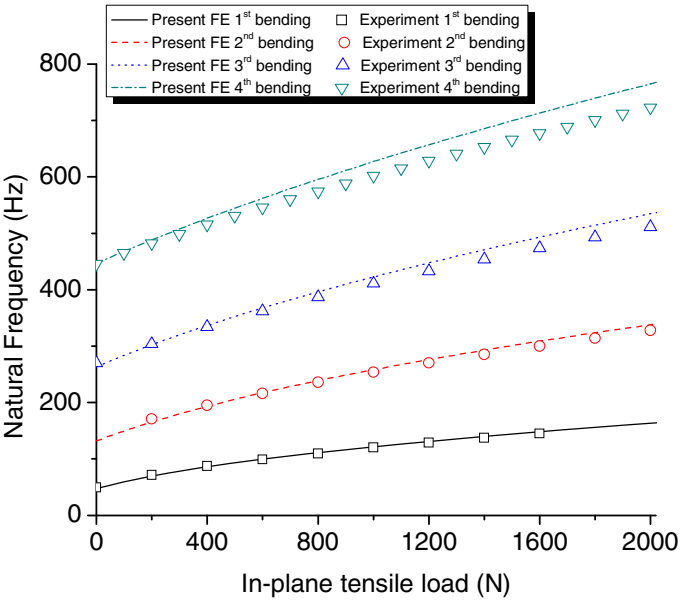

Fig. 5.15 Bending natural frequencies of the $[90_2/0_2]_s$ clamped-free Glass/Epoxy plate-beam under a increasing tensile load

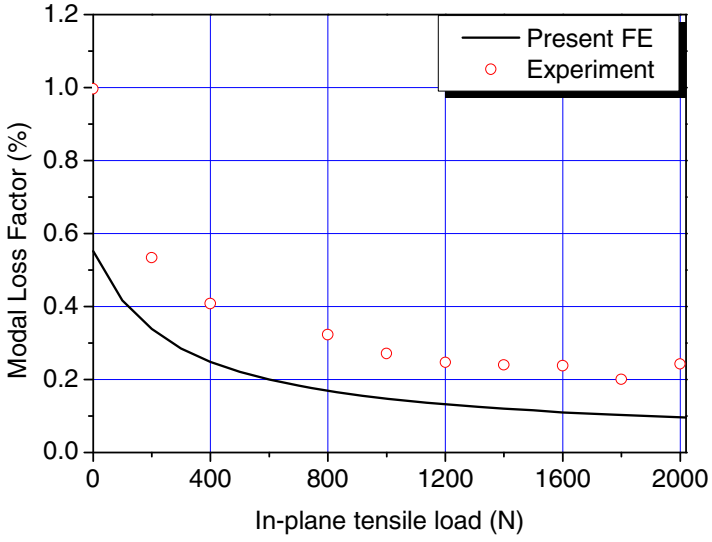

(a)

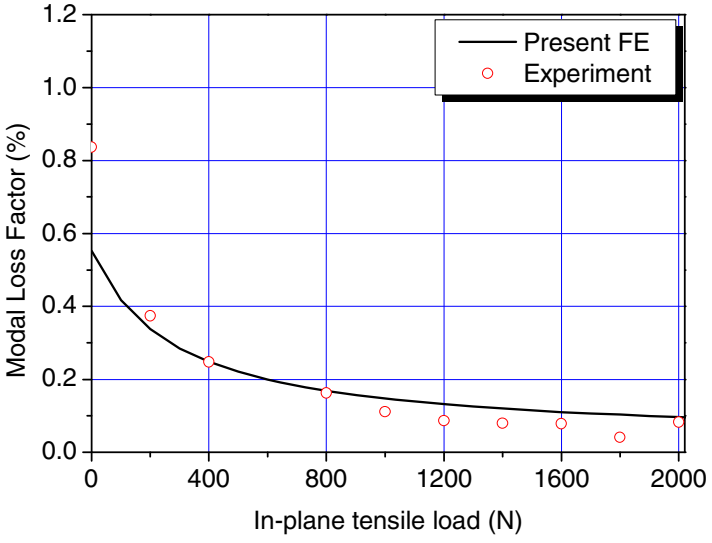

(b)

Fig. 5.16 Predicted and measured first bending modal loss factor of the $[0_2/90_2]_s$ Glass/Epoxy clamped-free plate-beam, under a tensile load: (a) As measured damping; (b) With damping of aluminum specimen subtracted.

Each symbol of the experimental scatter curves corresponds to a different load increment. Likewise, the numerical prediction curves correspond to a series of load increments, where in each increment the static solution has been calculated using the Newton-Raphson iterative technique. Based on this method, the small-amplitude dynamic response is solved and consequently, the eigenfrequencies of the composite strip are calculated.

B. Validation of nonlinear damping terms

The predicted and measured damping of the first mode of the $[0_2/90_2]_s$ beam is presented in Figure 5.16a. Both analytical and measured damping values decrease with the application of tensile load following a similar trend. The constant offset between the predicted and the experimental graph is attributed to external damping from the hydraulic grips. This hypothesis is corroborated in Figure 5.17, which shows the measured modal loss factor of the aluminum beam, tested in an identical way to the composite beam. Although aluminum has a nominal loss factor about 0.04% (Granick and Stern 1965), a substantially higher damping value of 0.22% was measured which remained nearly constant as the load increased, which more likely quantifies the extraneous damping induced by the grips.

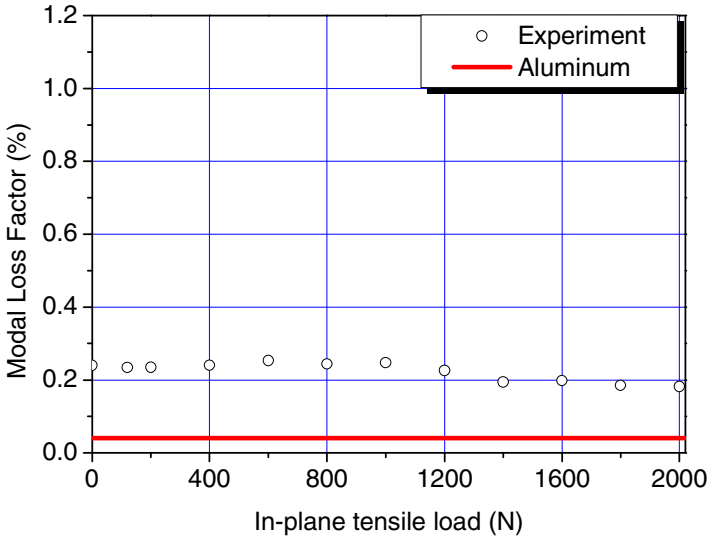

Fig. 5.17 Measured modal loss factor of aluminum plate-beam

Although the calibration of the measured data is a common practice, it is clearly stated that the difference between the nominal and the measured loss factor values was 0.18%. Indeed, after subtracting the grip damping from the damping of the composite beams, the correlation between the analytical and the experimental damping values is drastically improved (Figure 5.16b). The results in Figure 5.16 demonstrate that the differences between the "as measured" data and analytical predictions are mostly due to extraneous damping at the supports.

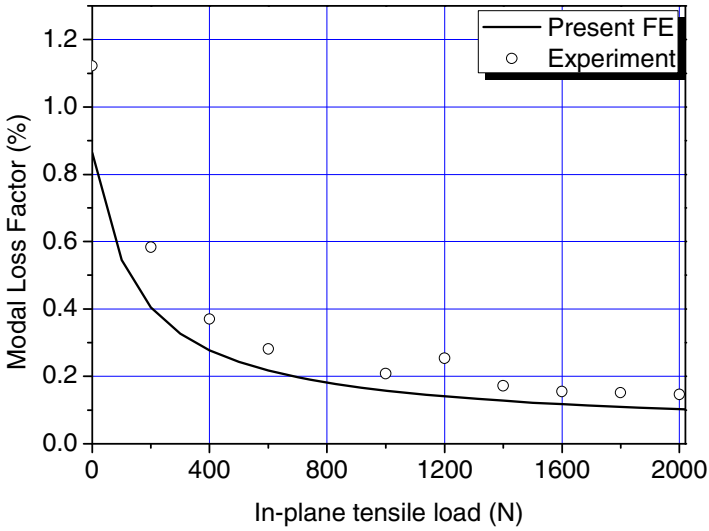

Fig. 5.18 First bending modal loss factor of a $[90_2/0_2]_s$ clamped-free Glass/Epoxy beam under a tensile load

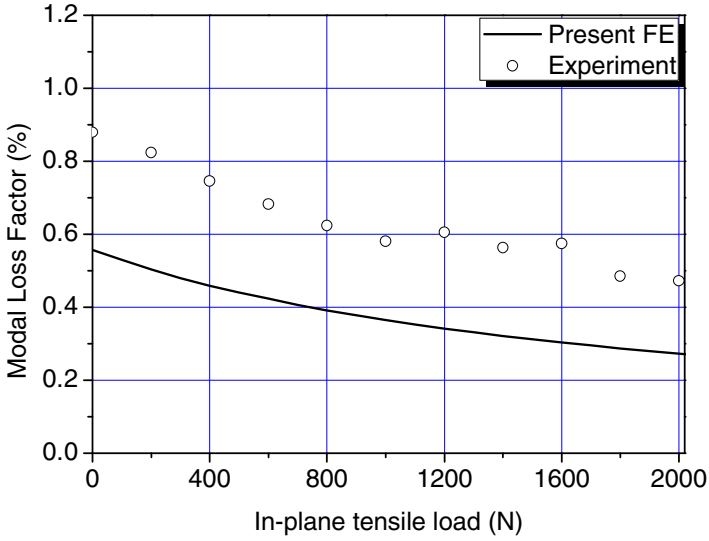

Fig. 5.19 Predicted and measured loss factor of $[0_2/90_2]_s$ clamped-free Glass/Epoxy beam under a tensile load of fourth bending mode

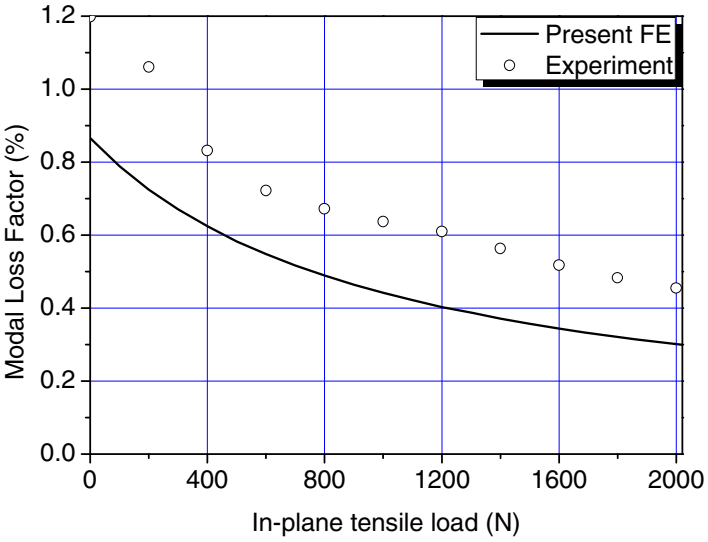

Fig. 5.20 Predicted and measured loss factor of $[90_2/0_2]_s$ clamped-free Glass/Epoxy beam under a tensile load of fourth bending mode

The measured and predicted first modal loss factor values of the $[90_2/0_2]_s$ composite beam are shown in Figure 5.18. This laminate configuration has higher modal damping, which also decreases with the application of in-plane load.

Predicted and measured modal damping of a higher beam mode are shown in Figure 5.19 and Figure 5.20 for the $[0_2/90_2]_s$ and $[90_2/0_2]_s$ beam, respectively. In these measurements the beam was excited using the PZT-5 piezoceramic actuator, which provided better FRF diagrams in comparison with the impact hammer.

In all cases the decreasing trend in measured damping upon application of tensile load remains. The results show that the present finite element captures the decrease of nonlinear damping for the fourth mode due to the stiffening effect. The offset is attributed to external damping.

In all previous cases the predicted results for the natural frequencies and the modal damping values are in excellent agreement with the experimental results, leading credence to the present finite element model. To further analyze the effect of nonlinear terms on damping, the dissipated and stored modal strain energies are shown in Figure 5.21 and Figure 5.22, for modes shapes normalized to a maximum value of unity.

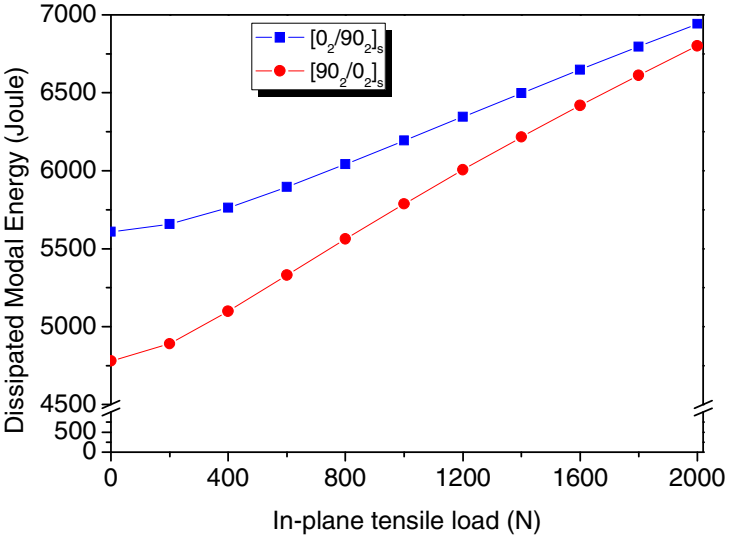

(a)

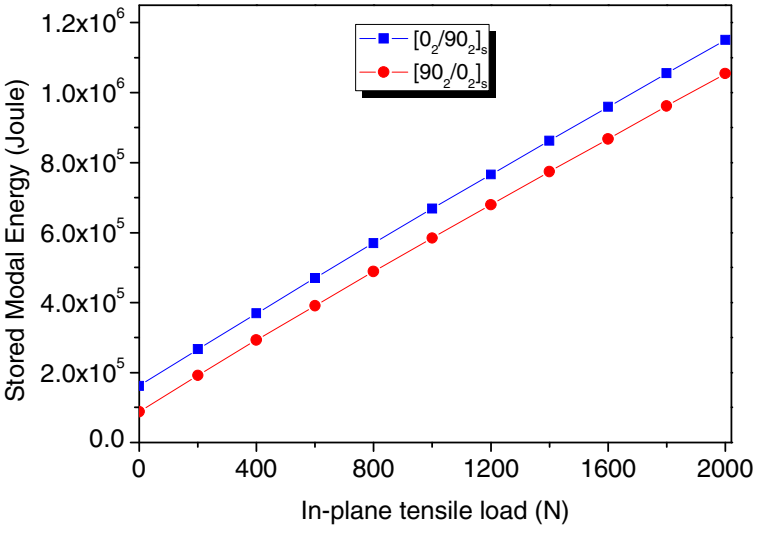

(b)

Fig. 5.21 Modal energies of the first bending mode of $[0_2/90_2]_s$ and $[90_2/0_2]_s$ Glass/Epoxy beams under a tensile load: (a) Dissipated energy; (b) Maximum stored energy

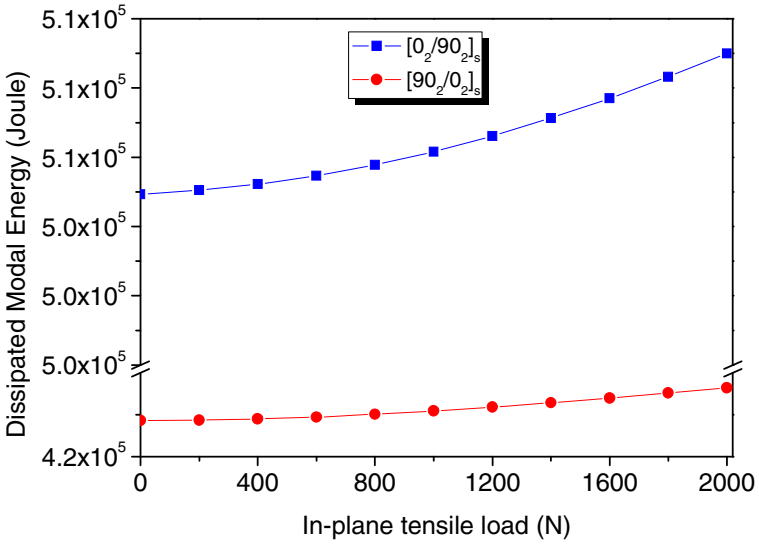

(a)

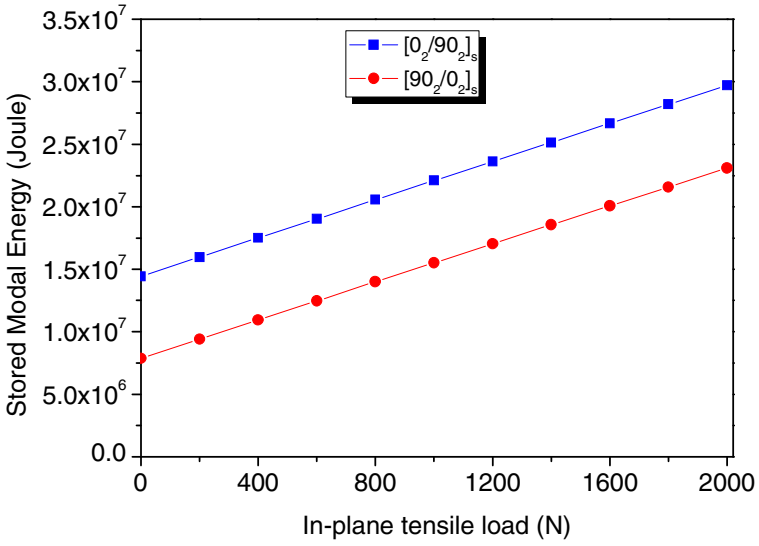

(b)

Fig. 5.22 Modal energies of the fourth bending mode of $[0_2/90_2]_s$ and $[90_2/0_2]_s$ Glass/Epoxy beams under a tensile load: (a) Dissipated energy; (b) Maximum stored energy

In all cases, it is obvious that the modal damping has decreased nonlinearly and monotonically, this effect has been previously experimentally observed by Kosmatka (2008). On the other hand, the dissipation of strain energy in absolute value has increased monotonically with the application of the tensile load. It is important to note, thereafter, that the reduction in damping is caused by the disproportional increase in the stored strain energy due membrane stiffening effects and not by a decrease in dissipated strain energy.

A careful observation of the obtained analytical and experimental damping results supports expected trends based on the analytical expressions of laminate damping matrices in Eqs. (4.27-4.28). The two cross-ply laminates, $[0_2/90_2]_s$ and $[90_2/0_2]_s$, have different flexural damping and stiffness terms D_d and D but equal extensional damping and stiffness A_d and A. The change in modal strain energy remains linear to the applied load and the extensional stiffness, explaining the same slopes between the two laminations. Interestingly, for both laminates and mode, the dissipated modal energy varies nonlinearly at low loads, while at higher loads it follows a linear trend.

As previously explained, at very low in-plane load values, the dissipated strain energy and modal damping are related to flexural laminate damping D_d, hence damping is higher for the $[90_2/0_2]_s$ laminate. There is a transition range, and then at high in-plane loads, the modal dissipated energy and the modal damping seems to be dominated by A_d. The transition from a flexural damping, to an extensional damping dominated dissipation mechanism, as the in-plane load increases, seems to depend also on the order of the bending mode due to the nonlinear behavior of the beam.

5.3.1.2 Quasi-isotropic Composite Strips

The modal characteristics of Glass/Epoxy composite strip-beams (Figure 5.23) having a quasi-isotropic lamination $[\theta/90+\theta/45+\theta/-45+\theta]_s$ at various orientations θ to the beam axis, were also predicted. The significant effect of laminate orientation is better illustrated through predictions with and without the nonlinear stiffness and damping terms.

The beams have identical dimensions and material properties (Table 5.6) with the cross-ply beams in the previous subsection being clamped at one and loaded with a constant tensile force at the free end.

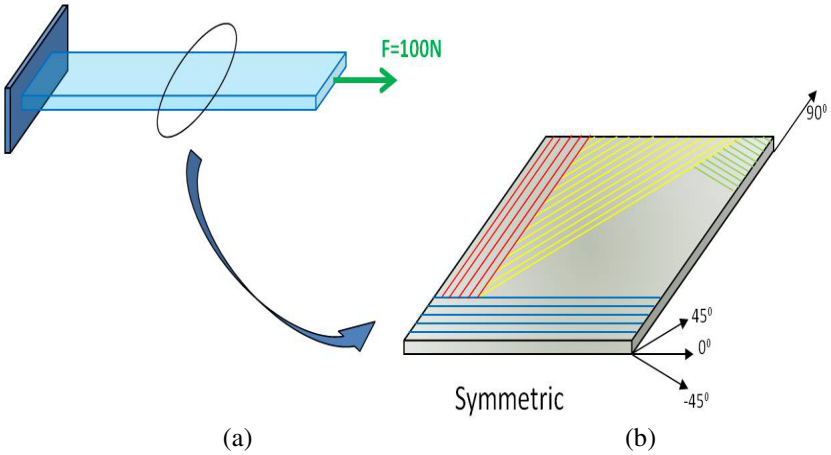

Fig. 5.23 Quasi-isotropic $[\theta/90+\theta/45+\theta/-45+\theta]_s$ composite strip-beam: (a) Under tensile loading; (b) Lay-up configuration

In Figure 5.24 and Figure 5.25 the variation of the modal frequencies and damping of the composite beam, as the constant axial force is applied, is presented. The nonlinear section stiffness terms contribute to the increased beam stiffness (Figure 5.24). This is indicated by the higher first two bending frequency predictions of the nonlinear code in comparison with the linear beam formulation.

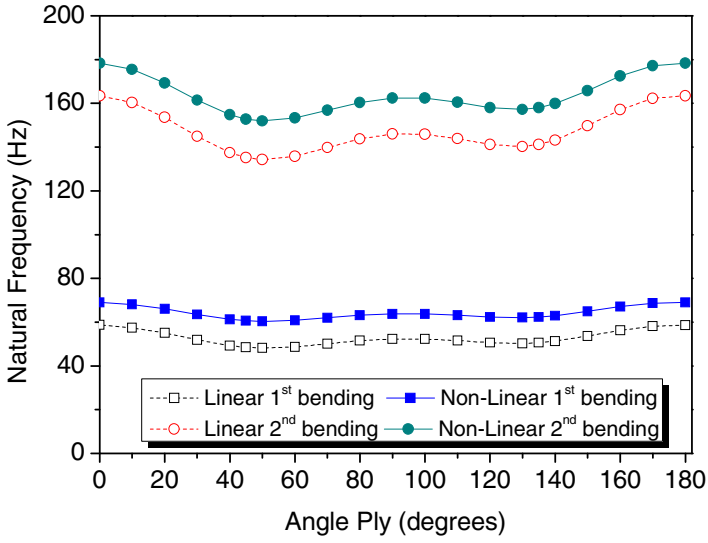

Fig. 5.24 Effect of laminate orientation on modal bending frequencies of a $[\theta/90+\theta/45+\theta/-45+\theta]_s$ beam; linear vs. nonlinear model predictions

On the other hand, the change of damping (Figure 5.25) highly depends on the lamination and the mode shape, and it has lower values with respect to the linear baseline. It is obvious that the modal loss factor takes its maximum values for θ near 45^0 where the off-axis plies are on the external side of the laminate and undergo higher deformations. Consequently, beam damping increases due the increased damping of the matrix material.

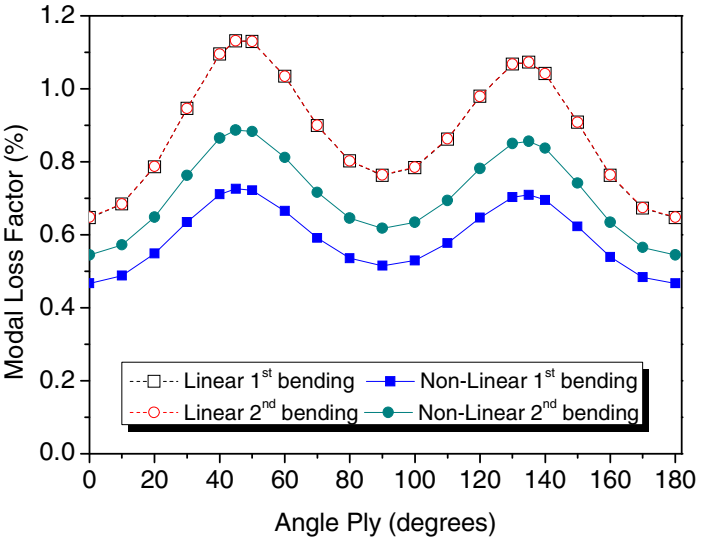

Fig. 5.25 Effect of laminate orientation on modal bending loss factors of a [θ/90+θ/45+θ/-45+θ]$_s$ beam; linear vs. nonlinear model predictions

In Figure 5.26 and Figure 5.27 the predicted first two bending modal frequencies and damping for beams with ([0/90/±45]$_s$) and [±45/90/0]$_s$ laminations are shown, considering: (i) only linear matrices $\left[\mathbf{K^0}\right]$, $\left[\mathbf{C^0}\right]$ and (ii) including both linear $\left[\mathbf{K^0}\right]$, $\left[\mathbf{C^0}\right]$ and nonlinear matrices $\left[\bar{\mathbf{K}}_{\mathbf{N1}}\right]$ and $\left[\mathbf{C}_{\mathbf{N1}}\right]$.

In Figure 5.25, Figure 5.26b and Figure 5.27b the modal damping factors of different modes predicted by the linear model coincide. This was expected, since in the specific material the term $\omega\left[\mathbf{Q}_{\mathbf{cd}}\right]$ was set to remain constant with frequency, as suggested by the measured material data. As the axial force increases, membrane stiffening occurs which has a strong effect on predicted modal frequencies and damping.

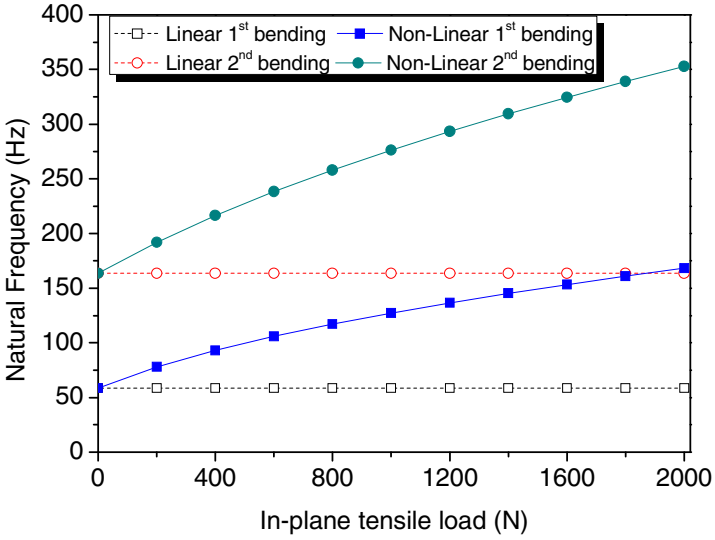

(a)

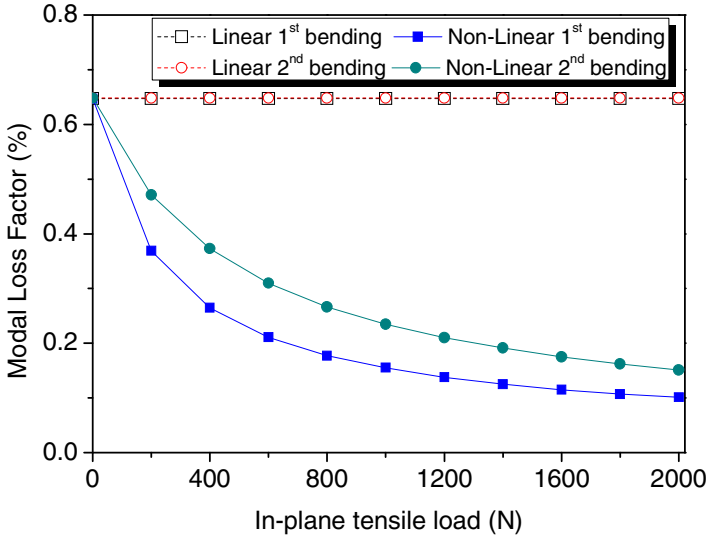

(b)

Fig. 5.26 Effect of an increasing tensile in-plane load on modal bending characteristics of a $[0/90/\pm45]_s$ clamped-free plate-beam: (a) Natural frequencies; (b) Modal loss factor

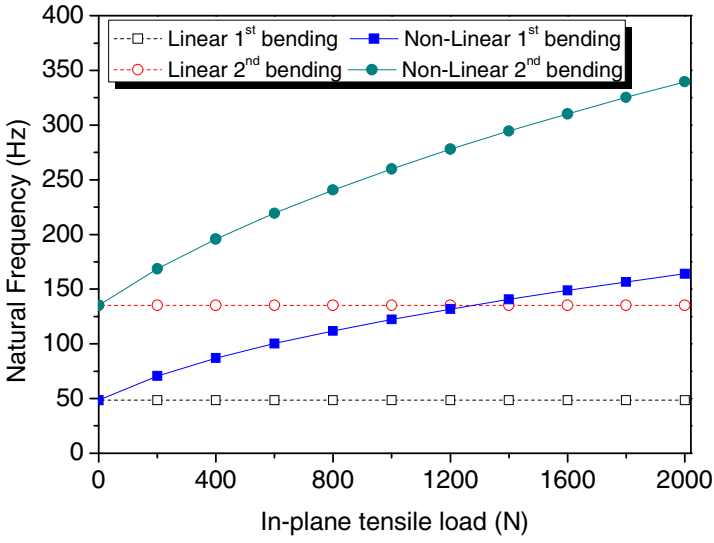

(a)

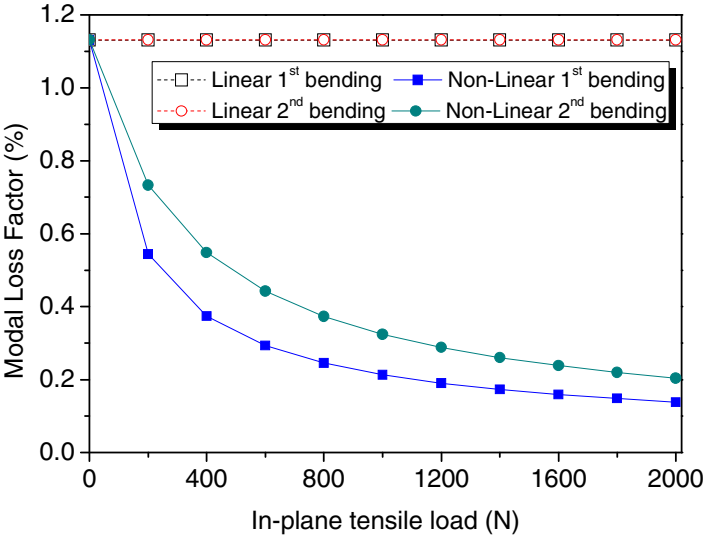

(b)

Fig. 5.27 Effect of an increasing tensile in-plane load on modal bending characteristics of a $[\pm 45/90/0]_s$ clamped-free plate-beam: (a) Natural frequencies; (b) Modal loss factor

The contribution of nonlinear damping $[\mathbf{C}_{\mathbf{N1}}]$ matrix on structural damping is presented in Figure 5.26b for the $[0/90/\pm45]_s$ laminations. The inclusion of nonlinear damping matrices has a drastic effect on the calculation of structural damping which is rapidly decreasing by the application of the tensile force, an effect not captured by the linear model. Similar results were obtained for the $[\pm45/90/0]_s$ beams as shown in Figure 5.27b.

Finally, the dissipated and stored modal strain energies for the first bending mode in both laminated beams are shown in Figure 5.28 and Figure 5.29, respectively, predicted with modes shape amplitudes normalized to a maximum value of unity for each case.

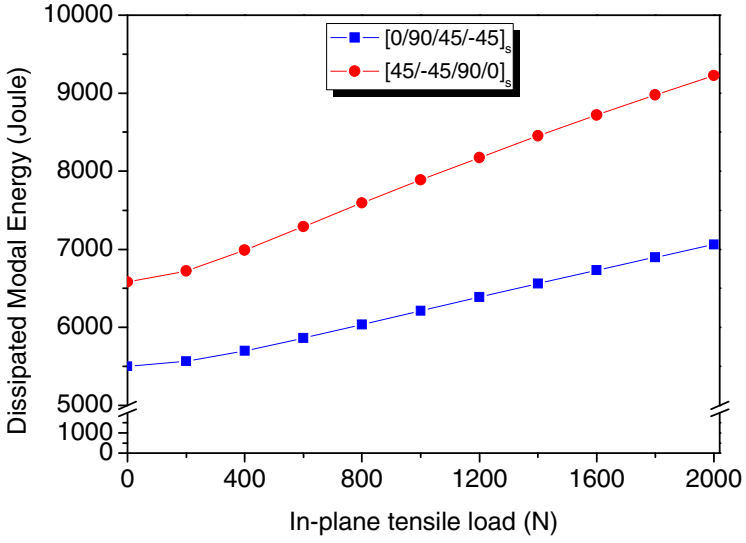

Fig. 5.28 Dissipated modal energy of the first bending mode of $[0/90/\pm45]_s$ and $[\pm45/90/0]_s$ Glass/Epoxy beams under a tensile load

In all cases, the dissipation of modal strain energy in absolute value has increased monotonically with the application of the tensile load. The reduction in damping is caused by the disproportional increase in the stored strain energy due to membrane stiffening effects and not by a decrease in dissipated strain energy. As in the previous case of cross-ply laminates, the above quasi-isotropic laminations have different flexural but equal extensional damping coefficients D_d and A_d, respectively. The predicted results validate the same theoretical observations, i.e.: at very low in-plane load values, the dissipated energy and modal damping of the bending modes is provided by flexural laminate damping D_d. As the load increases, the modal damping and dissipated energy is dominated

by the extensional laminate damping term A_d. Also, the reduction of modal damping with in-plane load depends on the order of the bending mode due to the nonlinear behavior of the beam.

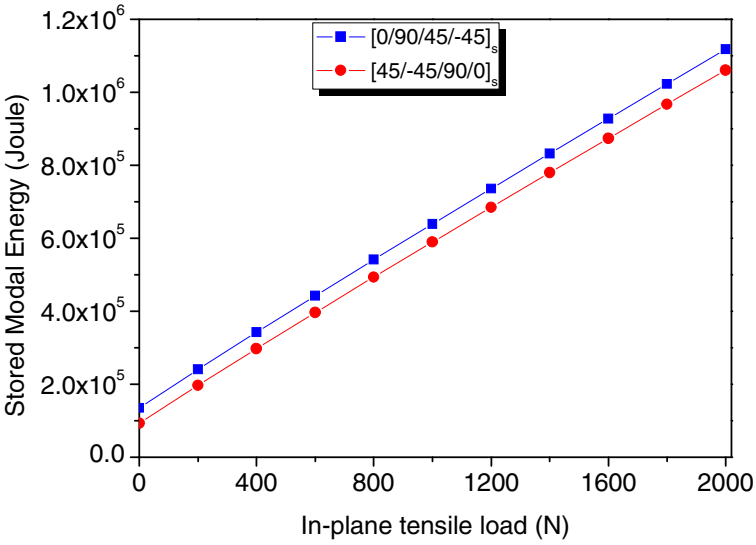

(b)

Fig. 5.29 Maximum stored modal energy of the first bending mode of $[0/90/\pm45]_s$ and $[\pm45/90/0]_s$ Glass/Epoxy beams under a tensile load

5.3.2 Aluminum Plate-Beam Model

The modal frequencies of an aluminum plate-beam subject to both tensile and compressive loads were predicted and correlated with experimental and numerical results provided by an eight node nonlinear shell finite element developed by Varelis and Saravanos (2006). The elastic properties of the aluminum material are shown in Table 5.8

Table 5.8 Material properties of the aluminum beam specimen

ρ (Kg/m^3)	E_{11} (GPa)	G_{12} (GPa)	v_{12}
2768	66	27	0.30

Likewise, the geometric characteristics of the aluminum beam specimen are included in Table 5.9.

Table 5.9 Geometric data of the aluminum beam specimen

Length, L (mm)	*Width, b* (mm)	*Thickness, h* (mm)
530	30	5.0

5.3.2.1 Static Response of Aluminum Beam Specimen Subject to Compressive In-Plane Load

Firstly, the variation of the in-plane axial reaction force, F at the tip of the aluminum beam specimen with regards to applied in-plane compressive displacement, u is illustrated in Figure 5.30.

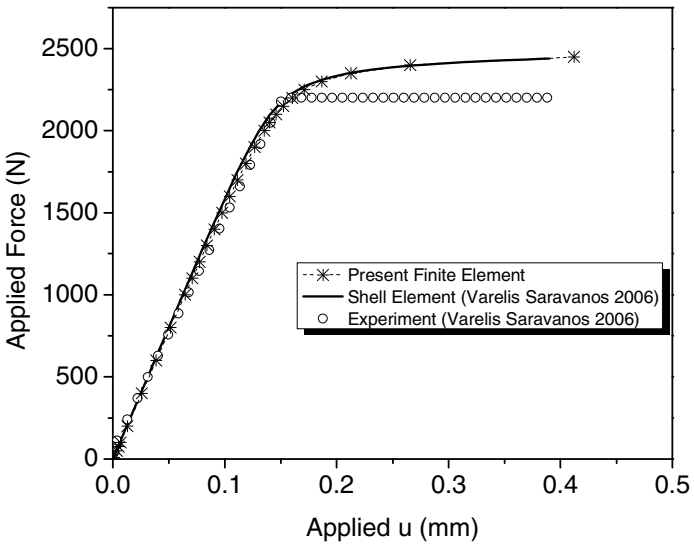

Fig. 5.30 Axial in-plane force at the beam end under axial in-plane compressive displacement

It is obvious that there is a linear relation between them till the critical buckling point, whereas beyond this point the axial force remains constant regardless the continuous increase of the applied axial displacement values. The loss of axial stiffness of the beam "transforms" the simultaneous additional energy offered by the compressive axial displacement, u into increase of the transverse displacement, w of the beam. It can be supported that there is good correlation with the experimental measurements and excellent validation with the respective eight node shell element numerical predictions (Varelis and Saravanos 2006).

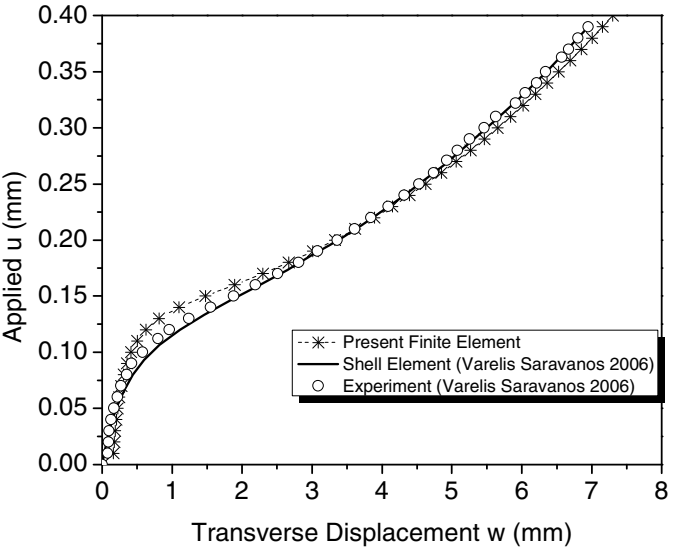

Fig. 5.31 Transverse midspan displacement of the aluminum clamped-free strip in pre- and post-buckling response under in-plane compressive displacement along the beam axis

Figure 5.31 presents the prediction of a stable buckling path for the transverse deflection w, while a compressive in-plane load is applied along the beam axis. The transverse response of the beam element is very close to shell element predictions and experimental results. The aluminum beam response in the pre-buckling region follows a rapid path, then it passes through the buckling critical point and finally it follows a more stable post-buckling path. In the present beam model it is assumed that an initial imperfection w_0, of the aluminum beam is induced by a transverse point force of F=3.5N at the midspan of the beam length.

5.3.2.2 Small-Amplitude Free-Vibration Response of Aluminum Beam Specimen Subject to In-Plane Tensile and Compressive Load

Figures 5.32a-c, show the predicted first, second and third bending natural frequencies of the aluminum beam specimen for increasing tensile in-plane displacement in comparison with the analytical and experimental results provided by Varelis and Saravanos (2006).

All bending natural frequencies increase with the applied in-plane displacement due to the increased stiffening of the aluminum beam, expressed by the first-order tangential terms. The results of the developed beam element are in excellent agreement both with the shell element predictions and the respective experimental measurements.

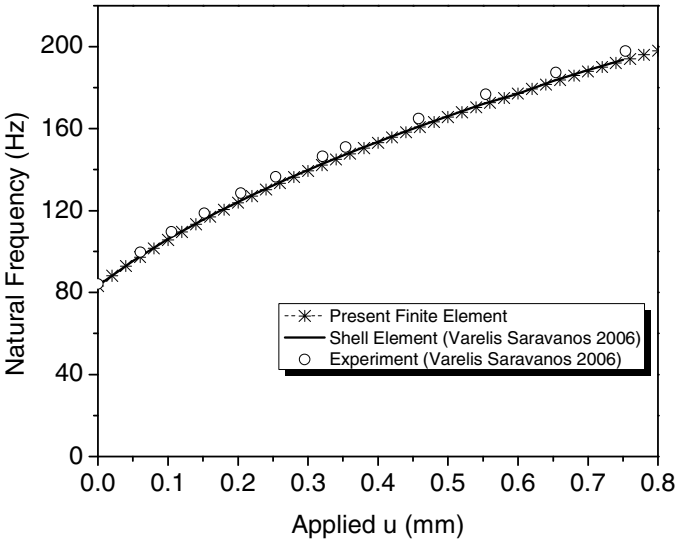

(a)

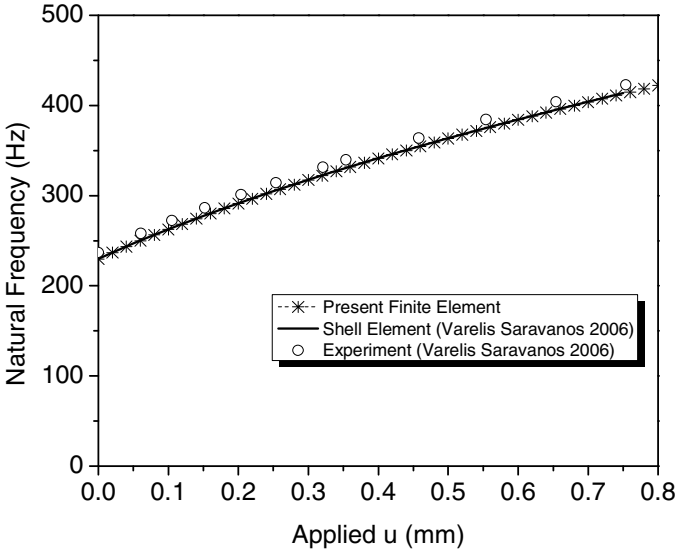

(b)

Fig. 5.32 Bending modal frequencies of an aluminum clamped-free strip under in-plane tensile displacement: (a) First; (b) Second; (c) Third mode

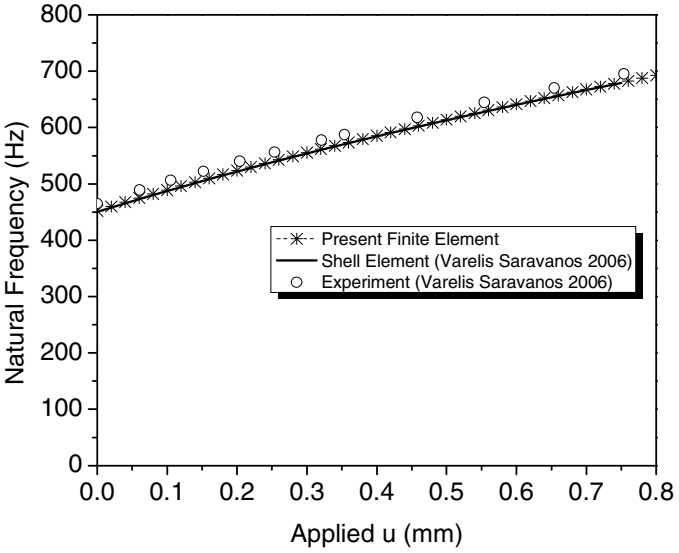

(c)

Fig. 5.32 (*continued*)

The capabilities of the beam element were further investigated on the aluminum specimen subject to an in-plane compressive load. Figures 5.33a, b and c show the predicted first, second and third bending modal frequency of the aluminum specimen, respectively, during the pre- and post-buckling response, where results of the present FE are compared with the nonlinear shell element and the respective experimental data.

The first natural frequency presents the higher sensitivity which is more obvious in the post-buckling region, where the frequency values increase rapidly. Both finite elements predict the same critical applied displacement value of $u = 0.15mm$. The beam element seems to underestimates the natural frequency at this point, whereas in the pre- and post-buckling area it yields predictions almost identical to the shell element predictions. The decreasing of the bending frequencies in the pre-buckling region for the second and third mode of the aluminum specimen is also shown in Figures 5.33b and c.

The decreasing frequency values in the pre-buckling region are attributed to the internal compressive stress which are developed within the beam structure. In the post-buckling region the beam regains its transverse stiffness and consequently the first bending frequency presents a rapid increase, whereas the second remains practically constant and the third one presents a slight increase.

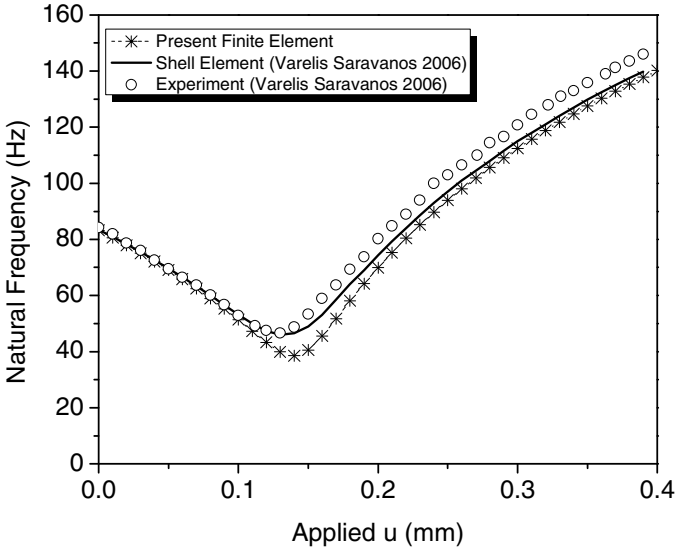

(a)

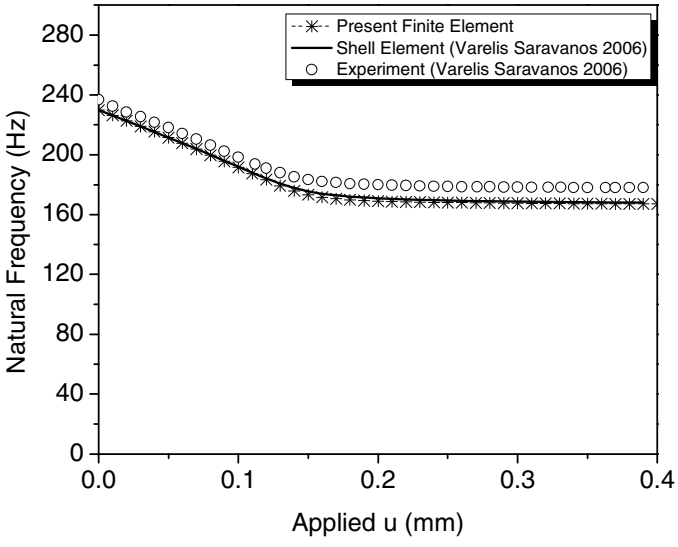

(b)

Fig. 5.33 Bending modal frequencies of an aluminum clamped-free strip under in-plane compressive displacement: (a) First; (b) Second; (c) Third mode

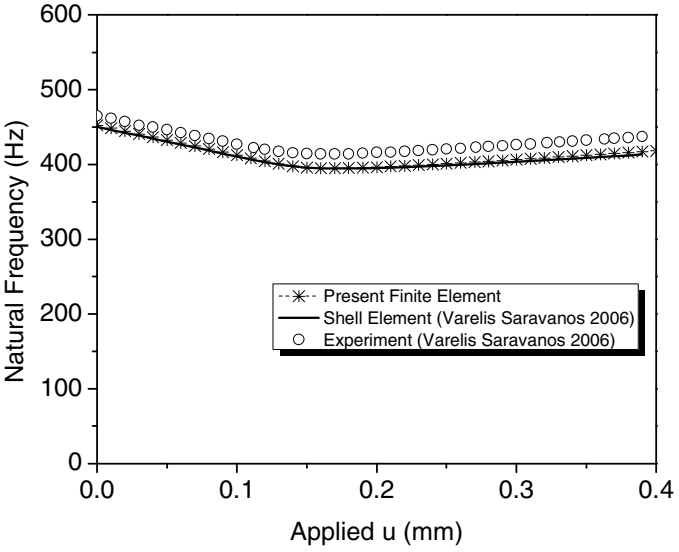

(c)

Fig. 5.33 (*continued*)

5.3.3 Nonlinear Buckling Analysis of Composite Strips

In this subsection the nonlinear buckling response of the same Glass/Epoxy beam-strip for various lay-up configurations will be investigated and correlated with experimental measurements.

5.3.3.1 Composite Cross-Ply Beam Specimens

The natural frequencies and the modal damping values of the $[0_2/90_2]_s$ Glass/Epoxy composite beam-strip, were predicted and correlated with measured experimental results conducted at AML. The finite element code solver was based on the displacement control method, which was extensively discussed in the fourth chapter of the manuscript. Figure 5.34 illustrates the testing apparatus used to validate the finite element code numerical predictions. Figure 5.35 shows the measured and predicted transverse deflection versus the applied compressive load; the latter was calculated as the reaction force at the node where the imposed compressive displacement was applied. In order to identify the sensitivity of the beam response to an initial imperfection, predicted results for w_0=0.14mm, w_0=0.28mm and w_0=0.55mm are presented, corresponding to an initial w_0 range of 0.1-0.3mm observed in the experiments, which consist of the two measurement sets, I and II.

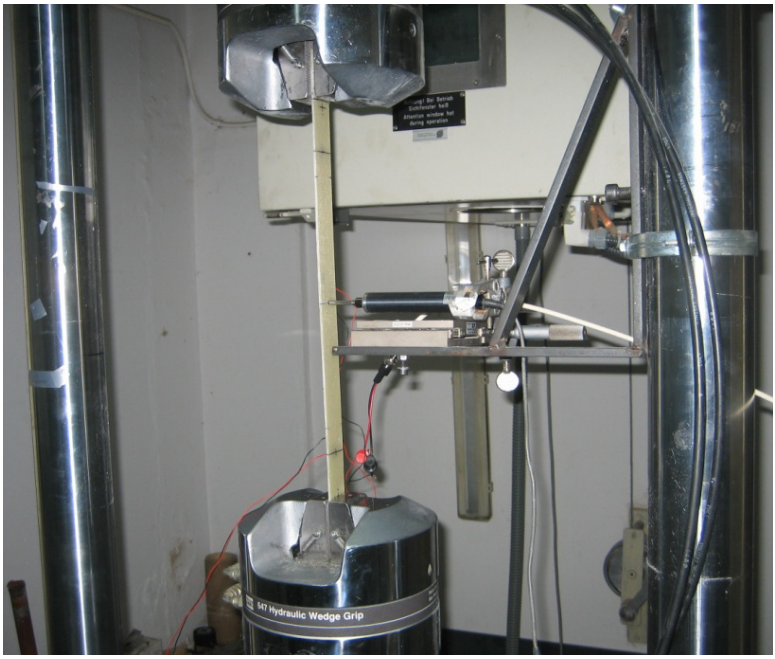

Fig. 5.34 Testing apparatus used in the buckling experiments of Glass/Epoxy beam specimens

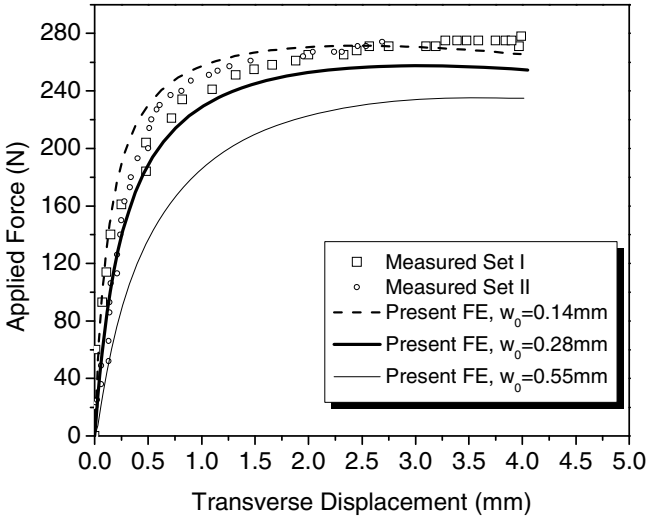

Fig. 5.35 Predicted and measured transverse displacement at the midspan of the $[0_2/90_2]_s$ clamped-free Glass/Epoxy plate-strip under in-plane compressive displacement along the beam axis

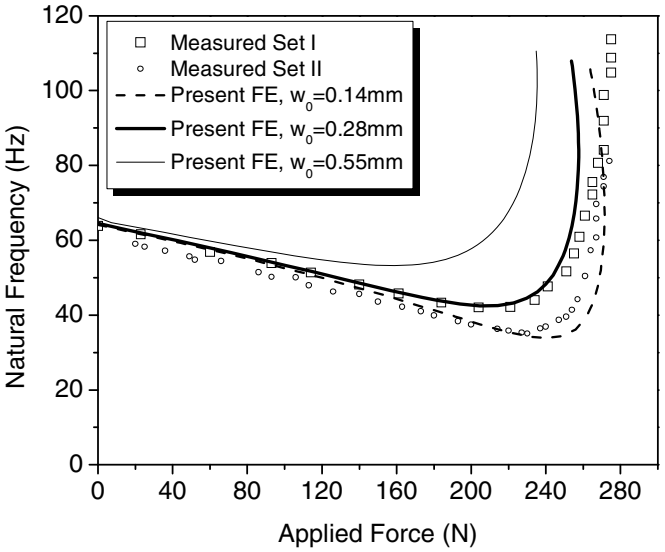

Fig. 5.36 Predicted and measured first bending modal natural frequency of a $[0_2/90_2]_s$ clamped-free Glass/Epoxy plate-strip under in-plane compressive displacement

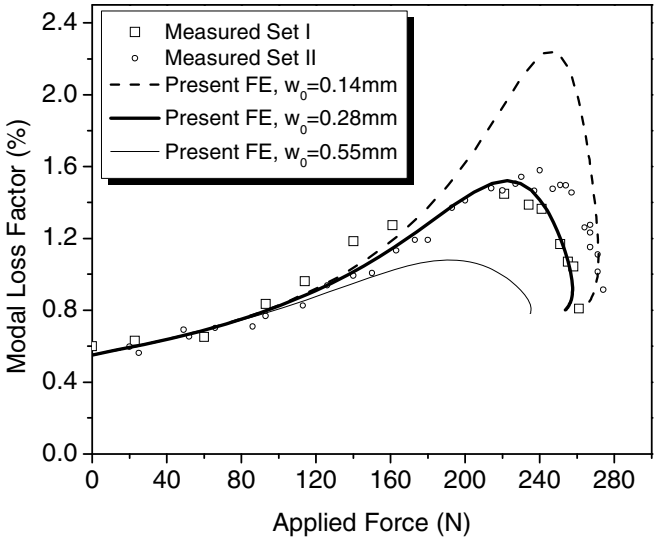

Fig. 5.37 Predicted and measured first bending modal loss factor of a $[0_2/90_2]_s$ clamped-free Glass/Epoxy plate-strip under in-plane compressive displacement

Figure 5.36 shows the variation of the first bending modal frequency for increasing compressive load. It is obvious that as the buckling path transitions from the pre- to post-buckling region, the natural frequency decreases and then increases, respectively. The higher the initial imperfection at the midspan the less severe is the aforementioned transition in modal frequency, a conclusion reported also by Kosmatka (2010). The credibility of the developed beam finite element is validated by the excellent correlation of the predicted results with the experimental measurements, for the case of initial w_0=0.28mm.

The new capabilities of the beam element are clearly illustrated in Figure 5.37, where the first modal loss factor of the composite beam is presented. In the pre-buckling region the modal damping gradually increases, reaches its maximum value near the critical load and thereafter it follows a decreasing path as the beam regains stiffness in the post-buckling region. The predicted results are in excellent agreement with the experimental measurements for the case of initial w_0=0.28mm. The significance of the nonlinear formulation has already been described in fourth chapter of the book and lies in part on the introduction of second-order nonlinear damping terms $\left[\mathbf{C}_{\mathbf{ds}_2}\right]$ (Eq. 4.29) into the governing equations of the system.

Figure 5.38 outlines the effect of second-order nonlinear stiffness $\left[\mathbf{K}_{\mathbf{s}_2}\right]$ and damping $\left[\mathbf{C}_{\mathbf{ds}_2}\right]$ terms on the first mode modal characteristics.

As shown in Figure 5.38b, the inclusion of such terms is essential in problems describing the dynamic response of composite beams and involving buckling, especially in the transition from the pre- to post-buckling region. The contribution of $\left[\mathbf{C}_{\mathbf{ds}_1}\right]$ terms in the pre-buckling region is also quantified.

Further analysis cases include a comparison of numerical code predictions between two cross-ply beam specimens in order to study the effect of laminate orientation on the static and modal characteristics of the beam structure. Therefore, Figure 5.39a-c show the transverse displacement, the first modal bending frequency and the modal damping, respectively, of Glass/Epoxy beams with $[0_2/90_2]_s$ and $[90_2/0_2]_s$ lay-up configurations while an in-plane compressive displacement is applied along the axis of the beam. It is obvious that the $[90_2/0_2]_s$ beam exhibits a more compliant behavior with lower modal frequency and a lower critical buckling point in comparison with the stiffer $[0_2/90_2]_s$ laminate. The predicted first modal bending loss factor, is presented in Figure 5.39c, and shows an interesting trend: at zero applied force the stiff $[0_2/90_2]_s$ beam exhibits low damping due to low D_{d11}, however, as both laminations have equal extension damping coefficients A_{d11}, the $[0_2/90_2]_s$ beam quickly exceeds the modal damping of the $[90_2/0_2]_s$ beam in the pre-buckling region. As the beam transitions to the post-buckling region, the damping in both beams remains comparable in trend and values.

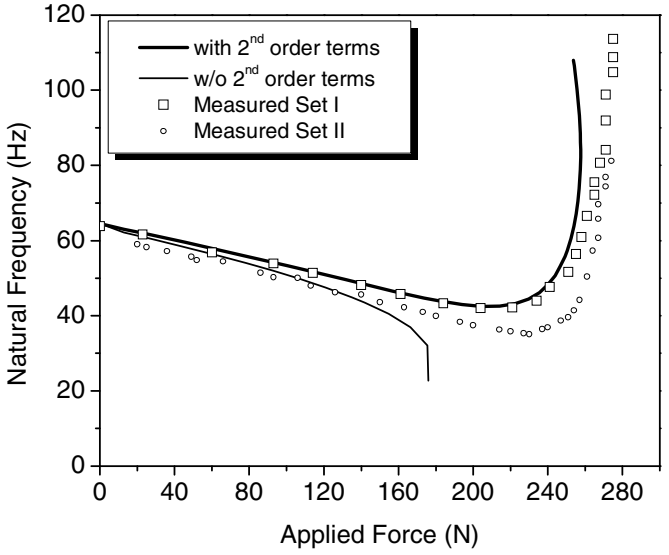

(a)

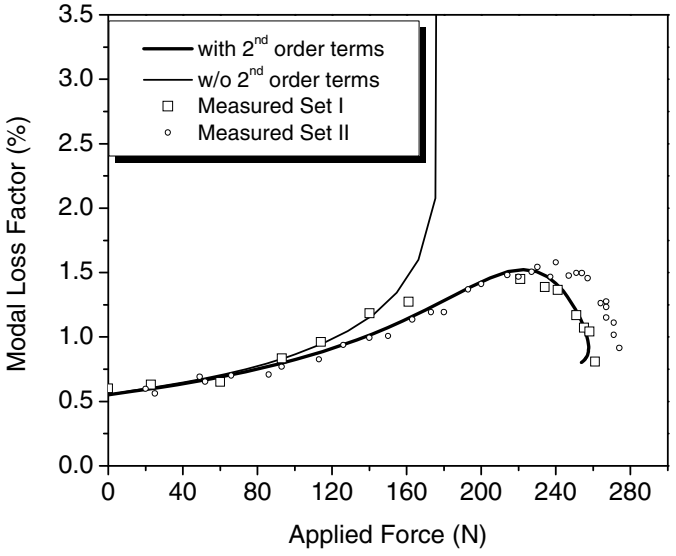

(b)

Fig. 5.38 Effect of second-order terms on the predicted modal characteristics for the $[0_2/90_2]_s$ clamped-free Glass/Epoxy plate-strip first mode: (a) Modal natural frequency; (b) Modal loss factor

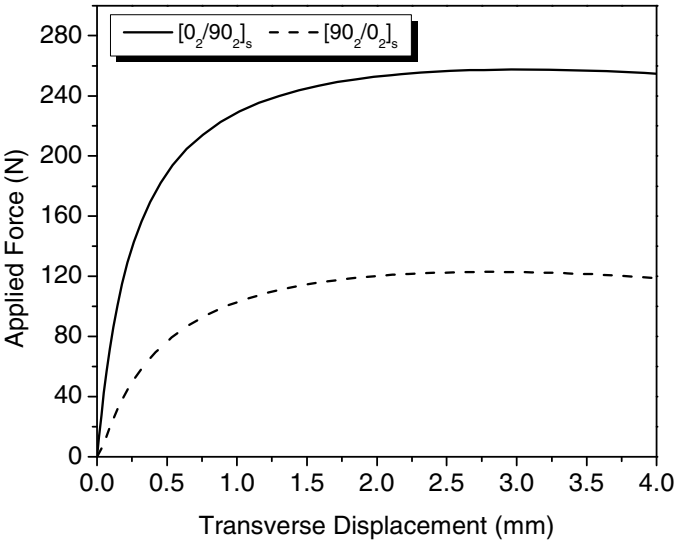

(a)

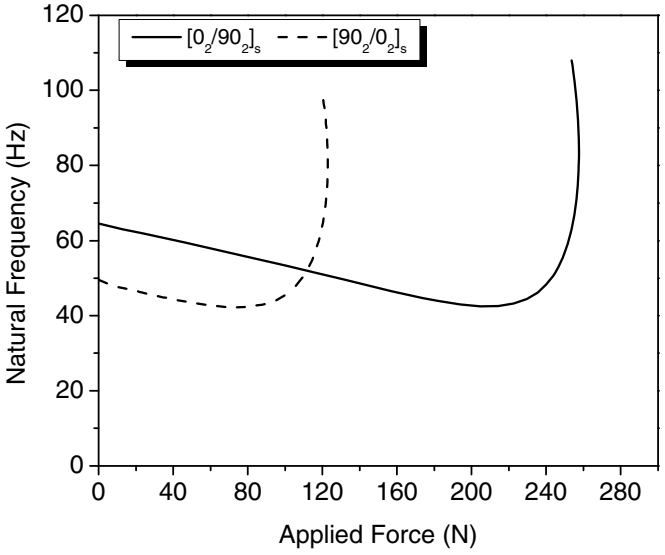

(b)

Fig. 5.39 $[0_2/90_2]_s$ and $[90_2/0_2]_s$ clamped-free Glass/Epoxy plate-strips under in-plane compressive displacement: (a) Predicted transverse displacement; (b) Predicted first modal natural frequency; (c) Predicted first modal loss factor

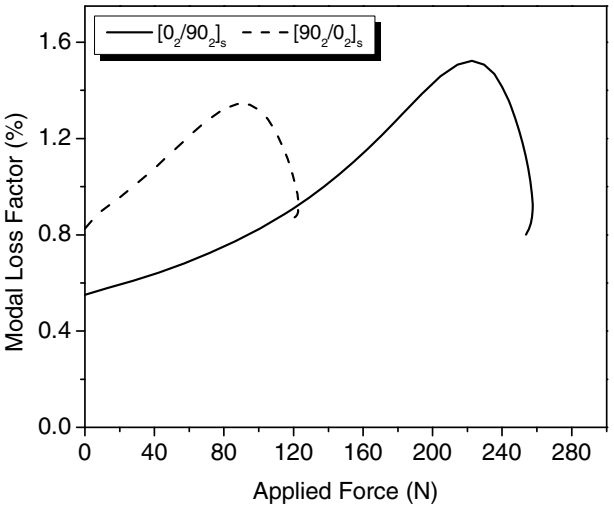

(c)

Fig. 5.39 (*continued*)

5.3.3.2 Composite Beams with Quasi-isotropic and Asymmetric Lamination

The second part of buckling numerical predictions deals with a quasi-isotropic and an asymmetric beam-strip having identical material properties and geometric data with the previous cases.

Quasi-isotropic case. The predicted transverse displacement at beam midspan, first natural frequency and respective modal loss factor of quasi-isotropic Glass/Epoxy lay-up configurations $[0+\theta/90+\theta/45+\theta/-45+\theta]_s$ are presented in Figures 5.40a-c, respectively. Four characteristic values of the ply angle θ are taken into account and are shown in Table 5.10. Similarly to the previous case, the stiffer lamination exhibits the higher increase of nonlinear damping in the pre-buckling range, due to the fact that all laminations have identical A_{d11} and A_{11} terms. Moreover, by observing Figures 5.40a-b, it is obvious that the stiffer lamination $[0/90/45/-45]_s$ presents the higher buckling critical point.

Table 5.10 Different quasi-isotropic beam laminate orientation depending on the selected ply angle

Ply Angle (Degrees)	*Beam Lamination*	*Ply Angle* (Degrees)	*Beam Lamination*
0^0	$[0/90/45/-45]_s$	90^0	$[90/0/-45/45]_s$
45^0	$[45/-45/90/0]_s$	-45^0	$[-45/45/0/90]_s$

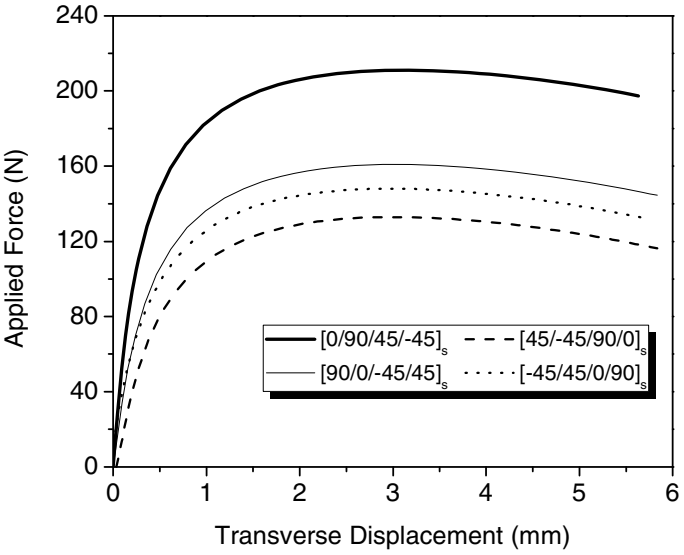

(a)

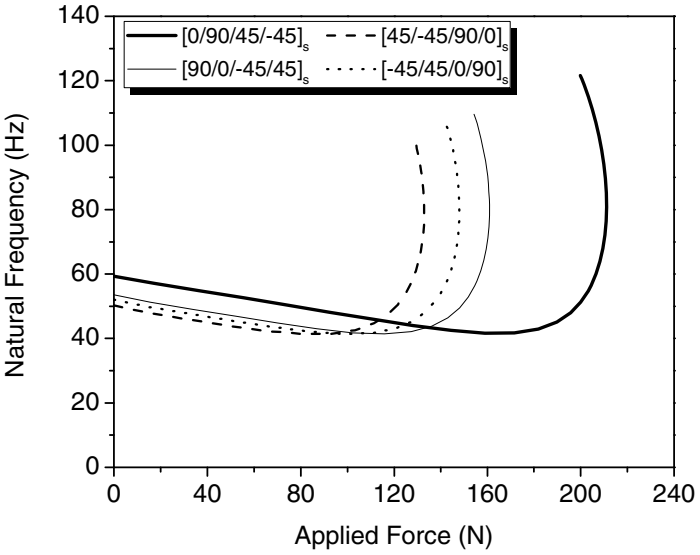

(b)

Fig. 5.40 Predicted free-vibration response for $[0+\theta/90+\theta/45+\theta/-45+\theta]_s$ clamped-free Glass/Epoxy plate-strips under in-plane compressive displacement: (a) Transverse displacement; (b) First modal natural frequency; (c) First modal loss factor

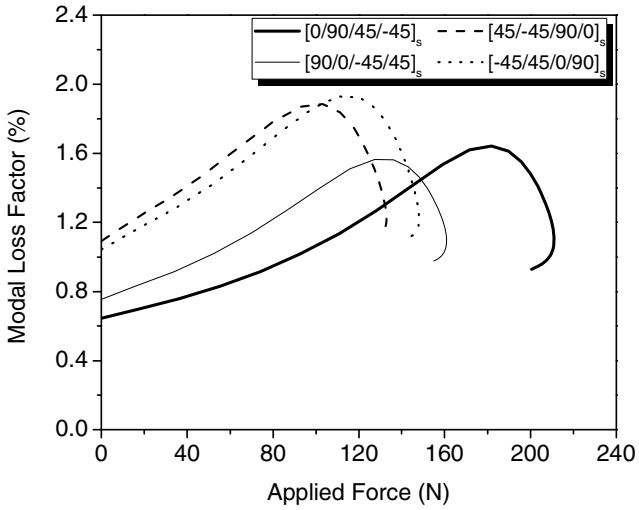

(c)

Fig. 5.40 (*continued*)

Asymmetric case. An asymmetric lamination case is presented in Figures 5.41a-b.

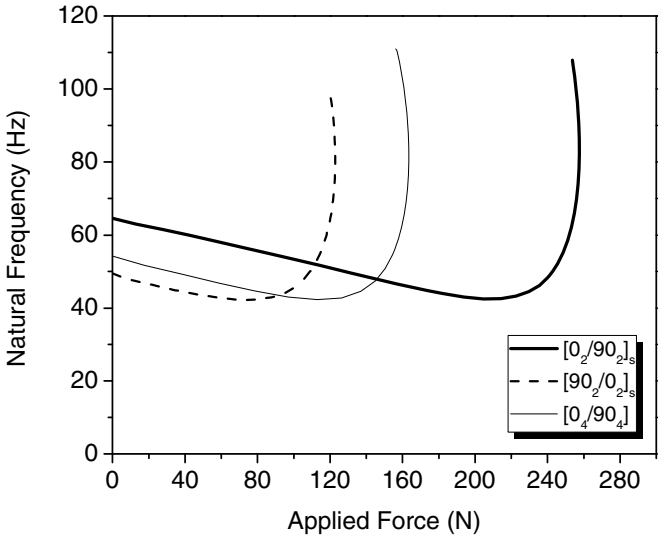

(a)

Fig. 5.41 Comparison of free-vibration characteristics between an asymmetric lamination $[0_4/90_4]$ and symmetric laminations $[0_2/90_2]_s$ and $[90_2/0_2]_s$: (a) First modal natural frequency; (b) First modal loss factor

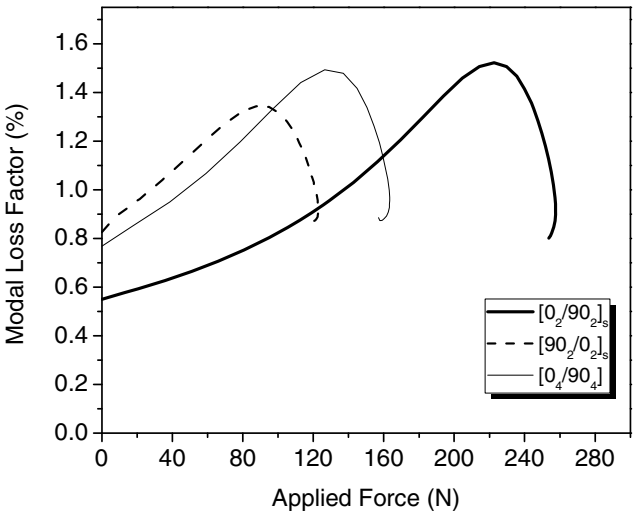

(b)

Fig. 5.41 (*continued*)

The predicted modal frequency and damping values of an asymmetric lamination $[0_4/90_4]$ are compared with the symmetric laminations $[0_2/90_2]_s$ and $[90_2/0_2]_s$ respective ones. The nonzero coupling terms B_{11} and B_{d11} seem to influence both the linear and nonlinear damping of the $[0_4/90_4]$ beam.

5.4 Conclusions

In fifth chapter the theoretical and computational framework of the nonlinear beam finite element was applied to predict the static and dynamic response of composite beams under large in-plane loads. A damped nonlinear beam finite element was formulated and the aforementioned nonlinear stiffness and damping mechanics were incorporated into a research finite element code enabling computational prediction of nonlinear damping and stiffness characteristics of composite strips. The following major conclusions can be summarized in two categories regarding the problems of tension and buckling, respectively:

I. Tension

- The introduction of the new nonlinear stiffness and damping section terms are essential for capturing the stiffening effects on vibrating damped composite beams under large in-plane extensional stresses.
- The prediction of both natural frequencies and modal loss factors appeared to correlate very well with measured data, thus demonstrating the value of developed finite element and nonlinear damped structural dynamic models.

- There exist strong effect of initial stresses on damping which is monotonic with respect to the linear baseline. In the case of tensile in-plane loads induces significant modal damping reductions depending on the mode shape and laminate configuration.
- The reduction of modal damping with in-plane load depends also on the order of the bending mode, due to the nonlinear behavior of the beam, and seems to be less as the mode order increases. This result is consistent with Lesieutre (2009).
- The new nonlinear damping terms due to tensile in-plane loads increase the dissipation of strain energy in absolute value. The reduction in damping is caused by the disproportional increase in the stored strain energy due to membrane stiffening effects and not by a decrease in dissipated strain energy.
- The strong dependence of modal damping on the laminate configuration was both experimentally and numerically illustrated. At very low in-plane load values, the modal damping of bending modes is provided by the flexural laminate damping D_d, while the reduction in modal damping as the load increases, is dominated by the extensional laminate damping A_d.
- The good correlations between analytical and experimental results suggest that the Kelvin viscoelastic model provided reasonably good predictions for the modal damping values in the pre-stressed strip.

II. Buckling

- The new beam finite element captures the effect of stress-stiffening and large rotations on the natural frequencies and modal loss factor values of composite strips subject to in-plane buckling loading. The good correlations between predicted results and experimental measurements underline the credibility of the formulated beam finite element.
- The inclusion of nonlinear damping and stiffness terms seems essential for predicting the small-amplitude free-vibration response of composite strips in the pre- and post-buckling region.
- The modal damping increases monotonically in the pre-buckling range, reaches a maximum at the critical load and then decreases in the post-buckling region. The second-order nonlinear terms dominate the damping in the post-buckling region.
- The excellent agreement between predicted results and experimental measurements also supports the credibility of the Kelvin viscoelastic strain model, to provide good modal damping predictions in the buckled strip.
- An initial imperfection does not change the trend but affects the overall damping values. Large imperfections tend to yield lower damping and vice versa. This is consistent with Kosmatka (2010)
- The nonlinear damping terms are proportional to the extensional damping coefficient of the laminate. Depending on the lamination, the contribution may be significant and may exceed the initial flexural damping of the beam.

Within this chapter the Newton-Raphson technique is combined with the detailed formulation reported in the fourth chapter. In addition, for the buckling case, the displacement control methodology was incorporated in the solver of the nonlinear beam finite element code. The novelty points of fifth chapter are:

* The existence of strong effect of initial stresses on the nonlinear damping of composite structures, which proved to be monotonic with respect to the linear baseline. The in-plane load as well as the order of beam bending mode are important factors regarding the modal damping trend values of a composite structure.
* The prediction of nonlinear damping trend as the composite beam transitions from the pre- to the post-buckling region. The nonlinear beam finite element captures the effect of stress-stiffening and large rotations on the natural frequencies and modal loss factor values of composite strips subject to in-plane buckling loading.
* The study of the dependence of modal damping on the laminate beam configuration, which was both numerically and experimentally illustrated. The excellent agreement between predicted results and experimental measurements, supported the credibility of the Kelvin viscoelastic strain model to the direction of providing good modal damping predictions of the strip subject to large displacements and rotations.
* The significance of the first-order stiffness and damping terms in the pre-stressing of the beam subject to in-plane tensile loading as well as the importance of the respective second-order damping nonlinear terms, which dominate damping in the post-buckling region.

Chapter 6

Prediction of Nonlinear Damped Response of Large-Scale Blade Composite Structures

The necessity for maximization of wind-turbine rotor performance has led to the design of longer and more flexible composite blade configurations. In that direction, new wind-turbine blade designs are introduced which exceed 60m in length and exhibit complex nonlinear structural behavior. These long blades are substantially more flexible and exhibit complex nonlinear geometric behavior which affects their static, dynamic and aeroelastic response, therefore, improvement of current blade modeling tools is required. In order to achieve this target, a new composite beam finite element formulation is presented which includes nonlinear effects due to large displacements and rotations. The new objective of the 3-D beam finite element is to provide a predictive capability for the static highly deflected shape, the damping, the eigenfrequencies and the vibrations of large scale composite blades in the nonlinear range. The tubular beam finite element entails a substantial extension of the formulation of the strip element, which was extensively described in the fourth chapter of the manuscript.

The first subsection of the present chapter presents the new nonlinear formulation from the level of beam cross-section and on. Introduction of the full Green-Lagrange normal strain expression into the variational form of section strain and dissipated energy gives out the nonlinear stiffness and damping matrices of the blade section. For the sake of completeness, all the formulated first- and second-order effective and tangential terms are presented in analytical expressions. Second subsection includes a brief description of the total matrices form of the damped tubular element, whereas in the third one, numerical predictions of the static and modal characteristics of composite box-section beams are presented. At this point, attention is given on the nonlinear modal damping (loss factor) values and their variation when the structure undergoes stiffening effects. The next subsection deals with the damped nonlinear response of a 54m girder box-section beam, which can be considered as the structural part of the UP 61.5m wind-turbine blade, described in the third chapter of the book. Assuming that the blade subjects to gravitational loads and rotates with increasing values of

D.I. Chortis, *Structural Analysis of Composite Wind Turbine Blades*,
Research Topics in Wind Energy 1,
DOI: 10.1007/978-3-319-00864-6_6, © Springer International Publishing Switzerland 2013

angular velocity, the stiffening effect on the natural frequencies and the modal loss factor of the first modes is investigated. In the last part of this chapter the concluding remarks are summarized.

6.1 Nonlinear Mechanics of Composite Blade Structures

The formulation of nonlinear damped structural dynamic mechanics and models for blades will be presented within this section. For the sake of brevity, the following considerations will be taken into account:

- The presented damped beam finite element can be considered as a substantial generalization of the nonlinear strip finite element which was developed in the fourth chapter. It builds on same governing relations at the material level, yet it differs in the formulation of the cross-section mechanics. For example, a strain based Kelvin viscoelastic constitutive model was considered to better describe the relation between the ply stresses and strains as indicated in Eq. (4.1)
- The new nonlinear formulation assumes the same hollow composite tubular beam element (Figure 3.3) with arbitrary geometry and skin lamination and 6 DOFs per node considered in the third chapter. However, the introduction of large deformations into finite element beam formulation leads to new and more complex nonlinear stiffness and damping matrices. Thus, the relation between the engineering strains and the displacements of the cross-section at the curvilinear system $O'_{xs\zeta}$ are described by Eq. (3.6).

6.1.1 Nonlinear Section Mechanics

Similarly to the linear section model described in the third chapter, the assumed section deformation is based upon a first-order shear deformation theory. Therefore, it admits extension along x-axis, bending in y and z directions, torsion about the x-axis and shear on xy and xz planes. In the curvilinear system $O'_{xs\zeta}$, the kinematic assumptions are expressed by Eq. (3.6). In order to capture the effect of large rotations, nonlinear Green-Lagrange strain expressions are considered for the normal strain component, which has the following form,

$$\varepsilon_x = u_{,x} + \frac{1}{2}v_{,x}^2 + \frac{1}{2}w_{,x}^2 \tag{6.1}$$

By substituting the kinematic assumptions of Eqs. (3.10) into the normal, ε_x (Eq. (6.1)) and shear ε_{xs}, $\varepsilon_{x\zeta}$ (Eqs. (3.11)) strain expressions of the nonlinear beam element cross-section, the former is updated to the following expression,

$$\varepsilon_x(x,s,\zeta,t)=\varepsilon_x^0(x)+\varepsilon_{x_{NL}}^0(x)+k_{xy}(x)(z^0+y_{,s}^o\zeta)+k_{xz}(x)(y^0-z_{,s}^o\zeta)+\theta_{,xx}(x)\left\{-r_\zeta^0\zeta+\Psi^o(s)\right\}+$$
$$+\frac{1}{2}\theta_{,x}^2(x)\left\{\left(r_\zeta^{0^2}+r_s^{0^2}\right)+2r_\zeta^0\zeta+\zeta^2\right\}-v_{,x}^0(x)\theta_{,x}(x)\left(r_\zeta^0+\zeta\right)+w_{,x}^0(x)\theta_{,x}(x)\left(r_s^0+\zeta\right)$$
$$\varepsilon_{xs}(x,s,\zeta,t)=\varepsilon_{xz}^0(x)z_{,s}^0+\varepsilon_{xy}^0(x)y_{,s}^0+\varepsilon_{xs}^{0_t}(x,s)-2k_\theta(x)\zeta \tag{6.2}$$
$$\varepsilon_{x\zeta}(x,s,\zeta,t)=\varepsilon_{xz}^0(x)y_{,s}^0-\varepsilon_{xy}^0(x)z_{,s}^0$$

As it has already been underlined, shear strain expressions of the cross-section are assumed to remain in the linear regime.

The equations of motion of the beam are described by the following variational form,

$$-\int_0^L \mathrm{d}x\int_A \delta H\,\mathrm{d}s\,\mathrm{d}\zeta+\int_0^L \mathrm{d}x\int_A \delta T\,\mathrm{d}s\,\mathrm{d}\zeta+\int_\Gamma \delta\bar{\mathbf{u}}^{\mathbf{T}}\bar{\boldsymbol{\tau}}\,\mathrm{d}\Gamma=0 \tag{6.3}$$

where H and T are the strain and kinetic energy, $\bar{\tau}$ are surface tractions on the free surface Γ, A is the cross-sectional areas covered by material and L is the length of the beam.

The kinetic energy variation of the section is represented by the respective integral over the cross-section area,

$$\delta T^{\sec}=\int_A -\delta\mathbf{u}^{\mathbf{T}}\,\mathrm{diag}(\boldsymbol{\rho})\ddot{\mathbf{u}}\,\mathrm{d}s\,\mathrm{d}\zeta=\oint \mathrm{d}s\int_h -\delta\mathbf{u}^{\mathbf{T}}\,\mathrm{diag}(\boldsymbol{\rho})\ddot{\mathbf{u}}\,\mathrm{d}\zeta \tag{6.4}$$

Due to the fact that mass terms are not affected by the new nonlinear formulation and for the sake of brevity, the detailed form of the equivalent mass cross-section terms is identical to the one reported in the third chapter of the present work and are also reported in Appendix C.

The variation of the strain energy of the section is represented by the respective integral over the cross-section area,

$$\delta H^{\sec}=\int_A \delta\boldsymbol{\varepsilon}_{\mathbf{c}}^{\mathbf{T}}\boldsymbol{\sigma}_{\mathbf{c}}\,\mathrm{d}s\,\mathrm{d}\zeta \tag{6.5}$$

Assuming that the polymer matrix composite behaves as Kelvin viscoelastic material, the following expression for the stresses of the composite ply is applied,

$$\boldsymbol{\sigma}_{\mathbf{c}}=\left[\mathbf{Q}_{\mathbf{cs}}\right]\boldsymbol{\varepsilon}_{\mathbf{c}}+\left[\mathbf{Q}_{\mathbf{cd}}\right]\dot{\boldsymbol{\varepsilon}}_{\mathbf{c}} \tag{6.6}$$

In the above equations, the assumed large off-axis strains and stresses of the composite ply take the following form, respectively,

$$\boldsymbol{\varepsilon}_{\mathbf{c}}=\left\{\varepsilon_{c1},\varepsilon_{c5},\varepsilon_{c6}\right\}=\left\{\varepsilon_{cx},\varepsilon_{cx\zeta},\varepsilon_{cxs}\right\}$$
$$\boldsymbol{\sigma}_{\mathbf{c}}=\left\{\sigma_{c1},\sigma_{c5},\sigma_{c6}\right\}=\left\{\sigma_{cx},\sigma_{cx\zeta},\sigma_{cxs}\right\} \tag{6.7}$$

The same issue with the size of strain/stress components is answered in Appendix C, where the laminate matrices reduction is extensively discussed.

In addition, $\left[\mathbf{Q_{cs}}\right]$ is the composite ply equivalent off-axis stiffness matrix and $\left[\mathbf{Q_{cd}}\right]$ is the composite ply equivalent off-axis damping matrix defined in Eq. (4.4) with respect to the local curvilinear system $O'_{xs\zeta}$.

Substituting Eq. (6.6) into Eq. (6.5), the final expression for the strain energy variation takes the form,

$$\delta H_{\text{sec}} = \oint \mathrm{d}s \int_h \left(\delta \boldsymbol{\varepsilon}_{\mathbf{c}}^{\mathbf{T}} \left(\left[\mathbf{Q_{cs}}\right] \boldsymbol{\varepsilon}_{\mathbf{c}} + \left[\mathbf{Q_{cd}}\right] \dot{\boldsymbol{\varepsilon}}_{\mathbf{c}} \right) \right) \mathrm{d}\zeta = \delta H_s + \delta H_{ds} \tag{6.8}$$

where, δH_s represents the strain energy and δH_{ds} the dissipated energy of the blade cross-section.

6.1.2 Nonlinear Stiffness Cross-Section Terms

Replacing the normal and shear strain expressions provided by Eq. (6.2), into Eq. (6.8), integrating firstly over the laminate thickness and then around the skin midline and assuming that the equivalent hoop force, moment and shear force N_s, M_s and $N_{s\zeta}$, respectively, defined with respect to the local section coordinates $O'_{xs\zeta}$ should be negligible, the stored strain energy in the section takes the form,

$$\delta H_s = \delta H_{s_0} + \delta H_{s_1} + \delta H_{s_2} \tag{6.9}$$

where, H_{s_0}, H_{s_1}, H_{s_2} are the cross-section strain energy terms, containing linear, first-order nonlinear and second-order nonlinear components. In detail, these terms provide the linear and the nonlinear stiffness terms of the cross-section, as follows,

$$\delta H_{s_0} = \left\{ \delta \varepsilon_x^0, \delta \varepsilon_{xz}^0, \delta \varepsilon_{xy}^0, \delta k_{xy}, \delta k_{xz}, \delta k_\theta \right\} \left[\mathbf{K_{s_0}}\right] \begin{Bmatrix} u_{,x}^0 \\ \varepsilon_{xz}^0 \\ \varepsilon_{xy}^0 \\ k_{xy} \\ k_{xz} \\ k_\theta \end{Bmatrix} \tag{6.10}$$

$$\delta H_{s_1} = \left\{ \delta u^0_{,x}, \delta \upsilon^0_{,x}, \delta w^0_{,x}, \delta k_{xy}, \delta k_{xz}, \delta k_\theta \right\} \left[\mathbf{K}_{\mathbf{s_1}} \right] \begin{Bmatrix} u^0_{,x} \\ \upsilon^0_{,x} \\ w^0_{,x} \\ k_{xy} \\ k_{xz} \\ k_\theta \end{Bmatrix} \tag{6.11}$$

$$\delta H_{s_2} = \left\{ \delta u^0_{,x}, \delta \upsilon^0_{,x}, \delta w^0_{,x}, \delta k_{xy}, \delta k_{xz}, \delta k_\theta \right\} \left[\mathbf{K}_{\mathbf{s_2}} \right] \begin{Bmatrix} u^0_{,x} \\ \upsilon^0_{,x} \\ w^0_{,x} \\ k_{xy} \\ k_{xz} \\ k_\theta \end{Bmatrix} \tag{6.12}$$

The linear stiffness matrix $\left[\mathbf{K}_{\mathbf{s_0}} \right]$ contains the well-known linear extensional-shear coupling and flexural-torsional stiffness terms $\left[\mathbf{A^0} \right]$, $\left[\mathbf{B^0} \right]$ and $\left[\mathbf{D^0} \right]$ of the cross-section (Saravanos et al. 2006) whose detailed expressions are reported in Appendix C,

$$\left[\mathbf{K}_{\mathbf{s_0}} \right] = \begin{bmatrix} A^0_{11} & \bar{A}^0_{15} & \bar{A}^0_{16} & B^0_{11} & B^0_{12} & \bar{B}^0_{16} \\ \bar{A}^0_{51} & A^0_{55} & A^0_{56} & \bar{B}^0_{51} & \bar{B}^0_{52} & B^0_{56} \\ \bar{A}^0_{61} & A^0_{65} & A^0_{66} & \bar{B}^0_{61} & \bar{B}^0_{62} & B^0_{66} \\ B^0_{11} & \bar{B}^0_{51} & \bar{B}^0_{61} & D^0_{11} & D^0_{12} & \bar{D}^0_{16} \\ B^0_{12} & \bar{B}^0_{52} & \bar{B}^0_{62} & D^0_{21} & D^0_{22} & \bar{D}^0_{26} \\ \bar{B}^0_{16} & B^0_{56} & B^0_{66} & \bar{D}^0_{61} & \bar{D}^0_{62} & D^0_{66} \end{bmatrix} \tag{6.13}$$

At this point it should be underlined that all linear and nonlinear terms indicated with an overbar are associated with material coupling effects.

First-Order Nonlinear Stiffness. The effective first-order nonlinear stiffness matrice $\left[\mathbf{K}_{\mathbf{s_1}} \right]$ refers to nonlinear strain terms with linear dependence to generalized section strains. The respective stiffness matrix has the following form,

$$\left[\mathbf{K_{s_1}}\right]=\begin{bmatrix} 0 & A_{15}^{nl1} & A_{16}^{nl1} & 0 & 0 & B_{16}^{nl1} \\ A_{51}^{nl1} & \bar{A}_{55}^{nl1} & \bar{A}_{56}^{nl1} & \bar{B}_{51}^{nl1} & \bar{B}_{52}^{nl1} & \bar{B}_{56}^{nl1} \\ A_{61}^{nl1} & \bar{A}_{65}^{nl1} & \bar{A}_{66}^{nl1} & \bar{B}_{61}^{nl1} & \bar{B}_{62}^{nl1} & \bar{B}_{66}^{nl1} \\ 0 & \bar{B}_{l51}^{nl1} & \bar{B}_{l61}^{nl1} & 0 & 0 & \bar{D}_{16}^{nl1} \\ 0 & \bar{B}_{l52}^{nl1} & \bar{B}_{l62}^{nl1} & 0 & 0 & \bar{D}_{26}^{nl1} \\ B_{l16}^{nl1} & \bar{B}_{l56}^{nl1} & \bar{B}_{l66}^{nl1} & \bar{D}_{61}^{nl1} & \bar{D}_{62}^{nl1} & \bar{D}_{66}^{nl1} \end{bmatrix} \tag{6.14}$$

The detailed expressions of each of these terms are:

$$A_{15}^{nl1}=\upsilon_{,x}^{0}\oint\frac{1}{2}A_{11}ds-\theta_{,x}\oint\left(A_{11}r_{\zeta}^{0}+B_{11}\right)ds$$

$$A_{16}^{nl1}=w_{,x}^{0}\oint\frac{1}{2}A_{11}ds+\theta_{,x}\oint A_{11}r_{s}^{0}ds$$

$$A_{51}^{nl1}=\upsilon_{,x}^{0}\oint A_{11}ds-\theta_{,x}\oint\left(A_{11}r_{\zeta}^{0}+B_{11}\right)ds$$

$$\bar{A}_{55}^{nl1}=\upsilon_{,x}^{0}\oint\frac{3}{2}A_{16}y_{,s}^{0}ds-\theta_{,x}\oint\left(2A_{16}y_{,s}^{0}r_{\zeta}^{0}+2B_{16}y_{,s}^{0}\right)ds$$

$$\bar{A}_{56}^{nl1}=\upsilon_{,x}^{0}\oint A_{16}z_{,s}^{0}ds+w_{,x}^{0}\oint\frac{1}{2}A_{16}y_{,s}^{0}ds+\theta_{,x}\oint\left(A_{16}\left(y_{,s}^{0}r_{s}^{0}-z_{,s}^{0}r_{\zeta}^{0}\right)-B_{16}z_{,s}^{0}\right)ds \tag{6.15}$$

$$A_{61}^{nl1}=w_{,x}^{0}\oint A_{11}ds+\theta_{,x}\oint A_{11}r_{s}^{0}ds$$

$$\bar{A}_{65}^{nl1}=\upsilon_{,x}^{0}\oint\frac{1}{2}A_{16}z_{,s}^{0}ds+w_{,x}^{0}\oint A_{16}y_{,s}^{0}ds+\theta_{,x}\oint\left(A_{16}\left(y_{,s}^{0}r_{s}^{0}-z_{,s}^{0}r_{\zeta}^{0}\right)-B_{16}z_{,s}^{0}\right)ds$$

$$\bar{A}_{66}^{nl1}=w_{,x}^{0}\oint\frac{3}{2}A_{16}z_{,s}^{0}ds+\theta_{,x}\oint 2A_{16}z_{,s}^{0}r_{s}^{0}ds$$

$$B_{16}^{nl1}=\theta_{,x}^{0}\oint\left(\frac{1}{2}A_{11}\left(r_{\zeta}^{0^{2}}+r_{s}^{0^{2}}\right)+B_{11}r_{\zeta}^{0}+\frac{1}{2}D_{11}\right)ds$$

$$\begin{aligned}\bar{B}_{51}^{nl1}=&\upsilon_{,x}^{0}\oint\left(A_{11}z^{0}+B_{11}y_{,s}^{0}\right)ds+\upsilon_{,x}^{0}\oint A_{16}z_{,s}^{0}ds\\&-\theta_{,x}\oint\left(A_{11}z^{0}r_{\zeta}^{0}+B_{11}\left(y_{,s}^{0}r_{\zeta}^{0}+z^{0}\right)+D_{11}y_{,s}^{0}\right)ds-\theta_{,x}\oint\left(A_{16}z_{,s}^{0}r_{\zeta}^{0}+B_{16}z_{,s}^{0}\right)ds\end{aligned} \tag{6.16}$$

$$\bar{B}_{52}^{nl1} = v_{,x}^0 \oint \left(A_{11} y^0 - B_{11} z_{,s}^0 \right) ds + v_{,x}^0 \oint A_{16} y_{,s}^0 ds$$
$$-\theta_{,x} \oint \left(A_{11} y^0 r_\zeta^0 - B_{11} \left(z_{,s}^0 r_\zeta^0 - y^0 \right) - D_{11} z_{,s}^0 \right) ds - \theta_{,x} \oint \left(A_{16} y_{,s}^0 r_\zeta^0 + B_{16} y_{,s}^0 \right) ds$$

$$\bar{B}_{56}^{nl1} = -v_{,x}^0 \oint (A_{16} A_h + 2B_{16}) ds$$
$$+\theta_{,x} \oint \left(A_{16} A_h r_\zeta^0 + B_{16} \left(2 r_\zeta^0 + A_h \right) + 2D_{16} \right) ds + \theta_{,x} \oint \left(\frac{1}{2} A_{16} y_{,s}^0 \left(r_\zeta^{0^2} + r_s^{0^2} \right) + B_{16} y_{,s}^0 r_\zeta^0 + \frac{1}{2} D_{16} y_{,s}^0 \right) ds$$

$$\bar{B}_{61}^{nl1} = w_{,x}^0 \oint \left(A_{11} z^0 + B_{11} y_{,s}^0 \right) ds + w_{,x}^0 \oint A_{16} z_{,s}^0 ds + \theta_{,x} \oint \left(A_{11} z^0 r_s^0 + B_{11} y_{,s}^0 r_s^0 \right) ds + \theta_{,x} \oint A_{16} z_{,s}^0 r_s^0 ds$$

$$\bar{B}_{62}^{nl1} = w_{,x}^0 \oint \left(A_{11} y^0 - B_{11} z_{,s}^0 \right) ds + w_{,x}^0 \oint A_{16} y_{,s}^0 ds + \theta_{,x} \oint \left(A_{11} y^0 r_s^0 - B_{11} z_{,s}^0 r_s^0 \right) ds + \theta_{,x} \oint A_{16} y_{,s}^0 r_s^0 ds$$

$$\bar{B}_{66}^{nl1} = -w_{,x}^0 \oint \left(A_{16} A_h + 2B_{16} \right) ds - \theta_{,x} \oint \left(A_{16} A_h r_s^0 + 2B_{16} r_s^0 \right) ds$$
$$+\theta_{,x} \oint \left(\frac{1}{2} A_{16} z_{,s}^0 (r_\zeta^{0^2} + r_s^{0^2}) + B_{16} z_{,s}^0 r_\zeta^0 + \frac{1}{2} D_{16} z_{,s}^0 \right) ds$$

$$\bar{B}_{l51}^{nl1} = v_{,x}^0 \oint \left(\frac{1}{2} A_{11} z^0 + \frac{1}{2} B_{11} y_{,s}^0 \right) ds + v_{,x}^0 \oint \frac{1}{2} A_{16} z_{,s}^0 ds$$
$$-\theta_{,x} \oint \left(A_{11} z^0 r_\zeta^0 + B_{11} \left(y_{,s}^0 r_\zeta^0 + z^0 \right) + D_{11} y_{,s}^0 \right) ds - \theta_{,x} \oint \left(A_{16} z_{,s}^0 r_\zeta^0 + B_{16} z_{,s}^0 \right) ds$$

$$\bar{B}_{l61}^{nl1} = w_{,x}^0 \oint \left(\frac{1}{2} A_{11} z^0 + \frac{1}{2} B_{11} y_{,s}^0 \right) ds + w_{,x}^0 \oint \frac{1}{2} A_{16} z_{,s}^0 ds + \theta_{,x} \oint \left(A_{11} z^0 r_s^0 + B_{11} y_{,s}^0 r_s^0 \right) ds + \theta_{,x} \oint A_{16} z_{,s}^0 r_s^0 ds$$

$$\bar{B}_{l52}^{nl1} = v_{,x}^0 \oint \left(\frac{1}{2} A_{11} y^0 - \frac{1}{2} B_{11} z_{,s}^0 \right) ds + v_{,x}^0 \oint \frac{1}{2} A_{16} y_{,s}^0 ds$$
$$-\theta_{,x} \oint \left(A_{11} y^0 r_\zeta^0 - B_{11} \left(z_{,s}^0 r_\zeta^0 - y^0 \right) - D_{11} z_{,s}^0 \right) ds - \theta_{,x} \oint \left(A_{16} y_{,s}^0 r_\zeta^0 + B_{16} y_{,s}^0 \right) ds$$

$$\bar{B}_{l62}^{nl1} = w_{,x}^0 \oint \left(\frac{1}{2} A_{11} y^0 - \frac{1}{2} B_{11} z_{,s}^0 \right) ds + w_{,x}^0 \oint \frac{1}{2} A_{16} y_{,s}^0 ds + \theta_{,x} \oint \left(A_{11} y^0 r_s^0 - B_{11} z_{,s}^0 r_s^0 \right) ds + \theta_{,x} \oint A_{16} y_{,s}^0 r_s^0 ds$$

$$B_{l16}^{nl1} = w_{,x}^0 \oint A_{11} ds - v_{,x}^0 \oint \left(A_{11} r_\zeta^0 + B_{11} \right) ds + \theta_{,x}^0 \oint \left(A_{11} \left(r_\zeta^{0^2} + r_s^{0^2} \right) + 2B_{11} r_\zeta^0 + D_{11} \right) ds$$

$$\bar{B}_{l56}^{nl1} = w_{,x}^0 \oint A_{16} y_{,s}^0 r_s^0 ds - v_{,x}^0 \oint \left(\frac{1}{2} A_{16} A_h + B_{16} \right) ds - v_{,x}^0 \oint \left(A_{16} y_{,s}^0 r_\zeta^0 + B_{16} y_{,s}^0 \right) ds$$
$$+\theta_{,x} \oint \left(A_{16} A_h r_\zeta^0 + B_{16} \left(2 r_\zeta^0 + A_h \right) + 2D_{16} \right) ds + \theta_{,x} \oint \left(A_{16} y_{,s}^0 \left(r_\zeta^{0^2} + r_s^{0^2} \right) + 2B_{16} y_{,s}^0 r_\zeta^0 + D_{16} y_{,s}^0 \right) ds$$

$$\bar{B}_{l66}^{nl1} = w_{,x}^0 \oint A_{16} z_{,s}^0 r_s^0 ds - w_{,x}^0 \oint \left(\frac{1}{2} A_{16} A_h + B_{16} \right) ds - v_{,x}^0 \oint \left(A_{16} z_{,s}^0 r_\zeta^0 + B_{16} z_{,s}^0 \right) ds$$
$$- \theta_{,x} \oint \left(A_{16} A_h r_s^0 + 2 B_{16} r_s^0 \right) ds + \theta_{,x} \oint \left(A_{16} z_{,s}^0 \left(r_\zeta^{0^2} + r_s^{0^2} \right) + 2 B_{16} z_{,s}^0 r_\zeta^0 + D_{16} z_{,s}^0 \right) ds$$

$$\bar{D}_{16}^{nl1} = \theta_{,x} \oint \left(\frac{1}{2} A_{11} z^0 \left(r_\zeta^{0^2} + r_s^{0^2} \right) + \frac{1}{2} B_{11} \left(2 z^0 r_\zeta^0 + y_{,s}^0 \left(r_\zeta^{0^2} + r_s^{0^2} \right) \right) + \frac{1}{2} D_{11} \left(z^0 + 2 y_{,s}^0 r_\zeta^0 \right) \right) ds$$
$$+ \theta_{,x} \oint \left(\frac{1}{2} A_{16} z_{,s}^0 \left(r_\zeta^{0^2} + r_s^{0^2} \right) + B_{16} z_{,s}^0 r_\zeta^0 + \frac{1}{2} D_{16} z_{,s}^0 \right) ds$$

$$\bar{D}_{26}^{nl1} = \theta_{,x} \oint \left(\frac{1}{2} A_{11} y^0 \left(r_\zeta^{0^2} + r_s^{0^2} \right) + \frac{1}{2} B_{11} \left(2 y^0 r_\zeta^0 - z_{,s}^0 \left(r_\zeta^{0^2} + r_s^{0^2} \right) \right) + \frac{1}{2} D_{11} \left(y^0 - 2 z_{,s}^0 r_\zeta^0 \right) \right) ds$$
$$+ \theta_{,x} \oint \left(\frac{1}{2} A_{16} y_{,s}^0 \left(r_\zeta^{0^2} + r_s^{0^2} \right) + B_{16} y_{,s}^0 r_\zeta^0 + \frac{1}{2} D_{16} y_{,s}^0 \right) ds$$

$$\bar{D}_{61}^{nl1} = w_{,x}^0 \oint \left(A_{11} z^0 r_s^0 + B_{11} y_{,s}^0 r_s^0 \right) ds + w_{,x}^0 \oint A_{16} z_{,s}^0 r_s^0 ds$$
$$- v_{,x}^0 \oint \left(A_{11} z^0 r_\zeta^0 + B_{11} \left(z^0 + y_{,s}^0 r_\zeta^0 \right) + D_{11} y_{,s}^0 \right) ds - v_{,x}^0 \oint \left(A_{16} z_{,s}^0 r_\zeta^0 + B_{16} z_{,s}^0 \right) ds$$
$$+ \theta_{,x} \oint \left(A_{11} z^0 \left(r_\zeta^{0^2} + r_s^{0^2} \right) + B_{11} \left(2 z^0 r_\zeta^0 + y_{,s}^0 \left(r_\zeta^{0^2} + r_s^{0^2} \right) \right) + D_{11} \left(z^0 + 2 y_{,s}^0 r_\zeta^0 \right) \right) ds$$
$$+ \theta_{,x} \oint \left(A_{16} z_{,s}^0 \left(r_\zeta^{0^2} + r_s^{0^2} \right) + 2 B_{16} z_{,s}^0 r_\zeta^0 + D_{16} z_{,s}^0 \right) ds \qquad (6.17)$$

$$\bar{D}_{62}^{nl1} = w_{,x}^0 \oint \left(A_{11} y^0 r_s^0 - B_{11} z_{,s}^0 r_s^0 \right) ds + w_{,x}^0 \oint A_{16} y_{,s}^0 r_s^0 ds$$
$$- v_{,x}^0 \oint \left(A_{11} y^0 r_\zeta^0 + B_{11} \left(y^0 - z_{,s}^0 r_\zeta^0 \right) + D_{11} z_{,s}^0 \right) ds - v_{,x}^0 \oint \left(A_{16} y_{,s}^0 r_\zeta^0 + B_{16} y_{,s}^0 \right) ds$$
$$+ \theta_{,x} \oint \left(A_{11} y^0 \left(r_\zeta^{0^2} + r_s^{0^2} \right) + B_{11} \left(2 y^0 r_\zeta^0 - z_{,s}^0 \left(r_\zeta^{0^2} + r_s^{0^2} \right) \right) + D_{11} \left(y^0 - 2 z_{,s}^0 r_\zeta^0 \right) \right) ds$$
$$+ \theta_{,x} \oint \left(A_{16} y_{,s}^0 \left(r_\zeta^{0^2} + r_s^{0^2} \right) + 2 B_{16} y_{,s}^0 r_\zeta^0 + D_{16} y_{,s}^0 \right) ds$$

$$\bar{D}_{66}^{nl1} = -w_{,x}^0 \oint \left(A_{16} A_h r_s^0 + 2 B_{16} r_s^0 \right) ds + v_{,x}^0 \oint \left(A_{16} A_h r_\zeta^0 + B_{16} \left(2 r_\zeta^0 + A_h \right) + 2 D_{16} \right) ds$$
$$- \theta_{,x} \oint \left(A_{16} A_h \left(r_\zeta^{0^2} + r_s^{0^2} \right) + 2 B_{16} \left(r_\zeta^{0^2} + r_s^{0^2} + A_h r_\zeta^0 \right) + D_{16} \left(4 r_\zeta^0 + A_h \right) \right) ds$$
$$- \theta_{,x} \oint \left(\frac{1}{2} A_{16} A_h \left(r_\zeta^{0^2} + r_s^{0^2} \right) + B_{16} \left(A_h r_\zeta^0 + r_\zeta^{0^2} + r_s^{0^2} \right) + D_{16} \left(2 r_\zeta^0 + \frac{1}{2} A_h \right) \right) ds$$

Second-Order Nonlinear Stiffness. $\left[\mathbf{K}_{\mathbf{s}_2} \right]$ matrix includes the respective second-order nonlinear stiffness terms,

$$\left[\mathbf{K}_{\mathbf{s}_2}\right]=\begin{bmatrix} 0 & 0 & 0 & 0 & 0 & 0 \\ 0 & A_{55}^{nl2} & A_{56}^{nl2} & 0 & 0 & B_{56}^{nl2} \\ 0 & A_{65}^{nl2} & A_{66}^{nl2} & 0 & 0 & B_{66}^{nl2} \\ 0 & 0 & 0 & 0 & 0 & 0 \\ 0 & 0 & 0 & 0 & 0 & 0 \\ 0 & B_{l56}^{nl2} & B_{l66}^{nl2} & 0 & 0 & D_{66}^{nl2} \end{bmatrix} \tag{6.18}$$

which have the detailed form,

$$\begin{aligned} A_{55}^{nl2} &= \upsilon_{,x}^{0^2}\oint\frac{1}{2}A_{11}ds-\upsilon_{,x}^{0}\theta_{,x}\oint\left(\frac{3}{2}A_{11}r_{\zeta}^{0}+2B_{11}\right)ds+\theta_{,x}^{2}\oint\left(A_{11}r_{\zeta}^{0^2}+2B_{11}r_{\zeta}^{0}+D_{11}\right)ds \\ A_{56}^{nl2} &= \upsilon_{,x}^{0}w_{,x}^{0}\oint\frac{1}{2}A_{11}ds+\upsilon_{,x}^{0}\theta_{,x}\oint A_{11}r_{s}^{0}ds-w_{,x}^{0}\theta_{,x}\oint\left(\frac{1}{2}A_{11}r_{\zeta}^{0}+\frac{1}{2}B_{11}\right)ds-\theta_{,x}^{2}\oint\left(A_{11}r_{\zeta}^{0}r_{s}^{0}+B_{11}r_{s}^{0}\right)ds \\ A_{65}^{nl2} &= \upsilon_{,x}^{0}w_{,x}^{0}\oint\frac{1}{2}A_{11}ds+\upsilon_{,x}^{0}\theta_{,x}\oint\frac{1}{2}A_{11}r_{s}^{0}ds-w_{,x}^{0}\theta_{,x}\oint\left(A_{11}r_{\zeta}^{0}+B_{11}\right)ds-\theta_{,x}^{2}\oint\left(A_{11}r_{\zeta}^{0}r_{s}^{0}+B_{11}r_{s}^{0}\right)ds \\ A_{66}^{nl2} &= w_{,x}^{0^2}\oint\frac{1}{2}A_{11}ds+w_{,x}^{0}\theta_{,x}\oint\frac{3}{2}A_{11}r_{s}^{0}ds+\theta_{,x}^{2}\oint A_{11}r_{s}^{0^2}ds \end{aligned} \tag{6.19}$$

$$\begin{aligned} B_{56}^{nl2} &= \upsilon_{,x}^{0}\theta_{,x}\oint\left(\frac{1}{2}A_{11}\left(r_{\zeta}^{0^2}+r_{s}^{0^2}\right)+B_{11}r_{\zeta}^{0}+\frac{1}{2}D_{11}\right)ds \\ &\quad-\theta_{,x}^{2}\oint\left(\frac{1}{2}A_{11}r_{\zeta}^{0}\left(r_{\zeta}^{0^2}+r_{s}^{0^2}\right)+\frac{1}{2}B_{11}\left(-3r_{\zeta}^{0^2}-r_{s}^{0^2}\right)-\frac{3}{2}D_{11}r_{\zeta}^{0}\right)ds \\ B_{66}^{nl2} &= w_{,x}^{0}\theta_{,x}\oint\left(\frac{1}{2}A_{11}\left(r_{\zeta}^{0^2}+r_{s}^{0^2}\right)+B_{11}r_{\zeta}^{0}+\frac{1}{2}D_{11}\right)ds+\theta_{,x}^{2}\oint\left(\frac{1}{2}A_{11}r_{s}^{0}\left(r_{\zeta}^{0^2}+r_{s}^{0^2}\right)+B_{11}r_{\zeta}^{0}r_{s}^{0}+\frac{1}{2}D_{11}r_{s}^{0}\right)ds \end{aligned}$$

$$\begin{aligned} B_{l56}^{nl2} &= -\upsilon_{,x}^{0^2}\oint\left(\frac{1}{2}A_{11}r_{\zeta}^{0}+\frac{1}{2}B_{11}\right)ds+\upsilon_{,x}^{0}w_{,x}\oint\frac{1}{2}A_{11}r_{s}^{0}ds \\ &\quad+\upsilon_{,x}^{0}\theta_{,x}\oint\left(A_{11}r_{\zeta}^{0^2}+2B_{11}r_{\zeta}^{0}+D_{11}\right)ds+\upsilon_{,x}^{0}\theta_{,x}\oint\left(\frac{1}{2}A_{11}\left(r_{\zeta}^{0^2}+r_{s}^{0^2}\right)+B_{11}r_{\zeta}^{0}+\frac{1}{2}D_{11}\right)ds \\ &\quad-w_{,x}^{0}\theta_{,x}\oint\left(A_{11}r_{s}^{0}r_{\zeta}^{0}+B_{11}r_{s}^{0}\right)ds-\theta_{,x}^{2}\oint\left(A_{11}r_{\zeta}^{0}\left(r_{\zeta}^{0^2}+r_{s}^{0^2}\right)+B_{11}\left(-3r_{\zeta}^{0^2}-r_{s}^{0^2}\right)-3D_{11}r_{\zeta}^{0}\right)ds \\ B_{l66}^{nl2} &= w_{,x}^{0^2}\oint\frac{1}{2}A_{11}r_{s}^{0}ds-\upsilon_{,x}^{0}w_{,x}\oint\left(\frac{1}{2}A_{11}r_{\zeta}^{0}+\frac{1}{2}B_{11}\right)ds \\ &\quad-\upsilon_{,x}^{0}\theta_{,x}\oint\left(A_{11}r_{\zeta}^{0}r_{s}^{0}+B_{11}r_{s}^{0}\right)ds+w_{,x}^{0}\theta_{,x}\oint\left(\frac{1}{2}A_{11}\left(r_{\zeta}^{0^2}+r_{s}^{0^2}\right)+B_{11}r_{\zeta}^{0}+\frac{1}{2}D_{11}\right)ds+w_{,x}^{0}\theta_{,x}\oint A_{11}r_{s}^{0^2}ds \\ &\quad+\theta_{,x}^{2}\oint\left(A_{11}r_{s}^{0}\left(r_{\zeta}^{0^2}+r_{s}^{0^2}\right)+2B_{11}r_{\zeta}^{0}r_{s}^{0}+D_{11}r_{s}^{0}\right)ds \end{aligned} \tag{6.20}$$

$$
\begin{aligned}
D_{66}^{nl2} = &-\upsilon_{,x}^{0}\theta_{,x}\oint\left(\frac{1}{2}A_{11}r_{\zeta}^{0}\left(r_{\zeta}^{0^2}+r_{s}^{0^2}\right)+\frac{1}{2}B_{11}\left(3r_{\zeta}^{0^2}+r_{s}^{0^2}\right)+\frac{3}{2}D_{11}r_{\zeta}^{0}\right)ds \\
&+w_{,x}^{0}\theta_{,x}\oint\left(\frac{1}{2}A_{11}r_{s}^{0}\left(r_{\zeta}^{0^2}+r_{s}^{0^2}\right)+B_{11}r_{s}^{0}r_{\zeta}^{0}+\frac{1}{2}D_{11}r_{s}^{0}\right)ds \\
&+\theta_{,x}^{2}\oint\left(\frac{1}{2}A_{11}\left(r_{\zeta}^{0^2}+r_{s}^{0^2}\right)^{2}+2B_{11}r_{\zeta}^{0}\left(r_{\zeta}^{0^2}+r_{s}^{0^2}\right)+D_{11}\left(3r_{\zeta}^{0^2}+r_{s}^{0^2}\right)\right)ds
\end{aligned}
\tag{6.21}
$$

6.1.3 *Linearized Stiffness Cross-Section Terms*

Similarly to the derivation of the effective section stiffness terms, linearized stiffness matrices were derived (see paragr. 4.5), providing the stored energy of the cross section, when the latter undergoes small deflections about a statically deformed position.

The new nonlinear tangential stiffness terms are expressed by $\left[\mathbf{K}_{\mathbf{Ts_1}}\right]$ and $\left[\mathbf{K}_{\mathbf{Ts_2}}\right]$, matrices, which refer to first- and second-order tangential nonlinear stiffness terms, respectively. The first-order nonlinear tangential stiffness matrix $\left[\mathbf{K}_{\mathbf{Ts_1}}\right]$ has the form,

$$
\left[\mathbf{K}_{\mathbf{Ts_1}}\right]=\begin{bmatrix}
0 & A_{t15}^{nl1} & A_{t16}^{nl1} & 0 & 0 & B_{t16}^{nl1} \\
A_{t51}^{nl1} & \bar{A}_{t55}^{nl1} & \bar{A}_{t56}^{nl1} & \bar{B}_{t51}^{nl1} & \bar{B}_{t52}^{nl1} & \bar{B}_{t56}^{nl1} \\
A_{t61}^{nl1} & \bar{A}_{t65}^{nl1} & \bar{A}_{t66}^{nl1} & \bar{B}_{t61}^{nl1} & \bar{B}_{t62}^{nl1} & \bar{B}_{t66}^{nl1} \\
0 & \bar{B}_{t51}^{nl1} & \bar{B}_{t61}^{nl1} & 0 & 0 & \bar{D}_{t16}^{nl1} \\
0 & \bar{B}_{t52}^{nl1} & \bar{B}_{62}^{nl1} & 0 & 0 & \bar{D}_{t26}^{nl1} \\
B_{t16}^{nl1} & \bar{B}_{t56}^{nl1} & \bar{B}_{t66}^{nl1} & \bar{D}_{t61}^{nl1} & \bar{D}_{t62}^{nl1} & \bar{D}_{t66}^{nl1}
\end{bmatrix}
\tag{6.22}
$$

where the overbar indicates terms with material coupling. The detailed expressions of these terms are,

$$
A_{t15}^{nl1} = A_{t51}^{nl1} = \upsilon_{,x}^{0}\oint A_{11}ds - \theta_{,x}\oint\left(A_{11}r_{\zeta}^{0}+B_{11}\right)ds
$$

$$
A_{t16}^{nl1} = A_{t61}^{nl1} = w_{,x}^{0}\oint A_{11}ds + \theta_{,x}\oint A_{11}r_{s}^{0}ds
\tag{6.23}
$$

$$
\begin{aligned}
\bar{A}_{t55}^{nl1} = &\, u_{,x}^{0}\oint A_{11}ds + \upsilon_{,x}^{0}\oint 3A_{16}y_{,s}^{0}ds + w_{,x}^{0}\oint A_{16}z_{,s}^{0}ds \\
&+\beta_{y}\oint\left(A_{11}z^{0}+B_{11}y_{,s}^{0}\right)ds + \beta_{y}\oint A_{16}z_{,s}^{0}ds + \beta_{z}\oint\left(A_{11}y^{0}-B_{11}z_{,s}^{0}\right)ds + \beta_{z}\oint A_{16}y_{,s}^{0}ds \\
&-\theta_{,x}\oint\left(2A_{16}y_{,s}^{0}r_{\zeta}^{0}+2B_{16}y_{,s}^{0}\right)ds - \theta_{,x}\oint\left(A_{16}A_{h}+2B_{16}\right)ds
\end{aligned}
$$

$$\bar{A}^{nl1}_{t56} = \bar{A}^{nl1}_{t65} = v^0_{,x}\oint A_{16} z^0_{,s} ds + w^0_{,x}\oint A_{16} y^0_{,s} ds - \theta_{,x}\oint \left(A_{16} z^0_{,s} r^0_\zeta + B_{16} z^0_{,s}\right) ds + \theta_{,x}\oint A_{16} y^0_{,s} r^0_s ds$$

$$\begin{aligned}\bar{A}^{nl1}_{t66} &= u^0_{,x}\oint A_{11} ds + v^0_{,x}\oint A_{16} y^0_{,s} ds + w^0_{,x}\oint 3A_{16} z^0_{,s} ds \\ &+\beta_y\oint \left(A_{11} z^0 + B_{11} y^0_{,s}\right) ds + \beta_y\oint A_{16} z^0_{,s} ds + \beta_z\oint \left(A_{11} y^0 - B_{11} z^0_{,s}\right) ds + \beta_z\oint A_{16} y^0_{,s} ds \\ &+\theta_{,x}\oint 2A_{16} z^0_{,s} r^0_s ds - \theta_{,x}\oint \left(A_{16} A_h + 2B_{16}\right) ds\end{aligned}$$

$$B^{nl1}_{t16} = -v^0_{,x}\oint \left(A_{11} r^0_\zeta + B_{11}\right) ds + w^0_{,x}\oint A_{11} r^0_s ds + \theta^0_{,x}\oint \left(A_{11}\left(r^{0^2}_\zeta + r^{0^2}_s\right) + 2B_{11} r^0_\zeta + D_{11}\right) ds$$

$$\begin{aligned}\bar{B}^{nl1}_{t51} &= v^0_{,x}\oint \left(A_{11} z^0 + B_{11} y^0_{,s}\right) ds + v^0_{,x}\oint A_{16} z^0_{,s} ds \\ &-\theta_{,x}\oint \left(A_{11} z^0 r^0_\zeta + B_{11}\left(y^0_{,s} r^0_\zeta + z^0\right) + D_{11} y^0_{,s}\right) ds - \theta_{,x}\oint \left(A_{16} z^0_{,s} r^0_\zeta + B_{16} z^0_{,s}\right) ds\end{aligned}$$

$$\begin{aligned}\bar{B}^{nl1}_{t52} &= v^0_{,x}\oint \left(A_{11} y^0 - B_{11} z^0_{,s}\right) ds + v^0_{,x}\oint A_{16} y^0_{,s} ds \\ &-\theta_{,x}\oint \left(A_{11} y^0 r^0_\zeta - B_{11}\left(z^0_{,s} r^0_\zeta - y^0\right) - D_{11} z^0_{,s}\right) ds - \theta_{,x}\oint \left(A_{16} y^0_{,s} r^0_\zeta + B_{16} y^0_{,s}\right) ds\end{aligned}$$

$$\begin{aligned}\bar{B}^{nl1}_{t56} &= -u^0_{,x}\oint \left(A_{11} r^0_\zeta + B_{11}\right) ds - v^0_{,x}\oint \left(2A_{16} y^0_{,s} r^0_\zeta + 2B_{16} y^0_{,s}\right) ds - v^0_{,x}\oint \left(A_{16} A_h + 2B_{16}\right) ds \\ &-w^0_{,x}\oint \left(A_{16} z^0_{,s} r^0_\zeta + B_{16} z^0_{,s}\right) ds + w^0_{,x}\oint \left(A_{16} y^0_{,s} r^0_s\right) ds \\ &-\beta_y\oint \left(A_{11} z^0 r^0_\zeta + B_{11}\left(y^0_{,s} r^0_\zeta + z^0\right) + D_{11} y^0_{,s}\right) ds - \beta_y\oint \left(A_{16} z^0_{,s} r^0_\zeta + B_{16} z^0_{,s}\right) ds \\ &-\beta_z\oint \left(A_{11} y^0 r^0_\zeta - B_{11}\left(z^0_{,s} r^0_\zeta - y^0\right) - D_{11} z^0_{,s}\right) ds - \beta_z\oint \left(A_{16} y^0_{,s} r^0_\zeta + B_{16} y^0_{,s}\right) ds \\ &+\theta_{,x}\oint \left(2A_{16} A_h r^0_\zeta + 2B_{16}\left(2r^0_\zeta + A_h\right) + 4D_{16}\right) ds + \theta_{,x}\oint \left(A_{16} y^0_{,s}\left(r^{0^2}_\zeta + r^{0^2}_s\right) + 2B_{16} y^0_{,s} r^0_\zeta + D_{16} y^0_{,s}\right) ds \\ &+\theta_{,x}\oint \left(A_{16} A_h r^0_\zeta + B_{16}\left(2r^0_\zeta + A_h\right) + 2D_{16}\right) ds + \theta_{,x}\oint \left(\frac{1}{2} A_{16} y^0_{,s}\left(r^{0^2}_\zeta + r^{0^2}_s\right) + B_{16} y^0_{,s} r^0_\zeta + \frac{1}{2} D_{16} y^0_{,s}\right) ds\end{aligned} \tag{6.24}$$

$$\bar{B}^{nl1}_{t61} = w^0_{,x}\oint \left(A_{11} z^0 + B_{11} y^0_{,s}\right) ds + w^0_{,x}\oint A_{16} z^0_{,s} ds + \theta_{,x}\oint \left(A_{11} z^0 r^0_s + B_{11} y^0_{,s} r^0_s\right) ds + \theta_{,x}\oint A_{16} z^0_{,s} r^0_s ds$$

$$\bar{B}^{nl1}_{t62} = w^0_{,x}\oint \left(A_{11} y^0 - B_{11} z^0_{,s}\right) ds + w^0_{,x}\oint A_{16} y^0_{,s} ds + \theta_{,x}\oint \left(A_{11} y^0 r^0_s - B_{11} z^0_{,s} r^0_s\right) ds + \theta_{,x}\oint A_{16} y^0_{,s} r^0_s ds$$

$$\begin{aligned}\bar{B}^{nl1}_{t66} &= u^0_{,x}\oint A_{11} r^0_s ds + v^0_{,x}\oint A_{16} y^0_{,s} r^0_s ds - v^0_{,x}\oint \left(A_{16} z^0_{,s} r^0_\zeta + B_{16} z^0_{,s}\right) ds \\ &-w^0_{,x}\oint \left(A_{16} A_h + 2B_{16}\right) ds + w^0_{,x}\oint 2A_{16} z^0_{,s} r^0_s ds \\ &+\beta_y\oint \left(A_{11} z^0 r^0_s + B_{11} y^0_{,s} r^0_s\right) ds + \beta_y\oint A_{16} z^0_{,s} r^0_s ds \\ &+\beta_z\oint \left(A_{11} y^0 r^0_s - B_{11} z^0_{,s} r^0_s\right) ds + \beta_z\oint A_{16} y^0_{,s} r^0_s ds \\ &-\theta_{,x}\oint \left(2A_{16} A_h r^0_s + 4B_{16} r^0_s\right) ds + \theta_{,x}\oint \left(A_{16} z^0_{,s}\left(r^{0^2}_\zeta + r^{0^2}_s\right) + 2B_{16} z^0_{,s} r^0_\zeta + D_{16} z^0_{,s}\right) ds\end{aligned}$$

$$\begin{aligned}\bar{D}_{t16}^{nl1} = \bar{D}_{t61}^{nl1} &= -v_{,x}^0 \oint \left(A_{11} z^0 r_\zeta^0 + B_{11} \left(z^0 + y_{,s}^0 r_\zeta^0 \right) + D_{11} y_{,s}^0 \right) ds - v_{,x}^0 \oint \left(A_{16} z_{,s}^0 r_\zeta^0 + B_{16} z_{,s}^0 \right) ds \\ &+ w_{,x}^0 \oint \left(A_{11} z^0 r_s^0 + B_{11} y_{,s}^0 r_s^0 \right) ds + w_{,x}^0 \oint A_{16} z_{,s}^0 r_s^0 ds \\ &+ \theta_{,x} \oint \left(A_{11} z^0 \left(r_\zeta^{0^2} + r_s^{0^2} \right) + B_{11} \left(2 z^0 r_\zeta^0 + y_{,s}^0 \left(r_\zeta^{0^2} + r_s^{0^2} \right) \right) + D_{11} \left(z^0 + 2 y_{,s}^0 r_\zeta^0 \right) \right) ds \\ &+ \theta_{,x} \oint \left(A_{16} z_{,s}^0 \left(r_\zeta^{0^2} + r_s^{0^2} \right) + 2 B_{16} z_{,s}^0 r_\zeta^0 + D_{16} z_{,s}^0 \right) ds \end{aligned}$$

$$\begin{aligned}\bar{D}_{t26}^{nl1} = \bar{D}_{t62}^{nl1} &= -v_{,x}^0 \oint \left(A_{11} y^0 r_\zeta^0 - B_{11} \left(z_{,s}^0 r_\zeta^0 - y^0 \right) - D_{11} z_{,s}^0 \right) ds - v_{,x}^0 \oint \left(A_{16} y_{,s}^0 r_\zeta^0 + B_{16} y_{,s}^0 \right) ds \\ &+ w_{,x}^0 \oint \left(A_{11} y^0 r_s^0 - B_{11} z_{,s}^0 r_s^0 \right) ds + w_{,x}^0 \oint A_{16} y_{,s}^0 r_s^0 ds \\ &+ \theta_{,x} \oint \left(A_{11} y^0 \left(r_\zeta^{0^2} + r_s^{0^2} \right) + B_{11} \left(2 y^0 r_\zeta^0 - z_{,s}^0 \left(r_\zeta^{0^2} + r_s^{0^2} \right) \right) + D_{11} \left(y^0 - 2 z_{,s}^0 r_\zeta^0 \right) \right) ds \\ &+ \theta_{,x} \oint \left(A_{16} y_{,s}^0 \left(r_\zeta^{0^2} + r_s^{0^2} \right) + 2 B_{16} y_{,s}^0 r_\zeta^0 + D_{16} y_{,s}^0 \right) ds \end{aligned} \tag{6.25}$$

$$\begin{aligned}\bar{D}_{t66}^{nl1} &= u_{,x}^0 \oint \left(A_{11} \left(r_\zeta^{0^2} + r_s^{0^2} \right) + 2 B_{11} r_\zeta^0 + D_{11} \right) ds \\ &+ v_{,x}^0 \oint \left(A_{16} y_{,s}^0 \left(r_\zeta^{0^2} + r_s^{0^2} \right) + 2 B_{16} y_{,s}^0 + D_{16} y_{,s}^0 \right) ds + v_{,x}^0 \oint \left(2 A_{16} A_h r_\zeta^0 + 2 B_{16} \left(2 r_\zeta^0 + A_h \right) + 4 D_{16} \right) ds \\ &+ w_{,x}^0 \oint \left(A_{16} z_{,s}^0 \left(r_\zeta^{0^2} + r_s^{0^2} \right) + 2 B_{16} z_{,s}^0 r_\zeta^0 + D_{16} z_{,s}^0 \right) ds - w_{,x}^0 \oint \left(2 A_{16} A_h r_s^0 ds + 4 B_{16} r_s^0 \right) ds \\ &+ \beta_y \oint \left(A_{11} z^0 \left(r_\zeta^{0^2} + r_s^{0^2} \right) + B_{11} \left(2 z^0 r_\zeta^0 + y_{,s}^0 \left(r_\zeta^{0^2} + r_s^{0^2} \right) \right) + D_{11} \left(z^0 + 2 y_{,s}^0 r_\zeta^0 \right) \right) ds \\ &+ \beta_y \oint \left(A_{16} z_{,s}^0 \left(r_\zeta^{0^2} + r_s^{0^2} \right) + 2 B_{16} z_{,s}^0 r_\zeta^0 + D_{16} z_{,s}^0 \right) ds \\ &+ \beta_z \oint \left(A_{11} y^0 \left(r_\zeta^{0^2} + r_s^{0^2} \right) + B_{11} \left(2 y^0 r_\zeta^0 - z_{,s}^0 \left(r_\zeta^{0^2} + r_s^{0^2} \right) \right) + D_{11} \left(y^0 - 2 z_{,s}^0 r_\zeta^0 \right) \right) ds \\ &+ \beta_z \oint \left(A_{16} y_{,s}^0 \left(r_\zeta^{0^2} + r_s^{0^2} \right) + 2 B_{16} y_{,s}^0 r_\zeta^0 + D_{16} y_{,s}^0 \right) ds \\ &- \theta_{,x} \oint \left(3 A_{16} A_h \left(r_\zeta^{0^2} + r_s^{0^2} \right) + 6 B_{16} \left(r_\zeta^{0^2} + r_s^{0^2} + A_h r_\zeta^0 \right) + 6 D_{16} \left(4 r_\zeta^0 + A_h \right) \right) ds \end{aligned}$$

Similarly, $\left[\mathbf{K}_{\mathbf{Ts_2}} \right]$ refers to the second-order nonlinear stiffness matrix,

$$\left[\mathbf{K}_{\mathbf{Ts_2}} \right] = \begin{bmatrix} 0 & 0 & 0 & 0 & 0 & 0 \\ 0 & A_{t55}^{nl2} & A_{t56}^{nl2} & 0 & 0 & B_{t56}^{nl2} \\ 0 & A_{t65}^{nl2} & A_{t66}^{nl2} & 0 & 0 & B_{t66}^{nl2} \\ 0 & 0 & 0 & 0 & 0 & 0 \\ 0 & 0 & 0 & 0 & 0 & 0 \\ 0 & B_{t56}^{nl2} & B_{t66}^{nl2} & 0 & 0 & D_{t66}^{nl2} \end{bmatrix} \tag{6.26}$$

and their respective detailed form is,

$$A_{t55}^{nl2} = v_{,x}^{0^2}\oint\frac{3}{2}A_{11}ds + w_{,x}^{0^2}\oint\frac{1}{2}A_{11}ds - v_{,x}^{0}\theta_{,x}\oint\left(3A_{11}r_\zeta^0 + 3B_{11}\right)ds + w_{,x}^{0}\theta_{,x}\oint A_{11}r_s^0 ds$$
$$+\theta_{,x}^2\oint\left(A_{11}\left(r_\zeta^{0^2} + \frac{1}{2}\left(r_\zeta^{0^2} + r_s^{0^2}\right)\right) + 3B_{11}r_\zeta^0 + 2D_{11}\right)ds$$

$$A_{t56}^{nl2} = A_{t65}^{nl2} = v_{,x}^{0}w_{,x}^{0}\oint A_{11}ds + v_{,x}^{0}\theta_{,x}\oint A_{11}r_s^0 ds - w_{,x}^{0}\theta_{,x}\oint\left(A_{11}r_\zeta^0 + B_{11}z\right)ds - \theta_{,x}^2\oint\left(A_{11}r_\zeta^0 r_s^0 + B_{11}r_s^0\right)ds \quad (6.27)$$

$$A_{t66}^{nl2} = v_{,x}^{0^2}\oint\frac{1}{2}A_{11}ds + w_{,x}^{0^2}\oint\frac{3}{2}A_{11}ds - v_{,x}^{0}\theta_{,x}\oint\left(A_{11}r_\zeta^0 + B_{11}\right)ds + w_{,x}^{0}\theta_{,x}\oint 3A_{11}r_s^0 ds$$
$$+\theta_{,x}^2\oint\left(A_{11}\left(r_s^{0^2} + \frac{1}{2}\left(r_\zeta^{0^2} + r_s^{0^2}\right)\right) + B_{11}r_\zeta^0 + \frac{1}{2}D_{11}\right)ds$$

$$B_{t56}^{nl2} = -v_{,x}^{0^2}\oint\left(\frac{3}{2}A_{11}r_\zeta^0 + \frac{3}{2}B_{11}\right)ds - w_{,x}^{0^2}\oint\left(\frac{1}{2}A_{11}r_\zeta^0 + \frac{1}{2}B_{11}\right)ds + v_{,x}^{0}w_{,x}^{0}\oint A_{11}r_s^0 ds$$
$$+v_{,x}^{0}\theta_{,x}\oint\left(A_{11}\left(2r_\zeta^{0^2} + \left(r_\zeta^{0^2} + r_s^{0^2}\right)\right) + 6B_{11}r_\zeta^0 + 3D_{11}\right)ds - w_{,x}^{0}\theta_{,x}\oint\left(2A_{11}r_\zeta^0 r_s^0 + 2B_{11}r_s^0\right)ds$$
$$-\theta_{,x}^2\oint\left(\frac{3}{2}A_{11}r_\zeta^0\left(r_\zeta^{0^2} + r_s^{0^2}\right) + \frac{3}{2}B_{11}\left(3r_\zeta^{0^2} + r_s^{0^2}\right) + \frac{9}{2}D_{11}r_\zeta^0\right)ds \quad (6.28)$$

$$B_{t66}^{nl2} = v_{,x}^{0^2}\oint\frac{1}{2}A_{11}r_s^0 ds + w_{,x}^{0^2}\oint\frac{3}{2}A_{11}r_s^0 ds - v_{,x}^{0}w_{,x}^{0}\oint\left(A_{11}r_\zeta^0 + B_{11}\right)ds$$
$$-v_{,x}^{0}\theta_{,x}\oint\left(2A_{11}r_\zeta^0 r_s^0 + 2B_{11}r_s^0\right)ds + w_{,x}^{0}\theta_{,x}\oint 2A_{11}r_s^{0^2}ds + w_{,x}^{0}\theta_{,x}\oint\left(A_{11}\left(r_\zeta^{0^2} + r_s^{0^2}\right) + 2B_{11}r_\zeta^0 + D_{11}\right)ds$$
$$+\theta_{,x}^2\oint\left(\frac{3}{2}A_{11}r_s^0\left(r_\zeta^{0^2} + r_s^{0^2}\right) + 3B_{11}r_\zeta^0 r_s^0 + \frac{3}{2}D_{11}r_s^0\right)ds$$

$$D_{t66}^{nl2} = v_{,x}^{0^2}\oint\left(A_{11}\left(r_\zeta^{0^2} + \frac{1}{2}\left(r_\zeta^{0^2} + r_s^{0^2}\right)\right) + 3B_{11}r_\zeta^0 + \frac{3}{2}D_{11}\right)ds$$
$$+w_{,x}^{0^2}\oint\left(\frac{1}{2}A_{11}\left(r_\zeta^{0^2} + r_s^{0^2}\right) + B_{11}r_\zeta^0 + \frac{1}{2}D_{11}\right)ds + w_{,x}^{0^2}\oint A_{11}r_s^{0^2}ds$$
$$-v_{,x}^{0}w_{,x}^{0}\oint\left(2A_{11}r_\zeta^0 r_s^0 + 2B_{11}r_s^0\right)ds - v_{,x}^{0}\theta_{,x}\oint\left(3A_{11}r_\zeta^0\left(r_\zeta^{0^2} + r_s^{0^2}\right) + 3B_{11}\left(3r_\zeta^{0^2} + r_s^{0^2}\right) + 9D_{11}r_\zeta^0\right)ds \quad (6.29)$$
$$+w_{,x}^{0}\theta_{,x}\oint\left(3A_{11}\left(r_\zeta^{0^2} + r_s^{0^2}\right)r_s^0 + 6B_{11}r_\zeta^0 r_s^0 + 3D_{11}r_s^0\right)ds$$
$$+\theta_{,x}^2\oint\left(\frac{3}{2}A_{11}r_\zeta^0\left(r_\zeta^{0^2} + r_s^{0^2}\right) + 6B_{11}r_\zeta^0\left(r_\zeta^{0^2} + r_s^{0^2}\right) + 3D_{11}\left(3r_\zeta^{0^2} + r_s^{0^2}\right)r_\zeta^{0^2}\right)ds$$

In the above Eqs. ((6.14)-(6.29)), $\mathbf{A_{ij}}$, $\mathbf{B_{ij}}$ and $\mathbf{D_{ij}}$ are the extensional, coupling and flexural stiffness matrices of the laminate section, respectively, which have already been defined in Appendix C (Eq. (c.10)).

6.1.4 Nonlinear Damping Cross-Section Terms

The same procedure is followed in order to formulate the expressions of the cross-section damping terms of the composite structure. Combining Eqs. (6.2), (6.6) and

(6.8) and collecting the terms based on their order of nonlinear terms, the dissipated strain of the section takes the form,

$$\delta H_{ds} = \delta H_{ds_0} + \delta H_{ds_1} + \delta H_{ds_2} \tag{6.30}$$

where H_{ds} represents the dissipated energy per unit length of the beam subject to an arbitrary combination of cyclic strain bending curvatures and twisting angles and H_{ds_0}, H_{ds_1}, H_{ds_2} are the cross-section dissipated energy terms, containing linear and nonlinear first- and second-order components, having the form, respectively,

$$\delta H_{ds_0} = \left\{\delta\varepsilon_x^0, \delta\varepsilon_{xz}^0, \delta\varepsilon_{xy}^0, \delta k_{xy}, \delta k_{xz}, \delta k_\theta\right\}\left[\mathbf{C_{ds_0}}\right]\begin{Bmatrix} \dot{u}_{,x}^0 \\ \dot{\varepsilon}_{xz}^0 \\ \dot{\varepsilon}_{xy}^0 \\ \dot{k}_{xy} \\ \dot{k}_{xz} \\ \dot{k}_\theta \end{Bmatrix} \tag{6.31}$$

$$\delta H_{ds_1} = \left\{\delta u_{,x}^0, \delta v_{,x}^0, \delta w_{,x}^0, \delta k_{xy}, \delta k_{xz}, \delta k_\theta\right\}\left[\mathbf{C_{ds_1}}\right]\begin{Bmatrix} \dot{u}_{,x}^0 \\ \dot{v}_{,x}^0 \\ \dot{w}_{,x}^0 \\ \dot{k}_{xy} \\ \dot{k}_{xz} \\ \dot{k}_\theta \end{Bmatrix} \tag{6.32}$$

$$\delta H_{ds_2} = \left\{\delta u_{,x}^0, \delta v_{,x}^0, \delta w_{,x}^0, \delta k_{xy}, \delta k_{xz}, \delta k_\theta\right\}\left[\mathbf{C_{ds_2}}\right]\begin{Bmatrix} \dot{u}_{,x}^0 \\ \dot{v}_{,x}^0 \\ \dot{w}_{,x}^0 \\ \dot{k}_{xy} \\ \dot{k}_{xz} \\ \dot{k}_\theta \end{Bmatrix} \tag{6.33}$$

Each one of them provides the linear and nonlinear loss stiffness terms of the section,

$$\left[\mathbf{C_{ds}}\right]=\left[\mathbf{C_{ds_0}}\right]+\left[\mathbf{C_{ds_1}}\left(u\right)\right]+\left[\mathbf{C_{ds_2}}\left(u^2\right)\right] \tag{6.34}$$

In the above expressions, $\left[\mathbf{C_{ds_0}}\right]$ is the linear laminate damping matrix, previously formulated by Saravanos et. al (2006).

$$\left[\mathbf{C_{ds_0}}\right]=\begin{bmatrix} A^0_{d11} & \bar{A}^0_{d15} & \bar{A}^0_{d16} & B^0_{d11} & B^0_{d12} & \bar{B}^0_{d16} \\ \bar{A}^0_{d51} & A^0_{d55} & A^0_{d56} & \bar{B}^0_{d51} & \bar{B}^0_{d52} & B^0_{d56} \\ \bar{A}^0_{d61} & A^0_{d65} & A^0_{d66} & \bar{B}^0_{d61} & \bar{B}^0_{d62} & B^0_{d66} \\ B^0_{d11} & \bar{B}^0_{d51} & \bar{B}^0_{d61} & D^0_{d11} & D^0_{d12} & \bar{D}^0_{d16} \\ B^0_{d12} & \bar{B}^0_{d52} & \bar{B}^0_{d62} & D^0_{d21} & D^0_{d22} & \bar{D}^0_{d26} \\ \bar{B}^0_{d16} & B^0_{d56} & B^0_{d66} & \bar{D}^0_{d61} & \bar{D}^0_{d62} & D^0_{d66} \end{bmatrix} \tag{6.35}$$

First-Order Nonlinear Damping. The first-order damping matrix, $\left[\mathbf{C_{ds_1}}\right]$ contains nonlinear terms, which imply first-order nonlinear dependence to the generalized section displacements,

$$\left[\mathbf{C_{ds_1}}\right]=\begin{bmatrix} 0 & A^{nl1}_{d15} & A^{nl1}_{d16} & 0 & 0 & B^{nl1}_{d16} \\ A^{nl1}_{d51} & \bar{A}^{nl1}_{d55} & \bar{A}^{nl1}_{d56} & \bar{B}^{nl1}_{d51} & \bar{B}^{nl1}_{d52} & \bar{B}^{nl1}_{d56} \\ A^{nl1}_{d61} & \bar{A}^{nl1}_{d65} & \bar{A}^{nl1}_{d66} & \bar{B}^{nl1}_{d61} & \bar{B}^{nl1}_{d62} & \bar{B}^{nl1}_{d66} \\ 0 & \bar{B}^{nl1}_{d51} & \bar{B}^{nl1}_{d61} & 0 & 0 & \bar{D}^{nl1}_{d16} \\ 0 & \bar{B}^{nl1}_{d52} & \bar{B}^{nl1}_{d62} & 0 & 0 & \bar{D}^{nl1}_{d26} \\ \bar{B}^{nl1}_{d16} & \bar{B}^{nl1}_{d56} & \bar{B}^{nl1}_{d66} & \bar{D}^{nl1}_{d61} & \bar{D}^{nl1}_{d62} & \bar{D}^{nl1}_{d66} \end{bmatrix} \tag{6.36}$$

and their detailed expressions are,

$$A^{nl1}_{d15}=A^{nl1}_{d51}=v^0_{,x}\oint A_{d11}ds-\theta_{,x}\oint\left(A_{d11}r^0_\zeta+B_{d11}\right)ds$$

$$A^{nl1}_{d16}=A^{nl1}_{d61}=w^0_{,x}\oint A_{d11}ds+\theta_{,x}\oint A_{d11}r^0_s ds$$

$$\bar{A}^{nl1}_{d55}=v^0_{,x}\oint 2A_{d16}y^0_{,s}ds-\theta_{,x}\oint\left(2A_{d16}y^0_{,s}r^0_\zeta+2B_{d16}y^0_{,s}\right)ds$$

$$\bar{A}^{nl1}_{d56}=\bar{A}^{nl1}_{d65}=v^0_{,x}\oint A_{d16}z^0_{,s}ds+w^0_{,x}\oint A_{d16}y^0_{,s}ds-\theta_{,x}\oint\left(A_{d16}z^0_{,s}r^0_\zeta+B_{d16}z^0_{,s}\right)ds+\theta_{,x}\oint A_{d16}y^0_{,s}r^0_s ds \tag{6.37}$$

$$\bar{A}^{nl1}_{d66}=w^0_{,x}\oint 2A_{d16}z^0_{,s}ds+\theta_{,x}\oint 2A_{d16}z^0_{,s}r^0_s ds$$

$$B_{d16}^{nl1} = -v_{,x}^0 \oint \left(A_{d11} r_\zeta^0 + B_{d11} \right) ds + w_{,x}^0 \oint A_{d11} r_s^0 ds + \theta_{,x}^0 \oint \left(A_{d11} \left(r_\zeta^{0^2} + r_s^{0^2} \right) + 2B_{d11} r_\zeta^0 + D_{d11} \right) ds$$

$$\begin{aligned} \bar{B}_{d51}^{nl1} &= v_{,x}^0 \oint \left(A_{d11} z^0 + B_{d11} y_{,s}^0 \right) ds + v_{,x}^0 \oint A_{d16} z_{,s}^0 ds \\ &\quad -\theta_{,x} \oint \left(A_{d11} z^0 r_\zeta^0 + B_{d11} \left(y_{,s}^0 r_\zeta^0 + z^0 \right) + D_{d11} y_{,s}^0 \right) ds - \theta_{,x} \oint \left(A_{d16} z_{,s}^0 r_\zeta^0 + B_{d16} z_{,s}^0 \right) ds \end{aligned}$$

$$\begin{aligned} \bar{B}_{d52}^{nl1} &= v_{,x}^0 \oint \left(A_{d11} y^0 - B_{d11} z_{,s}^0 \right) ds + v_{,x}^0 \oint A_{d16} y_{,s}^0 ds \\ &\quad -\theta_{,x} \oint \left(A_{d11} y^0 r_\zeta^0 - B_{d11} \left(z_{,s}^0 r_\zeta^0 - y^0 \right) - D_{d11} z_{,s}^0 \right) ds - \theta_{,x} \oint \left(A_{d16} y_{,s}^0 r_\zeta^0 + B_{d16} y_{,s}^0 \right) ds \end{aligned}$$

$$\begin{aligned} \bar{B}_{d56}^{nl1} &= -v_{,x}^0 \oint \left(A_{d16} A_h + 2B_{d16} \right) ds + w_{,x}^0 \oint A_{d16} y_{,s}^0 r_s^0 ds \\ &\quad +\theta_{,x} \oint \left(A_{d16} y_{,s}^0 \left(r_\zeta^{0^2} + r_s^{0^2} \right) + 2B_{d16} y_{,s}^0 r_\zeta^0 + D_{d16} y_{,s}^0 \right) ds + \theta_{,x} \oint \left(A_{d16} A_h r_\zeta^0 + B_{d16} \left(2r_\zeta^0 + A_h \right) + 2D_{d16} \right) ds \end{aligned}$$

$$\bar{B}_{d61}^{nl1} = w_{,x}^0 \oint \left(A_{d11} z^0 + B_{d11} y_{,s}^0 \right) ds + w_{,x}^0 \oint A_{d16} z_{,s}^0 ds + \theta_{,x} \oint \left(A_{d11} z^0 r_s^0 + B_{d11} y_{,s}^0 r_s^0 \right) ds + \theta_{,x} \oint A_{d16} z_{,s}^0 r_s^0 ds$$

$$\bar{B}_{d62}^{nl1} = w_{,x}^0 \oint \left(A_{d11} y^0 - B_{d11} z_{,s}^0 \right) ds + w_{,x}^0 \oint A_{d16} y_{,s}^0 ds + \theta_{,x} \oint \left(A_{d11} y^0 r_s^0 - B_{d11} z_{,s}^0 r_s^0 \right) ds + \theta_{,x} \oint A_{d16} y_{,s}^0 r_s^0 ds \tag{6.38}$$

$$\begin{aligned} \bar{B}_{d66}^{nl1} &= -v_{,x}^0 \oint \left(A_{d16} z_{,s}^0 r_\zeta^0 + B_{d16} z_{,s}^0 \right) ds - w_{,x}^0 \oint \left(A_{d16} A_h + 2B_{d16} \right) ds + w_{,x}^0 \oint 2A_{d16} z_{,s}^0 r_s^0 ds \\ &\quad -\theta_{,x} \oint \left(A_{d16} A_h r_s^0 + 2B_{d16} r_s^0 \right) ds + \theta_{,x} \oint \left(A_{d16} z_{,s}^0 \left(r_\zeta^{0^2} + r_s^{0^2} \right) + 2B_{d16} z_{,s}^0 r_\zeta^0 + D_{d16} z_{,s}^0 \right) ds \end{aligned}$$

$$\begin{aligned} \bar{D}_{d16}^{nl1} = \bar{D}_{d61}^{nl1} &= -v_{,x}^0 \oint \left(A_{d11} z^0 r_\zeta^0 + B_{d11} \left(z^0 + y_{,s}^0 r_\zeta^0 \right) + D_{d11} y_{,s}^0 \right) ds - v_{,x}^0 \oint \left(A_{d16} z_{,s}^0 r_\zeta^0 + B_{d16} z_{,s}^0 \right) ds \\ &\quad + w_{,x}^0 \oint \left(A_{d11} z^0 r_s^0 + B_{d11} y_{,s}^0 r_s^0 \right) ds + w_{,x}^0 \oint A_{d16} z_{,s}^0 r_s^0 ds \\ &\quad + \theta_{,x} \oint \left(A_{d11} z^0 \left(r_\zeta^{0^2} + r_s^{0^2} \right) + B_{d11} \left(2z^0 r_\zeta^0 + y_{,s}^0 \left(r_\zeta^{0^2} + r_s^{0^2} \right) \right) + D_{d11} \left(z^0 + 2y_{,s}^0 r_\zeta^0 \right) \right) ds \\ &\quad + \theta_{,x} \oint \left(A_{d16} z_{,s}^0 \left(r_\zeta^{0^2} + r_s^{0^2} \right) + 2B_{d16} z_{,s}^0 r_\zeta^0 + D_{d16} z_{,s}^0 \right) ds \end{aligned}$$

$$\begin{aligned} \bar{D}_{d26}^{nl1} = \bar{D}_{d62}^{nl1} &= -v_{,x}^0 \oint \left(A_{d11} y^0 r_\zeta^0 - B_{d11} \left(z_{,s}^0 r_\zeta^0 - y^0 \right) - D_{d11} z_{,s}^0 \right) ds - v_{,x}^0 \oint \left(A_{d16} y_{,s}^0 r_\zeta^0 + B_{d16} y_{,s}^0 \right) ds \\ &\quad + w_{,x}^0 \oint \left(A_{d11} y^0 r_s^0 - B_{d11} z_{,s}^0 r_s^0 \right) ds + w_{,x}^0 \oint A_{d16} y_{,s}^0 r_s^0 ds \\ &\quad + \theta_{,x} \oint \left(A_{d11} y^0 \left(r_\zeta^{0^2} + r_s^{0^2} \right) + B_{d11} \left(2y^0 r_\zeta^0 - z_{,s}^0 \left(r_\zeta^{0^2} + r_s^{0^2} \right) \right) + D_{d11} \left(y^0 - 2z_{,s}^0 r_\zeta^0 \right) \right) ds \\ &\quad + \theta_{,x} \oint \left(A_{d16} y_{,s}^0 \left(r_\zeta^{0^2} + r_s^{0^2} \right) + 2B_{d16} y_{,s}^0 r_\zeta^0 + D_{d16} y_{,s}^0 \right) ds \end{aligned}$$

$$\begin{aligned} \bar{D}_{d66}^{nl1} &= v_{,x}^0 \oint \left(2A_{d16} A_h r_\zeta^0 + 2B_{d16} \left(2r_\zeta^0 + A_h \right) + D_{d16} \right) ds - w_{,x}^0 \oint \left(2A_{d16} A_h r_s^0 ds + 4B_{d16} r_s^0 \right) ds \\ &\quad -\theta_{,x} \oint \left(2A_{d16} A_h \left(r_\zeta^{0^2} + r_s^{0^2} \right) + 4B_{d16} \left(r_\zeta^{0^2} + r_s^{0^2} + A_h r_\zeta^0 \right) + 2D_{d16} \left(4r_\zeta^0 + A_h \right) \right) ds \end{aligned} \tag{6.39}$$

Second-Order Nonlinear Damping. $\left[\mathbf{C}_{\mathbf{ds}_2}\right]$ contains nonlinear damping terms, which imply second-order nonlinear dependence to the generalized section displacements. Eq. (6.40) refers to general form of the second-order damping terms, whereas Eqs. (6.41) - (6.43) include the detailed expressions of each damping cross-section term.

$$\left[\mathbf{C}_{\mathbf{ds}_2}\right]=\begin{bmatrix} 0 & 0 & 0 & 0 & 0 & 0 \\ 0 & A_{d55}^{nl2} & A_{d56}^{nl2} & 0 & 0 & B_{d56}^{nl2} \\ 0 & A_{d65}^{nl2} & A_{d66}^{nl2} & 0 & 0 & B_{d66}^{nl2} \\ 0 & 0 & 0 & 0 & 0 & 0 \\ 0 & 0 & 0 & 0 & 0 & 0 \\ 0 & B_{d56}^{nl2} & B_{d66}^{nl2} & 0 & 0 & D_{d66}^{nl2} \end{bmatrix} \tag{6.40}$$

$$A_{d55}^{nl2}=\upsilon_{,x}^{0^2}\oint A_{d11}ds-\upsilon_{,x}^{0}\theta_{,x}\oint\left(2A_{d11}r_{\zeta}^{0}+2B_{d11}\right)ds+\theta_{,x}^{2}\oint\left(A_{d11}r_{\zeta}^{0^2}+2B_{d11}r_{\zeta}^{0}+D_{d11}\right)ds$$

$$\begin{aligned} A_{d56}^{nl2}=A_{d65}^{nl2}&=\upsilon_{,x}^{0}w_{,x}^{0}\oint A_{d11}ds+\upsilon_{,x}^{0}\theta_{,x}\oint A_{d11}r_{s}^{0}ds-w_{,x}^{0}\theta_{,x}\oint\left(A_{d11}r_{\zeta}^{0}+B_{d11}z\right)ds \\ &-\theta_{,x}^{2}\oint\left(A_{d11}r_{\zeta}^{0}r_{s}^{0}+B_{d11}r_{s}^{0}\right)ds \end{aligned} \tag{6.41}$$

$$A_{d66}^{nl2}=w_{,x}^{0^2}\oint A_{d11}ds+w_{,x}^{0}\theta_{,x}\oint 2A_{d11}r_{s}^{0}ds+\theta_{,x}^{2}\oint A_{d11}r_{s}^{0^2}ds$$

$$\begin{aligned} B_{d56}^{nl2}&=-\upsilon_{,x}^{0^2}\oint\left(A_{d11}r_{\zeta}^{0}+B_{d11}\right)ds+\upsilon_{,x}^{0}w_{,x}^{0}\oint A_{d11}r_{s}^{0}ds \\ &+\upsilon_{,x}^{0}\theta_{,x}\oint\left(A_{d11}\left(r_{\zeta}^{0^2}+\left(r_{\zeta}^{0^2}+r_{s}^{0^2}\right)\right)+4B_{d11}r_{\zeta}^{0}+2D_{d11}\right)ds-w_{,x}^{0}\theta_{,x}\oint\left(A_{d11}r_{\zeta}^{0}r_{s}^{0}+B_{d11}r_{s}^{0}\right)ds \\ &-\theta_{,x}^{2}\oint\left(A_{d11}r_{\zeta}^{0}\left(r_{\zeta}^{0^2}+r_{s}^{0^2}\right)+B_{d11}\left(3r_{\zeta}^{0^2}+r_{s}^{0^2}\right)+3D_{d11}r_{\zeta}^{0}\right)ds \\ B_{d66}^{nl2}&=w_{,x}^{0^2}\oint A_{d11}r_{s}^{0}ds-\upsilon_{,x}^{0}w_{,x}^{0}\oint\left(A_{d11}r_{\zeta}^{0}+B_{d11}\right)ds-\upsilon_{,x}^{0}\theta_{,x}\oint\left(A_{d11}r_{\zeta}^{0}r_{s}^{0}+B_{d11}r_{s}^{0}\right)ds \\ &+w_{,x}^{0}\theta_{,x}\oint A_{d11}r_{s}^{0^2}ds+w_{,x}^{0}\theta_{,x}\oint\left(A_{d11}\left(r_{\zeta}^{0^2}+r_{s}^{0^2}\right)+2B_{d11}r_{\zeta}^{0}+D_{d11}\right)ds \\ &+\theta_{,x}^{2}\oint\left(A_{d11}r_{s}^{0}\left(r_{\zeta}^{0^2}+r_{s}^{0^2}\right)+2B_{d11}r_{\zeta}^{0}r_{s}^{0}+D_{d11}r_{s}^{0}\right)ds \end{aligned} \tag{6.42}$$

$$\begin{aligned} D_{d66}^{nl2}&=\upsilon_{,x}^{0^2}\oint\left(A_{d11}r_{\zeta}^{0^2}+2B_{d11}r_{\zeta}^{0}+D_{d11}\right)ds+w_{,x}^{0^2}\oint A_{d11}r_{s}^{0^2}ds-\upsilon_{,x}^{0}w_{,x}^{0}\oint\left(2A_{d11}r_{\zeta}^{0}r_{s}^{0}+2B_{d11}r_{s}^{0}\right)ds \\ &-\upsilon_{,x}^{0}\theta_{,x}\oint\left(2A_{d11}r_{\zeta}^{0}\left(r_{\zeta}^{0^2}+r_{s}^{0^2}\right)+2B_{d11}\left(3r_{\zeta}^{0^2}+r_{s}^{0^2}\right)+6D_{d11}r_{\zeta}^{0}\right)ds \\ &+w_{,x}^{0}\theta_{,x}\oint\left(2A_{d11}\left(r_{\zeta}^{0^2}+r_{s}^{0^2}\right)r_{s}^{0}+4B_{d11}r_{\zeta}^{0}r_{s}^{0}+2D_{d11}r_{s}^{0}\right)ds \\ &+\theta_{,x}^{2}\oint\left(A_{d11}\left(r_{\zeta}^{0^2}+r_{s}^{0^2}\right)^{2}+4B_{d11}r_{\zeta}^{0}\left(r_{\zeta}^{0^2}+r_{s}^{0^2}\right)+2D_{d11}\left(3r_{\zeta}^{0^2}+r_{s}^{0^2}\right)\right)ds \end{aligned} \tag{6.43}$$

In the above linear and nonlinear damping equations, $\left[\mathbf{A_d}\right]$, $\left[\mathbf{B_d}\right]$ and $\left[\mathbf{D_d}\right]$ are equivalent extensional-shear, coupling and flexural damping matrices of the laminate, respectively, defined in Appendix C (Eq. (c.11)). The overbar, once again, indicates the material coupling damping terms.

First-order nonlinear terms are associated with the effect of rotational stresses on the modal characteristics of composite beams and blades, whereas second-order nonlinear damping terms, are critical in describing the nonlinear damping during the buckling and post-buckling response of composite strips.

6.2 Tubular Nonlinear Damped Beam Finite Element

Although the nonlinear beam finite element includes complex nonlinear stiffness and damping terms, the procedure followed in order to build the total structural matrices of the composite system is identical with those presented in third and fourth chapter. The element has two nodes, with six degrees of freedom per node (Eq. (3.30)) and approximates the strain field with linear shape functions (Eq. (4.35)).

Introduction of the shape functions into the formulation yields the discrete set of system equations at the global coordinate system of the structure. Thereafter, the total effective and tangential stiffness and damping matrices of the element are synthesized. The integrals of the structural terms are calculated using the Gauss integration method at the local coordinate system of the element. So, the necessary transformation both for the shape functions and the integration limits is also applied (Eq. (4.53)). The stiffness, damping and mass matrices of each element have square form with dimensions 12x12,

$$\left[Matrix\right] \mapsto \begin{bmatrix} \left[K\right]_{6x6} & \left[K\right]_{6x6} \\ \left[K\right]_{6x6} & \left[K\right]_{6x6} \end{bmatrix}_{12x12} \tag{6.44}$$

In order to build the final set of system equations, the contribution of each beam element should be taken into account. Thus, supposing that $\mathbf{U}$ represents the vector of the nodal degrees of freedom (DOF) of the total system, the latter may take the following form,

$$\left[\bar{\mathbf{K}}_{\mathbf{T}}\left(\mathbf{U}\right)\right]_{\mathbf{6Qx6Q}}\left\{\Delta\mathbf{U}\right\}_{\mathbf{6Qx1}} = \left[\mathbf{K}\left(\mathbf{U}\right)\right]_{\mathbf{6Qx6Q}}\left\{\mathbf{U}\right\}_{\mathbf{6Qx1}} - \left\{\mathbf{F}\right\}_{\mathbf{6Qx1}} \tag{6.45}$$

where Q indicates the total nodes of the structure, $\left[\bar{\mathbf{K}}_{\mathbf{T}}\right]$ is the tangential stiffness matrix; $\left[\mathbf{K}\right]$ is the effective stiffness matrix and $\mathbf{F}$ is the external forces vector; the number 6 indicates the number of the DOFs at each node of the beam

element. Application of the boundary conditions reduces the dimensions of the final system, which is solved by the Newton-Raphson incremental-iterative technique. The displacement control method could be also applied in problems involving buckling loads for the reasons discussed in the fourth chapter of the current work.

Modal damping

The modal damping is calculated following the same assumptions presented in subsection 5.1 and Eq. (5.2), where the numerical solution of the undamped system provides the undamped modal frequencies and the relative mode shapes of the beam structure.

Thus, based on the composite strip beam finite element, a further updated nonlinear code capable of predicting the static and the damped dynamic response of large composite structures was incorporated into the DAMPBEAM research structural dynamics tool.

6.3 Numerical Evaluation Cases on Box-Section Beams

In the present subsection some evaluation cases concerning the evaluation of the new nonlinear stiffness and damping terms will be presented. To that direction a Carbon/Epoxy box-section beam is considered with various ply angle laminations at its segments. Firstly the static bean response is studied and then the effect of rotational stresses is investigated.

6.3.1 Static Response under Large Loads

Various ply angle configurations as well as support conditions were considered for the Carbon/Epoxy box-section beam, whose material properties have already been shown in Table 3.1 of the third chapter. The length of the beam is 1.0m, while the cross-section dimensions and segment thickness are shown in Figure 3.5a. In the following cases the composite structure was discretized into 20 uniform beam finite elements, which ensured the convergence of the static response and the numerical prediction of the beam structure modal frequency and loss factor values.

6.3.1.1 Hinged-Hinged Beam

The hinged-hinged beam configuration shown in Figure 6.1 is effectively an evaluation case. For the first case a vertical force of F=100N was applied at the midspan of the beam and the vertical displacement along the beam was predicted and correlated with the respective values of the linear finite element code.

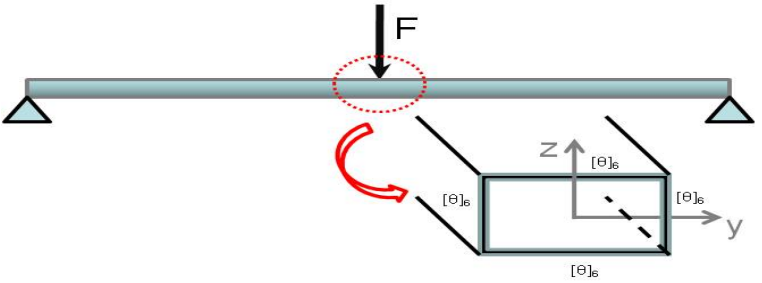

Fig. 6.1 Hinged-hinged Carbon/Epoxy composite box beam

The notable difference between the linear and the nonlinear formulation is illustrated in Figure 6.2, for $\theta=0^0$ and $\theta=45^0$ for all segments of the cross-section. It is obvious that the nonlinear element captures the stiffening of the beam and provides lower transverse displacement values than the linear ones.

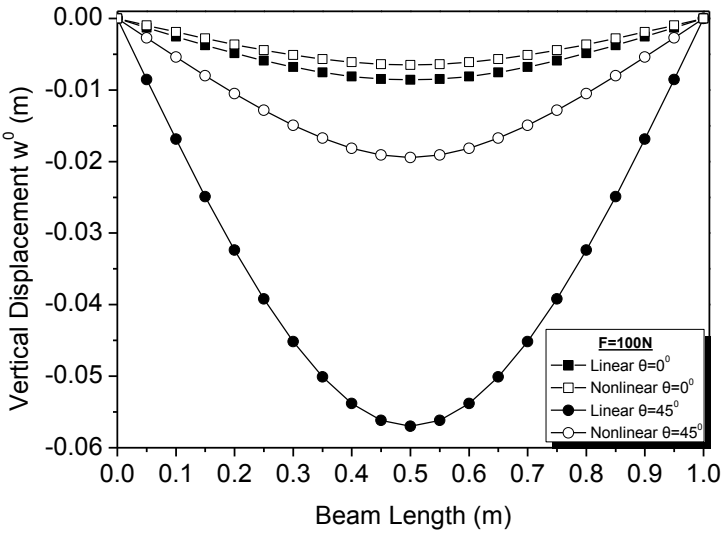

Fig. 6.2 Transverse displacement of the hinged-hinged box beam for linear vs. nonlinear FE code

The effect of nonlinear stiffness terms is better demonstrated in Figure 6.3, where the transverse displacement is plotted for increasing values of the vertical force at the beam midspan. Transverse displacement does not increase in a linear way, but on the contrary, the higher the force, the stiffer becomes the beam structure.

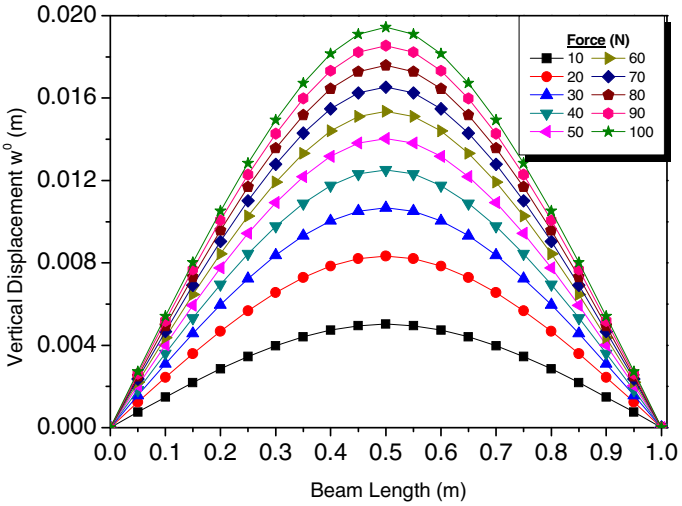

Fig. 6.3 Nonlinear prediction of transverse displacement of the hinged-hinged beam for increasing values of vertical force at its midspan

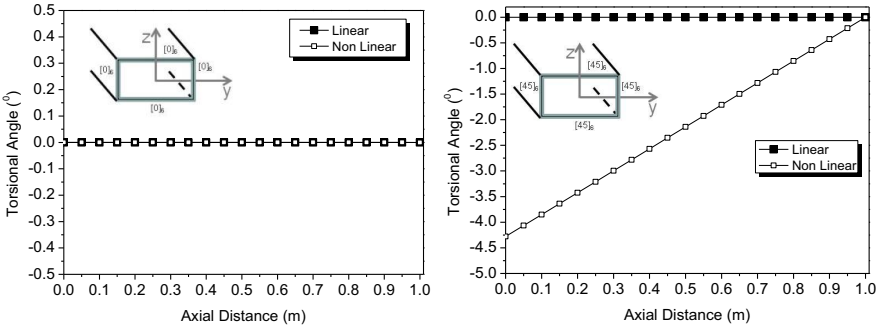

Fig. 6.4 Torsional angle of the hinged-hinged box beam for linear vs. nonlinear finite element code predictions and laminations of: (a) $\theta=0^0$; (b) $\theta=45^0$

The significance of the nonlinear formulation is also outlined by predicting the composite structure twisting angle, something that the linear code fails to do so, as illustrated in Figure 6.4b. For $\theta=0^0$ the twisting terms are deactivated, whereas for $\theta=45^0$ the nonlinear code yields predictions for the twisting angle of the composite beam.

6.3.1.2 Pressure Loaded Clamped-Free Beam

Composite structures, such as helicopter rotors or wind-turbine blades have one end clamped and actually behave as a clamped-free beam structures. To that

direction, evaluation cases on a clamped-free box section beam undergoing large static loads will be further presented. The clamped-free beam configuration is shown in Figure 6.5. The structure subjects to a vertical distributed load of p_0=50N/m along its length and the ply angle of $[45]_6$ was considered for the top and bottom flanges and the right and left shear webs of the cross-section.

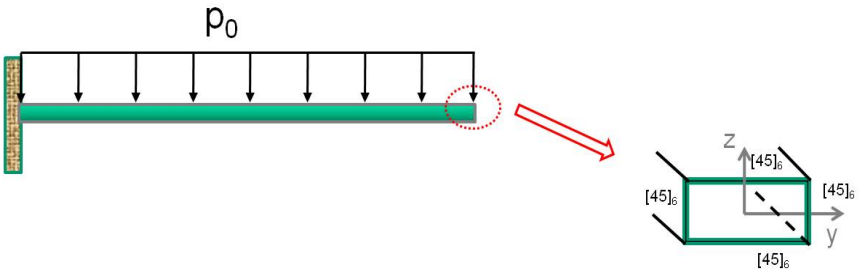

Fig. 6.5 Clamped-free Carbon/Epoxy composite box beam

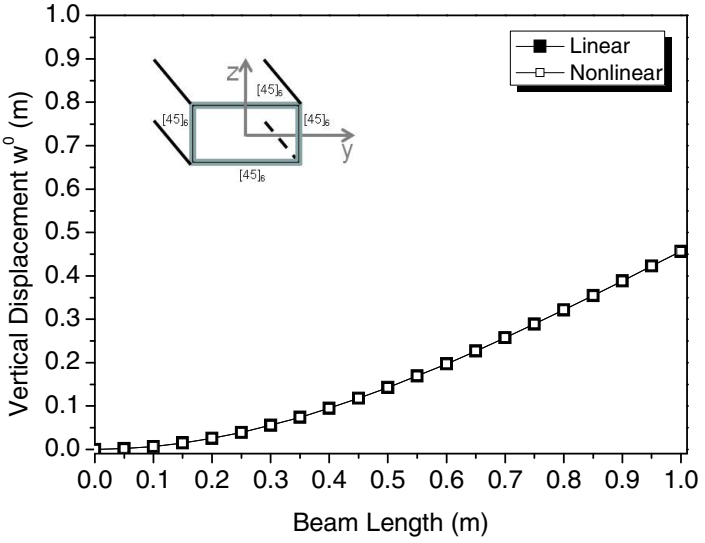

Fig. 6.6 Nonlinear prediction of vertical displacement along the clamped-free beam applying the linear vs. the nonlinear code

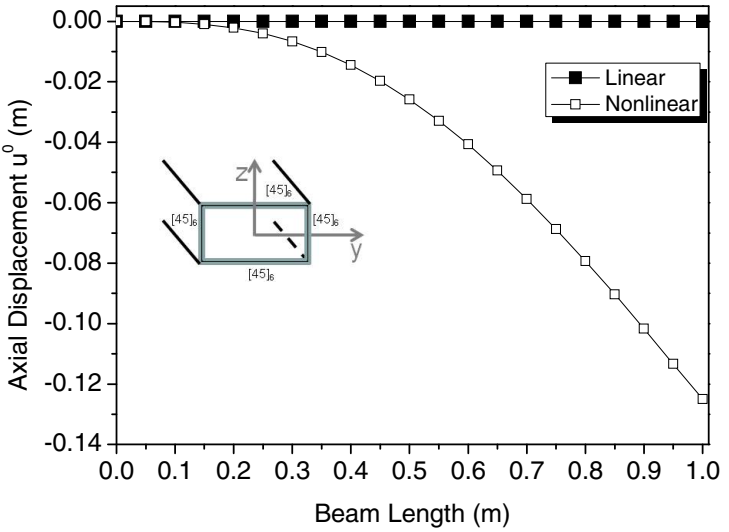

Fig. 6.7 Comparison of axial displacement of the clamped-free beam with linear vs. nonlinear code

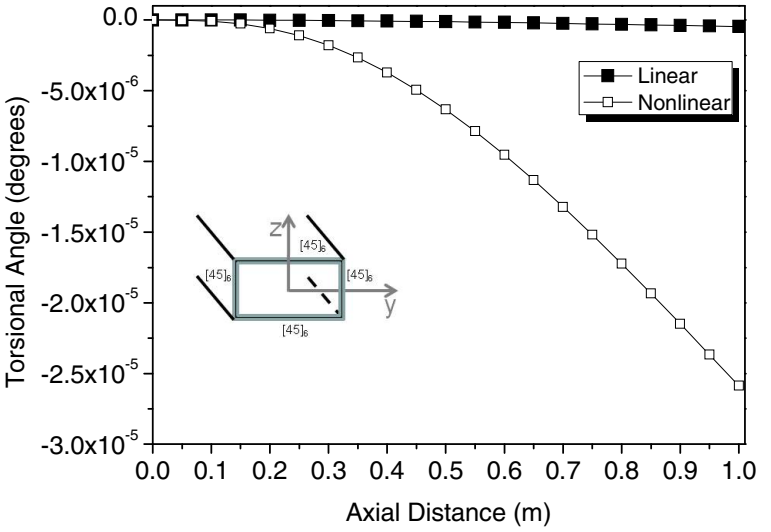

Fig. 6.8 Comparison of torsional angle of the clamped-free beam with linear vs. nonlinear code

Figure 6.6 presents the nodal vertical displacement along the box beam length. It is obvious that vertical displacement follows a linear trend and coincides with the simple linear finite element predictions. That implies that there are no stiffening effects at the clamped-free beam subject to static loading.

The significance of the new nonlinear formulation lies on the prediction of the nodal axial displacement, as well as, of the beam torsion due to resultant nonlinear bending-torsion coupling stiffness terms shown in Eqs. (6.17), (6.21), (6.25) and (6.29). This is better illustrated in Figure 6.7 and Figure 6.8, where the nonlinear finite element calculates a substantial axial displacement and a twisting angle, respectively, whereas the linear code does not provide that capability.

6.3.2 Effect of Rotational Stresses

The importance of non linear section stiffness terms is stronger in the case a clamped-free blade-beam subject to rotational effects due to distributed centrifugal loads. Skin laminations $[0_2/\pm45]_s$ at the upper and lower segment and $[(\pm45)_2]_s$ at the right and left shear web, are considered, typical of helicopter blade configurations. The new nonlinear beam finite element is applied to capture the stiffening of blades loaded by a transverse pressure, due to rotational initial stresses (Figure 6.9).

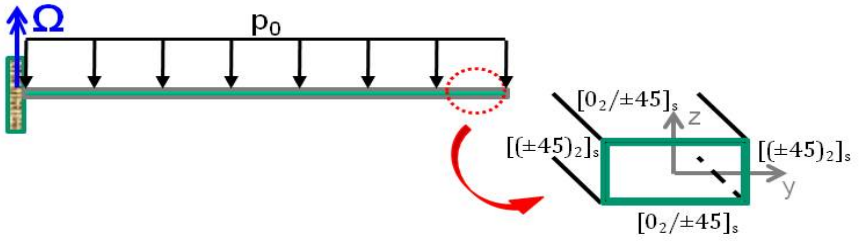

Fig. 6.9 Composite blade-beam subject to rotational stresses and cross-section lamination

The blade-beam has the same elastic and geometric properties like the previous case and the inertial rotational load is consistently discretized on the beam finite element nodes. Figure 6.10 illustrates the effect of angular velocity on the vertical displacement of the rotated clamped-free beam. The higher the angular velocity values the stiffer the beam becomes. The same outcome is obvious in Figure 6.11, where the vertical displacement of the beam nodes decreases for higher values of the angular velocity.

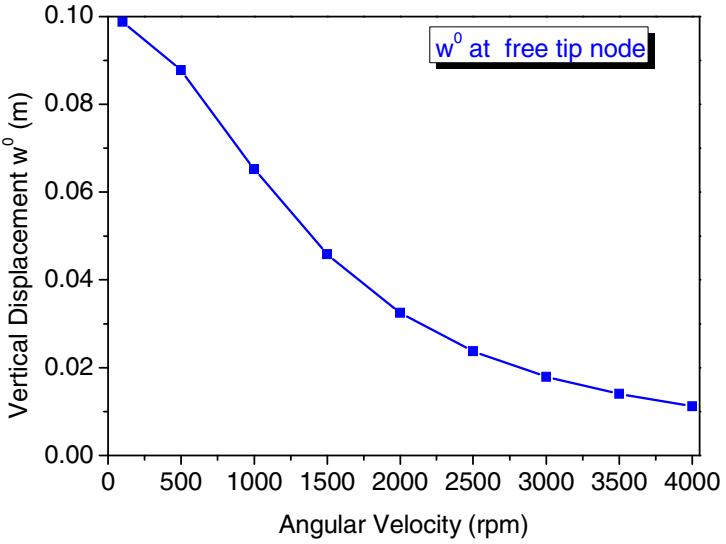

Fig. 6.10 Beam stiffening due to rotational effects

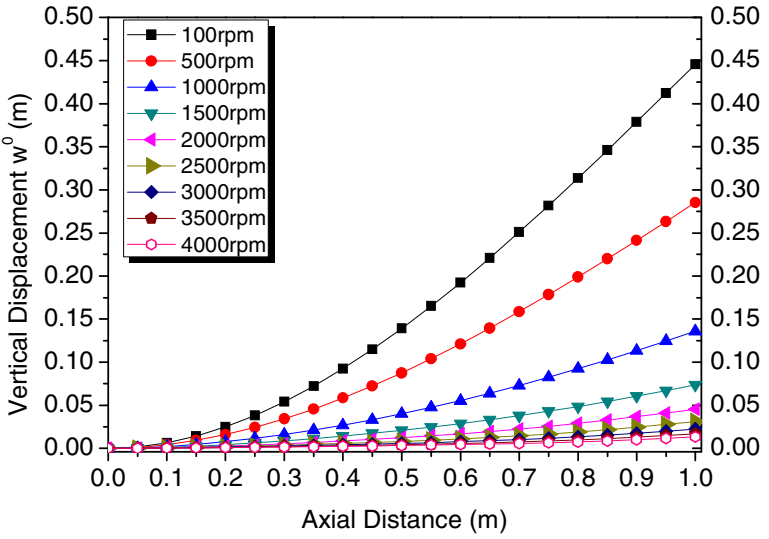

Fig. 6.11 Vertical displacement along beam length for increasing values of angular velocity

The next step of the nonlinear analysis includes the prediction of modal characteristics for the bending and sweeping modes of the beam-blade (Figure 6.9), taking into account only the angular velocity applied on the structure.

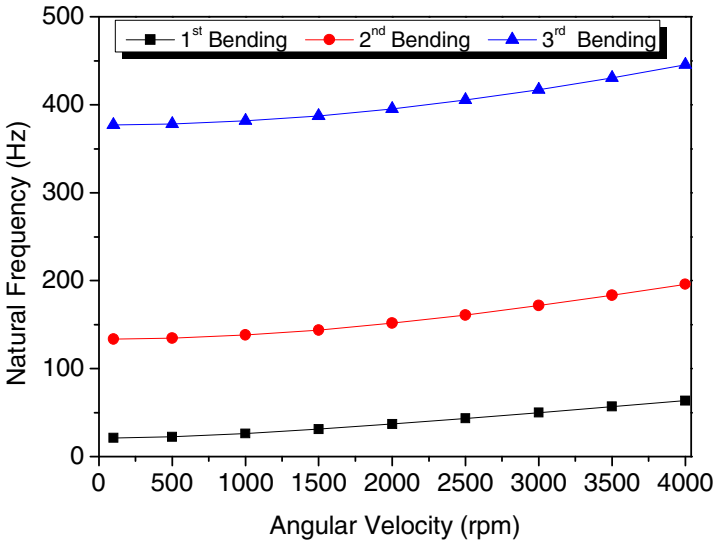

Fig. 6.12 First three bending frequencies for the composite blade with cross-ply lay-up

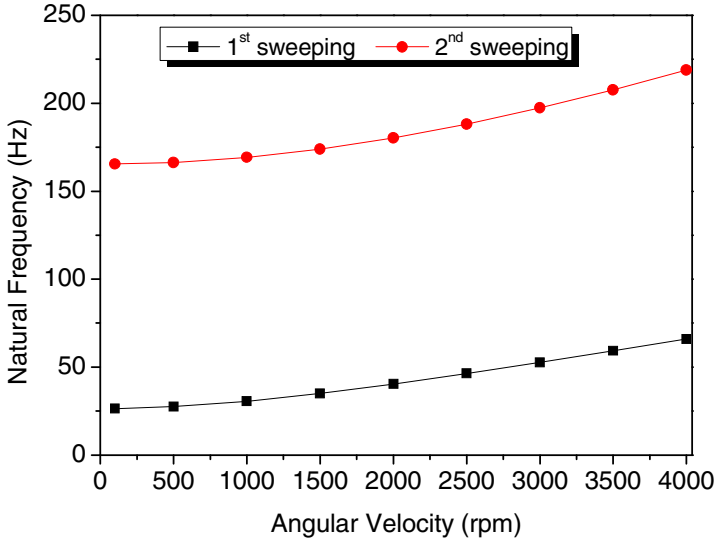

Fig. 6.13 First two sweeping frequencies for the composite blade with cross-ply lay-up

Similarly to the case of composite strip, shown in the fifth chapter, it is obvious that the higher the angular velocity, the higher the modal frequency values become, indicating the stiffening effects on the blade.

The main objective of the new nonlinear damped finite element code is the prediction of nonlinear damping in composite blade structures undergoing large displacements and rotations. This direction also necessitates the prediction of rotational stresses effect on the modal damping of large scale composite beams and blades. The first step was made in fifth chapter, where it was explained that damping is not monotonic and depends on the type of mode shape and the specific section lamination. The same conclusion is obtained by observation of Figure 6.14 and Figure 6.15, where the first three flapping and first two sweeping modal loss factor graphs are presented, respectively. Both figures illustrate that the first flapping and first sweeping modal loss factor curves present a higher sensitivity to rotational stiffening, which is less obvious in higher blade modes. In addition, the dash line in the graphs, indicates the respective modal loss factor values predicted by the linear finite beam element. The respective frequency and damping torsional mode values are omitted due to their low sensitivity to the increasing angular velocity and stiffening of the beam.

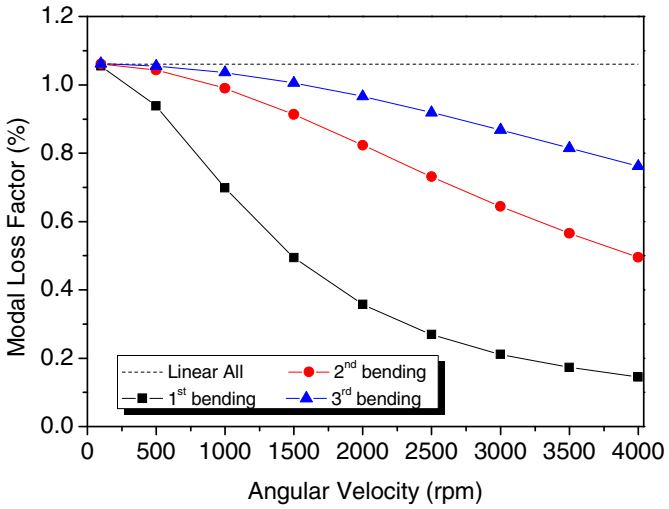

Fig. 6.14 First three bending modal loss factor values for the composite blade with cross-ply lay-up

The latter results set the basis for understanding the damping behavior in complex beams in order to apply the developed nonlinear beam finite element to the simulation of geometric up-scaled structures, such as wind-turbine blades. This will be the topic of the last section of the present chapter.

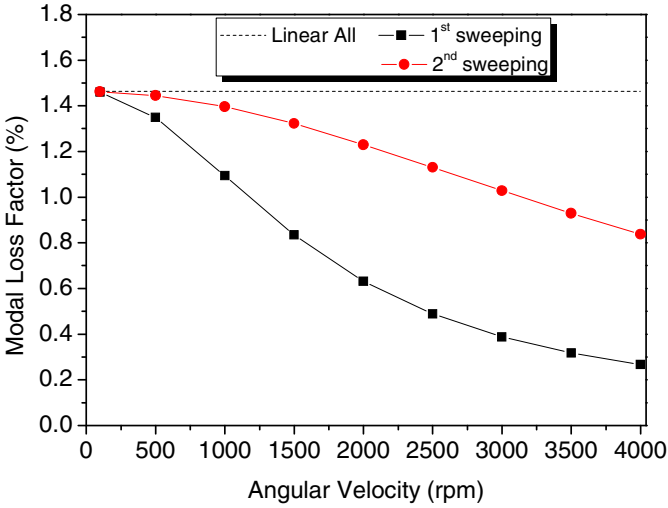

Fig. 6.15 First two sweeping modal loss factor values for the composite blade with cross-ply lay-up

6.4 Modal Analysis of a Girder Box-Section Beam of a 5MW Wind-Turbine Blade

The modal analysis of the UP 61.5m wind-turbine blade, using the linear code, was extensively presented in the third chapter of the book. The main structural part of such blade designs is a box-section beam, the so called "girder box-section beam", which runs along the most part of blade length. The girder beam consists of two girder segments (top end bottom flanges) and two shear webs (right and left flanges) for each cross-section. The girder segments and shear webs size correspond to the girder size and shear webs size, respectively, of the relative UP 61.5m blade model airfoil cross-sections. Details about the geometric data of the girder box-section beam are provided in Appendix E.

The four flanges of the girder beam are considered to be sandwich structures. Likewise the UP 61.5m blade model, each segment has the following laminations (Table 3.7):

- **Girder Segment**: Skins of TRIAX and multiple UD layers, whose number is eliminated with direction from the root to the tip of the blade.
- **Shear Webs**: Sandwich structures with ANGPLY skins and FOAM-2 core, whose thickness decreases towards the beam's tip.

In Figure 6.16, a typical cross-section of the girder box-section beam at 25.2m of wind-turbine blade span, is presented. The $[0^0]$ UD layers increase significantly

the flapping stiffness of the girder flanges and therefore of the whole wind-turbine blade. The shear webs are fabricated by multiple [±45] layers, whose number remains constant along the blade length and foam whose thickness is proportional to each cross-section size.

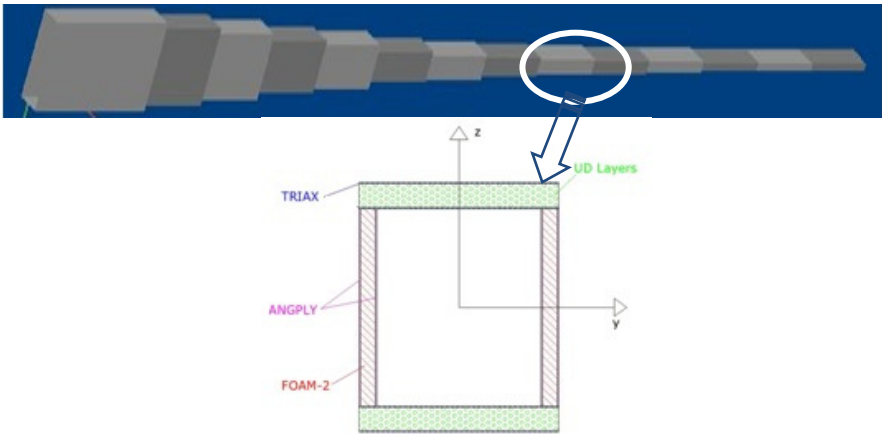

Fig. 6.16 Girder box cross-section variation size and typical cross-section at 25.2m of blade span

The new developed nonlinear code was applied to the small amplitude free-vibration analysis of the girder box-section beam and the calculation of its modal characteristics. The box-beam structure is subjected to gravitational loads and a centrifugal load due to its rotation, both acting on x-axis of the beam (Figure 6.17).

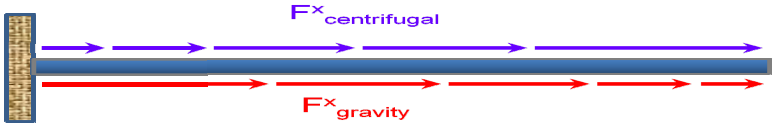

Fig. 6.17 Axial forces applied on the rotating girder box-section beam

The centrifugal force increases with direction from the root to the tip of the blade and the higher the rotation velocity of the beam, the higher its total value becomes. The gravity force does not depend on the rotation velocity and it is proportional to linear blade density (mass/length), hence it is maximum at beam root. This is attributed not only to the large shape of the cross-section but also to the increased material thickness due to the high number of UD Glass/Epoxy plies. Both of them are discretized on beam element nodes using the relations shown in Eqs. (6.46).

$$\left\{\mathbf{F}_{b_e}^{centrifugal}\right\}=\frac{\rho A\Omega^2 L_e}{6}\begin{Bmatrix}3r+L_e\\3r+2L_e\end{Bmatrix}$$

$$\left\{\mathbf{F}_{b_e}^{gravity}\right\}=\frac{\rho gAL_e}{2}\begin{Bmatrix}1\\1\end{Bmatrix} \tag{6.46}$$

where,

$\mathbf{F}_b^{centrifugal}$	is the discretized centrifugal force on each finite element node
$\mathbf{F}_b^{gravity}$	is the discretized gravity force on each finite element node
ρ	is the density of the material
g	is the gravity acceleration
A	is the area of each cross-section covered by material
Ω	is the rotational velocity of the beam
L_e	is the length of each cross-section (element)
r	is the distance of each cross-section from beam root.

The predicted first two flapwise, first sweeping and first torsional natural frequencies of the girder beam are presented in Figure 6.18-Figure 6.20, respectively. It is clear that the higher the angular velocity, the higher the modal frequency values become, indicating the stiffening effects on the blade.

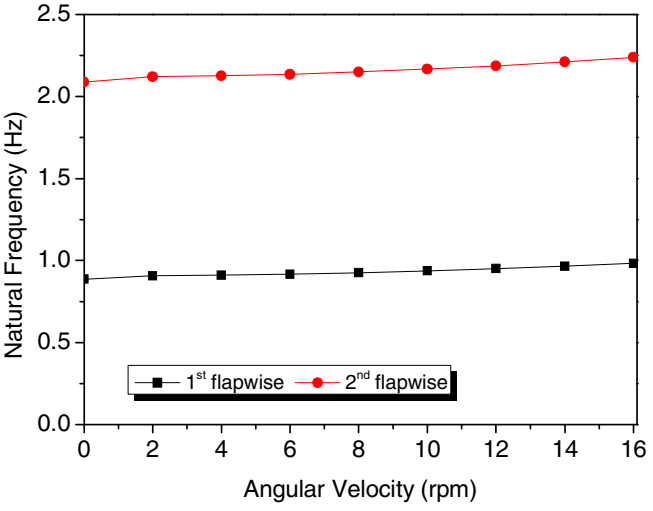

Fig. 6.18 First two flapping natural frequencies of the 54m girder box-section beam

The rotational stresses also effect on the respective modal damping values of the composite girder box-section beam, shown in Figure 6.21-Figure 6.23. Contrary to the natural frequency trends, the nonlinear finite element code predictions present a higher sensitivity in capturing the damping of the rotating composite beam structure.

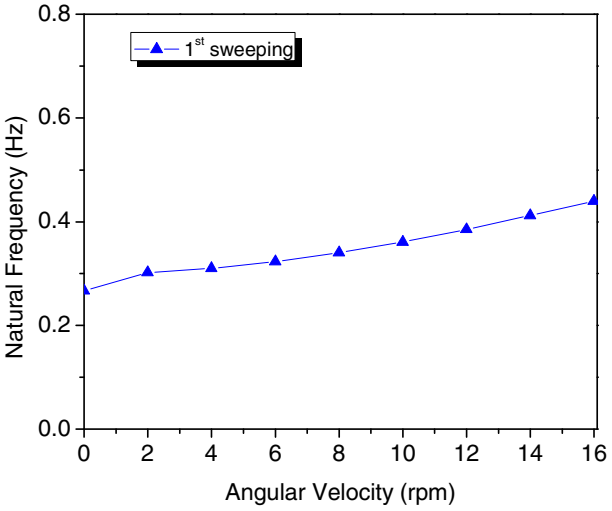

Fig. 6.19 First sweeping natural frequency of the 54m girder box-section beam

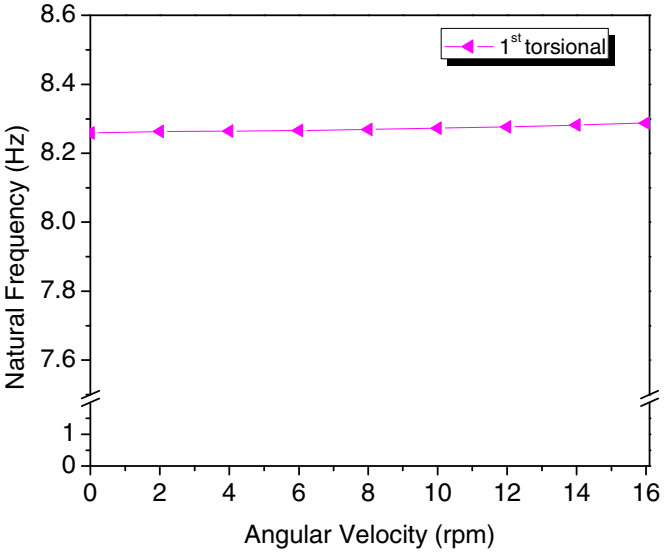

Fig. 6.20 First torsional natural frequency of the 54m girder box-section beam

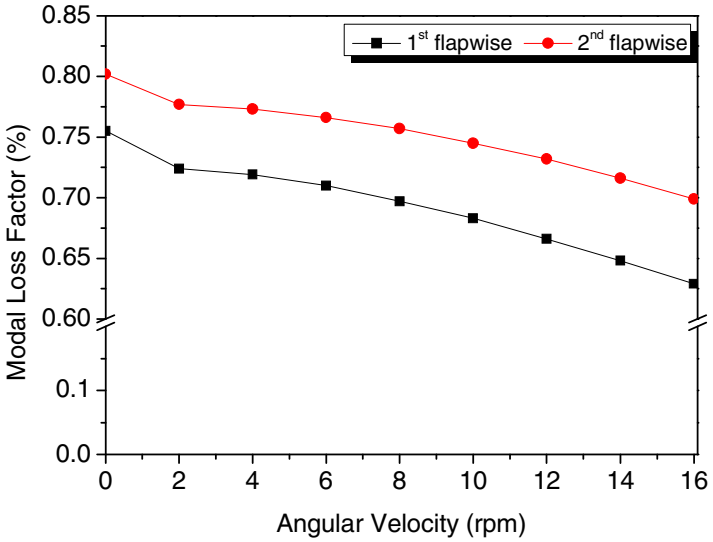

Fig. 6.21 First two bending modal loss factor values of the 54m girder box-section beam

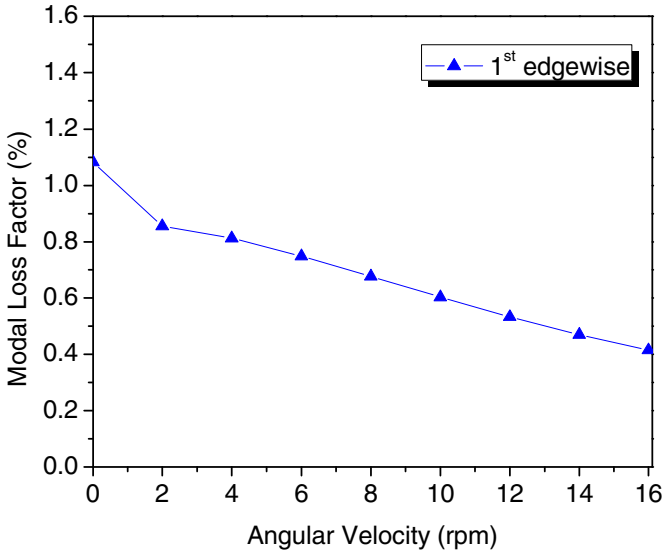

Fig. 6.22 First sweeping modal loss factor of the 54m girder box-section beam

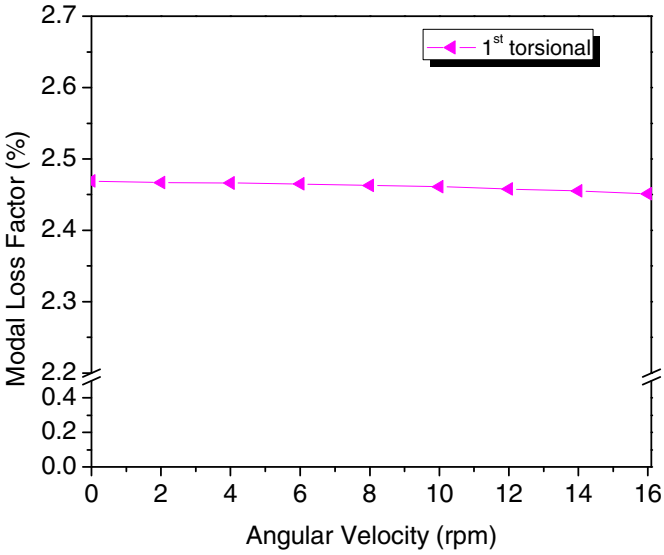

Fig. 6.23 First torsional modal loss factor of the 54m girder box-section beam

The stiffening effect is less severe in the case of the first torsional mode, probably due to the symmetry of box beam cross-sections.

6.5 Conclusions

A new 3-D damped nonlinear beam finite element and a research finite element code were developed and presented with capability to predict the static and damped structural dynamic response of composite beams and blades which undergo large displacements and rotations.

The effect of new nonlinear stiffness and damping terms was evaluated on a box-section beam for various loading cases, which included: large static loads and rotational stresses due to the assumed rotation of the beam. In addition, the small-amplitude free-vibration response of a girder box-section beam undergoing gravitational and centrifugal axial loads was studied and its modal characteristics were predicted for its first bending, sweeping and torsional modes. Based on the obtained numerical results the following major conclusions can be summarized:

- A nonlinear mechanics framework was developed, which provides both the nonlinear effective and tangential first- and second-order section stiffness and damping terms of blade cross-section. The synthesized nonlinear section matrices capture the first- and second-order effect of large static deformations on blade nonlinear behavior.

- Nonlinear blade deflections and damped free-vibrations are predicted. The new nonlinear beam finite element calculates the axial displacement and torsional angle of box-section composite beams with various skin laminations which were neglected by previous linear beam elements.
- The new nonlinear beam element captures the effect of initial stresses on the structural damping of composite blade-beams subject to rotational effects. The nonlinear effect of initial stresses on damping is not monotonic with respect to the linear baseline. The nonlinear damping may be higher or lower depending on the mode shape and laminate configuration.
- The prediction of both natural frequencies and modal loss factors values of composite structures indicates the significant role that nonlinear stiffness and damping terms play on blade nonlinear behavior and demonstrate the value of developed nonlinear structural dynamic model.
- The new 3-D blade element was applied on a "girder beam", which consists the structural part of a large-scale 61.5m wind-turbine blade. The new nonlinear code captures the nonlinear stiffening of the rotating 54m girder box-section beam, undergoing gravity and centrifugal tensional loads. This is demonstrated through the prediction of increased natural frequencies and decreased modal loss factor values as the angular velocity increases.

New Contribution. In the sixth chapter a fully updated version of the so called DAMPBEAM code was developed and its novelty points are:

* The development of a nonlinear damped computational structural dynamic model for the prediction of the nonlinear damping of large beams and blades. New nonlinear stiffness and loss factor cross-section terms are synthesized based on first- and second-order effective and tangential stiffness and damping terms, respectively.
* The nonlinear tubular beam element captures the initial stresses effect on the damping of composite blades subject to rotational effects. The nonlinear effect of initial stresses on damping is not monotonic with respect to the linear baseline. The nonlinear damping may be higher or lower depending on the mode shape and laminate configuration.
* The numerical prediction of the small-amplitude free-vibration response of a 54m girder box-section composite beam subject to tensile gravitational loads and rotational stresses. The stiffening effect on the modal characteristics of the first modes of the girder beam is also evaluated.

Chapter 7

Conclusions and Suggestions for Future Research Topics

This is the closing chapter of the book which presents a brief summary of the conclusions obtained along the current work. It also addresses some open issues and interesting topics for future research, regarding the evolution of the developed nonlinear beam finite element to better describe the structural analysis and structural dynamics of large-scale composite wind-turbine blades.

The manuscript consisted of two main topics concerning the prediction of damping in composite structures of various shapes and geometry. First, the effect of new linear damping coupling terms was quantified by predicting the static and modal characteristics of composite structures with various shapes and geometries. Material coupling effect was incorporated into the linear formulation and new linear damping coupling section terms were developed. Evaluation cases were carried out on box-section composite beams of various ply angle configurations, a small model blade with anti-symmetric lay-up at the top and bottom girder segments and a 19m realistic wind-turbine rotor with girder segments containing rotated plies, thus exhibiting material coupling effects. The capabilities of the complete linear finite element code were also evaluated on the prediction of the cross-sectional properties and modal characteristics of a 61.5m current wind-turbine blade design with complex geometry and lay-up configuration.

Thereafter, the main topic of this work dealt with the development of a theoretical framework for the nonlinear damped analysis of composite strips, beams and blades using the updated version of DAMPBEAM nonlinear finite element code. A damping mechanics and nonlinear structural dynamics formulation was developed enabling the inclusion of nonlinear effects due to in-plane loads and large deformations on both structural stiffness and damping of laminated composite strips. New nonlinear first- and second-order stiffness and damping section terms were formulated, essential for capturing the stiffening effects on vibrating composite beams subject to large deformations. An experimental procedure was set up to measure the modal frequencies and the nonlinear damping of cross-ply composite strips. Correlations cases between experimental measurements and theoretical code predictions gave credence to the developed nonlinear finite element for composite strips. This modeling tool was

D.I. Chortis, *Structural Analysis of Composite Wind Turbine Blades*,
Research Topics in Wind Energy 1,
DOI: 10.1007/978-3-319-00864-6_7, © Springer International Publishing Switzerland 2013

further updated to the direction of modeling the complex nonlinear damped dynamic behavior of slender and more flexible composite structures, such as helicopter and wind-turbine blades.

7.1 General Concluding Remarks

The summary of the most important concluding remarks obtained from the current work are reported in the following paragraphs.

Material Coupling Effect. Numerical comparisons regarding the static and dynamic response of composite box-section beams revealed that the inclusion of coupling terms led to a more compliant structure. The models including material coupling terms exhibited higher displacements and predicted the torsional angle under static loading, whereas their modal analysis calculated lower frequencies and higher damping values with refer to the uncoupled respective model. As far as the small model blade, notable differences in the predictions of modal characteristics were also exhibited for anti-symmetric ply-angle girder laminations $[0_6/(\pm 45)_2]$, when the [0] plies were rotated by an angle θ in the range from $\theta=5^0$ to 45^0. Numerical modal characteristic predictions were correlated well with available experimental data of the Glass/Epoxy small model blade. The next evaluation case concerned the inclusion of new coupling cross-section terms in a realistic 19m wind-turbine blade, which yielded substantial differences in modal damping and frequency predictions between sections with high coupling and the respective ones with negligible ply stiffness and damping coupling terms. The inclusion of material coupling provided significantly improvement of the structural damping behavior of the blade. The linear finite element code was also applied to the prediction of the modal frequency and damping values of a 61.5m wind-turbine blade model. Excellent correlations were achieved regarding the cross-section stiffness and mass properties between the UP blade and available paper case blade numerical results.

Nonlinear Finite Element for Composite Strips. The new nonlinear beam finite element considered the strain-based Kelvin viscoelastic constitutive equation, which subsequently yielded the linear and nonlinear stiffness and damping matrices of the element. Studying of the formulated cross-section nonlinear damping terms revealed that structural damping highly depends on the nonlinear response of the beam. If the beam remains in the linear regime, the flexural damping of the beam is contributed by the flexural damping term, whereas when it enters the nonlinear region strong additional damping terms are introduced which couple flexure and extension. These terms are proportional to the extensional damping term and section rotation. Furthermore, there is a strong effect of lamination lay-up on the structural damping of the composite structure. As the magnitude of the initial load increases, the effect of laminate configuration on

structural damping will be governed mainly by extensional damping terms and less by flexural damping.

Effect of Tensile In-Plane Load. Based on obtained numerical results, it was demonstrated that tension in-plane loads induce significant modal damping reductions, which depend on the mode shape and the laminate configuration of the composite structure and appeared to be monotonic with respect to the linear baseline. The reduction of modal damping with in-plane load depends also on the order of the bending mode, due to the nonlinear behavior of the beam, and seems to be less as the mode order increases. In addition, the new nonlinear damping terms increase the dissipation of strain energy in absolute value and therefore the reduction in damping is caused by the disproportional increase in the stored strain energy due to membrane stiffening effects and not by a decrease in dissipated strain energy. Last, the prediction of both natural frequencies and modal loss factors appeared to correlate very well with experimental measurements, thus demonstrating the value of developed finite element and nonlinear damped structural dynamic models.

Effect of Compressive In-Plane Load. Regarding the in-plane buckling loading case, the inclusion of nonlinear damping and stiffness terms seems essential for predicting the small-amplitude free-vibration response of composite strips in the pre- and post-buckling region. The modal damping increases monotonically in the pre-buckling range, reaches a maximum at the critical load and then decreases in the post-buckling region, where the second-order nonlinear terms dominate the damping. Based on the numerical predictions, the initial imperfection does not change the trend but affects the overall damping values. Consequently, large imperfections tend to yield lower damping and vice versa. The new nonlinear damping terms are proportional to the extensional damping coefficient of the laminate. Depending on the lamination, the contribution may be significant and may exceed the initial flexural damping of the beam. The agreement between predicted results and experimental measurements, for the buckling case, also supports the credibility of the Kelvin viscoelastic strain model, to provide good modal damping predictions of the pre-stressed strip.

Nonlinear Damped Response of Large-Scale Composite Beams and Blades. Taking into account the last statement of the previous paragraph, un updated tubular beam element with six degrees of freedom at each node was developed to better model the damped vibrational response of large beams and blades. To that direction, the complete form of the first- and second-order matrices was presented, regarding both the effective and the linearized matrices of the total system. The new nonlinear beam finite element calculates the axial displacement and torsional angle of box-section composite beams under static loading, whereas the linear finite element code fails to do so. The effect of initial stresses on the structural damping of composite blade-beams subject to rotational effects was also predicted. The nonlinear damping may be higher or lower depending on the mode

shape and laminate configuration, which indicates that the nonlinear effect of initial stresses on damping is not monotonic with respect to the linear baseline. To conclude, the new nonlinear code captures the stiffening of the 54m girder box-section rotating beam, undergoing gravity and centrifugal tensional loads. Increasing natural frequency and decreasing modal loss factor trends were predicted for the first bending, sweeping and torsional mode shapes of the girder beam for increasing values of angular velocity.

7.2 Future Research Topics

During the last years the field of the composite wind-turbine blades has been presenting a rapid evolution. Integrated projects aim to more efficient harvesting of the wind energy through longer and more flexible blade configurations. To that direction, improved modeling tools are continuously required to simulate and predict the complex dynamic and aeroelastic behavior of such composite structures.

The questions the current work has left open may include the following suggested future research topics:

- Integration of the developed nonlinear finite element code with aerodynamic models. This integration will provide a robust aeroelastic formulation which will lead to upgraded predictions of the rotor performance capturing the full potential of the coupled finite element on the prediction of damping of large-scale wind-turbine blades. The multi-disciplinary integration will bring the effects of material coupling, structural damping, and nonlinearity into the aeroelastic and aerodynamic performance prediction, as well as, into the prediction of dynamic stresses and fatigue life of composite blades.
- Evaluation, and subsequent improvement, of the capabilities of the nonlinear beam element to provide quick predictions of the stress, strength and fatigue life of composite blades. This will enable a quick sizing and tailoring of preliminary blade designs and/or upscaling of blade models. It will also lead to a better understanding of the structural response of the blade structure.
- Related to the previous issues, the investigation and optimization of the material coupling effects constitutes another future topic. The understanding of new stiffness and damping coupling terms effect could lead to the tailoring of blade structural properties. Formal optimization can consequently pursued to control the structure large displacements in the flapwise and edgewise direction and optimize aerodynamic loads, aeroelastic performance and fatigue life.
- Improvement of kinematic assumptions by means of considering more generalized deformations of the structure cross-section. An updated beam finite element with an updated number of nodes and nodal degrees of freedom at each node and c^1 continuity shape functions could describe more adequately the displacement field and the cross-section deformations, regarding both the linear and the nonlinear response of composite structures. In the same direction, pre-curved and pre-twisted blades could be considered.

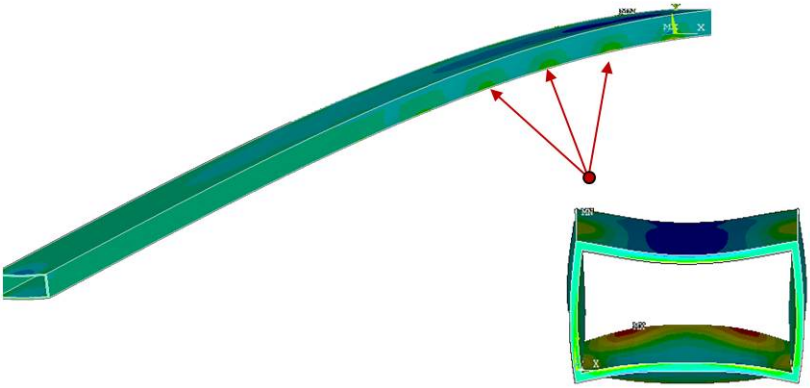

Fig. 7.1 Effect of the local buckling on the ovalization of a composite beam cross-section

- Introduction of more improved and robust viscoelastic models could be considered and evaluated on the prediction of modal damping. New stress-strain constitutive equations could describe more adequately the composite material damping behavior.
- Local blade buckling consists a significant failure mode of large-scale composite structures. New realistic blade designs undergo extreme loading cases, due to gravitational loads and rotational stresses, which affect their functionality and structural integrity. Preliminary results, conducted with a commercial FE code, on a tubular composite beam necessitates additional numerical results for simulating the buckling response of the girder beam (Figure 7.1). A new formulation and beam finite element, introducing the determination of local buckling points and studying the effect of cross-section ovalization and rimpling on the blade static and dynamic response are also steps of high importance.

References

Adams, R.D., Fox, M.A.O., Flood, R.J.L., Friend, R.J., Hewitt, R.L.: Dynamic properties of unidirectional carbon and glass fiber reinforced plastics in torsion and flexure. Journal of Composite Materials 3, 594–603 (1969)

Adams, R.D., Bacon, D.G.C.: Effect of fibre orientation and laminate geometry on the dynamic properties of CFRP. Journal of Composite Materials 7, 402–428 (1973a)

Adams, R.D., Bacon, D.G.C.: Measurement of the flexural damping capacity and dynamic Young's modulus of metals and reinforced plastics. Journal of Physics D: Applied Physics 6(1), 27–41 (1973b)

Alam, N., Asnani, N.T.: Refined vibration and damping analysis of multilayered rectangular plates. Journal of Sound and Vibration 119(2), 347–362 (1987)

Alam, N., Asnani, N.T.: Vibration and damping analysis of fibre reinforced composite material plates. Journal of Composite Materials 20(1), 2–18 (1986)

ANSYS, Academic Research, Release 10.0, Guide, ANSYS, Inc.

Bagley, R.L., Torvik, P.J.: Fractional calculus - a different approach to the analysis of viscoelastically damped structures. AIAA Journal 21(5), 741–748 (1983)

Bagley, R.L., Torvik, P.J.: On the fractional calculus model of viscoelastic behaviour. Journal of Rheology 30(1), 133–155 (1986)

Barbero, E.J., Anido, R.L., Davalos, J.F.: On the mechanics of thin-walled laminated composite beams. Journal of Composite Materials 27(8), 806–829 (1993)

Bathe, K.J.: Finite Element Procedures. Prentice-Hall International, Inc., Englewood Cliffs (1996)

Bathe, K.J., Ramm, E., Wilson, E.: Finite element formulations for large deformation dynamic analysis. International Journal for Numerical Methods in Engineering 9, 353–386 (1975)

Batoz, J.L., Dhatt, G.: Incremental displacement algorithms for nonlinear problems. International Journal for Numerical Methods in Engineering 14(8), 1262–1266 (1979)

Bauchau, O.A., Hong, C.H.: Finite element approach for rotor blades modelling. Journal of the American Helicopter Society 32(1), 60–67 (1987)

Bauchau, O.A., Hong, C.H.: Nonlinear composite beam theory. Journal of Applied Mechanics 55(1), 156–163 (1988)

Bauchau, O.A.: A beam theory for anisotropic materials. Journal of Applied Mechanics 107, 416–422 (1985)

Bauchau, O.A., Bottasso, C.L., Nikishkov, Y.G.: Modeling rotorcraft dynamics with finite element multibody procedures. Mathematical and Computer Modelling 33, 1113–1137 (2001)

Bazoune, A.: Survey on modal frequencies of centrifugally stiffened beams. Shock and Vibration Digest 37, 449–469 (2005)

Berdichevsky, V.L.: Variational-asymptotic method of constructing a theory of shells. Prikladnaya Matematika i Mekkanika 43, 664–687 (1979)

Berdichevsky, V.L.: On the energy of an elastic rod. Prikladnaya Matematika i Mekkanika 45, 518–529 (1981)

Berdichevsky, V.L., Armanios, E.A., Badir, A.M.: Theory of anisotropic thin-walled closed-section beams. Composites Engineering 2(5-7), 411–432 (1992)

Berthelot, J.-M.: Damping analysis of laminated beams and plates using the Ritz method. Composite Structures 74, 186–201 (2006)

Bhaskar, K., Librescu, L.: A geometrically non-linear theory for laminated anisotropic thin-walled beams. International Journal of Engineering Science 33(9), 1331–1344 (1995)

Bhumbla, R., Kosmatka, J.B.: Behavior of spinning pretwisted composite plates using a nonlinear finite element approach. AIAA Journal 34(8), 1686–1695 (1996)

Bicos, S., Springer, G.S.: Vibrational characteristics of composite panels with cutouts. AIAA Journal 28(8), 1116–1122 (1989)

Boutaghou, Z.-E., Erdman, A.G.: On various non-linear rod theories for the dynamic analysis of multi-body systems, Part I: Formulations. Journal of Sound and Vibration 164(2), 207–223 (1993a)

Boutaghou, Z.-E., Erdman, A.G.: On various non-linear rod theories for the dynamic analysis of multi-body systems, Part II: Applications. Journal of Sound and Vibration 164(2), 225–236 (1993b)

Carrera, E., Petrolo, M.: On the effectiveness of higher-order terms in refined beam theories. Journal of Applied Mechanics 78, 021013-1–021013-17 (2011a)

Carrera, E., Petrolo, M., Nali, P.: Unified formulation applied to free vibrations finite element analysis of beams with arbitrary section. Shock and Vibration 18, 485–502 (2011b)

Cawley, P., Adams, R.D.: The predicted and experimental natural modes of free-free CFRP plates. Journal of Composite Materials 12, 336–347 (1978)

Cesnik, C.E.S., Hodges, D.H.: VABS: A new concept for composite rotor bladescross-sectional modeling. Journal of the American Helicopter Society 42, 27–38 (1997)

Cesnik, C.E.S.: Cross-sectional analysis of initially twisted and curved composite beams. PhD Thesis, School of Aerospace Engineering, Georgia Institute of Technology, USA (1994)

Cesnik, C.E.S., Hodges, D.H., Sutyrin, V.G.: Cross-sectional analysis of composite beams including large initial twist and curvature effects. AIAA Journal 34(9), 1913–1920 (1996)

Chandra, R., Chopra, I.: Experimental-theoretical investigation of the vibration characteristics of rotating composite box beams. Journal of Aircraft 29(4), 657–664 (1992)

Chandra, R., Chopra, I.: Structural behaviour of two-cell composite rotor blades with elastic couplings. AIAA Journal 30(12), 2914–2921 (1992)

Chandra, R., Ngo, H., Chopra, I.: Experimental study of thin-walled composite beams. In: American Helicopter Society National Technical Specialist's Meeting on Advanced Rotorcraft Structures, Williamsburg, VA (1989)

Chandra, R., Singh, S.P., Gupta, K.: Damping studies in fiber-reinforced composites - a review. Composite Structures 46, 41–54 (1999)

Chandra, R., Stemple, A.D., Chopra, I.: Thin-walled composite beams under bending, torsional, and extensional loads. Journal of Aircraft 27(7), 619–626 (1990)

Chandrupalta, T.R., Belegundu, A.D.: Introduction to finite elements in engineering. Prentice-Hall, Inc., Englewood Cliffs (1991)

Chang, S., Bert, C.W.: Analysis of damping for filamentary composite materials. In: Composite Materials in Engineering Design (Proceedings of the 6th St. Louis Symposium, St. Louis, May 1972), pp. 51–62. American Society for Metals, Metals Park (1973)

Chaviaropoulos, P.K., Politis, E.S., Lekou, D.J., Sørensen, N.N., Hansen, M.H., Bulder, B.H., Winkelaar, D., Lindenburg, C., Saravanos, D.A., Philippidis, T.P., Galiotis, C., Hansen, M.O.L., Kossivas, T.: Enhancing the damping of wind turbine rotor blades, the DAMPBLADE project. Wind Energy 9(1-2), 163–177 (2006)

Chaviaropoulos, P., Politis, E.S., Sørensen, N.N., Hansen, M., Bulder, B.H., Winkelaar, D., Saravanos, D.A., Philippidis, T., Galiotis, C., Hansen, M.O.L., Kossivas, T.: Recent advances on damped wind turbine rotor blades, the DAMPBLADE project. In: Proceedings of EWEC, Madrid, Spain (2003)

Chortis, D.I., Chrysochoidis, N.A., Saravanos, D.A.: Damped structural dynamics models of large wind-turbine blades including material and structural damping. Journal of Physics: Conference Series 75(012076) (2007)

Chortis, D.I., Chrysochoidis, N.A., Varelis, D.S., Saravanos, D.A.: A damping mechanics model and a beam finite element for the free-vibration of laminated composite strips under in-plane loading. Journal of Sound and Vibration 330(23), 5660–5677 (2011)

Chortis, D.I., Varelis, D.S., Saravanos, D.A.: Prediction of material coupling effect on structural damping of composite beams and blades. Composite Structures 94(5), 1646–1655 (2012)

Chortis, D.I., Varelis, D.S., Saravanos, D.A.: Linearized frequencies and damping in composite laminated beams subject to buckling. Journal of Vibration and Acoustics 135(2), 021006 (2013)

Chrysochoidis, N.: Measurement of damping coefficients of Glass/Polyester composites. MS Thesis, Department of Mechanical Engineering & Aeronautics, University of Patras, Greece (2001)

Crane, R.M., Gillespie Jr., J.W.: Characterization of the vibration damping loss factor of glass and graphite fiber composites. Composites Science and Technology 40, 355–375 (1991)

Crane, R.M., Gillespie Jr., J.W.: Analytical model for prediction of the damping loss factor of composite materials. Polymer Composites 13(3), 179–190 (1992)

DAMPBLADE FP5-ENERGIE Program ENK6 CT2000 00320, Wind turbine rotor blades for enhanced aeroelastic stability and fatigue life using passively damped composites (2006)

Danielson, D.A., Hodges, D.H.: Nonlinear beam kinematics by decomposition of the rotation tensor. Journal of Applied Mechanics 54, 258–262 (1987)

Di Sciuva, M., Icardi, U.: Large deflection of adaptive multilayered Timoshenko beams. Composite Structures 31, 49–60 (1995)

Eldred, L.B., Baker, W.P., Palazotto, A.N.: Kelvin-Voigt vs fractional derivative model as constitutive relations for viscoelastic materials. AIAA Journal 33(3), 547–550 (1995)

Engelstad, S.P., Reddy, J.N., Knight, N.F.: Postbuckling response and failure prediction of graphite-epoxy plates loaded in compression. AIAA Journal 30, 2106–2113 (1992)

Finegan, I.C., Gibson, R.F.: Recent research on enhancement of damping in polymer composites. Composites Structures 44, 89–98 (1999)

Friedmann, Z., Kosmatka, J.B.: An improved two-node Timoshenko beam finite element. Computers and Structures 47(3), 473–481 (1993)

Ganguli, R., Chopra, I.: Aeroelastic optimization of a helicopter rotor with two-cell composite blades. AIAA Journal 34(4), 835–841 (1996)

Giavotto, V., Borri, M., Mantegazza, P., Ghiringhelli, G., Carmaschi, V., Maffioli, G.C., Mussi, F.: Anisotropic beam theory and applications. Computers and Structures 16(1-4), 403–413 (1983)

Gibson, R.F., Plunkett, R.: Dynamic mechanical behavior of fiber-reinforced composites: measurements and analysis. Journal of Composite Materials 10, 325–341 (1976)

Gibson, R.F., Chaturvedi, S.K., Sun, C.T.: Complex moduli of aligned discontinuous fiber reinforced polymer composites. Journal of Materials Science 17, 3499–3509 (1982)

Goezinne, F.: Terms of Reference DOWEC, 176-FG-R0300, DOWEC 10041_000 (2001)
Granick, N., Stern, J.E.: Material Damping of Aluminum by a Resonant - Dwell Technique. NASA Technical Report, Goddard Space Flight Center, USA (1965)
Hashin, Z.: Complex moduli of viscoelastic composites-I. General theory and application to particulate composites. International Journal of Solids and Structures 6, 539–552 (1970)
Hashin, Z.: Complex moduli of viscoelastic composites-II. Fiber reinforced materials. International Journal of Solids and Structures 6, 797–807 (1970)
Hodges, D.H., Dowell, E.H.: Nonlinear equations of motion for the elastic bending and torsion of twisted nonuniform rotor blades. Technical report TN D-7818, NASA, USA (1974)
Hodges, D.H.: Review of composite rotor blade modeling. AIAA Journal 28(3), 561–565 (1990)
Hodges, D.H., Atilgan, A.R., Fulton, M.V., Rehfield, L.W.: Free-vibration analysis of composite beams. Journal of the American Helicopter Society 36(3), 36–47 (1991)
Hodges, D.H., Atilgan, A.R., Cesnik, C.E.S., Fulton, M.V.: On a simplified strain energy function for geometrically nonlinear behaviour of anisotropic beams. Composite Engineering 2(5-7), 513–526 (1992)
Hodges, D.H., Harursampath, D., Volovoi, V.V., Cesnik, C.E.S.: Non-classical effects in non-linear analysis of pretwisted anisotropic strips. International Journal of Non-Linear Mechanics 34, 259–277 (1999)
Hodges, D.H.: Nonlinear composite beam theory. In: Progress in Astronautics and Aeronautics, USA, vol. 213. American Institute of Aeronautics and Astronautics Inc., Virginia (2006)
Hong, C.H., Chopra, I.: Aeroelastic stability of a composite blade. Journal of the American Helicopter Society 30, 57–67 (1985)
Hong, C.H., Chopra, I.: Aeroelastic stability analysis of a composite bearingless rotor blade. Journal of the American Helicopter Society 31, 29–35 (1986)
Houbolt, J.C., Brooks, G.W.: Differential equations of motion for combined flapwise bending, chordwise bending and torsion of twisted nonuniform rotor blades. Report 1346, NACA (Supersedes NACA technical note 3905, 1957), pp. 179–195 (1958)
Hufenbach, W., Holste, C., Kroll, L.: Vibration and damping behaviour of multi-layered composite cylindrical shells. Composite Structures 58, 165–174 (2002)
Hwang, S.J., Gibson, R.F.: The use of strain energy-based finite element techniques in the analysis of various aspects of damping of composite materials and structures. Journal of Composite Materials 26(17), 2585–2605 (1992)
Inman, D.: Damping models. In: Encyclopedia of Vibration, pp. 335–342 (2001), doi:10.1006/rwvb.2001.0060
Ishizaki, T., Bathe, K.-J.: In finite element large displacement and elastic-plastic dynamic analysis of shell structures. Computers and Structures 12, 309–318 (1980)
Jung, S.N., Nagaraj, V.T., Chopra, I.: Refined structural model for thin- and thick-walled composite rotor blades. AIAA Journal 40(1), 105–116 (2002)
Kalfon, J.P., Rand, O.: Nonlinear analysis of composite thin-walled helicopter blades. Computers and Structures 48(1), 51–61 (1993)
Kooijman, H.J.T., Lindenburg, C., Winkelaar, D., Van der Hooft, E.L.: DOWEC 6 MW Pre-Design: Aero-elastic modeling of the DOWEC 6 MW pre-design in PHATAS. ECN-CX–01-135, DOWEC 10046_009, Energy Research Center of the Netherlands, The Netherlands (2003)
Kosmatka, J.B., Friedmann, P.P.: Vibration analysis of composite turbopropellers using a nonlinear beam-type finite-element approach. AIAA Journal 27, 1606–1614 (1989)
Kosmatka, J.B.: On the behavior of pretwisted beams with irregular cross sections. Journal of Applied Mechanics 59(1), 146–152 (1992)

Kosmatka, J.B., Lapid, A.J.: The experimental behavior of spinning pretwisted laminated composite plates. Final report on a research project funded through NASA research grant number NCC 3-173, Report No. SSRP-93/10, University of California, San Diego, USA (1993)

Kosmatka, J.B.: An improved two-node finite element for stability and natural frequencies of axial-loaded Timoshenko beams. Computers and Structures 57(1), 141–149 (1995)

Kosmatka, J.B.: Damping behaviour of initially-stressed beams. In: Proceedings of the 49th AIAA/ASME/ASCE/AHS/ASC Structures, Structural Dynamics, and Materials Conference, Schaumburg, IL, pp. 1–11 (2008)

Kosmatka, J.B.: Damping variations in post-buckled structures having geometric imperfections. In: Proceedings of the 51st AIAA/ASME/ASCE/AHS/ASC Structures, Structural Dynamics, and Materials Conference, Orlando, Florida, pp. 1–7 (2010)

Kunz, D.L.: Survey and comparison of engineering beam theories for helicopter rotor blades. Journal of Aircraft 31(3), 473–479 (1994)

Kunz, D.L.: Multibody system analysis based on Hamilton's weak principle. AIAA Journal 39(12), 2382–2388 (2001)

Lee, D.G., Kosmatka, J.B.: Damping analysis of composite plates with zig-zag triangular element. AIAA Journal 40(6), 1211–1219 (2002)

Leissa, A.W.: A review of laminated composite plate buckling. Applied Mechanics Reviews 40, 575–591 (1987)

Lekou, D.J., Vionis, P., Philippidis, T.P.: Damping characterization of rotor blades by means of full-scale testing. In: Proceedings of EWEC, Copenhagen, Denmark (2001)

Lesieutre, G.A.: Finite elements for dynamic modeling of uniaxial rods with frequency-dependent material properties. International Journal of Solids and Structures 29(12), 1567–1579 (1992)

Lesieutre, G.A.: On the consistency of complex moduli for transversely-isotropic viscoelastic materials. Journal of Composite Materials 28(5), 382–391 (1994)

Lesieutre, G.A.: Damping in FE models. In: Encyclopedia of Vibration, pp. 321–327 (2004)

Lesieutre, G.A.: How membrane loads influence the modal damping of flexural structures. AIAA Journal 47, 1642–1646 (2009)

Lesieutre, G.A.: Frequency-independent modal damping for flexural structures via a viscous "Geometric" damping model. In: Proceedings of the 51st AIAA/ASME/ASCE/AHS/ASC Structures, Structural Dynamics, and Materials Conference, Orlando, FL, pp. 1–11 (2010)

Librescu, L., Song, O.: Thin-Walled Composite Beams, Theory and Application. Springer, The Netherlands (2006)

Librescu, L., Meirovitch, L., Na, S.S.: Control of cantilever vibration via structural tailoring and adaptive materials. AIAA Journal 35, 1309–1315 (1997)

Lin, D.X., Ni, R.G., Adams, R.D.: Prediction and measurement of the vibrational damping parameters of carbon and glass fibre-reinforced plastics plates. Journal of Composite Materials 18, 132–152 (1983)

Lindenburg, C.: Aeroelastic Analysis of the LMH64-5 Blade, ECN-C-03-020 (2003), http://www.ecn.nl

Lindgaard, E., Lund, E.: A unified approach to nonlinear buckling optimization of composite structures. Computers and Structures 89, 357–370 (2011)

Maheri, M.R., Adams, R.D.: Dynamic flexural properties of anisotropic fibrous composite beams. Composites Science and Technology 50, 497–514 (1994)

Maheri, M.R., Adams, R.D.: Finite-element prediction of modal response of damped layered composite panels. Composites Science and Technology 55, 12–23 (1995)

Maheri, M.R.: The effect of layup and boundary conditions on the modal damping of FRP composite panels. Journal of Composite Materials 45(13), 1411–1422 (2010)

Mansfield, E.H., Sobey, A.J.: The fibre composite helicopter blade - Part I: Stiffness properties-Part 2: Prospect for aeroelastic tailoring. Aeronautical Quarterly 30, 413–449 (1979)

Massa, J.C., Barbero, E.J.: A strength of materials formulation for thin walled composite beams with torsion. Journal of Composite Materials 32(17), 1560–1594 (1998)

Mindlin, R.D.: Influence of rotator inertia and shear on flexural motions of isotropic elastic plates. Journal of Applied Mechanics 18, 31–38 (1951)

Nashif, A.D., Jones, D.I.G., Henderson, J.P.: Vibration Damping. John Willey & Sons, Inc., USA (1985)

Ni, R.G., Adams, R.D.: The damping and dynamic moduli of symmetric laminated composite beams - theoretical and experimental results. Journal of Composite Materials 18(2), 104–121 (1984)

Nijssen, R.P.L., et al.: OPTIMAT database, http://www.wmc.eu

Nijssen, R.P.L., de Winkel, G.D., Peeringa, J.M.: WMC5MW laminate lay-out of reference blade for WP3 (2007), http://www.upwind.eu

Oh, S.-Y., Song, O., Librescu, L.: Effects of pretwist and presetting on coupled bending vibrations of rotating thin-walled composite beams. International Journal of Solids and Structures 40(5), 1203–1224 (2003)

Ormiston, R.A., Hodges, D.H.: Linear flap-lag dynamics of hingeless helicopter rotor blades in hover. Journal of the American Helicopter Society 17, 2–14 (1972)

Peeringa, J.M.: Comparison URT and WMC5MW.xls (2007), http://www.upwind.eu

Philippidis, T.P., Vionis, S.P., Lekou, D.J., Fragoulis, A.: Rotor blade design verification by means of full scale testing. In: Proceedings of EWEC, Dublin, Ireland (1997)

Philippidis, T.: Mechanics of composite materials. University of Patras Press, Patras (2002)

Plagianakos, T.S., Saravanos, D.A.: Hybrid multidamped composite plates with viscoelastic composite plies and shunted piezoelectric layers. Journal of Intelligent Material Systems and Structures 14, 57–66 (2003)

Plagianakos, T.S., Saravanos, D.A.: Mechanics and finite elements for the damped dynamic characteristics of curvilinear laminates and composite shell structures. Journal of Sound and Vibration 263(2), 399–414 (2003)

Plagianakos, T.S., Saravanos, D.A.: High-order layerwise mechanics and finite element for the damped dynamic characteristics of sandwich composite beams. International Journal of Solids and Structures 41, 6853–6871 (2004)

Plagianakos, T.S.: Development of mechanics and finite elements for the prediction of damping of composite structures with compliant interlaminar layers and piezoelectric components. PhD Thesis, Polytechnic School, Mechanical Engineering and Aeronautics dept., Patras, Greece (2004)

Plagianakos, T.S., Saravanos, D.A.: High-order layerwise finite element for the damped free-vibrarion response of thick composite and sandwich composite plates. International Journal for Numerical Methods in Engineering 77, 1593–1626 (2009)

Pritz, T.: Analysis of four-parameter fractional derivative model of real solid materials. Journal of Sound and Vibration 195(1), 103–115 (1996)

Qin, Z., Librescu, L.: Static and dynamic validations of a refined thin-walled composite beam model. AIAA Journal 39(12), 2422–2424 (2001)

Qin, Z., Librescu, L.: On a shear-deformable theory of anisotropic thin-walled beams: Further contribution and validations. Composite Structures 56(4), 345–358 (2002)

Reddy, J.N.: Mechanics of laminated composite plates, theory and analysis. CRC Press, Inc., USA (1997)

Reissner, E.: The effect of transverse shear deformation on the bending of elastic plates. Journal of Applied Mechanics 12, 69–77 (1945)

Rikards, R., Chate, A., Korjakin, A.: Vibration and damping analysis of laminated composite plates by the finite element method. Engineering Computations 12, 61–74 (1995)

Riziotis, V.A., Voutsinas, S.G.: GAST: A general aerodynamic and structural prediction tool for wind turbines. In: Proceedings of the EWEC 1997, Dublin, Ireland (1997)

Riziotis, V.A.: Aerodynamic and aeroelastic analysis of stall on wind turbine rotors. PhD Thesis, Mechanical Engineering School, National Technical University of Athens, Greece (2003)

Riziotis, V.A., Voutsinas, S.G.: Advanced aeroelastic modeling of complete wind turbine configurations in view of assessing stability characteristics. In: Proceedings of the EWEC 2006, Athens, Greece (2006)

Rosen, A., Friedmann, P.: Nonlinear Equations of Equilibrium for Elastic Helicopter or Wind Turbine Blades Undergoing Moderate Deformation. Technical report CR-9478, NASA

Saravanos, D.A., Chamis, C.C.: Unified micromechanics of damping for unidirectional and off-axis fiber composites. Journal of Composites Technology & Research 12(1), 31–40 (1990a)

Saravanos, D.A., Chamis, C.C.: Mechanics of damping for fiber composite laminates including hygro-thermal effects. AIAA Journal 28(10), 1813–1819 (1990b)

Saravanos, D.A., Chamis, C.C.: An integrated methodology for optimizing the passive damping of composite structures. Polymer Composites 11(6), 328–336 (1990c)

Saravanos, D.A., Chamis, C.C.: Computational simulation of damping in composite structures. Journal of Reinforced Plastics and Composites 10(3), 256–278 (1991)

Saravanos, D.A., Chamis, C.C.: Integrated mechanics for the passive damping of polymer-matrix composites and composite structures. In: M^3D: Mechanics and Mechanisms of Material Damping, ASTM STP 1169, pp. 471–489. American Society for testing and Materials, Philadelphia (1992a)

Saravanos, D.A., Chamis, C.C.: Multiobjective and material optimazation of composite structures including damping. AIAA Journal 30(3), 805–813 (1992b)

Saravanos, D.A., Pereira, J.M.: Effects of interply damping layers on the dynamic characteristics of composite blades. AIAA Journal 30(12), 2906–2913 (1992)

Saravanos, D.A., Pereira, J.M.: Dynamic characteristics of specialty composite structures with embedded damping layers. Transaction of the ASME 117, 62–69 (1995)

Saravanos, D.A.: Analysis of passive damping in thick composite structures. AIAA Journal 31(8), 1503–1510 (1993)

Saravanos, D.A.: Integrated damping mechanics for thick composite laminates and plates. Journal of Applied Mechanics 61, 375–383 (1994)

Saravanos, D.A., Varelis, D., Plagianakos, T., Chrysochoidis, N., Philippidis, T., Antoniou, A.: Modeling and Design of Composite Wind Turbine Blades for Enhanced Damping. In: European Wind Energy, The science of Making Torque from Wind, Delft, The Netherlands (2004)

Saravanos, D.A., Varelis, D., Plagianakos, T.S., Chrysochoidis, N.: A shear beam finite element for the damping analysis of tubular laminated composite beams. Journal of Sound and Vibration 291, 802–823 (2006)

Schultz, A.B., Tsai, S.W.: Dynamic moduli and damping ratios in fiber-reinforcement composites. Journal of Composite Materials 2, 368–379 (1968)

Schultz, A.B., Tsai, S.W.: Measurements of complex dynamic moduli for laminated fiber-reinforcement composites. Journal of Composite Materials 3, 434–443 (1969)

Shabana, A.: Viscoelastic analysis of multi-body systems using the finite element method. Journal of Sound and Vibration 100(2), 271–284 (1985)

Shabana, A.: Effect of using composites on the dynamic response of multi-body systems. Journal of Sound and Vibration 108(3), 487–502 (1986)

Shabana, A.A.: Flexible multibody dynamics: Review of past and recent developments. Multibody System Dynamics 1, 189–222 (1997)
Singer, J., Arbocz, J., Weller, T.: Buckling experiments: experimental methods in buckling of thin-walled structures, vol. 1. John Wiley & Sons, Inc., USA (1997)
Singh, S.P., Gupta, K.: Damped free vibrations of layered composite cylindrical shells. Journal of Sound and Vivration 172(2), 191–209 (1994)
Smith, E.C., Chopra, I.: Formulation and evaluation of an analytical model for composite box-beams. Journal of the American Helicopter Society 36(3), 23–35 (1991)
Song, O., Librescu, L.: Free vibration of anisotropic composite thin-walled beams of closed cross-section contour. Journal of Sound and Vibration 167(1), 129–147 (1993)
Song, O., Librescu, L.: Anisotropy and structural coupling on vibration and instability of spinning thin-walled beams. Journal of Sound and Vibration 204(3), 477–494 (1997)
Song, O., Jeong, N.H., Librescu, L.: Vibration and stability of pretwisted spinning thin-walled composite beams featuring bending-bending elastic coupling. Journal of Sound and Vibration 237(3), 513–533 (2000)
Starnes Jr., J.H., Rouse, M.: Postbuckling and failure characteristics of selected flat rectangular graphite/epoxy plates loaded in compressions. AIAA Journal 23(8), 1236–1246 (1985)
Stemple, A.D., Lee, S.W.: Finite-element model for composite beams with arbitrary cross-sectional warping. AIAA Journal 26(12), 1512–1520 (1988)
Stemple, A.D., Lee, S.W.: A finite element model for composite beams undergoing large deflection with arbitrary cross-sectional warping. International Journal for Numerical Methods in Engineering 28, 2143–2160 (1989)
Suarez, S.A., Gibson, R.F., Sun, C.T.: The influence of fiber length and fiber orientation on damping and stiffness of polymer composite materials. Experimental Mechanics 26, 175–184 (1986)
Taylor, T.W., Nayfeh, A.H.: Damping characteristics of laminated thick plates. Journal of Applied Mechanics 64(1), 132–138 (1997)
Tedesco, J.W., McDougal, W.G., Ross, C.A.: Structural dynamics: theory and applications. Addison Wesley Longman, Inc., USA (1999)
Torvik, J.P.: On evaluating the damping of a non-linear resonant system. In: Proceedings of the 43rd AIAA/ASME/ASCE/AHS/ASC Structures, Structural Dynamics, and Materials Conference, Denver, Colorado, pp. 1–14 (2002)
Torvik, J.P.: On estimating system damping from frequency response bandwidths. Journal of Sound and Vibration 330, 6088–6097 (2011)
Upwind integrated wind turbine design project, Advanced structural model of the 5MW reference wind turbine, Deliverable 2.10, pp. 1–62 (2011)
Varelis, D., Saravanos, D.A.: Coupled buckling and postbuckling analysis of active laminated piezoelectric composite plates. International Journal of Solids and Structures 41, 1519–1538 (2004)
Varelis, D., Saravanos, D.A.: Mechanics and finite element for nonlinear response of active laminated piezoelectric plates. AIAA Journal 42(6), 1227–1235 (2004)
Varelis, D., Saravanos, D.A.: Coupled mechanics and finite element for non-linear laminated piezoelectric shallow shells undergoing large displacements and rotations. International Journal for Numerical Methods in Engineering 66, 1211–1233 (2006a)
Varelis, D., Saravanos, D.A.: Small-amplitude free-vibration analysis of piezoelectric composite plates subject to large deflections and initial stresses. Journal of Vibration and Acoustics 128, 41–49 (2006b)
Virgin, L.N.: Vibration of axially loaded structures. Cambridge University Press, USA (2007)
Vo., T.P., Lee, J.: Geometrically nonlinear analysis of thin-walled composite box beams. Computers and Structures 87, 236–245 (2009)

Volovoi, V.V., Hodges, D.H., Cesnik, C.E.S., Popescu, B.: Assessment of beam modelling methods for rotor blade applications. Mathematical and Computer Modelling 33, 1099–1112 (2001)

Volovoi, V.V., Hodges, D.H.: Theory of anisotropic thin-walled beams. Journal of Appied Mechanics 67, 453–459 (2000)

Volovoi, V.V., Hodges, D.H.: Single and multicelled composite thin-walled beams. AIAA Journal 40(5), 960–965 (2002)

Wood, R.D., Zienkiewicz, O.C.: Geometrically nonlinear finite element analysis of beams, frames, arches and axisymmetric shells. Computers and Structures 7, 725–735 (1977)

Wren, G.G., Kinra, V.K.: Experimental technique for determining a measure of structural damping. Journal of Testing and Evaluation 16(1), 77–85 (1988)

Wren, C.G., Kinra, V.K.: Axial damping in metal-matrix composites, II: a theoretical model and its experimental verification. Experimental Mechanics 32(2), 172–178 (1992)

Yu, W., Hodges, D.H., Volovoi, V.V., Cesnik, C.E.S.: On Timoshenko-like modelling of initially curved and twisted composite beams. International Journal of Solids and Structures 39, 5101–5121 (2002)

Zapfe, J.A., Lesieutre, G.A.: A discrete layer beam finite element for the dynamic analysis of composite sandwich beams with integral damping layers. Computers and Structures 70, 647–666 (1999)

Appendix A

In the following tables the symbols, subscripts and superscripts which were used within the chapters of the book are explained.

Table A.1 Main symbols

Symbol	Explanation
σ	Engineering strains
ε	Engineering strains
Q	Ply stiffness matrix
η	Ply damping matrix
S	Compliance matrix
$u, \quad \upsilon, \quad w$	Displacements in three dimensions ($x, \quad y, \quad z$)
ρ	Density per unit volume
b_i	Body force per unit volume
Δ	Discrete amount of a symbol
δ	Virtual variation
V	Total volume of structure
$\overline{\tau}$	External forces applied at the free surface
Γ	Surface where external forces are applied
β	Rotation angle
θ	Twisting angle
O_{xyz}	Cartesian coordinate system
$O'_{xs\zeta}$	Local curvilinear coordinate system
r^0	Vector describing the distance between a point O' on the skin mid-surface from a point O on the cross-section
y^0, z^0	Projections of the r^0 vector on the O_{xyz} coordinate system
r_ζ^0, r_s^0	Projections of the r^0 vector on the $O'_{xs\zeta}$ curvilinear coordinate system

Table A.1 (*continued*)

k	Curvature
H	Strain energy of the cross-section
W_d	Dissipated energy of the cross-section
T	Kinetic energy of the cross-section
$A \sim A_s$	Skin extensional matrix
$B \sim B_s$	Skin coupling matrix
$D \sim D_s$	Skin flexural stiffness matrix
diag	Diagonal matrix
A^0	Cross-section extension-shear stiffness terms
B^0	Cross-section coupling stiffness terms
D^0	Cross-section flexure-torsion stiffness terms
A_d^0	Cross-section extension-shear damping terms
B_d^0	Cross-section coupling damping terms
D_d^0	Cross-section flexure-torsion damping terms
m^A, m^B, m^D	Equivalent linear, coupling and inertia mass matrix terms
K	Stiffness matrix
C	Damping matrix
M	Mass matrix
U_e^i	Nodal degrees of freedom vector
N^i	Displacement shape functions
R^i	Strain shape functions
ω	Natural frequency
η_m	Modal loss factor
h	Thickness of the skin laminate
A	Cross-sectional area covered by material

Table A.1 (*continued*)

More symbols describing the nonlinear formulation of the fourth, fifth and sixth chapter of the manuscript are the followings:	
H_s	Strain energy
H_{ds}	Dissipated energy
ε_x^L	Nonlinear axial strain component
Ψ	Imbalance vector between internal, inertial and external forces
F	External force
K_{s_0}	Linear section stiffness matrix
K_{s_1} , K_{s_2}	Nonlinear first- and second-order section stiffness matrix
K_{N_0}	Linear element stiffness matrix
K_{N_1} , K_{N_2}	Nonlinear first- and second-order element stiffness matrices
$\overline{K}_{N_0}$	Tangential element linear stiffness matrix
$\overline{K}_{N_1}$, $\overline{K}_{N_2}$	Tangential element nonlinear first- and second-order stiffness matrices
C_{ds_0}	Linear section damping matrix
C_{ds_1} , C_{ds_2}	Nonlinear first- and second-order section damping matrix
C_{N_0}	Linear element damping matrix
C_{N_1} , C_{N_2}	Nonlinear first- and second-order element damping matrix
$\overline{C}_{N_0}$	Tangential element linear damping matrix
$\overline{C}_{N_1}$, $\overline{C}_{N_2}$	Tangential element nonlinear first- and second-order damping matrix
ρ_L	Generalized mass matrix of the strip finite element
b	Width of the strip section
u_s	Nodal degrees of freedom vector at the nonlinear static equilibrium point
$\overline{u}$	Nodal degrees of freedom vector for the small-amplitude dynamic response

Table A.1 (*continued*)

$\bar{K}_T$	General expression for the tangential stiffness matrix
p_m	Pole of the system
p_0	Distributed load
Ω	Angular velocity

Table A.2 List of subscript symbols

Subscripts	Explanation
x, y, z	Global Cartesian coordinates
x, s, ζ	Local curvilinear coordinates
e	Element
s	Skin laminate level
c	Composite ply level
cs	Stiffness off-axis ply matrix
ds	Damping off-axis ply matrix
l	Material coordinate system
a	Indicate the strain shape function corresponding to normal generalized strains
b	Indicate the strain shape function corresponding to bending generalized strains
sa	Indicate the strain shape function corresponding to shear generalized strains
L	Indicate the strain shape function corresponding to nonlinear generalized strains
N	Indicates the total stiffness and damping matrices of the finite element
$0, \quad 1, \quad 2$	Linear, first- and second-order nonlinear terms
T	Indicates tangential matrix
f	Free (unknown) elastic degrees of freedom vector
a	Imposed (known) elastic degrees of freedom vector
t	Tangential nonlinear terms of the tubular beam finite eleemnt
,	Space differentiation

Table A.3 List of superscript symbols

Superscripts	Explanation
0	Terms referring to the mid-section of the laminate
L	Nonlinear terms
T	Transpose quantity
$nl1$	First-order nonlinear stiffness and damping terms of the tubular beam finite element
$nl2$	Second-order nonlinear stiffness and damping terms of the tubular beam finite element
f	Unknown degrees of freedom of the displacement vector U
c	Applied - known degrees of freedom of the displacement vector U
sec	Indicates the section of the structure
¨	Time differentiation
–	Stiffness and damping terms including material coupling
*	Reduced stiffness and damping matrices

Table A.4 Integration limit symbols

Integration Limit	Explanation
L	Element length
A	Cross-sectional area covered by material
h	Skin laminate thickness

Table A.5 Coordinate system notation

Coordinate system notation						
Tensor Notation	11	22	33	23	13	12
Contracted	1	2	3	4	5	6
Cartesian coordinate system	xx	yy	zz	yz	xz	xy
Cartesian coordinate system contracted	x	y	z	yz	xz	xy
Local curvilinear coordinate system	xx	ss	ζζ	sζ	xζ	xs
Local curvilinear coordinate system contracted	x	s	ζ	sζ	xζ	xs

Table A.6 Abbreviations

Abbreviations	Explanation
3-D	Three Dimensional
AML	Applied Mechanics Laboratory
CFRP	Carbon Fiber Reinforced Polymer
CLDT	Classical Laminate Damping Theory
CS	Coordinate System
DAQ	Data AcQuisition
DLDT	Discrete Layer Damping Theory
DOF	Degrees Of Freedom
EU	European Union
EAWE	European Academy of Wind Energy
FE	Finite Element
FEA	Finite Element Analysis
FFT	Fast Fourier Transform
FRF	Frequency Response Function
FRP	Fiber Reinforced Polymer
FSDT	First-order Shear Deformation Theory
GAST	General Aerodynamic and Structural prediction tool for wind Turbines
LE	Leading Edge
LVDT	Linear Variable Differential Transformer
RHS	Right Hand Side
RWT	Reference Wind Turbine
SAAM	Structural Analysis and Active Materials group
S/W	Shear Web
SDC	Specific Damping Capacity
TE	Trailing Edge
TWB	Thin Walled Beams or Blades
UD	Uni-Directional
UP	University of Patras wind-turbine blade model
VABS	Variational Asymptotical Beam Sectional analysis
VAM	Variational Asymptotic Method
WMC	Wind turbine Materials and Constructions

Appendix B

B.1 Damping Material Models

A damping material is a solid material capable of converting a significant amount of mechanical energy into heat (dissipation of energy) when it is subjected to cyclic strain. Damping materials combine energy dissipation (viscous) with energy storage (elastic) behavior and for that reason they are often called viscoelastic materials. In order to predict the damped structural response of such materials the characterization of two parameters is required; one associated with strain energy storage and the other with the dissipated energy of the vibrating system.

B.2 Viscous Damping

The response of a single DOF spring-mass model predicts that the system will oscillate indefinitely and its undamped motion could be described by the following relation,

$$m\ddot{x}(t)+kx(t)=0 \tag{b.1}$$

Taking into account that realistic material systems motion exhibit a die out response an extended form of Eq. (b.1) is suggested,

$$m\ddot{x}(t)+c\dot{x}(t)+kx(t)=0 \tag{b.2}$$

where c is the viscous damping coefficient. The damping of the system is represented by a damping force, having the form,

$$f_c=c\dot{x}(t) \tag{b.3}$$

Depending of the relative value of viscous damping coefficient the solution of Eq. (b.2) may include oscillation and decay (underdamped) or just exponentially decay (overdamped and critically damped).

Consider that Eq. (b.2) is divided by the mass term then it can be rewritten in the following form,

$$\ddot{x}(t)+2\zeta\omega_n\dot{x}(t)+\omega_m^2x(t)=0 \tag{b.4}$$

Assuming solutions of the form $x(t)=Ae^{st}$ for Eq. (b.4), then the latter is expressed as,

$$s^2 + 2\zeta\omega_n s + \omega_m^2 = 0 \tag{b.5}$$

which is satisfied for the following values of solution s ,

$$s_{1,2} = -\frac{c}{m} \pm \sqrt{\left(\left(\frac{c}{2m}\right)^2 - \frac{k}{m}\right)} \tag{b.6}$$

Thus for the case of the critically damped structure the natural frequency and the damping ratio are defined as,

$$\omega_n = \sqrt{\frac{k}{m}} = \frac{c_c}{2m} \quad \text{and} \quad \zeta = \frac{c}{2\sqrt{(km)}} = \frac{c}{c_c} \tag{b.7}$$

respectively. The parameter c_c is called critical damping constant (Inman 2001).

B.3 Hysteretic Damping

I. Energy Approach. During the cyclic loading of a material energy dissipation due to internal friction takes place. The material can be approximated by a spring-damper system where the spring elastic constant represents the material stiffness. The hysteretic closed loop of the cyclic loading represents the relationship between the total force (spring force and damping force) and the displacement (Figure B.1).

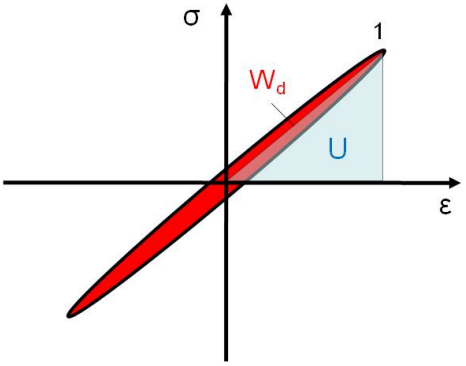

Fig. B.1 Hysteresis loop of a damping material

Taking into consideration that the material exhibits a linear viscoelastic behavior with low damping values, it therefore assumed that the point of maximum strain coincides with the respective point of maximum stress (point 1 in

Figure B.1). The shaded area represents the dissipated energy in one vibration cycle, whereas the maximum stored strain energy in the material is indicated by the area covered by the triangle on the upper right hand side of the diagram (Plagianakos 2004). Thus the next two parameters can be defined as follows:

- *Specific Damping Capacity (SDC)*, ψ, is the ratio of the dissipated energy in one vibration cycle to the maximum stored strain energy in the material,

$$\psi = \frac{W_d}{H} \tag{b.8}$$

- *Loss factor coefficient*, η, is the ratio of dissipated energy per radian to the maximum stored strain energy in the material,

$$\eta = \frac{1}{2\pi}\frac{W_d}{H} \tag{b.9}$$

Thus, substitution of Eq. (b.8) into Eq. (b.9) yields the relation between the SCD and the loss factor coefficient,

$$\psi = 2\pi\eta \tag{b.10}$$

II. Material complex modulus. For the case where a harmonic forcing is considered, the elastic constitutive equation could be modified to include the material loss factor η,

$$\sigma(\omega) = (1 + j\eta) E\varepsilon(\omega) \tag{b.11}$$

The material loss factor could essentially be the phase difference in forced harmonic response between an applied stress and the resultant strain. Eq. (b.11) could be rewritten in a form that express multiple material modulus and loss factors,

$$\sigma(\omega) = E^*(\omega)\varepsilon(\omega) \tag{b.12}$$

where E^* is the complex modulus of elasticity, which in the frequency domain is given by the following relation,

$$E^* = E' + jE'' \tag{b.13}$$

where the real part E' is the storage modulus and the imaginary part (loss modulus) E'' is associated with energy dissipation. The loss factor obeys,

$$\eta = E''/E' \tag{b.14}$$

At this point it should be underlined that the values of the aforementioned parameters, η, E', E'' vary with frequency.

B.4 Kelvin-Voigt Model

The stress-strain relationship in a material with viscoelastic damping can be expressed by a linear differential equation with respect to the time parameter. In the present work, the nonlinear analysis is based on the assumption of Kelvin material model (Figure B.2).

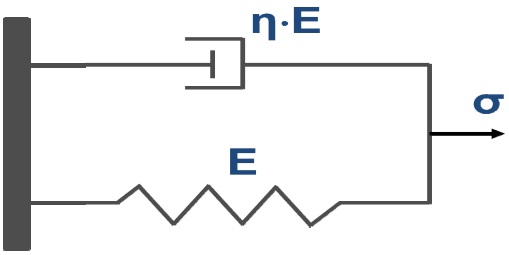

Fig. B.2 Kelvin material model

The Kelvin model consists of a spring and a dashpot in parallel as shown in Figure B.2. For a composite material the constitutive equation of Kelvin model takes the form,

$$\sigma = [Q_c]\varepsilon(t) + [Q_d]\frac{\mathrm{d}}{\mathrm{d}t}\varepsilon(t) \tag{b.15}$$

where σ is the material stress, ε is strain and Q_c, Q_d are the stiffness and damping matrices of the composite material related each other with the relation,

$$\omega[Q_d] = \eta[Q_c] \tag{b.16}$$

B.5 Relationship of Kelvin Modal Parameters to Measure Damping

The FRFs (Figure 5.7) of each specimen were obtained, the conjugate pairs of poles corresponding to the first and second bending mode were extracted, and equivalent damping ratios were measured, as the ratio of the real part to the magnitude of the pole,

$$\zeta_m = \frac{\mathrm{Re}(p_m)}{\| p_m \|} \tag{b.17}$$

The measured damping ratio of all tested specimens versus the respective modal frequency are shown in Figure 5.8, and remain practically constant to the variation of modal frequency, in the tested frequency range of 50-300 Hz.

The relationship between the measured modal loss factor and the damping matrix $[\mathbf{Q_{cd}}]$ in the strain-based Kelvin material model described by Eq. (4.1) was established by considering the analytical solution of the strip specimen. Lesieutre (2010) has reported such solution, however, for the sake of completeness, some key steps are overviewed in the following paragraphs. The simpler form of equation of motion (pure flexure) for a strip specimen, including damping, takes the form,

$$D_{11} w^0_{,xxxx} + D_{d11} w^0_{,xxxxt} + \rho^A w^0_{,tt} = 0 \tag{b.18}$$

Unforced motion is assumed, D_{11}, D_{d11} are flexural stiffness and damping laminate coefficients, ρ^A is linear density of the strip, and the comma in the subscripts indicates differentiation. The previous equation of motion, admits a solution of the form,

$$w^0 = W^0 e^{\xi x} e^{st} \tag{b.19}$$

which provides two poles for each mode related to the time response,

$$s_{1,2} = \frac{\xi^2}{2}\left(-\xi^2 \frac{D_{d11}}{\rho^A} \pm j\xi^2 \sqrt{4\frac{D_{11}}{\rho^A} - \xi^4 \left(\frac{D_{d11}}{\rho^A} \right)^2} \right) \tag{b.20}$$

where ξ is the wave-number. An equivalent flexural damping ratio of the strip is defined as the ratio of the real part over the magnitude of the pole, which after some substitutions takes the form,

$$\zeta_L = \frac{\mathrm{Re}(p)}{\| p \|} = \frac{1}{2}\xi^2 \frac{D_{d11}/\rho^A}{\sqrt{D_{11}/\rho^A}} = \frac{1}{2}\xi^2 \frac{D_{d11}/\rho^A}{\omega/\xi_0^2} \tag{b.21}$$

where, $\xi_0^{\,2} = \omega\sqrt{(\rho^A / D_{11})}$ is the wave-number of the undamped beam, ω is the time frequency. For the case of low damping, it can be assumed that $\zeta \ll 1$ and therefore $\xi \mapsto \xi_0$, thus, Eq. (b.21)becomes,

$$\zeta_L = \frac{1}{2}\xi^2\xi_0^2\frac{D_{d11}}{\rho^A}\frac{1}{\omega} = \frac{1}{2}\xi_0^4\frac{D_{d11}}{\rho^A}\frac{1}{\omega} = \frac{1}{2}\frac{D_{d11}}{D_{11}}\omega \tag{b.22}$$

Taking into account that $\eta_L = 2\zeta_L$, the relationship between the measured flexural damping coefficient of the beam and the equivalent flexural loss factor and stiffness simplifies is given by (Lesieutre 2010),

$$\omega D_{d11} = \eta_L D_{11} \tag{b.23}$$

The previous equation has two implications:

1) It should be valid on modal frequencies, hence, we extract D_{d11} by setting η_L equal to the measured loss factor of bending modes, while D_{11} is backalculated from the measured respective modal frequency value using the analytical solution of the undamped Eq. (b.18).

2) It is valid for all tested angle-ply specimens having various fiber orientation angles, which are used to extract the equivalent loss factor matrix $[\boldsymbol{\eta}_l]$ of the composite (Chrysochoidis 2001). Therefore, a similar Eq. (b.24) will relate the damping coefficient matrix $[\mathbf{Q_{cd}}]$ in Eq. (4.1), to the extracted loss factor matrix $[\boldsymbol{\eta}_l]$ and the stiffness matrix $[\mathbf{Q_{ls}}]$ of the composite material.

$$\omega[\mathbf{Q_{ld}}] = [\mathbf{Q_{ls}}][\boldsymbol{\eta}_l] \tag{b.24}$$

where subscript l indicates on-axis composite. Considering the above, the extracted equivalent loss factors matrix, of the composite material can be used to calculate the material damping matrix, at a specific frequency.

B.6 Other Damping Models

Viscoelasticity can be modeled by various combinations of elastic elements (linear springs) and viscous elements (dashpots). Apart from the Kelvin model, a brief description of other viscoelastic models is presented in Figure B.3. All models of this category are based on linear differential equations with respect to the time.

Beside these models and fractional derivative models with three (Bagley and Torvik 1983 & Eldred at al. 1995) or four parameters (Pritz 1996) are reported in the second chapter of the current work. The advantage of these models is that they provide the material damping in a wide frequency range. In addition, they are capable of representing relatively weak frequency-dependent properties in the frequency domain.

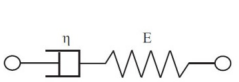

$$\frac{d\varepsilon_{total}}{dt} = \frac{d\varepsilon_{spring}}{dt} + \frac{d\varepsilon_{dashpot}}{dt} = \frac{\sigma}{\eta} + \frac{1}{E}\frac{d\sigma}{dt}$$

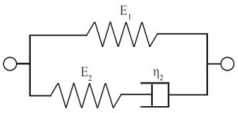

$$\frac{d\varepsilon}{dt} = \frac{\frac{E_2}{\eta}\left(\frac{\eta}{E_2}\frac{d\sigma}{dt} + \sigma - E_1\varepsilon\right)}{E_1 + E_2}$$

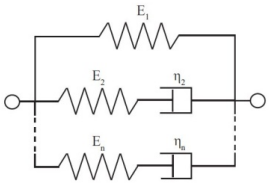

Consists of as many Maxwell elements as necessary to accurately represent the distribution of time.

Fig. B.3 Various viscoelastic models using combinations of linear springs and dashpots

Appendix C

C.1 Secondary Warping of the Cross-Section

The torsional strain on the mid-surface ε_{xs}^{ot} is evaluated by considering and solving the torsion stress equilibrium equation on the $s\zeta$ plane using a properly chosen torsional strain function Φ referred by Saravanos et al. (2006). The mid-surface torsional strain and the secondary warping function are found to be,

$$\varepsilon_{xs}^{0t}(s) = \frac{\Delta\Phi(s)}{h(s)}$$

(c.1)

$$\Psi^{0}(s) = \Delta A_0 - \frac{\Delta\Phi}{\theta_{,x}}\Delta\lambda$$

where $\Delta\Phi$ is the difference of the strain function between the inner and the outer surface and A_0 and λ are geometric section parameters defined by,

$$\frac{\Delta\Phi(s)}{\theta_{,x}} = -A_0 / \lambda$$

(c.2)

$$\Delta A_0 = \int_0^s r_\zeta^0 \mathrm{d}s, \quad \Delta\lambda = \int_0^s \frac{1}{h}\mathrm{d}s,$$

$$A_0 = \oint r_\zeta^0 \mathrm{d}s, \quad \lambda = \oint \frac{1}{h}\mathrm{d}s \tag{c.3}$$

C.2 Ply and Laminate Damping Matrices

The full form of the on-axis composite ply stiffness, $[\mathbf{Q}_1]$, is (Philippidis 2002),

$$[\mathbf{Q_l}]=\begin{bmatrix} Q_{l11} & Q_{l12} & Q_{l13} & 0 & 0 & 0 \\ Q_{l12} & Q_{l22} & Q_{l23} & 0 & 0 & 0 \\ Q_{l13} & Q_{l23} & Q_{l33} & 0 & 0 & 0 \\ 0 & 0 & 0 & Q_{l33} & 0 & 0 \\ 0 & 0 & 0 & 0 & Q_{l33} & 0 \\ 0 & 0 & 0 & 0 & 0 & Q_{l33} \end{bmatrix} \tag{c.4}$$

Each terms of the composite ply stiffness matrix is expressed through the mechanical properties of the material as follows,

$$Q_{l11}=\frac{E_1\left(1-\nu_{23}\nu_{32}\right)}{\Delta} \qquad Q_{l12}=\frac{E_2\left(\nu_{12}+\nu_{32}\nu_{13}\right)}{\Delta} \qquad Q_{l13}=\frac{E_3\left(\nu_{13}+\nu_{12}\nu_{23}\right)}{\Delta}$$

$$Q_{l22}=\frac{E_2\left(1-\nu_{13}\nu_{31}\right)}{\Delta} \qquad Q_{l23}=\frac{E_3\left(\nu_{23}+\nu_{21}\nu_{13}\right)}{\Delta} \qquad Q_{l33}=\frac{E_3\left(1-\nu_{12}\nu_{21}\right)}{\Delta} \tag{c.5}$$

$$Q_{l44}=G_{23} \qquad Q_{l55}=G_{13} \qquad Q_{l66}=G_{12}$$

$$\Delta=1-\nu_{12}\nu_{21}-\nu_{23}\nu_{32}-\nu_{13}\nu_{31}-2\nu_{21}\nu_{32}\nu_{13}$$

The kinematic assumptions used throughout the chapters of the current work, neglect transverse normal strain,

$$\left(\varepsilon_3=0\right) \tag{c.6}$$

The off-axis stiffness composite ply matrix is given by the relation,

$$[\mathbf{Q_c}]=[\mathbf{R}]^{-1}[\mathbf{Q_l}][\mathbf{R}]^{-T} \tag{c.7}$$

where, $[\mathbf{R}]$ is a proper rotation matrix, which has the following form,

$$[\mathbf{R}]=\begin{bmatrix} \cos^2\theta & \sin^2\theta & 0 & 0 & 2\cos\theta\sin\theta \\ \sin^2\theta & \cos^2\theta & 0 & 0 & -2\cos\theta\sin\theta \\ 0 & 0 & \cos\theta & -\sin\theta & 0 \\ 0 & 0 & \sin\theta & \cos\theta & 0 \\ -\cos\theta\sin\theta & \cos\theta\sin\theta & 0 & 0 & \cos^2\theta-\sin^2\theta \end{bmatrix} \tag{c.8}$$

and θ is the counterclockwise rotation angle from the global to the local coordinate system. Hence, incorporation of Eqs. (c.4) into Eq. (c.7) yields the full form of the composite ply stiffness $[\mathbf{Q_{cs}}]$ containing in-plane and out-of-plane shear terms, which therefore takes the form,

$$[\mathbf{Q_{cs}}]=\begin{bmatrix} Q_{c11} & Q_{c12} & 0 & 0 & Q_{c16} \\ Q_{c12} & Q_{c22} & 0 & 0 & Q_{c26} \\ 0 & 0 & Q_{c44} & Q_{c45} & 0 \\ 0 & 0 & Q_{c45} & Q_{c55} & 0 \\ Q_{c16} & Q_{c26} & 0 & 0 & Q_{c66} \end{bmatrix} \tag{c.9}$$

C.3 Skin Laminate Stiffness and Damping Matrices

The membrane, coupling and flexural stiffness and damping matrices are calculated based on the first-order shear deformation theory and have the following form, respectively,

$$\begin{aligned} \left\langle \mathbf{A_{ij}},\mathbf{B_{ij}},\mathbf{D_{ij}} \right\rangle &= \sum_{k=1}^{n}\int_{z_k}^{z_{k+1}} \mathbf{Q}^{\mathbf{k}}_{\mathbf{cs_{ik}}} \left\langle 1,\zeta,\zeta^2 \right\rangle \mathrm{d}\zeta \qquad i,j=1,2,6 \\ \mathbf{A_{ij}} &= \sum_{k=1}^{n}\int_{z_k}^{z_{k+1}} \mathbf{Q}^{\mathbf{k}}_{\mathbf{cs_{ik}}} \mathrm{d}\zeta \qquad i,j=4,5 \end{aligned} \tag{c.10}$$

$$\begin{aligned} \left\langle \mathbf{A_{d_{ij}}},\mathbf{B_{d_{ij}}},\mathbf{D_{d_{ij}}} \right\rangle &= \sum_{k=1}^{L}\int_{z_k}^{z_{k+1}} \mathbf{Q_{c_{ik}}}[\boldsymbol{\eta}_{\mathbf{c_{ik}}}] \left\langle 1,\zeta,\zeta^2 \right\rangle \mathrm{d}\zeta \qquad i,j=1,2,6 \\ \mathbf{A_{d_{ij}}} &= \sum_{k=1}^{L}\int_{z_k}^{z_{k+1}} \mathbf{Q_{c_{ik}}}[\boldsymbol{\eta}_{\mathbf{c_{ik}}}] \mathrm{d}\zeta \qquad i,j=4,5 \end{aligned} \tag{c.11}$$

C.4 Reduction of Stiffness and Damping Laminate Matrices

I. Tubular Beam Element

Assuming first-order shear deformation theory, the equivalent forces and moments acting on the laminate are,

$$\{\mathbf{N}\}=\begin{Bmatrix}N_x\\N_s\\N_{xs}\end{Bmatrix}=[\mathbf{A}]_{3x3}\boldsymbol{\varepsilon}^{\mathbf{0}}+[\mathbf{B}]_{3x3}\mathbf{k}=\begin{bmatrix}A_{11}&A_{12}&A_{16}\\A_{12}&A_{22}&A_{26}\\A_{16}&A_{26}&A_{66}\end{bmatrix}\boldsymbol{\varepsilon}^{\mathbf{0}}+\begin{bmatrix}B_{11}&B_{12}&B_{16}\\B_{12}&B_{22}&B_{26}\\B_{16}&B_{26}&B_{66}\end{bmatrix}\mathbf{k}$$

$$\{\mathbf{M}\}=\begin{Bmatrix}M_x\\M_s\\M_{xs}\end{Bmatrix}=[\mathbf{B}]_{3x3}\boldsymbol{\varepsilon}^{\mathbf{0}}+[\mathbf{D}]_{3x3}\mathbf{k}=\begin{bmatrix}B_{11}&B_{12}&B_{16}\\B_{12}&B_{22}&B_{26}\\B_{16}&B_{26}&B_{66}\end{bmatrix}\boldsymbol{\varepsilon}^{\mathbf{0}}+\begin{bmatrix}D_{11}&D_{12}&D_{16}\\D_{12}&D_{22}&D_{26}\\D_{16}&D_{26}&D_{66}\end{bmatrix}\mathbf{k} \tag{c.12}$$

$$\{\mathbf{N_{sh}}\}=\begin{Bmatrix}N_{s\zeta}\\N_{x\zeta}\end{Bmatrix}=[\mathbf{A_{sh}}]_{2x2}\boldsymbol{\varepsilon}^{\mathbf{0}}_{\mathbf{sh}}=\begin{bmatrix}A_{44}&A_{45}\\A_{45}&A_{55}\end{bmatrix}\boldsymbol{\varepsilon}^{\mathbf{0}}_{\mathbf{sh}}$$

For the case of the tubular beam element, presented within the third and the sixth chapter, the laminate stiffness and damping matrices are further reduced assuming diminishing in-plane transverse laminate force, N_s, out-of-plane shear force $N_{s\zeta}$ and transverse bending moment M_s. The laminate stiffness and damping matrices $\mathbf{C_L}$ and $\mathbf{C_{dL}}$ have the form,

$$\mathbf{C_L}=\begin{bmatrix}\mathbf{A}&\mathbf{B}\\\mathbf{B^T}&\mathbf{D}\end{bmatrix},\quad \mathbf{C_{dL}}=\begin{bmatrix}\mathbf{A_d}&\mathbf{B_d}\\\mathbf{B_d^T}&\mathbf{D_d}\end{bmatrix} \tag{c.13}$$

where, L indicates the laminate and $[\mathbf{A}]$ is the stiffness matrix containing both the extensional membrane $[\mathbf{A}]_{3x3}$ and shear terms $[\mathbf{A_{sh}}]_{2x2}$, respectively. By inverting we get the respective compliance counterparts $\mathbf{S_L}=\mathbf{C_L^{-1}}$ and $\mathbf{S_{dL}}=\mathbf{S_L^T}\mathbf{C_{dL}}\mathbf{S_L}$. Then,

$$\delta H_L=\{\delta\mathbf{N},\quad \delta\mathbf{M}\}^{\mathrm{T}}\mathbf{S_L}\begin{Bmatrix}\mathbf{N}\\\mathbf{M}\end{Bmatrix}=\{\delta\mathbf{N}^*,\quad \delta\mathbf{M}^*\}^{\mathrm{T}}\mathbf{S_L^*}\begin{Bmatrix}\mathbf{N}^*\\\mathbf{M}^*\end{Bmatrix}$$

$$\delta W_{dL}=\{\delta\mathbf{N},\quad \delta\mathbf{M}\}^{\mathrm{T}}\mathbf{S_{dL}}\begin{Bmatrix}\mathbf{N}\\\mathbf{M}\end{Bmatrix}=\{\delta\mathbf{N}^*,\quad \delta\mathbf{M}^*\}^{\mathrm{T}}\mathbf{S_{dL}^*}\begin{Bmatrix}\mathbf{N}^*\\\mathbf{M}^*\end{Bmatrix} \tag{c.14}$$

where asterisk superscript indicates the resultant reduced forces and moments vectors $\mathbf{N}^*=\{N_x\quad N_{xs}\quad N_{x\zeta}\}$ and $\mathbf{M}^*=\{M_x\quad M_{xs}\}$, respectively.

The reduced laminate stiffness and damping matrices take the form,

$$\mathbf{C}_{\mathbf{L}}^{*}=\mathbf{S}_{\mathbf{L}}^{*-1},\quad \mathbf{C}_{\mathbf{dL}}^{*}=\mathbf{C}_{\mathbf{L}}^{*\mathrm{T}}\mathbf{S}_{\mathbf{dL}}^{*}\mathbf{C}_{\mathbf{L}}^{*} \tag{c.15}$$

and contain the reduced extensional, coupling and flexural stiffness matrices used in the calculation of the structure cross-section,

$$\left[\mathbf{A}^{*}\right]=\begin{bmatrix} A_{11}^{*} & 0 & A_{61}^{*} \\ 0 & A_{55}^{*} & 0 \\ A_{16}^{*} & 0 & A_{66}^{*} \end{bmatrix},\quad \left[\mathbf{B}^{*}\right]=\begin{bmatrix} B_{11}^{*} & B_{61}^{*} \\ B_{16}^{*} & B_{66}^{*} \end{bmatrix},\quad \left[\mathbf{D}^{*}\right]=\begin{bmatrix} D_{11}^{*} & D_{61}^{*} \\ D_{16}^{*} & D_{66}^{*} \end{bmatrix} \tag{c.16}$$

The corresponding laminate damping matrices $\left[\mathbf{A}_{\mathbf{d}}^{*}\right]$, $\left[\mathbf{B}_{\mathbf{d}}^{*}\right]$ and $\left[\mathbf{D}_{\mathbf{d}}^{*}\right]$ have similar form,

$$\left\langle \mathbf{A}_{\mathbf{d}_{ij}}^{*},\mathbf{B}_{\mathbf{d}_{ij}}^{*},\mathbf{D}_{\mathbf{d}_{ij}}^{*}\right\rangle=\sum_{k=1}^{L}\int_{\zeta_k}^{\zeta_{k+1}}\left[\mathbf{Q}_{\mathbf{ij}}^{\mathbf{k}}\right]\left[\boldsymbol{\eta}_{\mathbf{c}_{jm}}\right]\left\langle 1,\zeta,\zeta^{2}\right\rangle \mathrm{d}\zeta \qquad i,j,m=1,6 \tag{c.17}$$

$$\mathbf{A}_{\mathbf{d}_{ij}}^{*}=\sum_{k=1}^{L}\int_{\zeta_k}^{\zeta_{k+1}}\left[\mathbf{Q}_{\mathbf{ij}}^{\mathbf{k}}\right]\left[\boldsymbol{\eta}_{\mathbf{c}_{jm}}\right]\mathrm{d}\zeta \qquad i,j,m=5$$

The star superscript is implied in Eqs. (3.20)-(3.26) of the third chapter and Eqs. (c.23)-(c.29) of current Appendix.

II. Beam-Strip Element

It should be pointed out that the same procedure is followed to build the formulation of the composite strip element, whose development is present in the fourth chapter of the manuscript. The main differences with refer to the tubular beam finite element have to do with the laminate stiffness and damping matrices, which are further reduced. Thus, the total assumptions include diminishing in-plane transverse and shear laminate forces N_y, N_{xy}, out-of-plane shear force N_{yz} and transverse bending and shear moments M_y and M_{xy}.

The laminate stiffness matrix $\mathbf{C}_{\mathbf{L}}$ has the form,

$$\mathbf{C}_{\mathbf{L}}=\begin{bmatrix} \mathbf{A} & \mathbf{B} \\ \mathbf{B}^{\mathbf{T}} & \mathbf{D} \end{bmatrix} \tag{c.18}$$

where, L indicates the laminate and $\left[\mathbf{A}\right]$ is the stiffness matrix containing both the extensional membrane $\left[\mathbf{A}\right]_{3x3}$ and shear terms $\left[\mathbf{A}_{\mathbf{s}}\right]_{2x2}$, respectively. Inversion gives out the respective compliance counterparts $\mathbf{S}_{\mathbf{L}}=\mathbf{C}_{\mathbf{L}}^{-1}$. Then,

$$\delta H_L = \left\{\delta \mathbf{N}, \quad \delta \mathbf{M}\right\}^{\mathrm{T}} \mathbf{S_L} \begin{Bmatrix} \mathbf{N} \\ \mathbf{M} \end{Bmatrix} = \left\{\delta \mathbf{N}^*, \quad \delta \mathbf{M}^*\right\}^{\mathrm{T}} \mathbf{S_L^*} \begin{Bmatrix} \mathbf{N}^* \\ \mathbf{M}^* \end{Bmatrix} \tag{c.19}$$

where asterisk superscript indicates the resultant reduced forces and moments vectors $\mathbf{N}^{*^{\mathrm{T}}} = \left\{N_x \quad N_{xz}\right\}$ and $\mathbf{M}^* = \left\{M_x\right\}$, respectively.

The reduced laminate stiffness matrix has 3x3 dimensions,

$$\mathbf{C_L^*} = \mathbf{S_L^{*-1}} \tag{c.20}$$

and contains the reduced stiffness matrix used in the calculation of the structure cross-section,

$$\mathbf{C_L^*} = \begin{bmatrix} A_{11}^* & 0 & B_{11}^* \\ 0 & A_{55}^* & 0 \\ B_{11}^* & 0 & D_{11}^* \end{bmatrix} \tag{c.21}$$

The corresponding damping matrices $\mathbf{A_d^*}$, $\mathbf{B_d^*}$, $\mathbf{D_d^*}$ have similar form,

$$\begin{aligned} \left\langle \mathbf{A_{d_{ij}}^*}, \mathbf{B_{d_{ij}}^*}, \mathbf{D_{d_{ij}}^*} \right\rangle &= \sum_{k=1}^{L} \int_{z_k}^{z_{k+1}} \mathbf{Q_{c_{ik}}}[\boldsymbol{\eta}_{\mathbf{c_{ik}}}] \left\langle 1, z, z^2 \right\rangle \mathrm{d}z \qquad i, j = 1 \\ \mathbf{A_{d_{ij}}^*} &= \sum_{k=1}^{L} \int_{z_k}^{z_{k+1}} \mathbf{Q_{c_{ik}}}[\boldsymbol{\eta}_{\mathbf{c_{ik}}}] \mathrm{d}z \qquad i, j = 5 \end{aligned} \tag{c.22}$$

The star superscript is implied in the equations of the fourth. fifth and sixth chapter, regarding the composite strip nonlinear finite element formulation.

C.5 Detailed Expressions of Section Stiffness, Damping and Mass Linear Terms of the Tubular Beam Finite Element

In this paragraph the section stiffness, damping and mass terms, previously formulated by Saravanos et al. (2006), are present for sake of completeness of the present work.

I. Section Stiffness Terms

Linear extensional-shear stiffness section terms,

$$A_{11}^0 = \oint \left(A_{11}\right) ds$$

$$\overline{A}_{15}^0 = \overline{A}_{51}^0 = \oint \left(A_{16} z_{,s}^0\right) ds$$

$$\bar{A}_{16}^0 = \bar{A}_{61}^0 = \oint \left(A_{16} y_{,s}^0 \right) ds$$

$$A_{55}^0 = \oint \left(A_{66} z_{,s}^{0^2} \right) ds + \oint \left(A_{55} y_{,s}^{0^2} \right) ds$$

$$A_{56}^0 = A_{65}^0 = \oint \left(A_{66} y_{,s}^0 z_{,s}^0 \right) ds - \oint \left(A_{55} y_{,s}^0 z_{,s}^0 \right) ds$$

$$A_{66}^0 = \oint \left(A_{66} y_{,s}^{0^2} \right) ds + \oint \left(A_{55} z_{,s}^{0^2} \right) ds \tag{c.23}$$

Linear coupling stiffness terms,

$$B_{11}^0 = \oint \left(A_{11} z^0 + B_{11} y_{,s}^0 \right) ds$$

$$B_{12}^0 = \oint \left(A_{11} y^0 - B_{11} z_{,s}^0 \right) ds$$

$$\bar{B}_{16}^0 = \oint \left(-A_{16} A_h - 2B_{16} \right) ds$$

$$\bar{B}_{51}^0 = \oint \left(A_{16} z^0 + B_{16} y_{,s}^0 \right) z_{,s}^0 ds$$

$$\bar{B}_{52}^0 = \oint \left(A_{16} y^0 - B_{16} z_{,s}^0 \right) z_{,s}^0 ds$$

$$B_{56}^0 = \oint \left(-A_{66} A_h - 2B_{66} \right) z_{,s}^0 ds$$

$$\bar{B}_{61}^0 = \oint \left(A_{16} z^0 + B_{16} y_{,s}^0 \right) y_{,s}^0 ds$$

$$\bar{B}_{62}^0 = \oint \left(A_{16} y^0 - B_{16} z_{,s}^0 \right) y_{,s}^0 ds$$

$$B_{66}^0 = \oint \left(-A_{66} A_h - 2B_{66} \right) y_{,s}^0 ds \tag{c.24}$$

Linear flexural and torsional stiffness terms,

$$D_{11}^0 = \oint \left(A_{11} z^{0^2} + 2B_{11} z^0 y_{,s}^0 + D_{11} y_{,s}^{0^2} \right) ds$$

$$D_{12}^0 = D_{21}^0 = \oint \left(A_{11} y^0 z^0 + B_{11} \left(y^0 y_{,s}^0 - z^0 z_{,s}^0 \right) - D_{11} y_{,s}^0 z_{,s}^0 \right) ds$$

$$\bar{D}_{16}^0 = \bar{D}_{61}^0 = \oint \left(-A_{16} A_h z^0 - B_{16} \left(A_h y_{,s}^0 + 2z^0 \right) - 2D_{16} y_{,s}^0 \right) ds$$

$$D_{22}^0 = \oint \left(A_{11} y^{0^2} - 2B_{11} y^0 z_{,s}^0 + D_{11} z_{,s}^{0^2} \right) ds$$

$$\bar{D}_{26}^0 = \bar{D}_{62}^0 = \oint \left(-A_{16} A_h y^0 + B_{16} \left(A_h z_{,s}^0 - 2y^0 \right) + 2D_{16} z_{,s}^0 \right) ds$$

$$D_{66}^0 = \oint \left(A_{66} A_h^2 + 4B_{16} A_h + 4D_{66} \right) ds \tag{c.25}$$

where,

$$A_h = \frac{\oint r_\zeta^0 ds}{h\oint \frac{1}{h} ds} \tag{c.26}$$

II. Section damping terms without material coupling

Linear extensional damping section terms,

$$A_{d11}^0 = \oint A_{d11} ds$$

$$A_{d55}^0 = \oint A_{d66} z_{,s}^{0^2} ds + \oint A_{d55} y_{,s}^{0^2} ds$$

$$A_{d56}^0 = A_{d65}^0 = \oint A_{d66} y_{,s}^0 z_{,s}^0 ds - \oint A_{d55} y_{,s}^0 z_{,s}^0 ds$$

$$A_{d66}^0 = \oint A_{d66} y_{,s}^{0^2} ds + \oint A_{d55} z_{,s}^{0^2} ds \tag{c.27}$$

Linear coupling damping terms,

$$B_{d11}^0 = \oint \left(A_{d11} z^0 + B_{d11} y_{,s}^0 \right) ds$$

$$B_{d12}^0 = \oint \left(A_{d11} y^0 - B_{d11} z_{,s}^0 \right) ds$$

$$B_{d56}^0 = \oint \left(-A_{d66} A_h - 2B_{d66} \right) z_{,s}^0 ds$$

$$B_{d66}^0 = \oint \left(-A_{d66} A_h - 2B_{d66} \right) y_{,s}^0 ds \tag{c.28}$$

Linear flexural and torsional damping terms,

$$D_{d11}^0 = \oint \left(A_{d11} z^{0^2} + 2B_{d11} z^0 y_{,s}^0 + D_{d11} y_{,s}^{0^2} \right) ds$$

$$D_{d12}^0 = D_{d21}^0 = \oint \left(A_{d11} y^0 z^0 + B_{d11} \left(y^0 y_{,s}^0 - z^0 z_{,s}^0 \right) - D_{d11} y_{,s}^0 z_{,s}^0 \right) ds$$

$$D_{d22}^0 = \oint \left(A_{d11} y^{0^2} - 2B_{d11} y^0 z_{,s}^0 + D_{d11} z_{,s}^{0^2} \right) ds$$

$$D_{d66}^0 = \oint \left(A_{d66} A_h^2 + 4B_{d16} A_h + 4D_{d66} \right) ds \tag{c.29}$$

III. Section Mass Terms

Average mass terms,

$$m_{11}^A = \oint \rho^A ds \tag{c.30}$$

Coupling mass terms,

$$m_{11}^B = \oint \left(\rho^A z^0 + \rho^B y_{,s}^0 \right) ds \tag{c.31}$$

$$m_{12}^{B} = \oint \left(\rho^{A} y^{0} - \rho^{B} z_{,s}^{0} \right) ds$$

$$m_{13}^{B} = \oint \left(\rho^{A} \Psi^{0} + \rho^{B} r_{\zeta}^{0} \right) ds$$

$$m_{23}^{B} = \oint \left(-\rho^{A} z^{0} - \rho^{B} y_{,s}^{0} \right) ds$$

$$m_{33}^{B} = \oint \left(\rho^{A} \left(-r_{\zeta}^{0} z_{,s}^{0} + r_{s}^{0} y_{,s}^{0} \right) - \rho^{B} z_{,s}^{0} \right) ds$$

Inertia mass terms,

$$m_{11}^{D} = \oint \left(\rho^{A} z^{0^2} + 2\rho^{B} z^{0} y_{,s}^{0} + \rho^{D} y_{,s}^{0^2} \right) ds$$

$$m_{12}^{D} = m_{21}^{D} = \oint \left(\rho^{A} y^{0} z^{0} + \rho^{B} (y^{0} y_{,s}^{0} - z^{0} z_{,s}^{0}) - \rho^{D} y_{,s}^{0} z_{,s}^{0} \right) ds$$

$$m_{13}^{D} = m_{31}^{D} = \oint \left(\rho^{A} \Psi^{0} z^{0} + \rho^{B} (\Psi^{0} y_{,s}^{0} + z^{0} r_{\zeta}^{0}) + \rho^{D} r_{\zeta}^{0} y_{,s}^{0} \right) ds$$

$$m_{22}^{D} = \oint \left(\rho^{A} y^{0^2} - 2\rho^{B} y^{0} z_{,s}^{0} + \rho^{D} z_{,s}^{0^2} \right) ds$$

$$m_{23}^{D} = m_{32}^{D} = \oint \left(\rho^{A} \Psi^{0} y^{0} + \rho^{B} (-\Psi^{0} z_{,s}^{0} + y^{0} r_{\zeta}^{0}) - \rho^{D} r_{\zeta}^{0} z_{,s}^{0} \right) ds$$

$$m_{33}^{D} = \oint \left(2\rho^{A} \Psi^{0} + 2\rho^{B} \Psi^{0} r_{\zeta}^{0} + \rho^{D} r_{\zeta}^{0^2} \right) ds \qquad \text{(c.32)}$$

In order to calculate the equivalent linear mass, coupling and rotational inertia matrices of the cross-section it is necessary to define the skin laminate densities of the composite structure,

$$\left\langle \rho^{A}, \rho^{B}, \rho^{D} \right\rangle = \sum_{k=1}^{L} \int_{\zeta_k}^{\zeta_{k+1}} \rho \left\langle 1, \zeta, \zeta^{2} \right\rangle \mathrm{d}\zeta, \qquad \text{(c.33)}$$

where ρ is the ply density and ζ is the distance from the skin midline.

Appendix D

D.1 Tangential Section Stiffness Matrix of the Composite Strip Finite Element

The tangential linear and nonlinear section stiffness matrices of the nonlinear strip finite element have the following form,

Linear component,

$$\left[\bar{\mathbf{K}}_{\mathbf{s_0}}\right]=\begin{bmatrix} A_{11} & 0 & B_{11} \\ 0 & A_{55} & 0 \\ B_{11} & 0 & D_{11} \end{bmatrix} \tag{d.1}$$

First-order nonlinear component,

$$\left[\bar{\mathbf{K}}_{\mathbf{s_1}}\right]=\begin{bmatrix} 0 & w^0_{,x}A_{11} & 0 \\ w^0_{,x}A_{11} & N_x & w^0_{,x}B_{11} \\ 0 & w^0_{,x}B_{11} & 0 \end{bmatrix} \tag{d.2}$$

Second-order nonlinear component,

$$\left[\bar{\mathbf{K}}_{\mathbf{s_2}}\right]=\begin{bmatrix} 0 & 0 & 0 \\ 0 & \frac{3}{2}w^{0^2}_{,x}A_{11} & 0 \\ 0 & 0 & 0 \end{bmatrix} \tag{d.3}$$

D.2 Section Mass Matrices

The equivalent mass, coupling and rotational inertia matrices of the laminate of the composite strip per unit length $\mathbf{m^A}$, $\mathbf{m^B}$ and $\mathbf{m^D}$ are,

$$\mathbf{m^A}=\begin{bmatrix} m^A_{11} & 0 \\ 0 & m^A_{11} \end{bmatrix},\quad \mathbf{m^B}=\left[m^B_{11}\right],\quad \mathbf{m^D}=\left[m^D_{11}\right] \tag{d.4}$$

The detailed terms expressions of previous matrices are found to have the following form,

$$m_{11}^{A} = \int_{h} \rho^{A} \mathrm{d}z$$

$$m_{11}^{B} = \int_{h} \rho^{B} \mathrm{d}z \tag{d.5}$$

$$m_{11}^{D} = \int_{h} \rho^{D} \mathrm{d}z$$

where ρ^{A}, ρ^{B} and ρ^{D} are the equivalent average, coupling and inertia densities of the skin laminate,

$$\left\langle \rho^{A}, \rho^{B}, \rho^{D} \right\rangle = \int_{h} \rho \left\langle 1, z, z^{2} \right\rangle \mathrm{d}z \tag{d.6}$$

where ρ is the ply density and h is the thickness of the composite ply, indicated also in the manuscript.

D.3 Shape Function Matrices for the Two-Node Beam-Strip Finite Element

The strain shape functions used for the approximation of the displacement field of the nonlinear composite strip finite element have different form according to the corresponding strain term of the cross section.

Shape function matrix of normal strain,

$$\left[R_{a}^{oi} \right] = \left[N_{,x} \quad 0 \quad 0 \right] \tag{d.7}$$

Shape function matrix of shear strain,

$$\left[R_{sa}^{oi} \right] = \left[0 \quad N_{,x} \quad N \right] \tag{d.8}$$

Shape function matrix of curvature,

$$\left[R_{b}^{oi} \right] = \left[0 \quad 0 \quad N_{,x} \right] \tag{d.9}$$

Shape function matrix of nonlinear strain,

$$\left[R_{L}^{i} \right] = \left[H \right] \left[G^{i} \right] \tag{d.10}$$

where the matrices $[H]$ and $[G^i]$ have the following analytical forms,

$$[H] = \begin{bmatrix} 0 & w^0_{,x} & 0 \end{bmatrix} \tag{d.11}$$

and

$$[G^i] = \begin{bmatrix} 0 & 0 & 0 \\ 0 & N_{,x} & 0 \\ 0 & 0 & 0 \end{bmatrix} \tag{d.12}$$

Appendix E

E.1 61.5m Wind-Turbine Blade Configuration

The large-scale blade model was developed within the activities UpWind integrated project (2011). In Table E.1 the lay-up configuration per blade section and materials thicknesses are presented. Each cross-section is noticed by a capital letter which corresponds to a specific blade span.

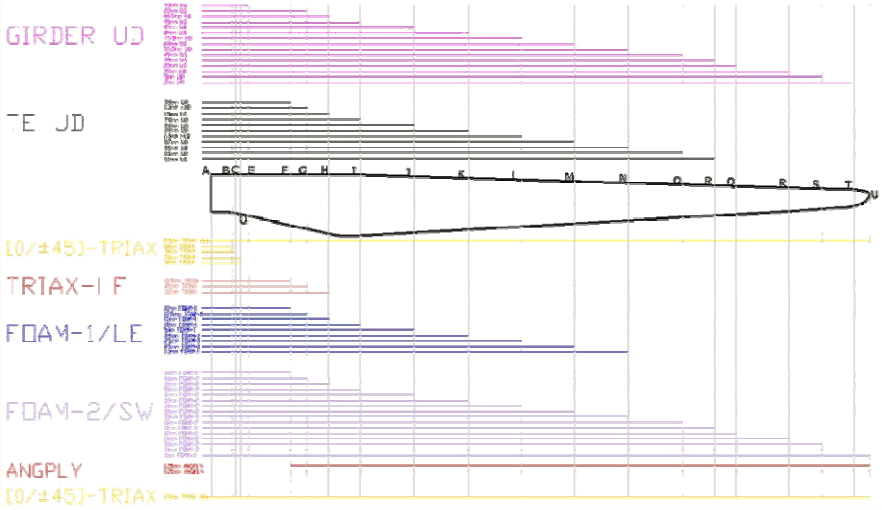

Fig. E.1 Material lay-up configuration for UP 61.5m blade model

The UP blade model geometrical characteristics for the twenty (20) sections along its length are presented in Table E.1. Apart from the blade root where the cross-section has a circular shape, the majority of the sections have the airfoil shape with two shear webs. For each cross-section both the centre of gravity (CG) and the shear centre (SC) were calculated.

Table E.1 Geometrical data of 61.5 rotor blade cross-sections

Element Number	*Section Number*	*Rotor Radius* (m)	*Twist* (deg)	*Chord* (m)	*Center of Gravity [CG]*		*Shear Center [CS]*	
					X_{CG} (m)	Y_{CG} (m)	X_{CS} (m)	Y_{CS} (m)
1	B	2.0	15.00	3.542	1.7110	0.4583	-1.5183	-0.4062
2	C	2.3	15.00	3.542	1.7110	0.4583	-1.5183	-0.4062
3	D	2.8	15.00	3.542	1.7110	0.4583	-1.5183	-0.4062
4	E	3.5	15.00	3.542	1.5510	0.3869	-0.5794	-0.1320
5	F	7.5	15.00	4.344	1.6940	0.05519	-1.8360	-0.1468
6	G	9.0	12.51	4.537	1.8230	0.0344	-1.0730	-0.2169
7	H	11.0	10.6	4.559	1.7460	0.302	-1.1370	-0.2450
8	I	14.0	8.48	4.618	1.5070	0.1082	-0.965	-0.0840
9	J	19.0	4.24	4.435	1.4197	-	-0.8782	-0.0094
10	K	24.0	0.00	4.150	1.2630	-	-0.7129	-0.0315
11	L	29.0	-3.24	3.846	1.1791	-0.0937	-0.6288	0.04831
12	M	34.0	-4.21	3.594	1.0631	-0.112	-0.5177	0.05362
13	N	39.0	-5.95	3.234	1.0163	-0.1099	-0.4959	0.05370
14	O	44.0	-5.98	2.943	0.9071	-0.1211	-0.4120	0.05330
15	P	47.0	-6.79	2.786	0.9535	-0.1309	-0.4210	0.05910
16	Q	49.0	-7.64	2.676	0.8510	-0.1118	-0.3820	0.03520
17	R	54.0	-7.70	2.347	0.8320	-0.144	-0.3510	0.06000
18	S	57.0	-8.61	2.182	0.9050	-0.1415	-0.399	0.04581
19	T	60.0	-9.92	1.417	0.6970	-0.1101	-0.2964	0.03521
20	U	61.5	-9.93	0.127	0.6970	-0.1101	-0.2964	0.03521

Typical cross-section shapes are better illustrated in Figure E.2 (Nijssen et al. 2007). Each shape corresponds to a different distance from the blade root, which is indicated by the respective capital letter of the section number shown in Table E.1. The blade cross section near its root has a circular shape, which gradually turns into an elliptical shape. At this stage the shear webs are included in the blade structural design. Thereafter, the cross-section takes the airfoil shape, whose chord length firstly increases (up to 14m of blade length) and then decreases. Near the blade tip the cross-sections consist of one shear web.

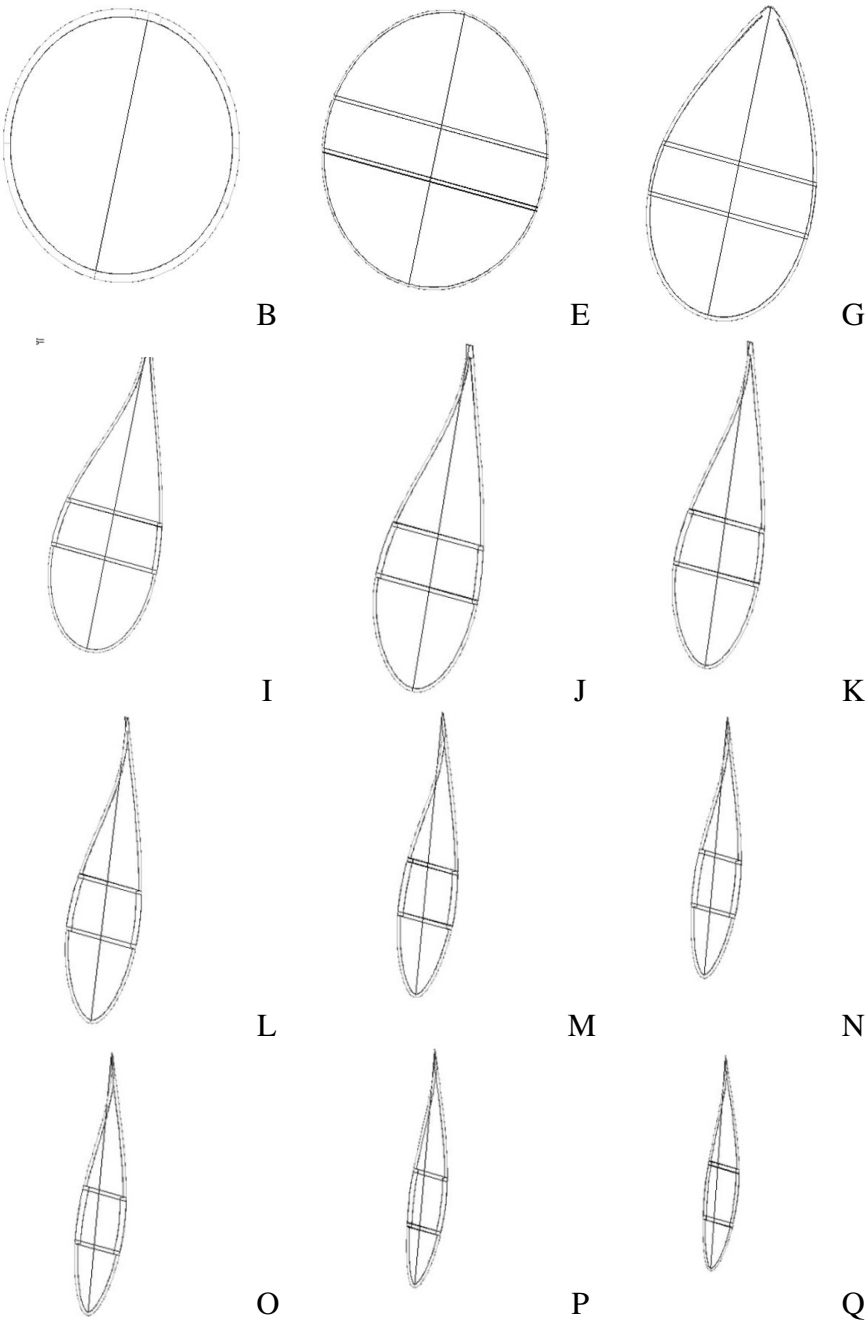

Fig. E.2 Typical cross-section shapes along the 61.5m wind-turbine blade model

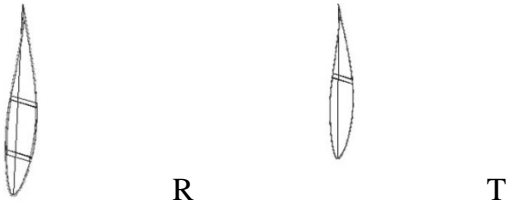

Fig. E.2 (*continued*)

Similarly, Table E.2 presents the mass and stiffness properties of UP wind-turbine blade per cross-section, as they were predicted by the developed linear beam finite element. The comparisons with the respective values provided from DOWEC and WMC are illustrated in Figures 3.28-3.32 of the third chapter of the manuscript.

Table E.2 Structural properties of UP blade model

Element Number	*Rotor Radius* (m)	*Blade Mass* (Kg/m)	*Stiffness Properties*		
			FlpStff (Nm^2)	*EdgStff* (Nm^2)	*GJStff* (Nm^2)
1	2.0	777.0	1.636E10	1.671E10	6.580E9
2	2.3	777.0	1.636E10	1.671E10	6.580E9
3	2.8	683.5	1.448E10	1.479E10	5.755E9
4	3.5	622.6	1.318E10	1.346E10	5.246E9
5	7.5	507.2	6.229E9	1.112E10	1.874E9
6	9.0	387.3	5.319E9	7.536E9	1.272E9
7	11.0	388.6	5.476E9	7.309E9	1.201E9
8	14.0	423.7	4.554E9	7.414E9	5.892E8
9	19.0	360.7	2.868E9	4.851E9	3.799E8
10	24.0	330.0	1.797E9	4.159E9	2.425E8
11	29.0	314.0	9.383E8	3.511E9	1.394E8
12	34.0	284.8	5.795E8	2.972E9	9.923E7
13	39.0	232.4	2.521E8	2.184E9	4.259E7
14	44.0	184.8	1.632E8	1.585E9	2.649E7
15	47.0	148.8	9.213E7	1.078E9	1.350E7
16	49.0	130.6	7.102E7	1.066E9	1.517E7
17	54.0	99.14	3.840E7	6.300E8	9.87E6
18	57.0	71.19	2.418E7	4.570E8	6.207E6
19	60.0	51.08	1.492E7	3.145E8	4.424E6
20	61.5	8.187	1.202E6	2.765E7	3.015E5

E.2 54m Girder Box-Section Beam Cross-Sectional Geometric Properties

The girder box-section beam consists the structural part of the a large-scale wind-turbine blade. Table E.3 presents the variation of girders and shear webs size with refer to the relative chord length of UP 61.5m wind-turbine model. The aspect ratios n_Y and n_Z imply the ratio of the blade radius (fifth column) to the width Y and the height Z of the girders and shear webs of the beam, respectively.

Table E.3 Girder beam radius correspondence with the UP wind-turbine model radius

Element Number	*Section Number*	*Beam Radius* (m)	*Corresponding UP Blade Radius* (m)	*Corresponding UP Blade Chord* (m)	*Girders Aspect Ratio* n_Y	*Shear Webs Aspect Ratio* n_Z
	B	0.0	6.0			
1	C	3.6	9.6	4.344	5.8	1.8
2	D	7.2	13.2	4.537	6.0	1.9
3	E	10.8	16.8	4.559	6.1	2.2
4	F	14.4	20.4	4.618	6.2	2.6
5	G	18.0	24.0	4.435	5.9	3.1
6	H	21.6	27.6	4.150	5.5	3.5
7	I	25.2	31.2	3.846	5.1	4.6
8	J	28.8	34.8	3.594	4.8	5.4
9	K	32.4	38.4	3.234	4.3	6.7
10	L	36.0	42.0	2.943	3.9	7.0
11	M	39.6	45.6	2.786	3.7	7.7
12	N	43.2	49.2	2.676	3.6	8.9
13	O	46.8	52.8	2.347	3.1	9.8
14	P	50.4	56.4	2.182	2.9	12.1
15	Q	54.0	60.0	1.417	1.9	7.9

In Figure E.3 the distance of each cross-section from beam's root, is presented.

In Figure E.4 the lay-up configuration per section is shown. Each cross-section is noticed by a capital letter which corresponds to a specific girder box-section span. It is obvious that the UD Glass/Epoxy ply number of the girder segments decreases with direction from the root to the tip of the blade. The foam thickness of the right and left shear webs follows a similar trend.

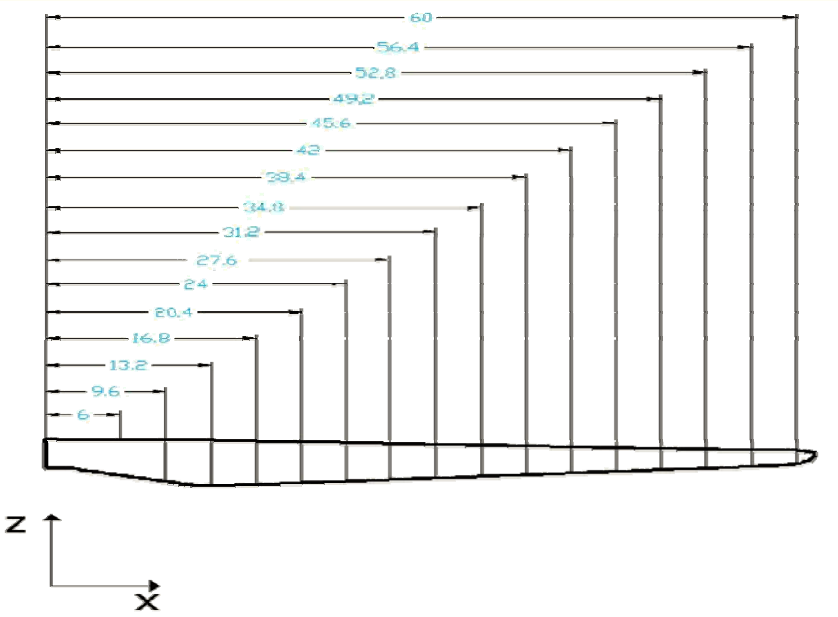

Fig. E.3 Distance of box-beam girder sections from UP blade root

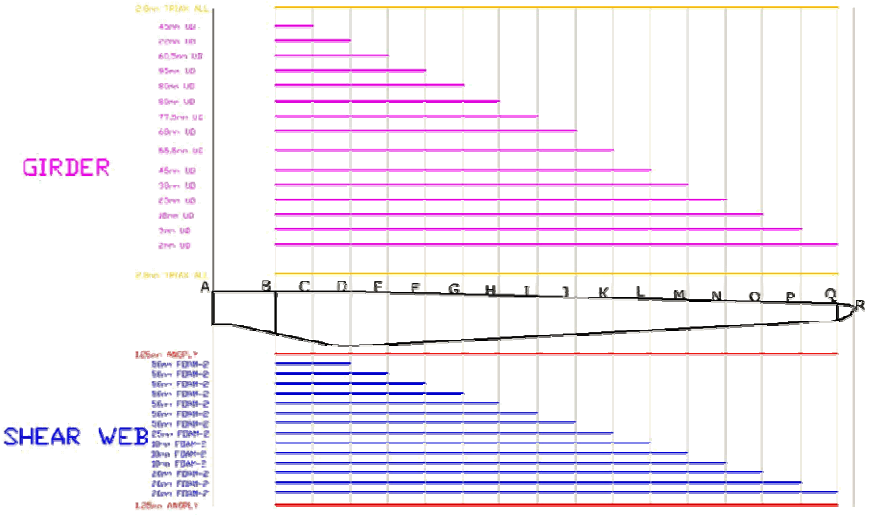

Fig. E.4 Material lay-up configuration for the girder box-section composite beam

About the Author

Dimitris Chortis was born on 13th of August, 1980 in Greece. He grew up in Lefkada island, where he obtained his basic grammar studies diploma from the 1st Lyceum of Lefkada town. In 1999 he moved to the city of Patras, where he entered the Polytechnic School of the University of Patras. In 2004 he completed a degree in Mechanical and Aeronautical Engineering. His diploma thesis involved in the analysis of the dynamic response of plates using active piezoelectric sensors, under the existence of transverse crack. He then pursued a Master degree at the Mechanical Engineering department of National Technical University of Athens from October 2004 to February 2006. His master thesis topic dealt with the estimation of the structural integrity of beams made of composite materials (sandwich beam).

In March 2006 he started his Ph.D. research with the Structural Analysis and Active Materials group at the department of Mechanical & Aeronautical Engineering of the University of Patras, which has resulted in the current work.

As a Ph.D. candidate his scientific interests included the finite element method and its implementation to damping prediction of composite beams and wind-turbine blades. He participated in several meetings of the UpWind EU integrated project (2006-2011), dealing with the structural analysis of a large-scale 5MW wind-turbine blade model. During his Ph.D. studies, he was given also the chance to give undergraduate laboratory lectures regarding the application of finite element commercial packages to realistic engineering problems.

In October 2012 he was awarded by the European Academy of Wind Energy (EWEA) with the Excellent Young Wind Doctor Award 2012 for the contribution and innovation of his Ph.D. Thesis in the Wind Energy scientific field.